ADVANCED STEEL CONSTRUCTION

An International Journal

Volume 14 Number 2

June 2018

CONTENTS

Technical Papers

A Simple Analytical Method for Evaluation of Flexible Rockfall Barrier,
Part 1: Working Mechanism and Analytical Solution
Z.X. Yu, Y.K. Qiao, L. Zhao, H. Xu, S.C. Zhao and Y.P. Liu

A Simple Analytical Method for Evaluation of Flexible Rockfall Barrier, Part 2: Application and Full-Scale Test
Z.X. Xu, Y.K. Qiao, L. Zhao, H. Xu, S.C. Zhao and Y.P. Liu

Investigating the Effect of Joint Behavior on the Optimum Design of Steel Frames via Hunting Search Algorithm
Erkan Doğan, Soner Şeker, M. Polat Saka and Celalettin Kozanoğlu

Flexural Buckling Design of Fabricated Austenitic and Duplex Stainless Steel Columns
Yang-Lu, Zhao-Menghan, Chan Takming and Shang Fan

Pre-Tensioned Steel Cables Exposed to Localised Fires
Yong Du, J.Y. Richard Liew, Hao Zhang and Guoqiang-Li

Dynamic Response Analysis of Wind Turbine Tubular Towers under
Long-Period Ground Motions with the Consideration of Soil-Structure Interaction
Tao Huo, Lewei Tong and Yunfeng Zhang

Use of Different Shaped Steel Slit Dampers in Beam to Column Connections of Steel Frames under Cycling Loading
Mehmet Alpaslan Köroğlu, Ali Köken and Yunus Dere

Composite Effect of Stub Square Steel Tubed Columns under Axia Compression
X.H. Zhou, D. Gan, J.P. Liu and Y.F. Chen

Structural Performance and Design Method of New Mortise-Tenon Full Steel-Tube Scaffold
Liu Hongbo, Zhou Yuan, Chen Zhiua and Liu Qun

Numerical Analysis of Plain and Steel Fiber Reinforced Concrete Filled Steel Tubular Slender Column
Kingsley U. Ukanwa, Charles G. Clifton, James B.P. Lim, Stephen Hicks and Umesh K. Sharma

Announcements by IJASC :
Announcement for ICASS 2018

Website: *http://www.hkisc.org*
ISSN 1816-112X
Science Citation Index Expanded, Materials Science Citation Index and ISI Alerting

Cover: The MGM Mansion Roof in Macau, China. Designed by "Second-order Direct Analysis" without effective length.

e-copy of IJASC is free to download at "www.ascjournal.com" in internet and mobile apps.

ADVANCED STEEL CONSTRUCTION

VOL.14, NO.2 (2018)

ADVANCED STEEL CONSTRUCTION

an International Journal

ISSN 1816-112X

Volume 14 Number 2 *June 2018*

ISSN 1816-112X

Science Citation Index Expanded, Materials Science Citation Index and ISI Alerting

Advanced Steel Construction
an international journal

Cover: MGM Mansion Roof in Macau, China. Designed by "Second-order Direct Analysis" without effective length.
e-copy of IJASC is free to download at "www.ascjournal.com" in internet and mobile apps.

General Information
Advanced Steel Construction, an international journal

Aims and scope

The International Journal of Advanced Steel Construction provides a platform for the publication and rapid dissemination of original and up-to-date research and technological developments in steel construction, design and analysis. Scope of research papers published in this journal includes but is not limited to theoretical and experimental research on elements, assemblages, systems, material, design philosophy and codification, standards, fabrication, projects of innovative nature and computer techniques. The journal is specifically tailored to channel the exchange of technological know-how between researchers and practitioners. Contributions from all aspects related to the recent developments of advanced steel construction are welcome.

Instructions to authors

Submission of the manuscript. Authors may submit on-line at **www.hkisc.org**

Asian Pacific , African and organizing editor :	Professor S.L. Chan, Email: ceslchan@polyu.edu.hk
American editor :	Professor W.F. Chen, Email: waifah@hawaii.edu
European editor :	Professor R. Zandonini, Email: riccardo_zandonini@ing.unitn.it

All manuscripts submitted to the journal are recommended to accompany with a list of four potential reviewers suggested by the author(s). This list should include the complete name, address, telephone and fax numbers, email address, and at least five keywords that identify the expertise of each reviewer. This scheme will improve the process of review.

Style of manuscript

General. Author(s) should provide full postal and email addresses and fax number for correspondence. The manuscript including abstract, keywords, references, figures and tables should be in English with pages numbered and typed with double line spacing on single side of A4 or letter-sized paper. The front page of the article should contain:

a) a short title (reflecting the content of the paper);
b) all the name(s) and postal and email addresses of author(s) specifying the author to whom correspondence and proofs should be sent;
c) an abstract of 100-200 words; and
d) 5 to 8 keywords.

The paper must contain an introduction and a conclusion. The length of paper should not exceed 25 journal pages (approximately 15,000 words equivalents).

Tables and figures. Tables and figures including photographs should be typed, numbered consecutively in Arabic numerals and with short titles. They should be referred in the text as Figure 1, Table 2, etc. Originally drawn figures and photographs should be provided in a form suitable for photographic reproduction and reduction in the journal.

Mathematical expressions and units. The Systeme Internationale (SI) should be followed whenever possible. The numbers identifying the displayed mathematical expression should be referred to in the text as Eq. 1, Eq. 2.

References. References to published literature should be referred in the text, in the order of citation with Arabic numerals, by the last name(s) of the author(s) (e.g. Zandonini and Zanon [3]) or if more than three authors (e.g. Zandonini et al. [4]). References should be in English with occasional allowance of 1-2 exceptional references in local languages and reflect the current state-of-technology. Journal titles should be abbreviated in the style of the Word List of Scientific Periodicals. References should be cited in the following style [1, 2, 3].

Journal: [1] Chen, W.F. and Kishi, N., "Semi-rigid Steel Beam-to-column Connections, Data Base and Modelling", Journal of Structural Engineering, ASCE, 1989, Vol. 115, No. 1, pp. 105-119.

Book: [2] Chan, S.L. and Chui, P.P.T., "Non-linear Static and Cyclic Analysis of Semi-rigid Steel Frames", Elsevier Science, 2000.

Proceedings: [3] Zandonini, R. and Zanon, P., "Experimental Analysis of Steel Beams with Semi-rigid Joints", Proceedings of International Conference on Advances in Steel Structures, Hong Kong, 1996, Vol. 1, pp. 356-364.

Proofs. Proof will be sent to the corresponding author to correct any typesetting errors. Alternations to the original manuscript at this stage will not be accepted. Proofs should be returned within 48 hours of receipt on-line.

Copyright. Submission of an article to "Advanced Steel Construction" implies that it presents the original and unpublished work, and not under consideration for publication nor published elsewhere. On acceptance of a manuscript submitted, the copyright thereof is transferred to the publisher by the Transfer of Copyright Agreement and upon the acceptance of publication for the papers, the corresponding author must sign the form for Transfer of Copyright.

Permission. Quoting from this journal is granted provided that the customary acknowledgement is given to the source.

Page charge and Reprints. There will be no page charges if the length of paper is within the limit of 25 journal pages. A total of 30 free offprints will be supplied free of charge to the corresponding author. Purchasing orders for additional offprints can be made on order forms which will be sent to the authors. These instructions can be obtained at the Hong Kong Institute of Steel Construction, Journal website: http://www.hkisc.org

The International Journal of Advanced Steel Construction is published quarterly by learnt society, The Hong Kong Institute of Steel Construction, c/o Department of Civil & Environmental Engineering, The Hong Kong Polytechnic University, Hung Hom, Kowloon, Hong Kong.

Subscription inquiries and change of address. Address all subscription inquiries and correspondence to Member Records, IJASC. Notify an address change as soon as possible. All communications should include both old and new addresses with zip codes and be accompanied by a mailing label from a recent issue. Allow six weeks for all changes to become effective.

The Hong Kong Institute of Steel Construction
HKISC
c/o Department of Civil and Environmental Engineering,
The Hong Kong Polytechnic University,
Hunghom, Kowloon, Hong Kong, China.
Tel: 852- 2766 6047 Fax: 852- 2334 6389
Email: *ceslchan@polyu.edu.hk* Website: *http://www.hkisc.org/*
ISSN 1816-112X
Science Citation Index Expanded, Materials Science Citation Index and ISI Alerting

ISSN 1816-112X

Science Citation Index Expanded, Materials Science Citation Index and ISI Alerting

Advanced Steel Construction
an international journal

VOLUME 14 NUMBER 2 JUNE 2018

Technical Papers

A Simple Analytical Method for Evaluation of Flexible Rockfall Barrier, Part 1: Working Mechanism and Analytical Solution 115
Z.X. Yu, Y.K. Qiao, L. Zhao, H. Xu, S.C. Zhao and Y.P. Liu

A Simple Analytical Method for Evaluation of Flexible Rockfall Barrier, Part 2: Application and Full-Scale Test 142
Z.X. Xu, Y.K. Qiao, L. Zhao, H. Xu, S.C. Zhao and Y.P. Liu

Investigating the Effect of Joint Behavior on the Optimum Design of Steel Frames via Hunting Search Algorithm 166
Erkan Doğan, Soner Şeker, M. Polat Saka and Celalettin Kozanoğlu

Flexural Buckling Design of Fabricated Austenitic and Duplex Stainless Steel Columns 184
Yang-Lu, Zhao-Menghan, Chan Takming and Shang Fan

Pre-Tensioned Steel Cables Exposed to Localised Fires 206
Yong Du, J.Y. Richard Liew, Hao Zhang and Guoqiang-Li

Dynamic Response Analysis of Wind Turbine Tubular Towers under Long-Period Ground Motions with the Consideration of Soil-Structure Interaction 227
Tao Huo, Lewei Tong and Yunfeng Zhang

Use of Different Shaped Steel Slit Dampers in Beam to Column Connections of Steel Frames under Cycling Loading 251
Mehmet Alpaslan Köroğlu, Ali Köken and Yunus Dere

Composite Effect of Stub Square Steel Tubed Columns under Axia Compression 275
X.H. Zhou, D. Gan, J.P. Liu and Y.F. Chen

Structural Performance and Design Method of New Mortise-Tenon Full Steel-Tube Scaffold 292
Liu Hongbo, Zhou Yuan, Chen Zhiua and Liu Qun

Numerical Analysis of Plain and Steel Fiber Reinforced Concrete Filled Steel Tubular Slender Column 309
Kingsley U. Ukanwa, Charles G. Clifton, James B.P. Lim, Stephen Hicks and Umesh K. Sharma

Announcements by IJASC :

Announcement for ICASS 2018

A SIMPLE ANALYTICAL METHOD FOR EVALUATION OF FLEXIBLE ROCKFALL BARRIER PART 1: WORKING MECHANISM AND ANALYTICAL SOLUTION

Z.X. Yu[1,2], Y.K. Qiao[1], L. Zhao[1], H. Xu[1*], S.C. Zhao[1,2] and Y.P. Liu[3]

[1]*School of Civil Engineering, Southwest Jiaotong University, Chengdu, China*
[2]*National Engineering Laboratory for prevention and control of geological disasters in land transportation, Chengdu, China*
[3]*Department of Civil and Environmental Engineering, The Hong Kong Polytechnic University, Hung Hom, Kowloon, Hong Kong, China*
[*]*(Corresponding author: E-mail: xuhu@home.swjtu.edu.cn)*

Received: 4 January 2017; Revised: 25 May 2017; Accepted: 5 June 2017

ABSTRACT: The flexible rockfall barrier system exhibits large deflection and complex contact behaviors such that sophisticated finite element method and full-scale test are widely used to design this kind of structures, which causes inconvenient for most engineers. In this paper, a simple analytical method is proposed for fast evaluation of the performance of the flexible rockfall barrier system on the basis of system deflection characteristics observed in the full-scale impact tests and, the component deflection characteristics from component tests such as the puncturing deflection of steel wire-ring net, elongation of energy dissipating device, sliding movement of supporting rope and rotation of support structure. The equation for prediction of large deflection of flexible rockfall barrier system was established. The overall deflection is contributed by its components and therefore the analytical solutions for calculation of component deflections were derived based on the space geometry analysis and verified by component tests. The analytical solution for steel wire-ring nets were validated by 17 puncturing tests and the maximum difference was less than 7.4%. Using the discrete ring net model, an explicit dynamic method was employed to simulate the nonlinear behaviors of flexible rockfall barriers with different design energies, i.e. 2000 kJ, 3500 kJ and 5000 kJ. The deflection of each component and the overall deflections from analytical solutions were compared with the numerical simulations with the maximum difference less than 7.9%. Thus, the proposed analysis solution for evaluation of large deflection of flexible rockfall barrier system is valid and ready for engineering design. A companion paper is presented in part two separately with full-scale test for further verification of the proposed method.

Keywords: flexible rockfall barrier, impact, buffer performance, large deflection, analytical solution, full-scale test

DOI: 10.18057/IJASC.2018.14.2.1

1. INTRODUCTION

Flexible rockfall barrier is extensively used as geological disaster protection measure, which is composed of steel wire-ring nets, support structures and energy dissipating devices, using large deformation to achieve buffering and energy dissipation [1]. As shown in Figure 1, when rockfalls impact the flexible rockfall barrier, the impact force will be induced on the steel wire-ring net and then transmit to the support ropes with which the energy dissipating devices are attached. The devices undergo inelastic deformation such that energy dissipation and interception protection are realized. The whole process is accompanied by highly nonlinear mechanical behaviors such as large deformation, significant sliding, material yielding, contact and separation. This process is essentially a conversion between the work and the energy as expressed in Eq. 1.

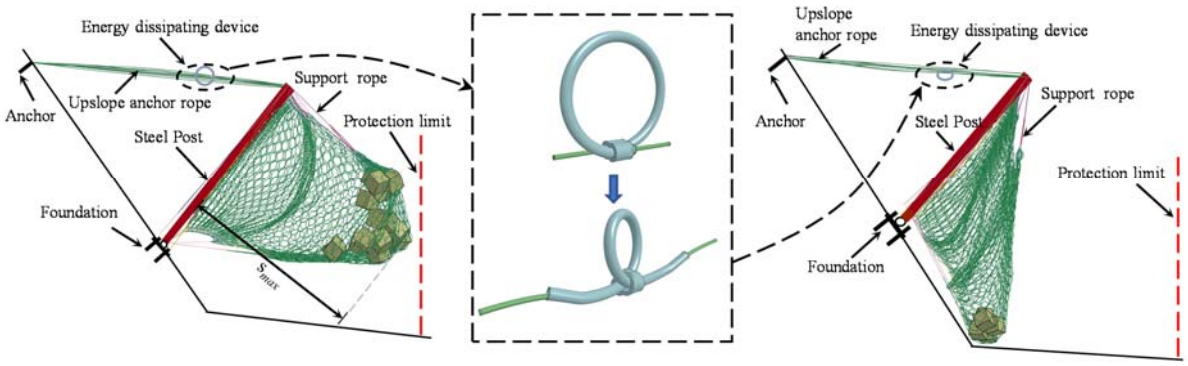

(a) Maximum deflection of system (b) Deformed shape of energy dissipating device (c)Final state of system

Figure 1. Work Process of Flexible Rockfall Barrier System

$$\frac{1}{2}mv^2+E_g=\int_0^{s_{max}}F(s)ds \tag{1a}$$

$$E_{total}=\alpha F_{max}s_{max} \tag{1b}$$

in which, F is the impact force on the system; s is the impact deformation of system; m is the mass of rockfall; v is the velocity of rockfall; E_g is the gravity work after the impact between rockfall and system, depending on the buffer distance; E_{total} is the total energy of rockfall; F_{max} is the maximum impact force; s_{max} is the maximum deformation; α is an empirical coefficient obtained from the tests, ranging from 0.3 to 0.35.

The maximum impact force F_{max} and the maximum deformation s_{max} are two important variables for assessment of system performance. The design of F_{max} and s_{max} within a limit means not only the demand of the bearing capacity of the system, but also the demand of protection limit. For a given demand of protection requirement, the cooperative control of F_{max} and s_{max} determines the configuration of the flexible rockfall barrier system.

According to Eq. 1b, the development of deflection directly affects the buffering performance of the system. The larger of s_{max} within the design limit, the smaller of F_{max} will be obtained and as a result, the better system performance is produced. If s_{max} can be calculated efficiently, F_{max} can be calculated from Eq. 1b, and accordingly, the internal force of each component can be computed based on classical mechanics. Compared with the commonly used numerical simulation methods, the above analytical method provides a new direction for the design of flexible rockfall barrier. It is clear that if the deflection of each component could be obtained accurately at different stages, the system deflection would be well-controlled and therefore the system with optimal suitability between impact deflection and resistance would be designed. However, due to the complex behaviors of flexible rockfall barrier undergoing large deflection, the effective and simple calculation method for the impact deflection of the system is not available in the literature.

Previous researches [2-5] show that the impact process of flexible rockfall barrier generally has three-stage deflection characteristic, as indicated in Figure 2. The first stage is that the steel-wire ring net starts from loose state to tighten state while the internal force of system is low and the energy absorbed is small. The second stage often shows significant sliding movement of support ropes, and clear tensile deformation and energy dissipation of energy dissipating devices. Many full-scale tests show that the percentage of energy consumption in the second stage is 60-80% of the whole impact energy [6, 7]. The third stage is mainly the puncturing deflection of the ring net in the contact area with rockfall, namely bending-straight deformation of the ring net. Due to the different constraints between the rings, the ring deflection generally has two typical modes, i.e. diagonal stretching and diametrical stretching [2, 3]. The elastoplastic deformation of several steel-wire rings, the friction and sliding between the rings are significant and contribute to a portion of energy dissipation. Once the above-mentioned three-stage deflections are completed, the flexible rockfall barrier will eventually show a funnel-shaped deflection, as shown in Figure 3a.

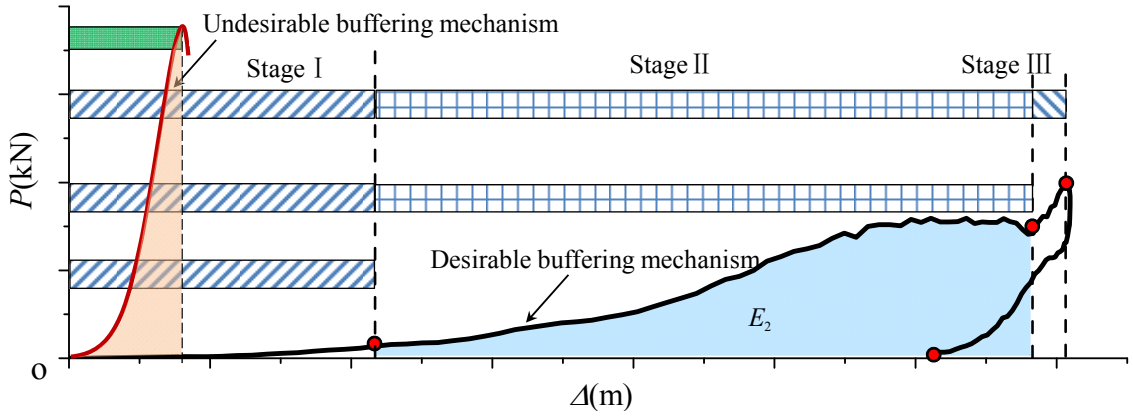

Figure 2. Three-stage Defection and Buffering Mechanism

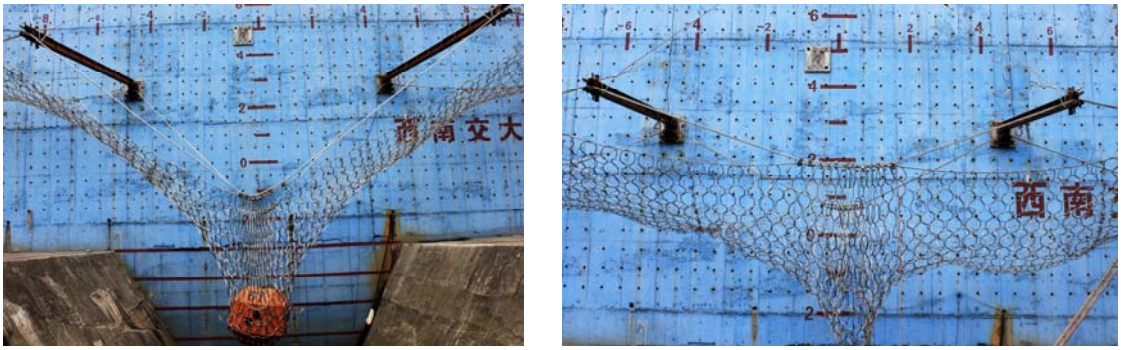

(a) Desired deformed shape (b) Undesired deformed shape

Figure 3. Typical Deformed Shapes

However, due to different level and accuracy of design methods used, different products show very different three-stage deformed shapes, especially in the second stage in which a significant inelastic sliding movement and energy dissipation are occurred due to the mobilization of energy dissipating

device. It can be seen from Figure 2 that the deflection in the second stage is the most prominent one during the overall system deflection. The preferred working characteristics of the energy dissipating device in practical application are tensile deformation, which is depended on the traction-sliding ability of the rope. Thus, the energy dissipating device and the rope have appropriate adaptation relationship so that the system buffering mechanism can be well-developed and leads to a better system performance. The experimental tests showed that the system performance is significantly different for different design of energy dissipating devices of two systems with same configurations of other components, as shown in Figure 3.

In recent years, the researches on study of buffering performance of flexible rockfall barrier system mainly adopted full-scale impact tests and numerical simulations [2-20]. Peila D *et al*. [5] conducted the full-scale impact tests of the flexible rockfall barrier system with various energy levels. For the system with energy level of 400 kJ, the sliding behavior of the support rope is as follows. When the system was impacted by a rockfall, the net ring would slide along the support ropes. However, the motion interference between the nets and the post may easily happen, resulting in a sudden stop of sliding and insufficient development of large deformation. The impact test result also showed that the maximum deformation of the system was only 2.80 m. Based on a field investigation in Jordan Valley, Hong Kong and combined with inverse analysis, Kwan *et al*. [9] found that although the flexible rockfall barrier system with a nominal energy level of 1000 kJ attempted to intercept a rockfall with actual impact energy of 463 kJ, the steel post was seriously damaged, losing the ability of protection. The reason was that the energy dissipating device did not mobilize effectively, leading to inadequate buffering deformation of the system, which is not a desirable performance of the system. The measured and calculated results also showed that the impact deformation was only about 2.5 m. Escallón *et al*. [10] improved the system by releasing several rings on the support rope near the post ends, and formed the bypassing length to defer the motion interference. The improved system enhances the sliding ability of support ropes and increases the buffering performance of the system. The full-scale test result showed that the maximum impact deformation was increased up to 9 m. Unfortunately, due to limited bypassing length, the sliding deformation of support rope is still insufficient and as a result, the motion interference was commonly observed. Therefore, the system cannot be applied to intercept rockfall with high impact energy requiring high demand of large deformation. Gottardi *et al*. [4] carried out 5 full-scale impact tests of flexible rockfall barrier with impact energies of 500 kJ, 1000 kJ, 2000 kJ, 3000 kJ and 5000 kJ respectively. For the 500 kJ and 1000 kJ systems, the control method for support rope sliding is the same as paper [5]; for the systems with design energy greater than 2000 kJ, the transitional ropes are added to the system along the bypassing length, whose principle of sliding control was similar to that in the paper [10]. The difference is that the transitional rope can provide support for the ring net along the bypassing length, but motion interference may still occur. Obviously, the support ropes sliding on the post end smoothly restricts the impact deflection of the system and further affects the buffering performance of the system.

In reality, the causes for the development of large deflection of flexible rockfall barrier system are complicated. The limited number of full-scale tests under idealized conditions can only partially reflect the large deflection behavior of the system, further researches are still needed. Morton *et al.* [11] pointed out that the three-dimensional nonlinear analysis was the most effective complementary means. The technical difficulty of the three-dimensional nonlinear analysis of

flexible rockfall barrier system mainly lies in the establishment of the mechanics model of the steel wire-ring net. At present, there are two representative methods. The first one is the continuous medium model, in which, the discrete ring net elements are modeled by continuous beam elements with a similar restoring force model [12, 13]. However, this method commonly overestimates the stiffness of system and leads to a result with poor accuracy. The second method is a discrete beam element model, which uses the contact boundary to simulate the sliding contact between the rings [4, 15]. This method produces more accurate results, but the modeling is complex with high computational cost. The simple and effective method for quick design of the system is urgently required. Besides, initial stress and initial shape also have great influence on the accurate prediction of the impact deflection, but force-finding and form-finding analysis of such cable-supported structures are major difficulties [21-23].

In this paper, based on the phenomena of impact deformation observed in full-scale impact tests, the working mechanism the flexible barrier system is analyzed. The major factors affecting the large deflection of the system are well considered, for example, the puncturing deformation of net, the stretching of the energy dissipator, the sliding of support rope and the rotation of support structure. Further, an analytical equation for prediction of the large deflection of flexible rockfall barrier system is proposed. The analytical solution accounts for deformation of each component such as the rotation of support structure, the sliding of the support rope and the puncturing deformation of net. Finally, the analytical solution method is verified by 17 puncturing tests with different specifications of ring nets and 3 groups of numerical simulations of whole system.

2. LARGE DEFLECTION MECHANISM AND INFLUENCE FACTORS

The deflection development of a flexible barrier system under 5000 kJ full-scale impact test was recorded by 1000 fps (frames per second) high-speed camera and shown in Figure 4. From the observation of high-speed photos, the process of the deflection development of the system can be described as follows:

In stage I, the ring net slid along the support ropes and gathered in the mid-span of the support ropes near impact area, as shown in Figure 4b. Due to the small deflection characteristics, like bending and straightening, it was easy to find that the internal forces of the rings were small at this stage. From the statistical point of view, although the deflection in stage I accounted for about 30% of the total deflection, the energy dissipated was almost zero since all components were basically in elastic state and at the same time, the energy dissipators remained in the inactive stage.

In stage II, with the increasing of impact force, the internal forces of the support ropes increase dramatically. If the load transferred to the support rope reached a certain value, the energy dissipation device connected to the rope would be triggered and then maintained a steady tensile force, resulting in inelastic tensile deformation and dissipation of impact energy. When the tension of the support rope increased to a certain level fitting with the energy dissipation device, the ring net slid along ropes together forming a funnel-shaped deformation, as shown in Figures 4c and 4d. Along with the sliding of support rope, the funnel-shaped deformation of the system was more distinct, as shown in Figure 4e. Correspondingly, the vertical force of the steel post was rapidly

increased due to the vertical force component in the support rope, and the energy dissipating device connected to anchor rope was activated with rotational behavior of steel post. The impact energy was largely dissipated and the deflection in this stage was up to 60-70% of the total deflection.

In stage III, the deflection of the steel-wire ring net in the contact area was continuously increased. The impact force on the system reached the maximum F_{max}. Finally, the steel-wire rings in the impact zone experienced clear diametrical and diagonal stretching behaviors. The rockfall gradually stopped moving, with a small amplitude of rebounding phenomenon.

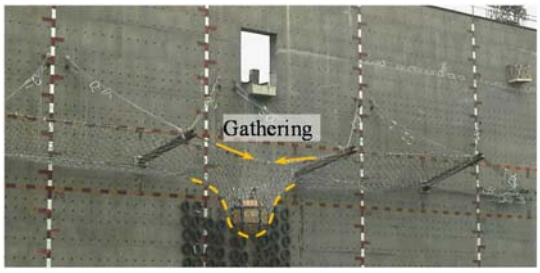

(a) Overall deflection of the system at 0.12s

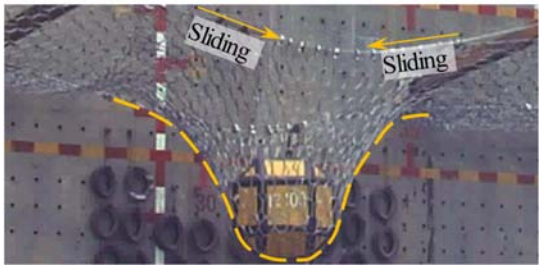

(b) Sliding of the ring net at 0.12s

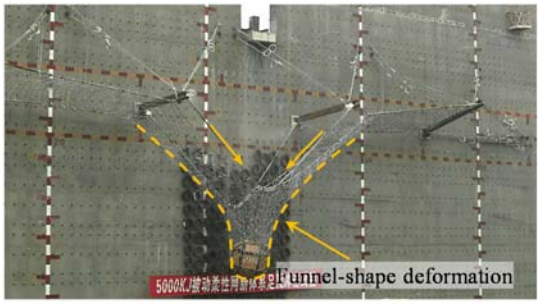

(c) Overall deflection of the system at 0.26s

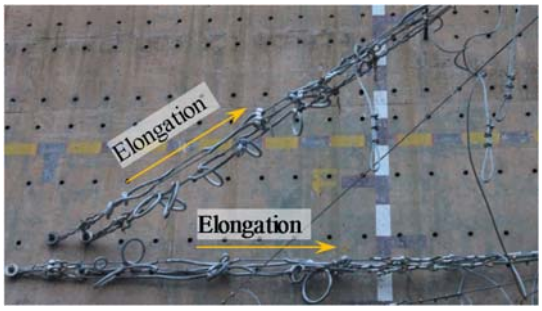

(d) Elongation of energy dissipating devices of support ropes at 0.26s

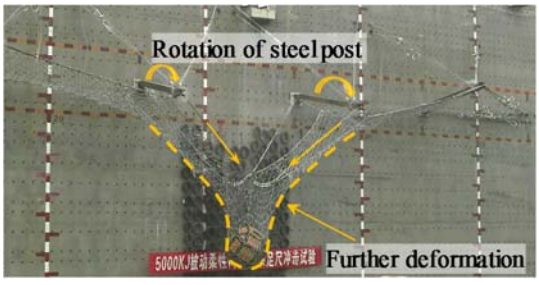

(e) Overall deflection of the system at 0.40s

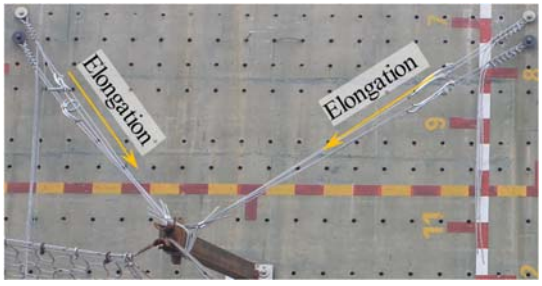

(f) Elongation of energy dissipating devices of upslope anchor ropes at 0.40s

Figure 4. Deflection Process of a Typical Flexible Barrier System

The studies [2-4, 8, 10] showed that the impact time associated with the impact deflection S_{max} were extremely short, ranging from 0.2 to 0.5 second. The impact deflection of a typical flexible

rockfall barrier was shown in Figure 5. The total deflection includes the deformation Δ_1 of supporting structure, deflection Δ_2 of support ropes, deflection Δ_3 of ring net, installation sag f_r and f_n of rope and ring net respectively, and the deflection due to other components. The total deflection may be up to 10 meters [2-7, 15-20, 24-27] and therefore, the behavior of flexible rockfall barrier is a typical large deflection problem. In fact, many factors might affect the buffering behavior of the system, such as the large deflection of the mesh, the deformation of the energy dissipation device connected to ropes, the movement of the post end, the interference of the mesh and support structure. The clear understanding the large defection mechanism and the factors influencing system behavior forms a solid foundation to propose an analytical solution to predict the overall behavior of the flexible rockfall barriers.

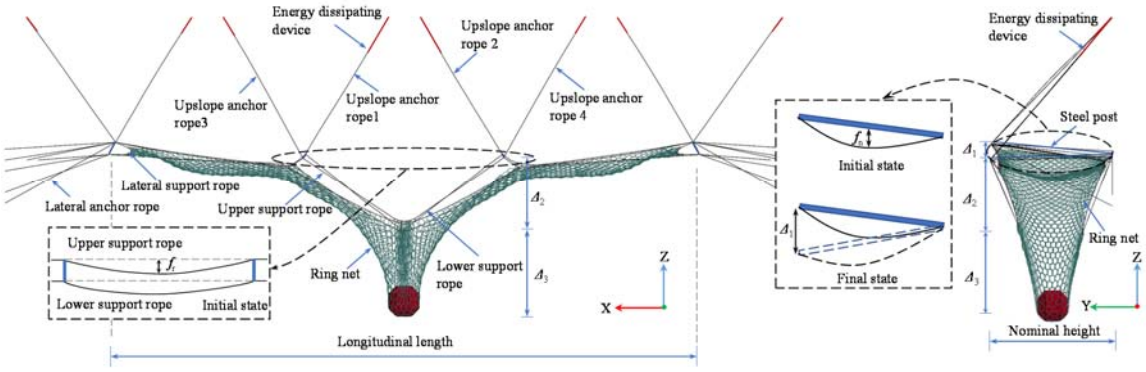

Figure 5. Impact Behavior of Flexible Rockfall Barrier

2.1 Deflection of Ring Net in Impact Zone

Steel wire-ring nets, as the most important component in flexible rockfall barrier system, are subjected to impact load directly. According to European standard [1], ring nets are recommended to use when the protection energy level is from 2000 kJ to 8000 kJ. A steel ring is made of high-strength steel wire woven in parallel or winding way. As shown in Figure 6a, a typical mesh element is composed of five steel rings, the inner one is loosely connected to four outer rings. When the net is loaded, this loose configuration allows the rings to change their positions, achieving an optimal configuration to resist the load. Thus, the deflection of rings is self-adapting. Actually, this self-adapting deflection is also applied to rings and support ropes due to similar loose connection. Morton *et al.* [11] studied the influence of the boundary effect between ring nets on the load transfer and deflection development. They pointed out that the loose connection is favorable to self-adapting deflection and can increase almost 3 times the nominal resistance of the meshes. Based on the field investigations and full-scale impact tests [2], it was found that the deflection characteristics in different regions of the flexible barrier are different due to the sliding between rings. Specifically, the rings in the impact region along the nominal height direction are diametrically stretched with significant elastoplastic deformation. Along the direction of the column spacing, the rings are generally in loose state with sliding-gather phenomenon. In the direct contact region, the rings are diagonally stretched, as shown in Figure 6b. Meanwhile, the remained rings in the non-impact region stay loosely due to lower stress level. The rings in different regions exhibit different behaviors due to various constraint conditions. This provides a basis for describing the

deflection of the mesh in different regions.

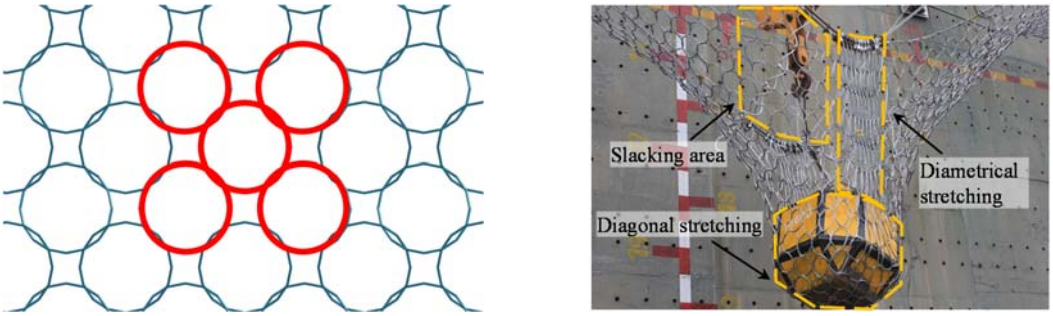

(a) Nesting forms of ring net (b) Deflection of ring net in impact area

Figure 6. Ring Net of Flexible Rockfall Barrier

For simplicity, a ring chain unit as shown in Figure 7 is studied here. The unit is connected to two ropes vertically and several spring elements horizontally, representing the boundary conditions of support ropes and adjacent rings respectively. Under the tensile force T, the ring chain unit shows two typical behaviors, i.e. diametrical stretching and diagonal stretching, depending on the stiffness k of the springs. Assuming that the initial length of the ring chain unit is l_0, and the final length is l_1 on diametrical stretching state or l_2 on diagonal stretching state after the deformation. It was reported from the reference [24] that, if the rings contact each other closely, l_1 will be significantly longer than l_0 while l_2 will be slightly smaller than l_0. However, the full-scale tests [2, 3] show that the ultimate tensile length of the mesh will increase, regardless of the stiffness k of the springs, which is mainly due to the initial gaps between steel-wire rings. In order to simplify the calculation procedure, the authors introduce a coefficient φ associated with tensile deformation as expressed in Eq. 2, which represents the combined effect of diagonal stretching, diametrical stretching and sliding of rings. Based on statistical regularities, φ approximately equals to 0.55 when the surrounding rings are fixed or the rings are impacted by the block directly; φ approximately equals to 0.9 when the surrounding rings are supported by steel ropes with sliding and gathering.

$$\varphi = \frac{l_i}{l_{ni}} = \frac{l_i}{0.5 n_{\text{total}} \pi \text{D}} \quad (i=1, 2) \tag{2}$$

where D is the nominal diameter of the mesh, n is the number of rings connected end to end, and l_i is the actual stretch length, and l_{ni} is the ideally-stretching length.

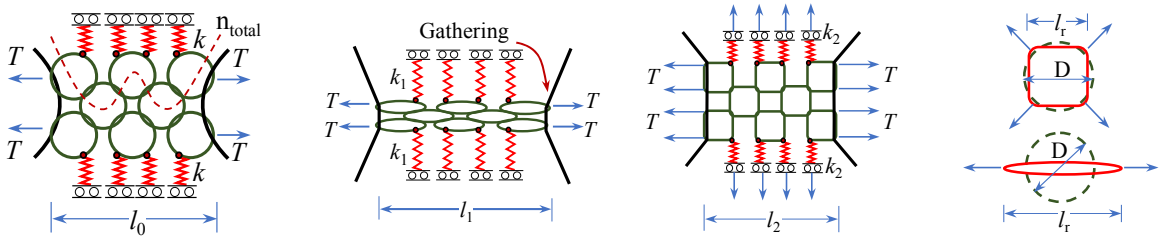

(a) Initial state (b) Diametrical stretching (c) Diagonal stretching (d) Deflection mode

Figure 7. Deflection of Meshes in Partition.

2.2 Deflection of Energy Dissipating Device

When the system is attacked by the rockfall, the impact force is transferred to the ring nets and then to the support ropes. Due to limited energy dissipation capacities provided by elastoplastic deformation of the ring net and steel ropes, the energy dissipating devices connected with steel ropes, as shown in Figure 8a, are necessary to absorb impact energy and protect the ropes and ring nets. Once the tension force in the rope reaches a certain value, the energy dissipating device will start to work, as shown in Figure 8b, leading to the sliding of the connected ropes. The energy dissipating devices attached to steel ropes can consume 60-80% of total impact energy on the system [6, 7]. The research [25] shows that no matter frictional, yielding and hybrid energy dissipating devices, the restoring force characteristics of them are similar, as shown in Figure 8b. The effect of energy dissipating device on the impact deformation of the system is directly related to the mechanical behavior of the connected rope. The key parameters of energy dissipating device include the ultimate elongation δ_{max}, mobilizing force P_a and working force P_s. The elongation δ_{max} determines the sliding distance while P_a and P_s determine the tensile force of connected rope. It should be emphasized that as the energy dissipating devices are directly connected to the ropes, the buffer performance of the system can be ensured only if they are adaptive each other. The energy absorbed by an energy dissipator can be expressed as

$$E_d = \int_0^{\delta_{max}} P(\delta) d\delta \tag{3}$$

where E_d, $P(\delta)$, δ are the energy dissipated, the working force and the elongation of the energy dissipating device respectively.

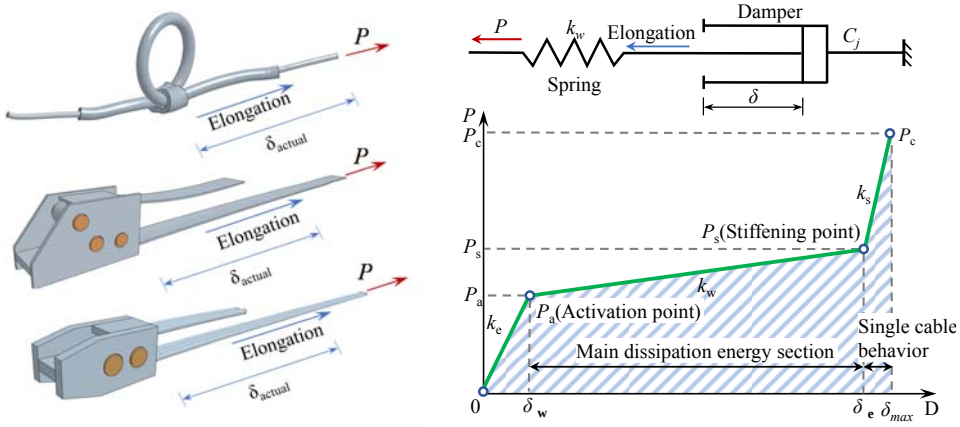

(a) Typical energy dissipating device

(b) Working principle and P-D characteristic of energy dissipating device

Figure 8. Energy Dissipating Device in Flexible Rockfall Barrier System

For practical use with consideration of cost efficiency, the required minimum elongation of the

energy dissipating device can be determined by the energy dissipating demand of the connected ropes in different locations, as shown in Eq.4.

$$\delta_{\min}^{\mathrm{a}} = \frac{E_{\mathrm{a}}}{0.5(P_{\mathrm{a}} + P_{\mathrm{s}})} \tag{4a}$$

$$\delta_{\min}^{\mathrm{s}} = \frac{E_{\mathrm{s}}}{0.5(P_{\mathrm{a}} + P_{\mathrm{s}})} \tag{4b}$$

$$\mu_{\mathrm{a}} = \frac{\delta_{\mathrm{actual}}^{\mathrm{a}}}{\delta_{\min}^{\mathrm{a}}} \tag{4c}$$

$$\mu_{\mathrm{s}} = \frac{\delta_{\mathrm{actual}}^{\mathrm{s}}}{\delta_{\min}^{\mathrm{s}}} \tag{4d}$$

where E_{a} and E_{s}, $\delta_{\mathrm{actual}}^{\mathrm{a}}$ and $\delta_{\mathrm{actual}}^{\mathrm{s}}$, μ_{a} and μ_{s} are the energy dissipating demand, the actual elongation and the efficiency factor of energy dissipating device connected to upslope anchor ropes and support ropes respectively.

Previous researches [6,7] show that, energy dissipation ratios of energy dissipating devices connected to different ropes over whole system present a specific statistical characteristic, as shown in Table 1. When designing a flexible rockfall barrier, the number and configuration of energy dissipating devices connected to different types of ropes can be determined, provided that the performance parameters of a single energy dissipating device are known.

Table 1. Energy Dissipation Ratio

Composition	Upslope anchor ropes	Support ropes	Others
Energy dissipation ratio	0.2	0.6	0.2

2.3 Sliding of Support Rope

The support ropes usually are passed through the ends of steel posts with initial state of suspension, as shown in Figure 9a, and hang the ring nets as shown in Figure 9b. When the ring nets transfer the impact force to the support ropes, the energy dissipating devices connected to these ropes will be mobilized and then dissipate energy via plastic deformation. The mobilization of the energy dissipating device depends on the tension of the associated rope, while the total tensile deformation depends on the available sliding distance of the associated rope. To ensure smooth sliding of support ropes upon the steel posts, movement interferences between different components must be avoided via proper configuration of the whole system. Generally, the dissipating devices usually are set at the anchorages of the ropes, as shown in Figure 9c. Meanwhile, it should be pointed out that the ropes should not wrap with rings to ensure sufficient sliding distance.

(a) Connection between support rope and steel post

(b) Connection between support rope and ring net

(c) Location of energy dissipating devices in the support rope

Figure 9. Setting of Support Rope

At the end of steel post, the support rope will slide upward through the base connection. The mesh or transitional rope will move reversely during the impact of rockfalls, which will alleviate the movement interference problem between the components nearby the post, as shown in Figure 10a. If the support rope or mesh has sufficient sliding distance at the end of the post, the sliding movement can be regarded as a gradual process and therefore, will be beneficial for the improvement of the structural buffering performance. In the mid-span of the support rope, the ring net and the rope are connected by shackles and thereby, the axial direction of the rope is free to slide, as shown in Figure 10b. In the normal direction, the ring net and the rope work together such that the internal force of the rope is self-adaptive and tend to be uniform along the length in the impact zone. When the impact load is longitudinally transferred to the non-impact zones, the internal force of the rope will be rapidly reduced with the increasing distance to the rockfall impact zone. As the actual rockfall impact area is unknown, the end ring nets are often connected to the lateral support ropes with energy dissipating devices to minimize the potential damage, in case the rockfalls hit the end spans, as shown in Figure 10c. The energy dissipating device on the lateral rope will be functioned when the force transferred to the lateral support rope is large to activate it, protecting the lateral post and adjacent structural components.

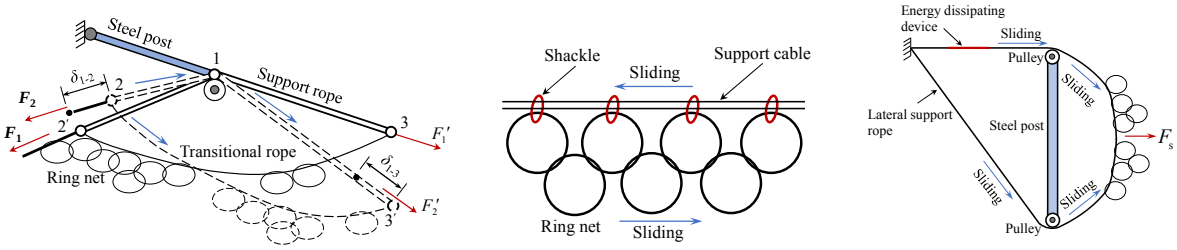

(a) Sliding of support rope at post end

(b) Sliding of support rope at mid-span

(c) Sliding of support rope at end span

Figure 10. Sliding of Support Rope

2.4 Deflection of Support Structure

The support structure is the key component to maintain the integrity of the flexible rockfall barrier. In practice, the form of the support structure should be determined by the actual terrain condition. Under the impact of falling rock, the support structure may undergo elastoplastic deformation, which is undesirable because the support structure has limited energy dissipating capacity compared to the whole system. Also, the main duty of the support structure is to support the steel ropes and ring nets. To reduce the direct impact load on the support structure, the structural forms as shown in Figure 11 are widely used. Generally, the support structure is composed of a rotatable steel post and upslope anchor ropes with energy dissipating devices. The rotation of steel post caused by the elongation of energy dissipating device is significant, leading to the rigid body movement of ring net. The structural form in Figure 11c is most welcomed due to simple configuration and clear deflection. This form is mainly governed by the elongation of the energy dissipating devices connected to upslope anchor ropes, which can be accurately calculated by the geometric method. It should be pointed out that the deflection contribution of the support structure to the total deflection of the system is negligible if it is well designed with careful consideration of structural stability.

(a) Type 1 (b) Type 2 (c) Type 3

Figure 11. Typical Configurations of Support Structure

3. ANALYTICAL SOLUTION OF LARGE DEFLECTION

At present, the prediction of impact response of flexible rockfall barrier is mainly relied on numerical simulation method [2, 4, 6, 8, 10]. However, according to the observation from full-scale tests [3, 4, 5], the deflections of flexible rockfall barriers show typical characteristics and statistical trend. For this reason, an analytical method based on space geometry is proposed in this paper to approximately predict the deflection of a flexible barrier subjected a rockfall impact, as shown in Eq. 5.

$$\Delta_{1a} + \Delta_{2s} + \Delta_{3n} \approx s_{max} \tag{5}$$

in which, Δ_{1a} is the deflection of the support structure, Δ_{2s} is the sliding movement of support ropes, and Δ_{3n} is the deflection of ring net. The detailed calculation of each component will be presented in the followings. The deflection from Eq. 5 can provide a simple and quick method for the selection

and design of flexible rockfall barrier according to the work-energy principle.

3.1 Deflection of Support Structure

As mentioned above, if the stiffness of support structure is large enough, the natural deflection associated with elastoplasticity deformation could be neglected while the rigid body movement associated with rotation of steel post caused by elongation of energy dissipating device connected to upslope anchor ropes should be considered in the prediction of total deflection of a flexible barrier system, as shown in Figure 11c. The spatial positions of a steel post before and after impact are shown in Figure 12. The deflection Δ_1 of the steel post head is the projective height difference in XZ plane before and after the impact, which can be calculated from Eq. 6. The required parameters are obtained on the basis of experimental tests and the assumptions as follows: (1) the configuration of the system is symmetrical; (2) the axial compression deformation of steel post and the sag of upslope anchor rope are ignored; (3) the minimum elongation of energy dissipating device $\delta_{\min}^{i}$ is determined by Eq. 4a; (4) the stretching efficiency of energy dissipating device is defined in Eq. 4b, in which μ_1 is taken as 1.0 while μ_2 is related to the design energy level E. If E is not greater than 2000 kJ, μ_2 is taken as 0.2; if E is not less than 3000 kJ, μ_2 is taken as 0.75. As there is no product with design energy between 2000 kJ and 3000 kJ in market, μ_2 should be further studied if a new system is developed in this range. After the impact, the post was deformed rotationally in both the vertical and horizontal directions at the same time. Because of the different forces on the energy dissipating devices at two sides of the steel post, the elongations of the connected upslope anchor ropes are unequal. The length of upslope anchor rope 1 and 2 change from L_0 to L_1, while the length of upslope anchor rope 3 and 4 change from L_0 to L_2. According to the triangular similarity relation, the deflection in the middle of the steel post Δ_{1a} equals to $0.5\Delta_1$ as

$$\Delta_{\mathrm{a}} = 0.5\Delta_1 = 0.5(H-h) = 0.5\left[L_{\mathrm{AB'}}\cdot\cos\alpha - (H_{\mathrm{d}} - H_{\mathrm{p}}\sin\beta)\right] \tag{6a}$$

$$\cos\alpha = \frac{H_{\mathrm{d}}^2 + {L_{\mathrm{AB'}}}^2 - H_{\mathrm{p}}^2}{2H_{\mathrm{d}}L_{\mathrm{AB'}}} \tag{6b}$$

$$L_{\mathrm{AB'}} = \sqrt{\left(\frac{U_{\mathrm{h}}}{2}\right)^2 + L_2^2 - 2\cdot\frac{U_h}{2}\cdot L_2\cdot\cos\theta} = \sqrt{\left(\frac{U_{\mathrm{h}}}{2}\right)^2 + (L_0+\mu_2\delta_1)^2 - 2\cdot\frac{U_h}{2}\cdot(L_0+\mu_2\delta_1)\cdot\cos\theta} \tag{6c}$$

$$\cos\theta = \frac{{L_2}^2 + U_{\mathrm{h}}^2 - L_1^2}{2L_2U_{\mathrm{h}}} = \frac{(L_0+\mu_2\delta_1)^2 + U_{\mathrm{h}}^2 - (L_0+\mu_1\delta_1)^2}{2(L_0+\mu_2\delta_1)U_{\mathrm{h}}} \tag{6d}$$

where H_{d} is the distance from the anchorage of the upslope anchor rope to the foundation of the steel post in Z direction, H_{p} is the length of the steel post, U_h is the distance between the anchorages of the adjacent upslope anchor ropes, β is the initial angle between post and XY plane. These parameters can be determined in the stage of preliminary design, the projective angle α is the angle between the auxiliary line $L_{\mathrm{AB'}}$ and the XZ plane, which can be determined according to the trigonometric relationship.

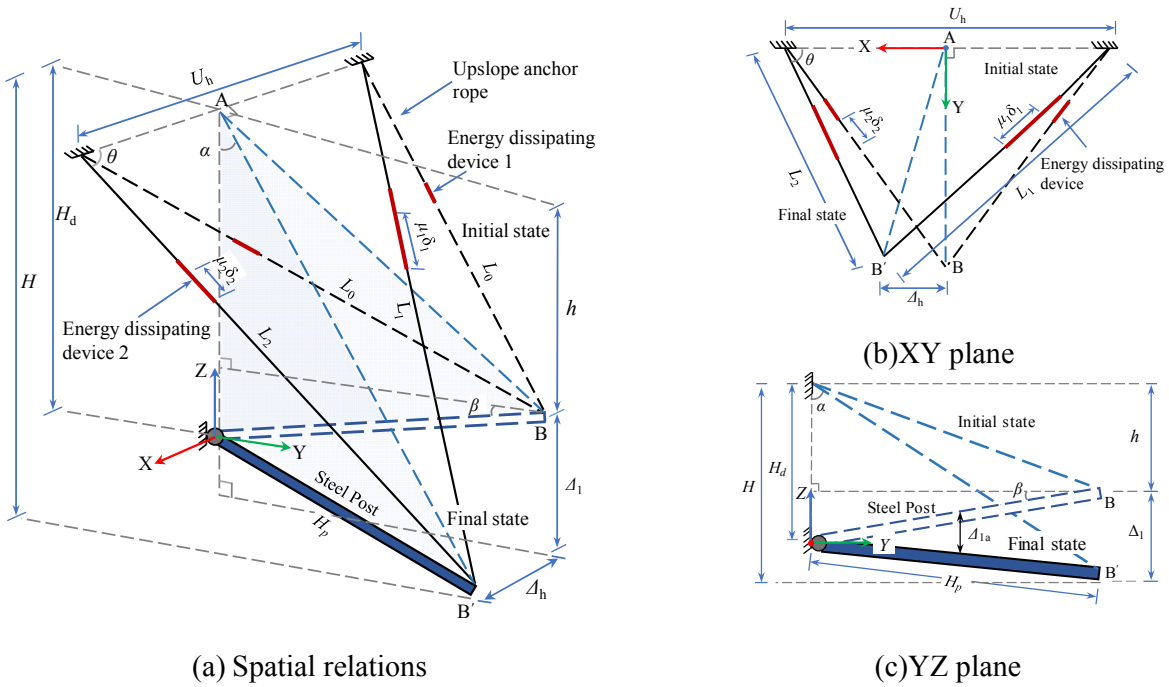

Figure 12. Deflection Δ_{1a} of Support Structure

3.2 Sliding Movement of Support Rope

Owing to the elongation of the energy dissipating device, the support rope on the impact span will deform in a tilted V-shape, as shown in Figure 13a. The projective height of the V-shaped deflection in XZ plane is the component Δ_2 of support rope. The value of Δ_2 is the elevation difference between the end of the steel post and the bottom of the support rope in Z direction. After deducting the initial sag of the support rope f_r, the vertical deflection Δ_{2s} due to the sliding of support rope can be obtained from Eq. 7 as

$$\Delta_{2s} = \Delta_2 - f_r \approx \sqrt{\left(\frac{L_d + \mu_{3L}\delta_{3L} + \mu_{3R}\delta_{3R} - 0.5w_s}{2}\right)^2 - \left[(L_{hd})^2 + (0.25H_p)^2\right]} - f_r \tag{7a}$$

$$L_{hd} \approx \frac{L_d - 0.5w_s}{2} \tag{7b}$$

where L_d is the steel post spacing, μ_{3L} and μ_{3R}, δ_{3L} and δ_{3R} represent the stretching efficiency and the designed elongation of energy dissipating devices connected to support ropes at the left and right respectively. The statistics analysis based on full-scale tests and numerical simulations show that both μ_{3L} and μ_{3R} are close to 1.0.

The experimental tests are also shown that f_r is around 4% of the spacing between steel posts; the bottom of V-shaped deflection can be simplified to a straight segment; and the width of straight segment is around 0.5 times of the diameter of rockfall w_s, as shown in Figure 13b. Considering the

European standard with experimental statistics, the remaining width of the support rope in XY plane h_R is $0.5H_p$ [1-5], which means that the total deflection of support ropes 1 and 2 in Y direction is $0.25H_p$, as shown in Figure 13(b, c).

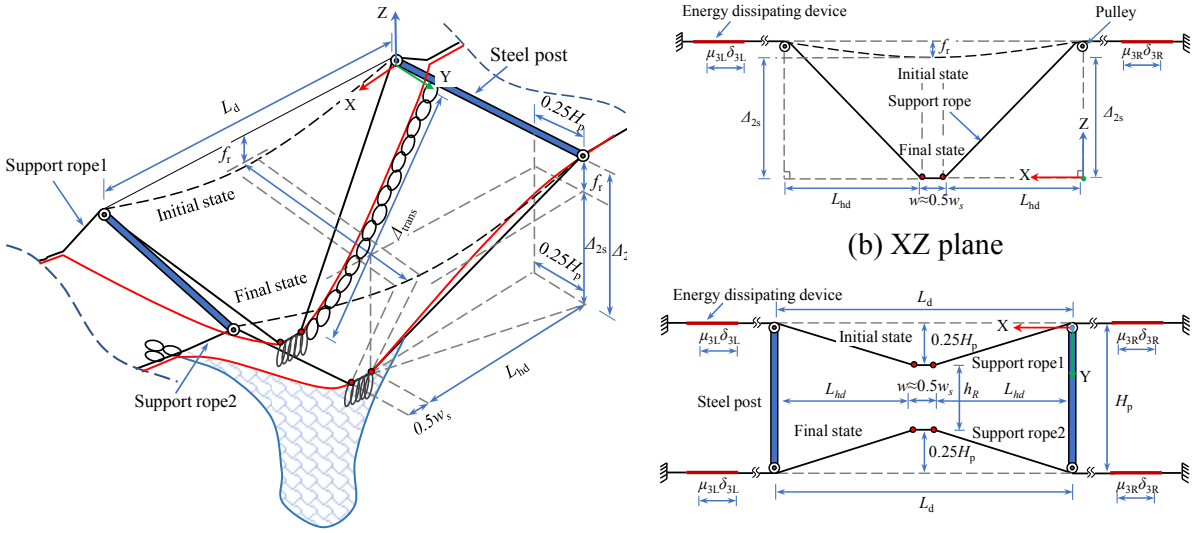

Figure 13. Sliding Movement Δ_{2s} of Support Rope

The sliding of support rope is restricted by the limited stretching length of steel-wire rings along the bypassing length Δ_{trans}, as shown in Figure 13. The length Δ_{trans} can be computed from the geometric relationship, which is the product of the maximum diameter stretching deflection of a single ring and the number of diametrical stretching rings on transitional rope n_t. However, the insufficient development of the diametrical stretching deformation of the steel-wire rings cannot be ignored, and therefore a reduction factor φ defined in Eq. 2 should be adopted. In summary, Δ_{trans} can be calculated as

$$\Delta_{trans} = n_t\left(\frac{\pi D}{2} - D\right)\varphi \tag{8}$$

where D is the diameter of the ring, n_t is the number of diametrical stretching rings on transitional rope. According to the statistics of full-scale tests and numerical simulations, φ is close to 0.8.

From the above, the actual allowable elongation $[\delta_{es}]$ of energy dissipating device on support rope can be estimated from Eq. 9.

$$[\delta_{es}] = [\min(\delta_3, \Delta_{trans}) + \delta_3]/2 \tag{9}$$

where δ_3 is the designed elongation of energy dissipating devices connected to support ropes.

3.3 Puncturing Deflection of Ring Net

As shown in Figure 14, after subjected to the impact of rockfall, the ring net will present an clear funnel-shape. The total deflection of ring net due to sliding, diametrical stretching and diagonal stretching, can be calculated by the elevation difference between the bottom of the funnel-shaped ring net and the bottom of the V-shaped support rope Δ_3. After deducting the initial sag f_n, the puncturing deflection Δ_{3n} of ring net can be obtained. Because the nominal height of the flexible rockfall barrier is less than the longitudinal length, the internal forces as well as deflection are mainly depended on the nominal height direction, which is similar to the one-way slab. The experimental tests show that in the nominal height direction, the steel-wire rings deform as diametrical and diagonal stretching in noncontact and impact areas respectively, as shown in Figure 14a. The relaxation of longitudinal steel-wire rings is worse than that of transverse steel-wire rings, as shown in Figure 14b. For this reason, the internal forces of longitudinal steel-wire rings are also smaller.

From the above, an analytic model, as shown in Figure 14b, can be established according to the deformed shape of ring net to estimate the puncturing deflection Δ_{3n} as

$$\Delta_{3n} \approx \Delta_3 - f_n = \sqrt{\left(\frac{l_i - w_s}{2}\right)^2 - \left(\frac{h_R - w_s}{2}\right)^2} + h_c - f_n \tag{10a}$$

$$l_i = l_{i0} + \left(n_{total} - n_{contact}\right)\left(\frac{\pi D}{2} - D\right)\varphi \tag{10b}$$

$$n_{diagonal} = INT\left(\frac{4w_s}{\pi D}\right) + 1 \tag{10c}$$

where, l_{i0} is the initial nominal height of the ring net, which approximately equals to H_p; l_i is the total stretching deformation in nominal height direction in non-contact area; h_R is the residual interception height; $n_{contact}$ is the number of steel-wire rings impacted by the rockfall; h_c is the local puncturing depth in the contact area. These parameters can be determined in the preliminary design stage.

It is noted that the puncturing deflection of the ring net mainly occurs in the impacting span. Thus, the deflection relies on the gaps between rings in nominal height direction, the number n_{total} of steel-wire rings continuously connected in nominal height direction, the deflection development coefficient φ in the contact and non-contact areas as defined by Eq. 2. The mentioned parameters should be determined by experimental tests.

Assuming that Δ_{3n} mainly depends on the sliding movement between steel-wire rings in nominal height direction and the diametrical stretching deflection of the ring net in non-contact area. According to the statistics of tests, the parameter φ is 0.55 and 0.9 for contact area and non-contact area respectively. The initial gap f_n of the ring net is approximately equal to 15% of H_p.

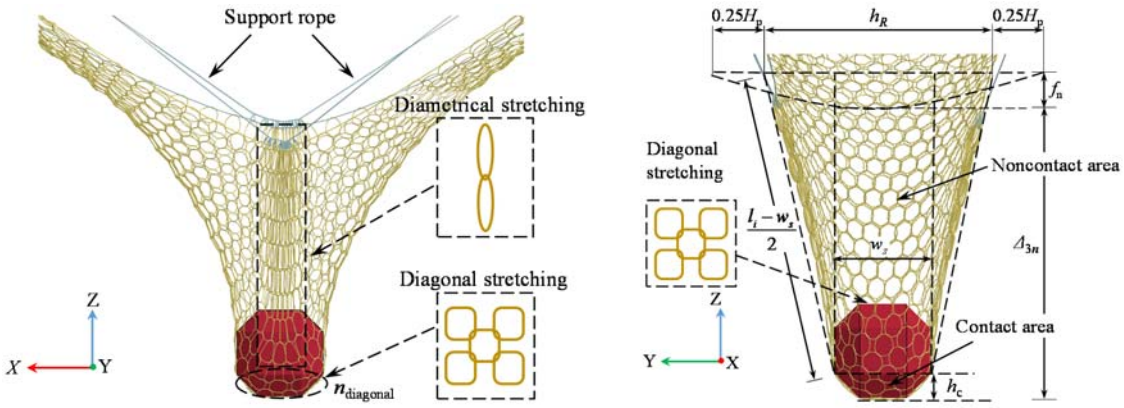

(a) XZ plane (b) YZ plane

Figure 14. Puncturing Deflection Δ_{3n} of Ring Net

4. VERIFICATION EXAMPLES

From the mentioned above, the calculation of Δ_{1a} is based on a relatively accurate spatial geometrical relationship, which mainly relies on the elongation of the energy dissipating device connected to the upslope anchor rope. The calculation of Δ_{2s} is based on several assumptions and therefore the analytical solution is approximate. The deflection Δ_{3n} is mainly affected by the stretching behaviors of the steel rings. Particularly, the sliding and gathering movement of the steel-wire ring net in the impact zone along the longitudinal direction of the support rope has a significant influence on the development of the diametrical stretching behavior of the ring net. The gathering behavior observed from full-scale tests is the dominant one [2, 3]. In addition, Δ_{3n} is the relative deflection of the steel-wire ring net controlled by limiting factors. The accuracy of Δ_{3n} can be improved clearly by increasing the accuracy of coefficient φ. The proposed analytical solution will be validated in this section and the accuracy will be discussed.

4.1 Puncturing Test of Ring Net

Totally 17 ring nets made of different sizes of steel rings were tested in this paper. The specimens in puncturing test were 2800mm×2800mm with the steel rings of R5/3/300, R7/3/300, R9/3/300, R12/3/300, R16/3/300 and R19/3/300. The steel rings are denoted as R*a*/*b*/*c*, where *a* is the number of the windings of steel wire, *b* is the diameter of steel wire and *c* is the diameter of single steel-wire ring. For each kind of steel ring, there were three ring nets except R19/3/300, which only has two specimens. For each specimen, its edges were connected to a reaction frame by shackles. Each ring net was punctured vertically by the displacement loading with a speed of 2 mm/s till the fracture of the net, seen in Figure 15.

The force-displacement curves of the ring nets with different specifications of rings obtained from test were plotted in Figure 16. The test results showed that with the increase of the winding numbers, the puncturing deflection of the net will be decreased with small variation. The total deflection of each specimen was around 1000 mm.

(a) Initial state

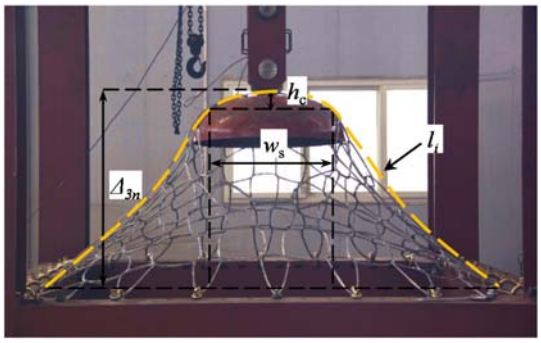

(b) Broken state

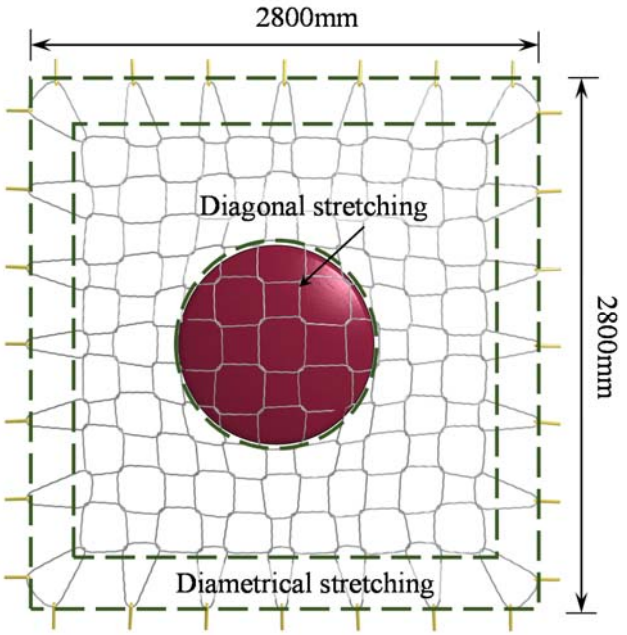

(c) Deformation of ring net

Figure 15. Puncturing Test of Ring Net

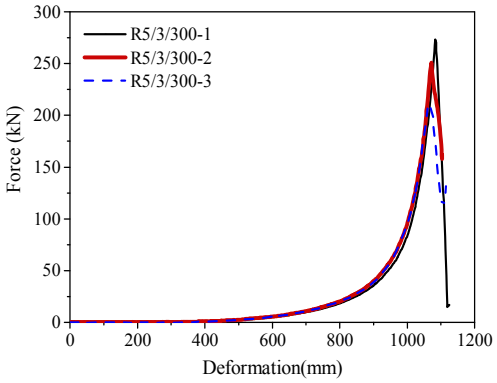

(a) R5/3/300

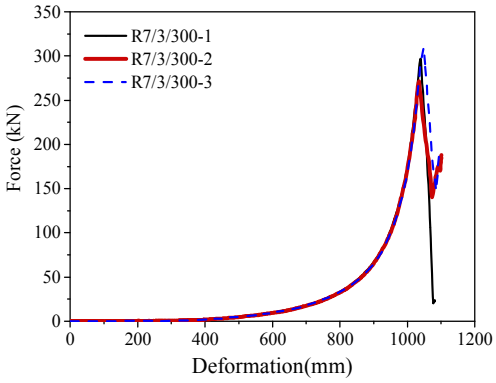

(b) R7/3/300

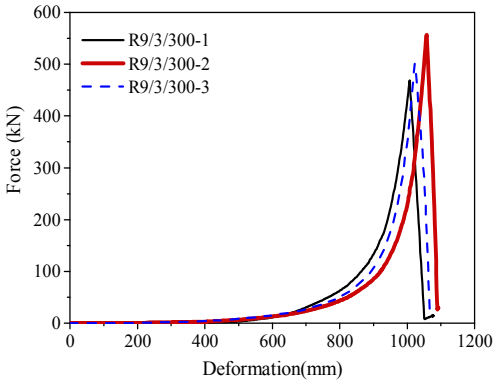

(c) R9/3/300

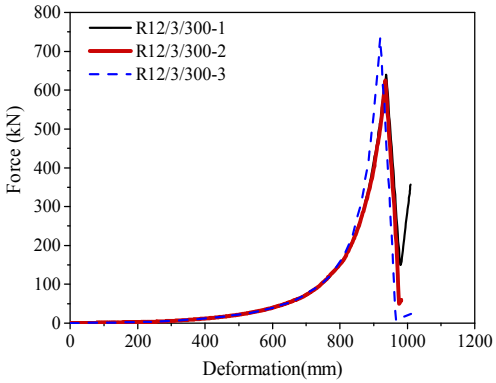

(d) R12/3/300

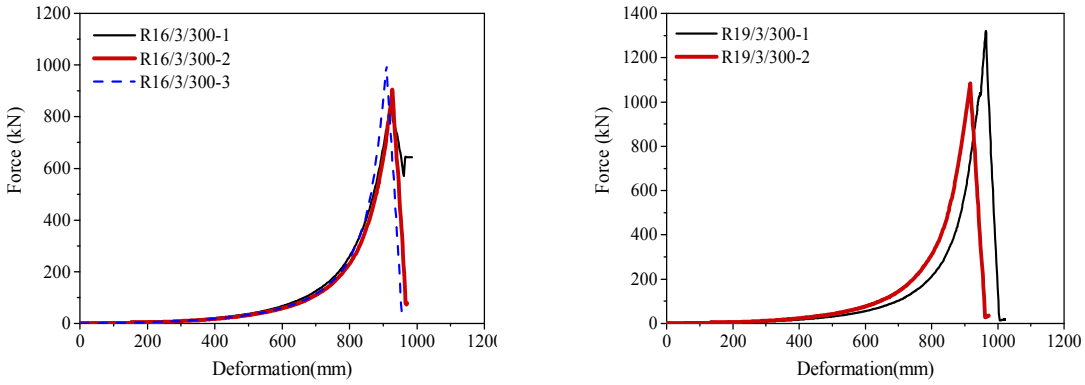

(e) R16/3/300 (f) R19/3/300

Figure 16. Force-Displacement Curves of Ring Nets

The average puncturing deflections of these nets with different specifications of rings are shown in Table 2. The actual stretching deflection l_i is shown in Figure 15b while l_n is the ideally-stretching length, as defined in Eq. 2. The coefficient φ is also defined in Eq. 2. The initial nominal height l_{i0} of the ring net is 2.8 m. The diameter w_s of the press is 1 m, and h_c is 0.11 m. The initial sags f_n of these nets were approximately zero. The parameters n_{total} and $n_{contact}$ are taken as 13 and 5 respectively. As the edge of the net was connected to a reaction frame by shackles, h_R is taken as 2.80 m in the calculation of Δ_{3n}.

Accordingly, the puncturing deflection of the net was 1.02 m calculated from Eq. 10 with φ taken as 0.55. The maximum difference compared with the test results was 7.4%. The value of φ from tests was ranged from 0.56 and 0.57, and therefore the maximum difference between the statistic value of 0.55 was 3.5%.

Table 2 Puncturing Deflection and Coefficients from Test

Deflection	R5/3/300	R7/3/300	R9/3/300	R12/3/300	R16/3/300	R19/3/300
Δ_{3n} (m)	1.07	1.04	1.03	0.98	0.96	0.95
l_i(m)	3.48	3.43	3.43	3.46	3.47	3.49
l_n(m)	6.13	6.13	6.13	6.13	6.13	6.13
φ	0.57	0.56	0.56	0.56	0.57	0.57

4.2 Numerical Simulation of Flexible Barrier Systems

4.2.1 Introduction of Three Flexible Barriers

Three flexible barrier systems with design energy capacities of 2000 kJ, 3500 kJ and 5000 kJ are studied here. The layouts of the models are same and shown in Figure 17. For each system, it is mainly composed of steel posts, steel-wire ring nets, upper support ropes, lower support ropes,

lateral support ropes, upslope anchor ropes, lateral anchor ropes, energy dissipating devices and connected components. The energy dissipating devices are located at the outside of end spans when connecting to support ropes and placed at the anchorage points when connecting to upslope anchor ropes. The configuration and the combination of the energy dissipating devices were determined according to the design impact energy, as given in Table 3. All models have three typical spans. The parameters such as L_d, H_p, H_u, H_d, β and n_t defined in previous sections are listed in Table 4. The steel ropes were made of 6x19S+IWR with tensile strength of 1770 MPa. The ring nets were woven by the high-strength steel-wire, whose diameter was 3 mm and the tensile strength was 1770 MPa [31]. The specifications of the components were detailed in Table 5.

Table 3. Configuration of Energy Dissipation Devices

Model	Energy dissipating device							
	Upper support rope		Lower support rope		Anchor rope		Lateral support rope*	
	P_a/P_s (kN)	δ_{3L}/δ_{3R} (m)	P_a/P_s (kN)	δ_{3L}/δ_{3R} (m)	P_a/P_s (kN)	δ_1/δ_2 (m)	P_a/P_s (kN)	δ_4 (m)
2000 kJ	120/150	2.1/2.1	120/150	2.1/2.1	80/100	1.1/1.1	40/50	1.1
3500 kJ	240/270	2.1/2.1	240/270	2.1/2.1	160/180	1.1/1.1	80/90	1.1
5000 kJ	300/420	2.1/2.1	300/420	2.1/2.1	200/280	1.1/1.1	50/70	1.1

*Note：The energy dissipating devices on lateral support ropes are for conservative design.

Table 4. Geometrical Information of Three Models

Model	L_d(m)	H_p(m)	U_h(m)	H_d(m)	β（°）	n_t
2000 kJ	9.00	5.50	7.50	6.25	10	24
3500 kJ	9.00	6.10	7.50	6.25	10	24
5000 kJ	10.00	5.16	10.00	5.00	0	25

Table 5. Component Specifications

Component		2000 kJ	3500 kJ	5000 kJ
Ring net		R16/3/300	R19/3/300	R19/3/300
Steel wire rope	Upper support	3φ22	5φ22	8φ22
	Lower support	3φ22	5φ22	8φ22
	Lateral support	1φ22	1φ22	1φ22
	Lateral anchor	1φ22	2φ22	2φ22
	Upslope anchor	1φ22	2φ22	4φ22
Steel post		HW200×200×8×12	HW250×250×9×14	□HW250×250×20

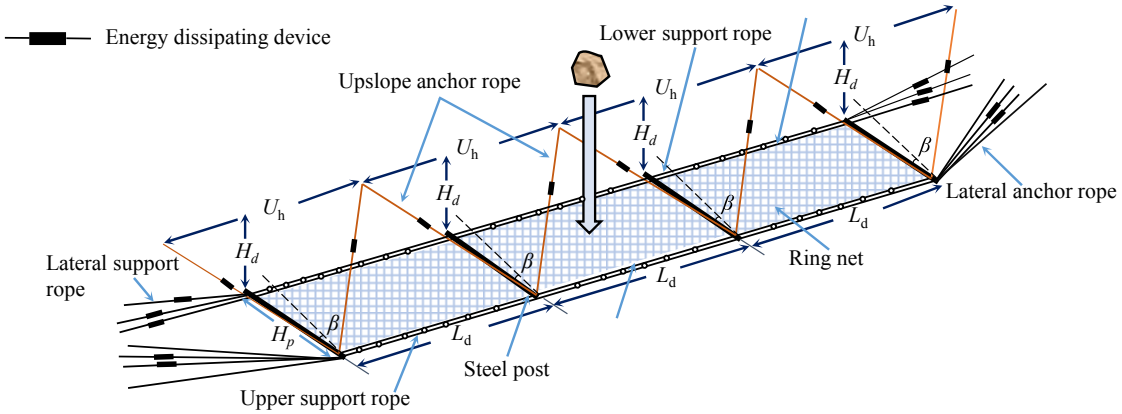

Figure 17. Layout of Three Models

4.2.2 Numerical Models

The computer program LS-DYNA [32] has been employed for the numerical simulation of flexible barrier system. The detailed finite element model can be found in the literature [2, 3]. The Hughes-Liu beam element combined with material type 24, which has the characteristics of piecewise linear plastic, were adopted to model steel-wire rings and energy dissipating devices. The steel posts were modeled by the user-defined integration beam element using I-shape section and the material type 3 with elastic-perfectly-plastic behavior. The steel posts were able to rotate freely in the vertical plane and rotate finitely in the horizontal plane [2, 3, 8]. A special element called seatbelt was adopted to model the support ropes sliding through the post end. The automatic contact of beam to surface was adopted to simulate the actual contact between the rockfall and the steel-wire ring net. The automatic general contact was adopted to simulate the contact between steel-wire rings, support ropes and shackles. Mass-scaling technique was adopted to enhance computational efficiency. In the explicit dynamic analysis, the time step was set to 0.00001s so that the additional mass was less than 5% [32]. Meanwhile, the dynamic relaxation technique has been used to consider the initial stress and the initial deflection due to gravity loads on the systems. The rockfall and steel-wire ring nets were set to be closely at the initial state, and the impact energy of rockfall was considered by modifying its initial velocity. In order to reduce the computational cost and balance the stability of energy state, the termination time was set to 1.0 s uniformly. The material parameters adopted in the numerical model were listed in Table 6.

Table 6. Material Parameters of Component

Component	Density	Poisson's ratio	Elastic modulus	Yield stress
Steel wire ring net	7900 kg.m^{-3}	0.3	1.5×10^5 MPa	1770 MPa
Steel wire rope	7900 kg.m^{-3}	0.3	1.2×10^5 MPa	1770 MPa
Steel post	7900 kg.m^{-3}	0.3	2.0×10^5 MPa	235 MPa
Energy dissipating device	7900 kg.m^{-3}	0.3	1.5×10^5 MPa	-
Rockfall	2500 kg.m^{-3}	0.2	2.0×10^4 MPa	-

4.2.3 Result Comparison and Discussion

The numerical simulations show that the three systems can stop the falling rocks successfully without structural damage. During the impact process, the support ropes slid on the post end smoothly, without interference and buckling of steel posts. The final deformed shapes of the models were shown in Figure 18. The parameters s, Δ_{1a}, Δ_{2s} and Δ_{3n} of each model under the impact of rockfall are plotted in Figure 19. Although each model subjected to different impact energy, the maximum elongation s_{max} were very close to each other, because the deflection of each component was designed with same criterion. From Figure 19b, although the deflection Δ_{1a} due to support structure of each model was largely different, its contribution on the total deflection s was very low. The deflection Δ_{2s} duo to support ropes of each model was close to each other, as shown in Figure 19c, because the working force on the energy dissipating devices connected to the support ropes were well controlled at the same level. Although the performance of these energy dissipating devices were different, the design tensile deformations were consistent, as shown in Table 3. The deflection Δ_{3n} due to ring net of each model also agreed with each other, seen in Figure 19d. The behaviors of the ring nets in the three models show in same trend as reported in the puncturing tests of 17 groups of steel-wire ring nets. It is indicated that Δ_{3n} is less relevant to the configurations of the flexible rockfall barrier.

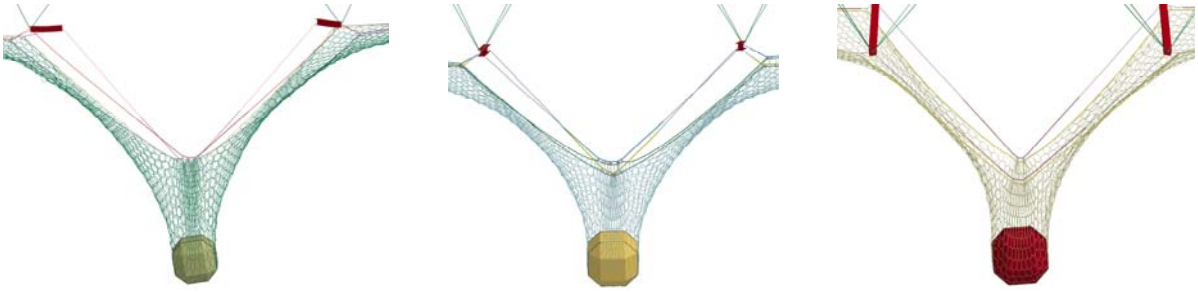

(a) 2000 kJ System (b) 3500 kJ System (c) 5000 kJ System

Figure 18. Final Deformed Shapes of Three Models

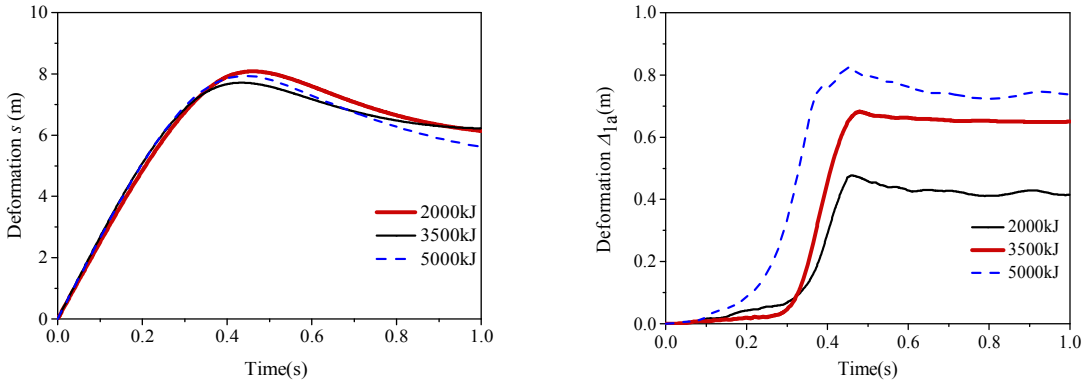

(a) Total Deflection s of System (b) Deflection Δ_{1a} of Support Structure

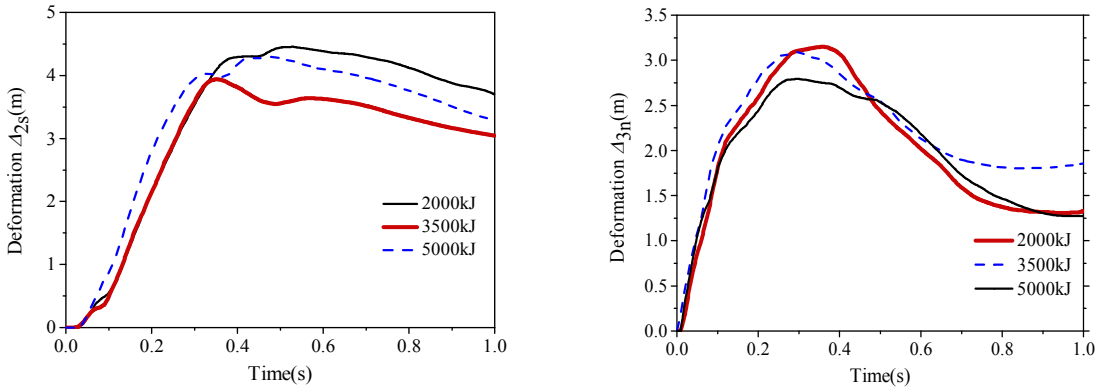

(c) Sliding Movement Δ_{2s} of Support Rope (d) Puncturing Deflection Δ_{3n} of Ring Net

Figure 19. System Elongations and Deflections of Components

When using the proposed analytical solution, the ultimate elongations of the steel-wire rings in 'bypassing length' are 3.28 m, 3.28 m and 3.42 m respectively according to Eq. 8. The elongation δ_3 of the energy dissipating device of support rope all are 2.1 m according to Eq. 4. As $\delta_3<\Delta_{trans}$, Δ_{2s} could be calculated by Eq. 7 and Eq. 9. The deflections Δ_{1a} and Δ_{3n} are calculated by Eq. 6 and Eq. 10 and verified by the numerical simulation results. The parameters involved in the analytic method are listed in Table 7.

Table 7. Parameters used in Analytical Solution

Model	L_0(m)	μ_1	μ_2	w_s(m)	h_c(m)	μ_{3L}	μ_{3R}	n_{toal}	$n_{diagnoal}$
2000 kJ	8.45	1.0	0.20	1.49	0.37	1.0	1.0	27	7
3500 kJ	8.78	1.0	0.75	1.78	0.44	1.0	1.0	28	8
5000 kJ	8.67	1.0	0.75	1.90	0.47	1.0	1.0	26	9

As shown in Table 8, φ_{c1} and φ_{c2} of each model are in the range of 0.54 to 0.60 and 0.89 to 0.92 respectively. Compared with the above statistical values, the maximum difference was 9.1% and 2.2% respectively. Thus, the values of φ_{c1} and φ_{c2} are reasonable and acceptable.

Table 8. Tensile Deformation Coefficient

Model	l_{n1}(m)	l_1 (m)	φ_{c1}	l_{n2}(m)	l_2(m)	φ_{c2}
2000 kJ	1.79	3.30	0.54	8.57	9.42	0.92
3500 kJ	2.15	3.77	0.57	8.48	9.42	0.90
5000 kJ	2.28	3.77	0.60	7.55	8.48	0.89

Accordingly, the analytical deflection Δ_{1a}, Δ_{2s} and Δ_{3n} of each model can be calculated from Eqs. (6, 7, 10). The result indicated as 'Analytical 1' in Table 9 is the analytical deflection when the parameters of $\mu_1\delta_1$, $\mu_2\delta_2$, $\mu_{3L}\delta_3$ and $\mu_{3R}\delta_3$ obtained from numerical simulations are adopted; while the result 'Analytical 2' in Table 9 is the analytical deflection when the statistical value of μ_1, μ_2, μ_{3L}, μ_{3R} shown in Table 7 are adopted. The deflection of each component obtained from numerical simulations directly is also given in Table 9.

Compared with the results from numerical simulation, the analytic solution reproduces the spatial relationship of the system after impact with acceptable accuracy. The difference of system elongation s in 'Analytical 2' is slightly higher than that in 'Analytical 1', because μ is a statistic value in the calculation of 'Analytical 2'. Generally speaking, the accuracy of 'Analytical 2' is acceptable for practical applications. When calculating 'Analytical 1', the data of the elongation of energy dissipating devices are derived from the numerical results directly and therefore, this set results are more accurate. The differences mainly come from the approximation coefficients of deflection in the analytic method, such as the coefficient of ring deflection and the development factor φ, the sag f_r of support ropes, the initial sag f_n of the mesh, the neglection of the initial sag of the upslope anchor ropes and the approximation of the calculating diagrams. The results of large deflection analysis also show that Δ_{2s} accounts for more than 50% of the total deflection of the system, which means that the sliding movement of support ropes has a significant influence on the buffering performance of the system.

Table 9. Result Comparison

Results	Δ_{1a}			Δ_{2s}			Δ_{3n}			s_{max}		
	2000	3500	5000	2000	3500	5000	2000	3500	5000	2000	3500	5000
Simulation (m)	0.49	0.69	0.83	4.45	3.94	4.30	3.15	3.09	2.80	8.09	7.71	7.93
Analytical 1 (m)	0.48	0.68	0.81	4.18	4.05	4.45	3.06	3.17	2.61	7.72	7.90	7.87
Analytical 2 (m)	0.47	0.72	0.81	4.10	4.01	4.26	3.06	3.17	2.61	7.63	7.90	7.68
Error 1 (%)	2.0	1.4	2.4	6.0	2.8	3.5	2.9	2.6	6.8	4.5	0.6	0.8
Error 2 (%)	4.1	4.3	2.4	7.9	1.8	0.9	2.9	2.6	6.8	5.7	2.5	3.2

5. CONCLUSIONS

The flexible rockfall barrier system exhibits large deflection and complex contact behaviors such that sophisticated finite element method and full-scale test are widely used to design this kind of structures, which causes inconvenient for most engineers. In this paper, a simple analytical method is proposed for fast evaluation of the performance of the flexible rockfall barrier system on the basis of system deformation characteristics observed in the full-scale impact tests and, the component deformation characteristics from component tests. The proposed analytical solution is verified by the experimental tests and numerical simulation. The examples show that the proposed method has reasonable accuracy and therefore it is acceptable for practical use.

In summary, the following conclusions could be made from this paper:

(1) The large deflection of flexible rockfall barrier is caused by several factors such as the puncturing deflection of steel-wire ring net, the elongation of energy dissipating device, the sliding movement of support rope and the deflection of support structure. The puncturing deflection of steel-wire ring net is affected by its own configuration and therefore its deformed shape is relatively consistent and predictable. The second main part of total deflection of flexible barrier system is due to the elongation of energy dissipating device, relating to the work efficiency of energy dissipating device.

(2) An analytical method for prediction of the large deflection of flexible rockfall barrier is established based on the linear superposition of the deflection Δ_1 of support structure, the sliding movement Δ_{2s} of support rope, the puncturing deflection Δ_{3n} of steel-wire ring net and the sags of ropes and mesh. The analytical solution of each component has been established based on the spatial geometry relationship. The validity of the analytic solution has been verified by the results of 17 groups of puncturing tests on steel-wire ring net and numerical simulation of three flexible barrier systems. It should be pointed out that the sliding movement of support ropes has a significant influence on the large deflection of the system.

For the typical flexible rockfall barrier system shown in this paper, the proposed analytic method can be used to predict the maximum system deflection effectively. Thus, this method can be used to quickly design the system configuration on the basis of the acceptable maximum deflection and the protection energy requirement. It should be pointed out that if the structural system form is different from that studied in this paper, the proposed equations should be revised with similar procedure. The relevant parameters need to be updated with test results accordingly. The part two of this paper will further verify the proposed method by full-scale test of a flexible barrier system.

ACKNOWLEDGMENTS

The authors are grateful for financial support from the National Natural Science Foundation of China under Grant No. 51678504 and No. 51408498, Department of Science and Technology of Sichuan Province under Grant No. 2018JY0029, Open Fund of National Engineering Laboratory for Bridge Structure Safety Technology under Grant No.310821151102, and the Fund of State Key Laboratory of Geohazard Prevention and Geoenvironment Protection under Grant No.SKLGP2016K013. The last author is grateful for financial support the Innovation and Technology Fund of the Hong Kong SAR Government for the project “Development of an Energy Absorbing Device for Flexible Rock-Fall Barriers (ITS/059/16FP)”.

REFERENCES

[1] EOTA. Guideline for European technical approval of falling rock protection kits (ETAG 027), 2012, Brussels.
[2] Zhao Shichun, Yu Zhixiang, Zhao Lei, et al. “Damage mechanism of rockfall barriers under strong impact loading”, Journal of Engineering Mechanics, 2016, Vol. 33, No. 10, pp. 24-34.
[3] Zhao Shichun, Yu Zhixiang, Wei Tao, et al. “Test study of force mechanism and numerical

calculation of safety netting system [J]". Journal of China Civil Engineering Journal, 2013, Vol.46, No. 5, pp. 122-128.

[4] Gottardi G, Govoni L. "Full-scale Modelling of Falling Rock Protection Barriers". Journal of Rock Mechanics & Rock Engineering, 2010, Vol. 43, No. 3, pp. 261-274.

[5] Peila D, Pelizza S, Sassudelli F. "Evaluation of Behaviour of Rockfall Restraining Nets by Full Scale Tests". Journal of Rock Mechanics & Rock Engineering, 1998, Vol. 31, No. 1, pp. 1-24.

[6] Grassl H, Bartelt P A, Volkwein A, et al. "Experimental and numerical modeling of highly flexible rockfall protection barriers" Proceedings of 12th Panamerican Conference on Soil Mechanics and Geotechnical Engineering, Cambridge, Massachusetts, USA, 2003, Vol. 2589—2594.

[7] Qi Xin. "The Mechanics Performance of Passive Flexible Protection Structure". Southwest Jiaotong University, 2014.

[8] Escallón J P, Wendeler C, Chatzi E, et al. "Parameter identification of rockfall protection barrier components through an inverse formulation". Journal of Engineering Structures, 2014, Vol. 77, pp. 1-16.

[9] Kwan J S H,Chan S L, Cheuk J C Y, et al. "A case study on an open hillside landslide impacting on a flexible rockfall barrier at Jordan Valley", Journal of Hong Kong. Landslides, 2014, Vol. 11, No. 6, pp. 1-14.

[10] Escallón J P, Boetticher V, Wendeler C, et al. "Mechanics of chain-link wire nets with loose connections". Journal of Engineering Structures, 2015, Vol. 101, pp. 68-87.

[11] Morton E.C., Thompson A.G., Villaescusa E. "Testing and analysis of steel wire mesh for mining applications of rock surface support[J]". Proceedings of 5thWorld Congress on Computational Mechanics, Vienna, Austria.

[12] Gentilini C, Gottardi G, Govoni L, et al. "Design of falling rock protection barriers using numerical models". Journal of Engineering Structures, 2013, Vol.50, No. 3, pp. 96-106.

[13] Nicot F., Cambou B., and Mazzoleni G. "Design of Rockfall Restraining Nets from a Discrete Element Modeling".Journal of Rock Mechanics and Rock Engineering. 2001, Vol. 34, No. 2, pp. 99-118.

[14] Bertrand D, Trad A, Limam A, et al. "Full-Scale Dynamic Analysis of an Innovative Rockfall Fence Under Impact Using the Discrete Element Method: from the Local Scale to the Structure Scale". Journal of Rock Mechanics & Rock Engineering, 2012, Vol. 45, No. 5, pp. 885-900.

[15] Moon T, Oh J, Mun B. "Practical design of rockfall catchfence at urban area from a numerical analysis approach". Journal of Engineering Geology, 2014, Vol. 172, No. 5, pp. 41-56.

[16] Gentilini C, Govoni L, Miranda S D, et al. "Three-dimensional numerical modelling of falling rock protection barriers". Journal of Computers & Geotechnics, 2012, Vol. 44, No. 44, pp. 58-72.

[17] Volkwein A. "Numerical modelling of flexible rockfall protection systems". Journal of American Society of Civil Engineers, 2013, Vol. 11, No. 179, pp. 1-11.

[18] De Miranda, S., Gentilini, C., Gottardi, G., Govoni, L., Mentani, A., Ubertini, F. "Virtual testing of existing semi-rigid rockfall protection barriers". Journal of Engineering Structures, 2015, Vol. 85, pp. 83-94.

[19] Govoni, L., de Miranda, S., Gentilini, C., Gottardi, G., Ubertini, F. "Modelling of falling rock

protection barriers" Journal of Physical Modelling in Geotechnics, 2011, Vol. 11, No. 4, pp. 126-137.

[20] De Miranda, S., Gentilini, C., Gottardi, G., Govoni, L., Ubertini, F.,"A simple model to simulate the full-scale behaviour of falling rock protection barriers Physical Modelling in Geotechnics",Proceedings of the 7th International Conference on Physical Modelling in Geotechnics 2010, Vol. 2, pp. 1247-1252.

[21] Qiao Wentao, An Qi, Zhao Mingshan, et al., "Experimental study on the fundamental mechanical features of cable-supported ribbed beam composite slab structure", Advanced Steel Construction, 2017, Vol. 13, No. 2, pp. 96-116.

[22] Guo Jiamin, Yuan Xingfei, Xiong Zhixin, et al., "Force finding of suspended-domes using back propagation (BP) algorithm", Advanced Steel Construction, 2016, Vol. 12, No. 1, pp. 17-31.

[23] Luo Bin, Guo Zhengxing, Chen Xiangnan, et al., "Static equilibrium form-finding analysis of cable-strut system based on nonlinear dynamic finite element method", Advanced Steel Construction, 2015, Vol. 11, No. 4, pp. 452-468.

[24] Escallón J P, Wendeler C.,"Numerical simulations of quasi-static and rockfall impact tests of ultra-high strength steel wire-ring nets using Abaqus/Explicit", 2013 SIMULIA community conference, 2013.

[25] Castanon-Jano L, Blanco-Fernandez E., "Castro-Fresno D, et al Energy Dissipating Devices in Falling Rock Protection Barriers", Journal of Rock Mechanics & Rock Engineering, 2017, Vol 50, pp. 1-17.

[26] J.J. del Coz Díaz,P.J. García Nieto , D. Castro-Fresno , J. Rodríguez Hernández .,"Nonlinear explicit analysis and study of the behaviour of a new ring-type brake energy dissipator by FEM and experimental comparison", Journal of Applied Mathematics and Computation 2010, Vol. 216, No. 5, pp. 1571–1582.

[27] Dhakal S, Bhandary N P, Yatabe R, et al.," Numerical and analytical investigation towards performance enhancement of a newly developed rockfall protective cable-net structure", Journal of Natural Hazards & Earth System Sciences, 2012, Vol. 12, No. 4, pp. 1135-1149.

[28] D. Castro-Fresno, J.J. del Coz Diaz, L.A. López, P.J. García Nieto., "Evaluation of the resistant capacity of cable nets using the finite element method and experimental validation", Engineering Geology, 2008, Vol. 100, No. 1-2, pp. 1–10.

[29] Grassl H, Volkwein A, Anderheggen E, et al., "Steel-net Rockfall Protection – Experimental And Numerical Simulation", Seventh international conference on structures under shock and impact. Montreal, Canada, pp 143–153.

[30] Muhunthan, B., H. Radhakrishnan, "Finite Element Analysis of Hybrid Barrier for Rock Fall Slope Protection", Final Report, Department of Civil and Environmental Engineering, Washington State University, 2007.

[31] GB/T 20118-2006, Steel wire ropes for general purpose, Standardization Administration of the People's Republic of China, Beijing, 2006.

[32] Livermore software technology corporation (LSTC), "LS-DYNA keyword user's manual volume I", 2007.

A SIMPLE ANALYTICAL METHOD FOR EVALUATION OF FLEXIBLE ROCKFALL BARRIER PART 2: APPLICATION AND FULL-SCALE TEST

Z.X. Yu[1,2], Y.K. Qiao[1], L. Zhao[1*], H. Xu[1], S.C. Zhao[1,2] and Y.P. Liu[3]

[1]*School of Civil Engineering, Southwest Jiaotong University, Chengdu, China*
[2]*National Engineering Laboratory for prevention and control of geological disasters in land transportation, Chengdu, China*
[3]*Department of Civil and Environmental Engineering, The Hong Kong Polytechnic University, Hung Hom, Kowloon, Hong Kong, China*
[*]*(Corresponding author: E-mail: zhaolei@my.swjtu.edu.cn)*

Received: 4 January 2017; Revised: 25 May 2017; Accepted: 5 June 2017

ABSTRACT: The companion paper proposed an analytical solution for design of flexible rockfall barrier undergoing large deflection. The part one also reported that the elongation of energy dissipating device plays an important role in buffer mechanism of the system. This paper further studies the governing factors on large deflection of flexible barrier system and then establishes a deflection-control-based mechanical model with improved buffer performance. The factors include the matching property between the energy dissipating device and the support rope, the motion interference during sliding along support ropes, overload protection from lateral support ropes. A prototype model with a nominal energy level of 2000 kJ was designed using the analytical method introduced in part one of the paper. Both full-scale test and numerical simulation were carried out to investigate the response of the prototype model under impact load. The results show that the motion interference and the braking effect during impact test are effectively controlled by the proposed deflection-control-based mechanical model, leading to an optimized design in terms of system buffer performance. Thus, this paper demonstrates the application of the analytical method presented in part one. The full-scale test and numerical simulation prove the validity and accuracy of the proposed method.

Keywords: flexible barrier, buffer performance, rockfall, full-scale test, mechanical behavior, deflection control

DOI: 10.18057/IJASC.2018.14.2.2

1. INTRODUCTION

As discussed in the companion paper, the buffer performance of flexible rockfall barrier system is characterized by significantly large deflection, as shown in Figure 1. The researches [1-8] show that the large deflection of flexible rockfall barrier systems generally includes three parts: elastic deformation, inelastic deformation, and sliding movements between the components. The energy absorbed due to inelastic deformation is mainly caused by the plastic deformation of energy dissipating devices, accounting for 60-80% of the total impact energy on the system [7, 8]. The buffer mechanism mainly provided by energy dissipators and ring net is essentially the working mechanism of flexible rockfall barrier system. The rational design by controlling the inelastic deformation is the key aspect to ensure the performance objectives of the flexible rockfall barrier system.

The full-scale tests [3, 4, 8] show that the system buffer performance is mainly depended on two aspects: the first is the mechanical properties such as working force and potential elongation of the energy dissipating device, and the second is the sliding movements between the ropes with energy

dissipating devices and the support structure, as shown in Figure 1. The poor design on one of them will lead to an invalid buffer mechanism and further cause failure of the system [3, 4]. Qi [8] reported a failure full-scale test due to the broken of support ropes, as the energy dissipating device was failed to trigger due to large activation force required.

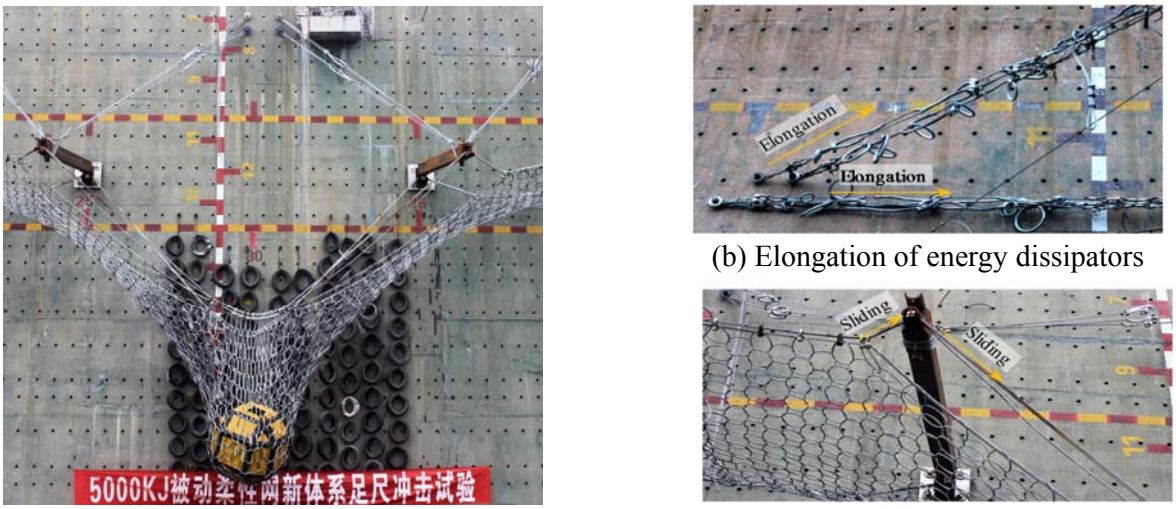

(a) Large deflection of the system (b) Elongation of energy dissipators (c) Sliding of support ropes

Figure 1. Full-scale Test of 5000 kJ Flexible Barrier System (Sichuan, China)

Figure 2 shows the unexpected failure modes of the system caused by the motion interference between ropes and other components. As illustrated in Figure 2a, a brake ring on the support rope was stuck by the post head as the rope slid, resulting in a sudden increase of internal force called brake effect in dynamic response of the system. Once the peak force produced by this brake effect grows excessively, the unpredictable damage occurs such as buckling of the steel posts, rupture of the ropes, or puncture of the net as shown in Figure 2b. To the authors' best knowledge, there is few research on the optimized design by improving the buffer mechanism of the flexible barrier system.

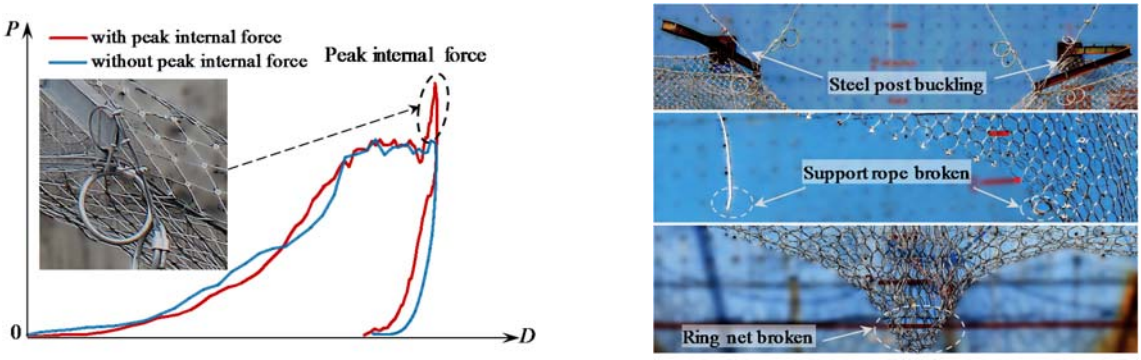

(a) Comparison of P-D curve (b) Failure modes

Figure 2. Structural Failure Caused by Brake Effect

Recently, many researchers studied the mechanical performance of flexible barrier system by means of full-scale tests and numerical simulations [1-18]. The advantages and disadvantages of three commonly used structural forms to overcome the motion interference problem in the vicinity

of steel posts are discussed below.

Peila D *et al*. [1] conducted full-scale impact tests of flexible rockfall barrier systems under various impact energy levels. Regarding the system with nominal energy level of 400 kJ, the configuration of the steel post, support ropes, and steel wire-ring net is illustrated in Figure 3a. The support ropes will slide through the end of the post when the system is subjected to impact load; while the wire-ring net woven into the ropes will easily jammed by the post, leading to limited development of the system deflection. Their test result showed that the maximum elongation of the system under impact load is only 2.80 m, which indicates that the system is not good enough with poor buffer performance.

Escallon *et al*. [2] designed a flexible barrier system with nominal energy level of 2000 kJ. In this system, no shackles were used to connect the steel rings (called free ring hereafter) and the support ropes in the region near the steel post to avoid motion interference and stress concentration. They reported that the support ropes are not threaded through wire-rings (or meshes) of the net at the locations close to steel posts. However, several "free" rings located on the top and bottom of the net are attached to the support ropes via connectors, which were seven round clips made of galvanized steel wire with the maximum breaking force of 13.7 kN [2]. All the connectors allow failing in the maximum energy level (MEL) impact test so that a bypassing length can be created as shown in Figure 3b. Through this treatment, the support ropes slid more smoothly under the impact load and the maximum system deflection was increased up to around 9 m. Nevertheless, this method cannot eliminate the interference problem if larger deflection is required since the net will slide along with the ropes simultaneously. Also, the number of "free" rings is limited.

Gottardi *et al*. [5] carried out a series of full-scale impact tests of flexible barrier systems with nominal energy levels of 500 kJ, 1000 kJ, 2000 kJ, 3000 kJ and 5000 kJ. For the 500 kJ and 1000 kJ systems, the arrangement in the vicinity of the post is the same as that illustrated in Figure 3a. For the systems with higher nominal energy levels (2000-5000 kJ), the bypassing length is created by adding a transitional rope as shown in Figure 3c, performing the similar mechanism to that implemented by Escallon *et al*. [2]. However, a sudden brake of sliding motion of support ropes possibly occurs when the connecting joint between the support rope and the transitional rope (point A) moves to the position of the post (point B). Thus, sufficient length for the transitional rope should be reserved when the system is expected a large deflection. The more length for transitional rope means less length for connecting the ring net, resulting in stress concentration in both the support ropes and the net and consequently weakening the protection ability of the system.

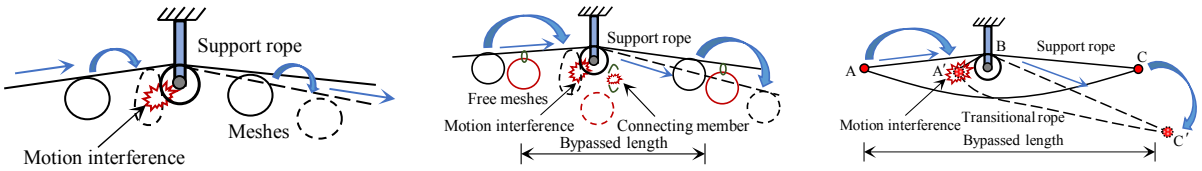

(a) Method 1 (b) Method 2 (c) Method 3

Figure 3. Three Typical Configurations Solving Motion Interference Problem

The above typical configurations from the literature cannot completely solve the motion interference problem in the system involving the large deflection, especially under the extreme loading conditions. Hence, the improvement on buffer performance of flexible barrier system is limited.

This paper aims to improve the system by controlling the large deflection based on the key influence factors. The ratio of the activation force of energy dissipating devices energy to the breaking force of support rope should be designed in a range to ensure their functionality. An improved configuration form for smooth sliding of support ropes was also presented, and the corresponding mechanical model was established. A prototype model of flexible rockfall barrier system with nominal energy level of 2000 kJ was designed based on the analytical solution proposed in the companion paper. Both full-scale impact test and numerical simulation were carried out to investigate the system response under impact load. Furthermore, eight numerical models with different force-displacement relationships of the energy dissipating devices on support ropes were built to investigate their influence on the controlling of large deflection of the system, which provides a case study for system design.

2. BUFFER MECHANISM AND DEFLECTION CONTROL

The layout of support ropes in a typical flexible rockfall barrier system is shown in Figure 4, including the upper and lower support ropes, as well as the lateral support ropes. As mentioned above, a good buffer mechanism is determined by full traveling distance of the energy dissipating devices and the sliding without any stuck of the support rope at the ends of the steel post. It is affected by many factors, such as the ratio of tensile force in the rope to activation force of the energy dissipating device, the configuration of the post end, and the motion interference between components, etc. Thus, the matching design of mechanical properties between components and the optimization design on structural arrangement is of importance for improving the buffer performance of the system.

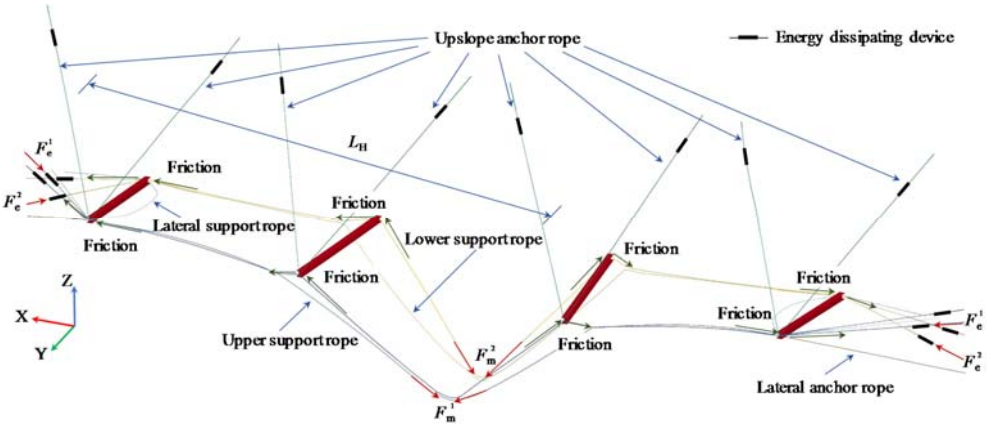

Figure 4. Layout of Support Ropes in Typical Flexible Rockfall Barrier System

2.1 Matching Design of Energy Dissipating Device and Support Rope

The performance of the energy dissipating device is depended on the working tension forces (P_a and P_b) and the elongation (δ). The traction force of the support rope determines whether the energy dissipating device can be activated and work properly. In a typical flexible rockfall barrier system, in order to avoid that the energy dissipating device is interfered by other components during working, it is often connected to the anchorage points of support rope, as shown in Figure 4. Under the impact of rockfall, the support rope in the impact area firstly generates the tension, which will be transferred to two ends of the rope longitudinally. Due to the friction effect of the post-end bearing and the restraining effect of the ring net on the support rope, when the tension is transmitted to the anchorage point on both sides, the internal force of the rope will be certainly

reduced. The relationship between the internal force F_e^i of the rope at anchorage and the internal force F_m^i of the rope at the impact zone is shown in Eq. 1a, in which the transfer coefficient η_i is affected by the traveling distance of the tension and the friction effect along the transmission path. If the tension is largely reduced, the force F_e^i may be less than the activation force P_a of the energy dissipator. In such case, energy dissipator will stop working, and as a result the system buffer performance will be significantly weakened. Being aware of this, it is necessary to properly design the relationship between P_a and F_e^i. In reality, F_e^i is unknown and therefore the ratio (λ_i) of the P_a to the breaking force of support rope (F_u^i) is proposed in Eq. 1b to establish the relationship for practical application.

$$F_e^i = \eta_i F_m^i \left(i = 1,\ 2\right) \tag{1a}$$

$$\lambda_i = P_a^i / F_u^i \left(i = 1,\ 2\right) \tag{1b}$$

Noted that i equals to 1 and 2 for the upper and lower support ropes, respectively.

In this paper, the numerical simulation of flexible rockfall barrier model with the energy level of 500-5000 kJ under MEL state was carried out to study the attenuation relationship between the forces F_e^i and F_m^i. The configuration parameters of the model are referred to GEOBRUGG [19]. The program LS-DYNA [20] was adopted for numerical simulation and the detailed modeling method was referred to the literature [3, 4, 21]. All the numerical simulation models with three functional modules are impacted vertically at the central point of the middle module. The friction coefficient between the support rope and the end of steel post is taken as 0.15 [2]. Table 1 shows the tension forces on the ropes. L_H is the distance between the impact point and the location of energy dissipating device, which is the traveling distance of the tension, as shown in Figure 4.

As shown in Table 1, η_i varied considerably in different models. With the increase of traveling distance and energy level, η_i tended to attenuate. For the energy level is 5000 kJ, the η_i is reduced to 0.57. It means that when the tension transferred from the impact area to the anchorages of support ropes, the reduction is more than 40%, indicating inefficient usage of steel rope. At the same time, excessive reduction of tensile force would make the energy dissipating device out of work and consequently induce large impact force on the system. For safety design of steel rope and anchorage, P_a should be lower than F_e^i. In a word, the energy dissipating device should be properly designed with compatibility of steel rope considering friction effect. For example, Castanon-Jano L [22] suggests that P_a should be less than 50% of F_u^i.

Table 1. Tension Forces on Support Ropes

Energy levels (kJ)	Upper support rope						Lower support rope						
	F_m^1 (kN)	F_e^1 (kN)	F_u^1 (kN)	P_a^1 (kN)	η_1	λ_1	F_m^2 (kN)	F_e^2 (kN)	F_u^2 (kN)	P_a^2 (kN)	η_2	λ_2	L_H (m)
500	149	126	304	50	0.85	0.16	158	139	304	50	0.88	0.16	18.25
1000	159	117	504	50	0.74	0.10	157	104	504	50	0.71	0.10	18.25
2000	161	132	608	100	0.82	0.16	335	274	608	100	0.82	0.16	18.25
3000	231	146	912	100	0.63	0.11	318	175	912	100	0.55	0.11	22.50

5000	496	285	1216	200	0.57	0.16	493	292	1216	200	0.59	0.16	22.50

2.2 An Improved Configuration for Support Ropes

2.2.1 Longitudinal Support Ropes

As discussed in previous section, the improper connection details and structural arrangement may cause the motion interference and further the unexpected damage. In this paper, an improved configuration is proposed for both upper and lower support. The proposed details are presented as follows.

The longitudinal support rope is replaced by a primary support rope and a secondary support rope which are parallel to each other. The wire-ring net is woven through the secondary support rope, which is connected with the primary support rope by shackles. The primary support rope is supported by the ends of posts. The secondary support rope bypasses the ends of posts at the middle functional modules and is only supported by the ends of the edge posts, as shown in Figure 5a. Apparently, the tensile force in the primary support rope increases along with the secondary support rope owing to the connection of the shackles, such that the energy dissipating device mounted on both of them can be activated. It should be pointed out that the angle between the primary and secondary support ropes increases due to the constraints from steel post. This restricts the shackles and wire-ring net to slide towards the post ends. This effect becomes more significant with the increase of the angle θ, as illustrated in Figure 5b. When the system reaches the maximum deflection, the angle θ also reaches the maximum value, approaching to 180° in some cases. The motion interference between support ropes, wire-ring net and post ends can be effectively avoided by using primary and secondary support ropes, seen in Figure 5c.

In the proposed approach, the increment of the angle θ is in a gradual way instead of a sudden change. Besides, the impact force is shared by the primary and secondary support ropes simultaneously and as a result, the risk of overloading on a single support rope as used in the previous systems can be reduced. Moreover, the secondary support rope can mount an additional energy dissipating device to absorb more impact energy. Thus, under the same energy level, the proposed method will lead to a more efficient system regarding better buffer mechanism and consequently the larger deflection. Nowadays, the high strength steel ropes have been extensively used in many kinds of structures, lowering down the cost of this material. One more ropes used in the proposed system only slightly influence the total cost.

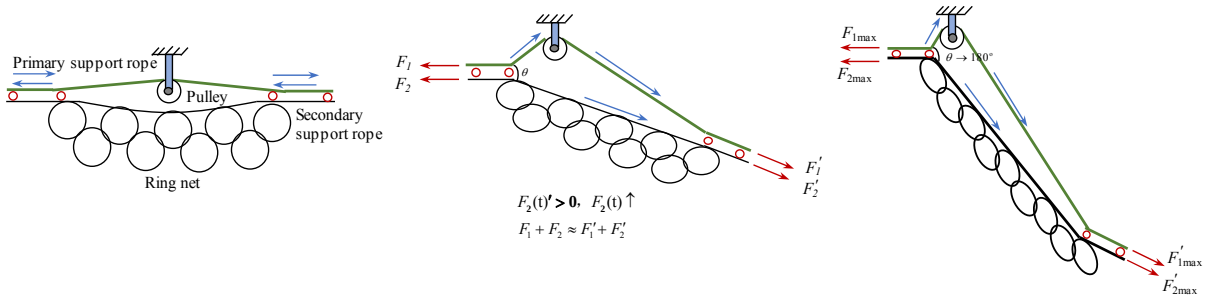

(a) Initial state (b) Intermediate state (c) Limit state

Figure 5. Working States of the Proposed Structural Form

At the mid-span, the primary support rope and the secondary support rope are connected by shackles. They can relatively slide in longitudinal direction as the friction force is small. In the normal direction, the ropes cannot separate freely due to the shackles. This relative sliding movement is extremely beneficial to the restricted effect as mentioned above. The independent movement is essentially a good self-adaptive ability of the system, causing the efficient use of the material as the internal force in the rope tends to be more uniform.

2.2.2 Lateral Support Ropes

As the impact location of the system is unknown in the actual case, the wire-ring net is not directly connected to the edge post so that no additional bending moment will be induced on it if the end span is hit by rockfalls. In previous studies [2, 5], the lateral support ropes were set as a loop to wrap around the top and bottom ends of the edge post, providing longitudinal restraint for the wire-ring net. The edge posts directly resist the lateral loads from the lateral support ropes. To reduce this unfavorable effect, this paper introduces an improved arrangement form for the lateral support rope, seen in Figure 6. The lateral support rope goes through two ends of the edge post, and then extends to the lateral anchorages in the ground rather than ends as a loop. Since tensile force in the lateral rope is directly transferred to the foundation, the extra force on the edge post will be significantly reduced. Besides, more energy dissipating devices can be added to the lateral support rope to archive larger system deflection and at the same time, provide overload protection for the lateral support rope and the edge post.

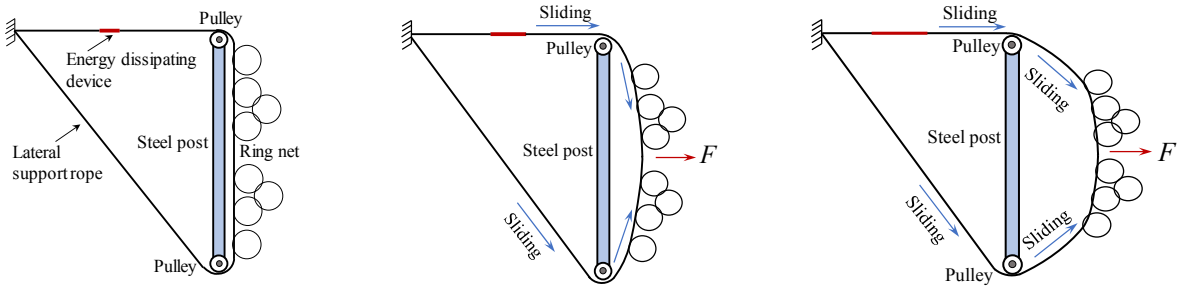

(a) Initial state (b) Intermediate state (c) Limit state

Figure 6. Sliding Control of Lateral Support Rope

2.3 Mechanical Model and Prototype Model of the System

In this paper, a mechanical model of the flexible barrier based on the improved arrangement of the support ropes is established, as shown in Figure 7. The model is composed of spring-damper elements, cable elements, pulley elements and sliding-spring elements. The stiffness k_d and damping C of the spring-damper element can be determined by the properties of the energy dissipating device. The cable element is for modeling of the steel wire rope in the flexible rockfall barrier system, and its characteristic is determined by the actual properties of steel wire rope. The pulley element represents the sliding constraint of the support rope at the post ends, and its sliding ability depends on the friction coefficient μ. The sliding-spring element represents the ring of wire-ring net, whose spring stiffness k_n and the displacement of sliding d can be determined by the puncturing test of the net. For the net complied with given specification, the parameters k_n and d are constant.

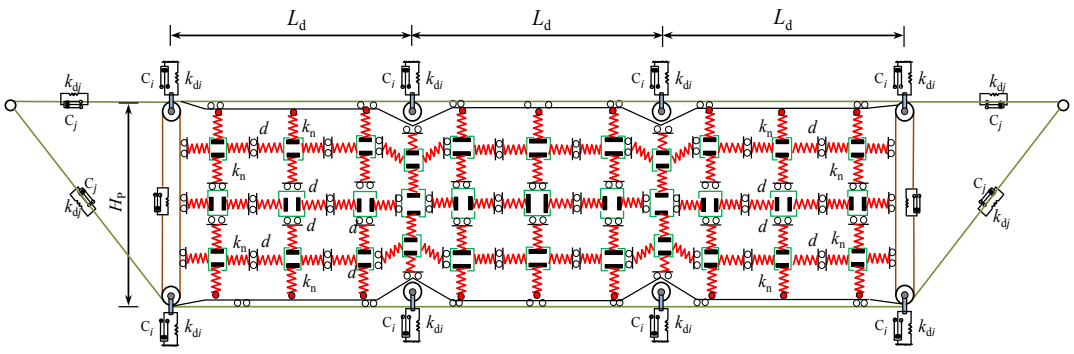

Figure 7. Mechanical Model of the Flexible Barrier System

Accordingly, the prototype model of the proposed flexible rockfall barrier system as shown in Figure 8 is designed to demonstrate the efficiency of the proposed arrangement and analytical method. The system includes steel posts, ring nets, upper and lower primary support ropes, upper and lower secondary support ropes, lateral support ropes, upslope anchor ropes and lateral anchor ropes. The energy dissipating devices are mounted on the extended sections of the primary support ropes, the secondary support ropes and the lateral support ropes. The type, number and arrangement of energy dissipating devices can be determined according to the requirement of protective performance, such as the nominal energy level and the maximum deflection. This system realizes smooth sliding of the support rope and controls the buffer performance by adjusting type, number and arrangement of the energy dissipating devices. Additionally, in order to further increase the buffer performance of system, middle secondary ropes, which are woven through the wire-ring net and anchored to the ground out of the edge posts, can be added between the upper and lower support ropes. The middle secondary ropes are also supported on the steel edge posts, so that they could slide along the steel edge posts. The energy dissipating devices can also be mounted on the middle secondary ropes like other longitudinal support ropes.

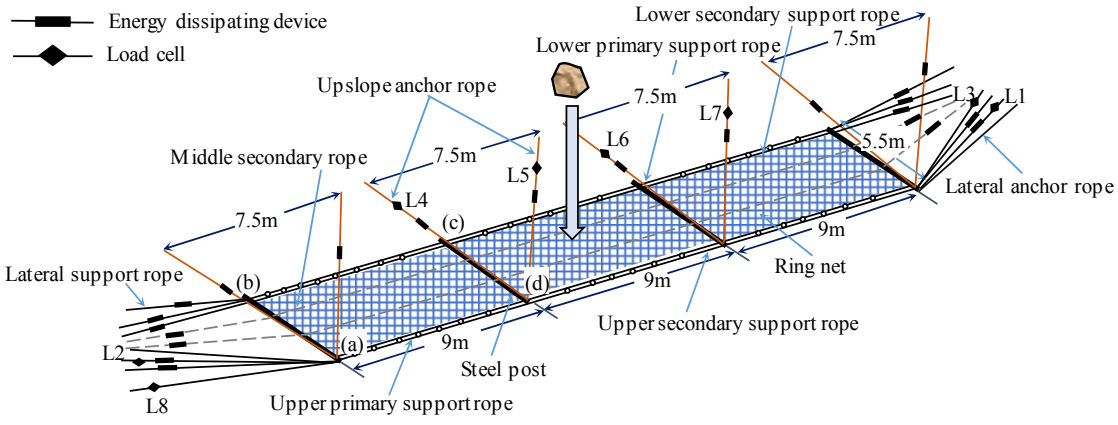

Figure 8. Prototype Model of the Proposed System

3. FULL-SCALE TEST AND NUMERICAL SIMULATION

3.1 Full-scale Test Model

In order to verify the reliability of the proposed system and to further reveal its mechanical behavior under impact load, an experimental prototype model of the flexible barrier system with nominal energy level of 2000 kJ was preliminarily designed according to the analytical solution presented in the companion paper. Figure 9 shows the flowchart of the design procedure, in which the final criterion is depended on whether the maximum deflection is within the design limit or not.

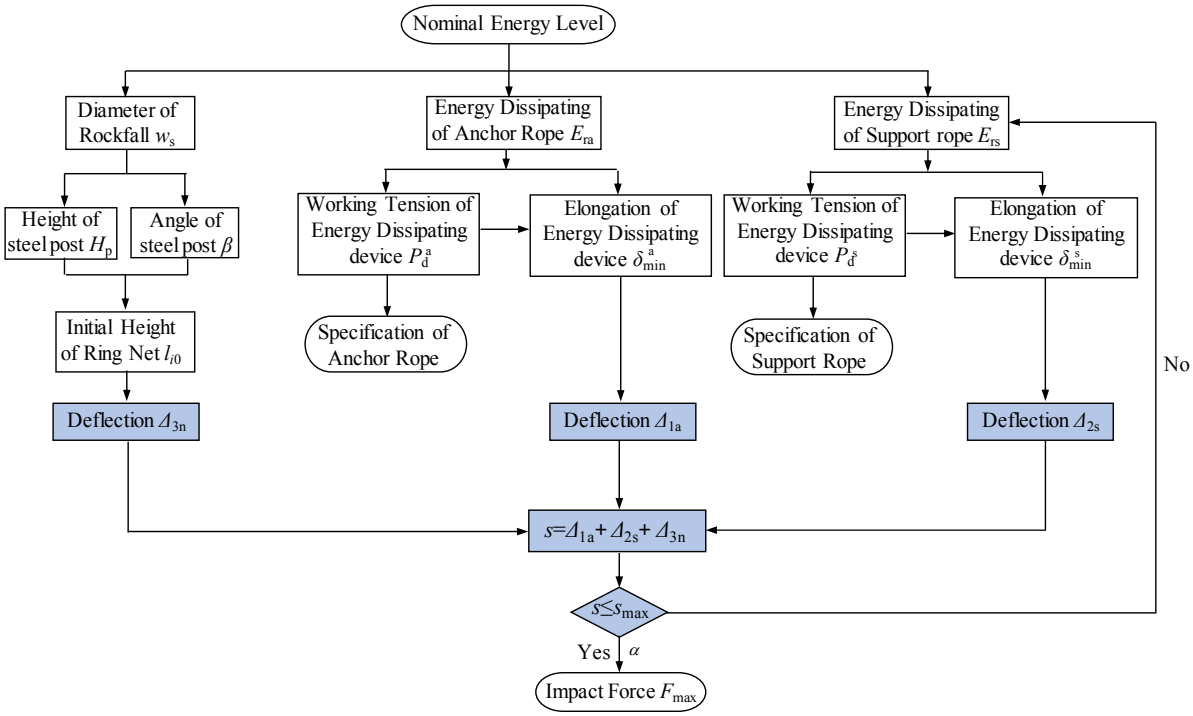

Figure 9. Design Procedure of Flexible Barrier System

In the full-scale test, the height of steel posts H_p is 5.5m, and the post is inclined upwards by 10^o in the vertical plane. The strength grade of steel posts is Q235. The specification of the steel wire ropes is 6x19s+IWR (steel core) with tensile strength of 1770 MPa. The wire-ring net is manufactured by winding high strength steel wires with the diameter of 3 mm and the tensile strength of 1770 MPa [23]. The energy dissipating devices used in the model are brake rings. The maximum elongation (δ) of a single brake ring is 1.1 m, while the working forces P_a and P_s are 40 kN and 50 kN respectively. The universal steel posts with wide-flange are fixed to the reaction wall by pin hinges, which enables the posts to rotate freely in the vertical plane and to rotate finitely in the horizontal plane. The arc-shaped steel plates are constructed on the post caps to reduce the friction effect and to increase the bending radius, also a specific construction is applied for the post foot to ensure smooth sliding of support ropes, as illustrated in Figure 10. The layout of energy dissipating devices and the load cells are shown in Figure 8.

Table 2 shows the details of all main components, the mechanical properties of the energy dissipating devices and deformation of each component based on the analytical solution presented in the companion paper. Energy dissipating ratio in Table 2 refers the ratio between the capacity of the energy dissipating device and the nominal energy level of the system. In particular, the energy dissipating ratio of the upslope anchor rope only involves the ropes connected to the inner post, rather than all the brake rings on the upslope anchor ropes.

Table 2. The Parameters of Main Components

Component		Specification	Energy dissipating device			Deflection
			Energy dissipating ratio	P_a~P_s	δ	
Ring net		R16/3/300		-		Δ_{1a}=3.06m
Steel wire rope	Upper primary support	2φ22	18.9%	80~100kN	2.1m	
	Lower primary support	2φ22	18.9%	80~100kN	2.1m	
	Upper secondary support	1φ22	9.5%	40~50kN	2.1m	Δ_{2s}=4.18m
	Lower secondary support	1φ22	9.5%	40~50kN	2.1m	
	Lateral support	1φ22	4.5%	40~50kN	1.1m	
	Upslope anchor	1φ22	19.8%	80~100kN	1.1m	Δ_{3n}=0.48m
	Lateral anchor	1φ22		-		
Steel post		HW200×200		-		

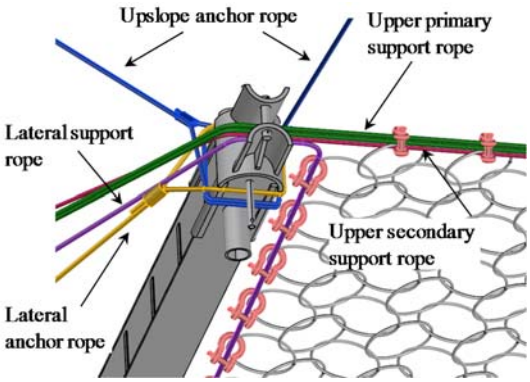

(a) Cap of edge post

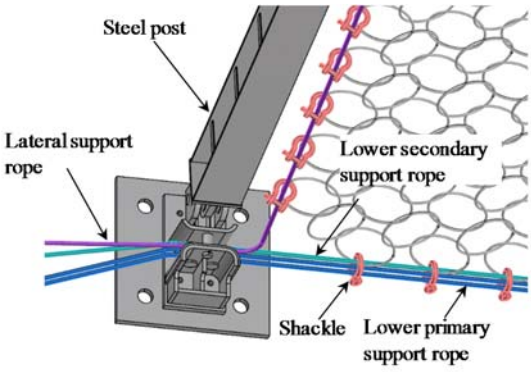

(b) Foot of edge post

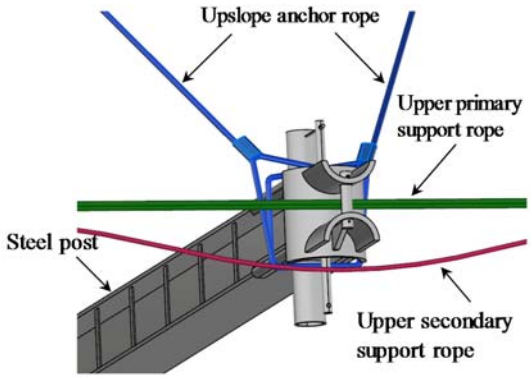

(c) Cap of inner post

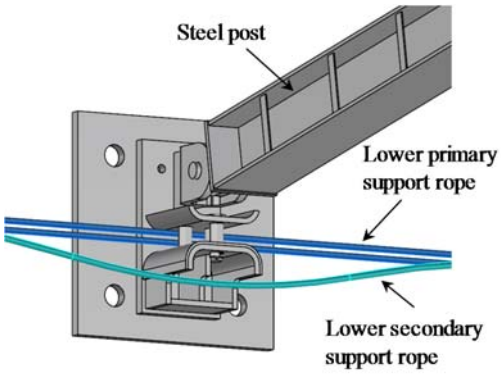

(d) Foot of inner post

Figure 10. Construction Details of Steel Post

The model for the full-scale test has three functional modules. The photos in Figure 11 show the full-scale test model before impact test.

(a) Axonometric view (b) Side view

Figure 11. Full-scale Test Model before Impact Test

3.2 Test Setup

The Full-scale impact test was conducted in the National Engineering Laboratory for Prevention and Control of Geological Disasters in Land Transportation of Southwest Jiaotong University (Sichuan, China). The experimental test system mainly consists of reaction wall, impact pool, traveling portal crane, impactor, high-speed camera, load cells, and data acquisition instrument, as shown in Figure 12. The impact test was conducted according to the European and U.S. standards [21, 24-26]. The impactor is a polyhedral reinforced concrete block and weighs 6 tons. During the test, the traveling portal crane was used to lift the impactor to a target height of 34 meters, aiming at the central point of the middle functional module and then releasing the impactor freely, which can generate a velocity of 26 m/s to impact the barrier structure. The high-speed camera was used to record the whole process of impacting, monitoring the deformation of system and the elongation of energy dissipating devices. The acceleration versus time curve of impactor can be obtained by differential of the velocity-time curve, and then the time-history curves of impact force of impactor can be also obtained. In addition, the tensile force versus time curves of the support ropes and the anchor ropes can be obtained by the load cells which were pre-arranged on the ropes. The sampling frequency of the test is 1 kHz.

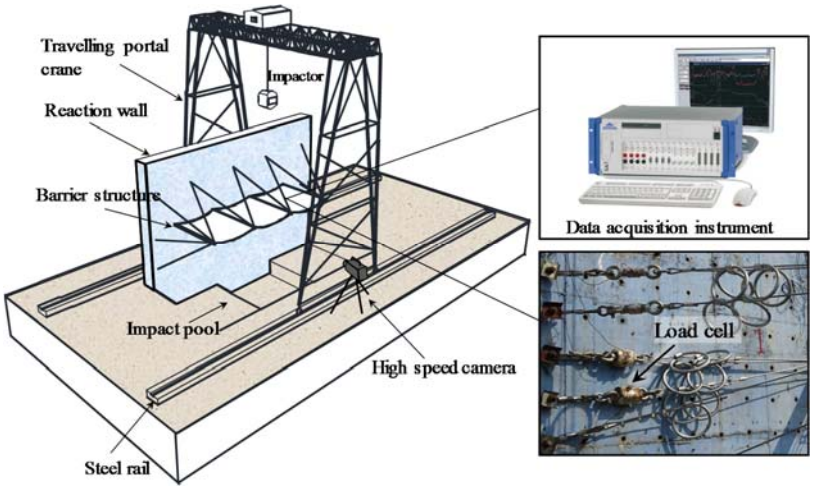

Figure 12. Artificial Test Site and Experimental Equipment

3.3 Performance of the Proposed System

The numerical modeling approach used in the previous companion paper is adopted to build a numerical model with energy level of 2000 kJ [3, 4, 21]. Form-finding analysis [27-29] of the model has been done before the impact process. The mechanical behavior of the deflection-control-based system under the impact load is investigated by the full-scale test and numerical simulation. At the same time, the accuracy of the numerical simulation used in this paper can be verified by the full-scale test results, so that the following parametric analysis can be further conducted based on the numerical model.

The curves of displacement versus time and impact force versus time from full-scale test are plotted in Figure 13 against the numerical simulation results. It can be seen that the deflection-control-based flexible barrier system has no clear peak internal force under the impact of rockfall. Figure 14 compares the results of the full-scale test (first column) and the numerical simulation (second column) at the four typical moments during the whole impact: (1) impactor began to contact with the ring net; (2) the energy dissipating devices on support ropes was activated; (3) the maximum displacement of impactor was reached and; (4) the impactor rebounded and finally stopped. The third column depicts the z-location of the impactor measured by the full-scale test. Both the full-scale test and numerical simulation show that the deflection-control-based flexible barrier system has a three-stage deflection characteristic under the impact of rockfall [3, 4].

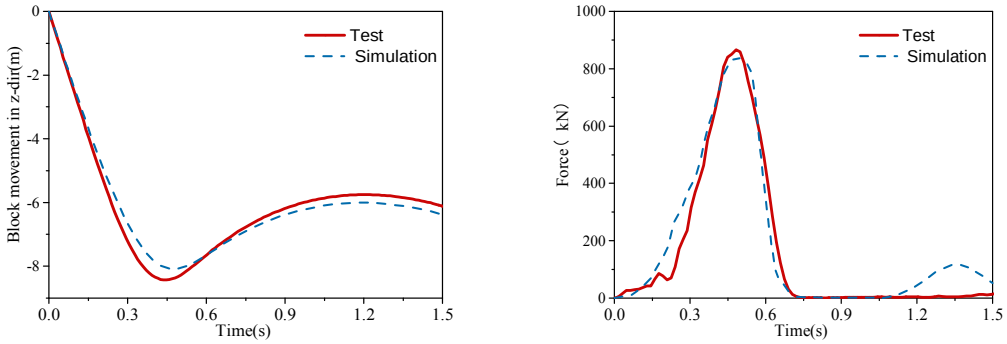

(a) Displacement time-history of the block (b) Impact force time-history of the block

Figure 13. Deflection and Force Responses

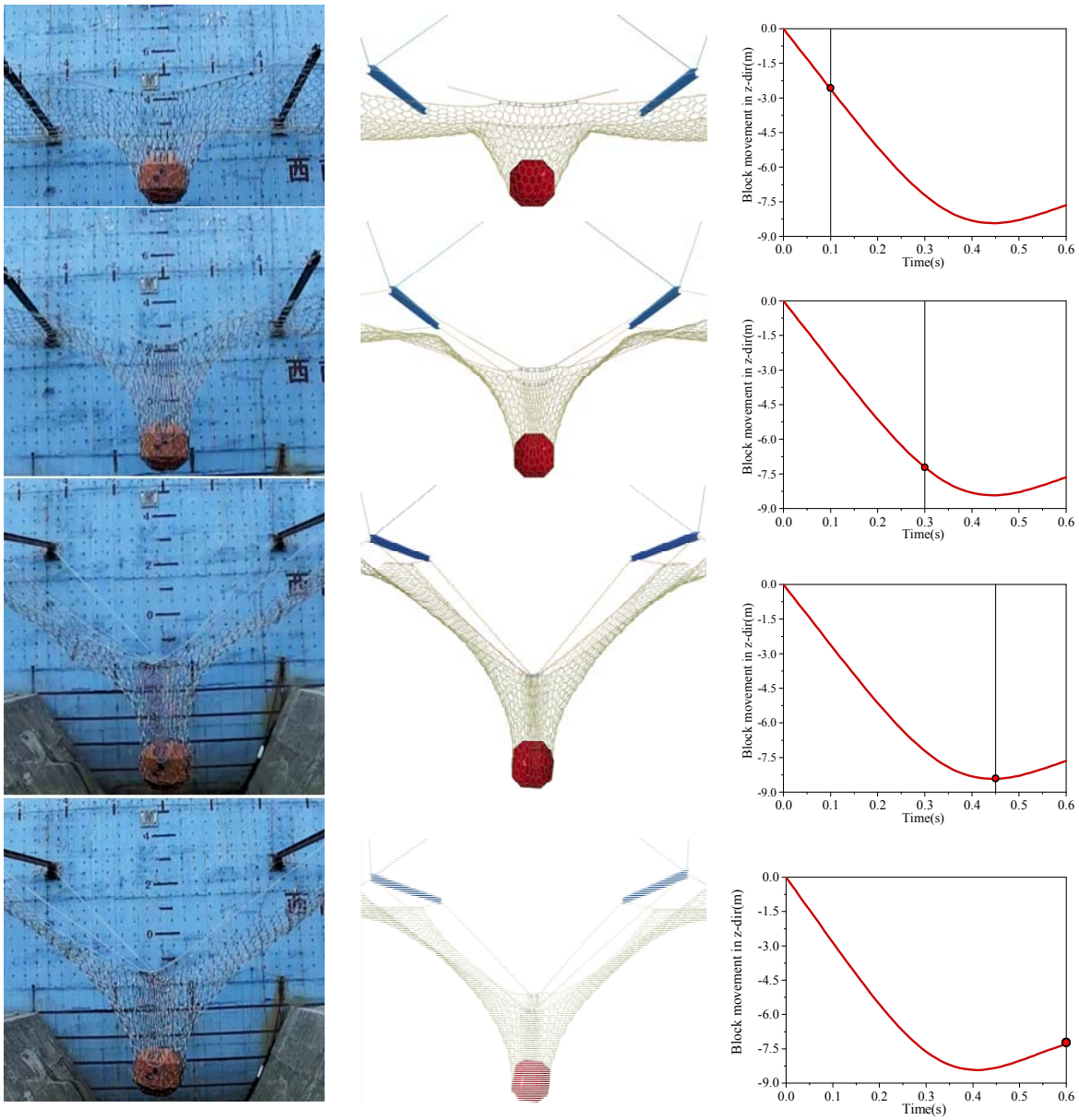

Figure 14. Deformed Shapes at Typical Moments (Test vs. Simulation)

After the impact test, all energy dissipating devices were activated. The energy dissipating devices mounted on support ropes show good utilization. Especially the energy dissipating devices mounted on the lower support ropes almost reaches the ultimate elongation, as shown in Figure 15(a, b). The energy dissipating devices mounted on upslope anchor ropes (L5, L6) in the impact zone also reaches the ultimate elongation, as shown in Figure 15(c, d). The maximum elongation of the energy dissipating devices mounted on the adjacent upslope anchor ropes (L4, L7) was small and around 0.2 m. Because the edge functional modules are not directly subjected to impact load, the elongation of energy dissipating devices mounted on the upslope anchor ropes was also small. In general, the system still has safety reserves. The performance of system is checked according to European standards [21], and the key parameters are shown in Table 3.

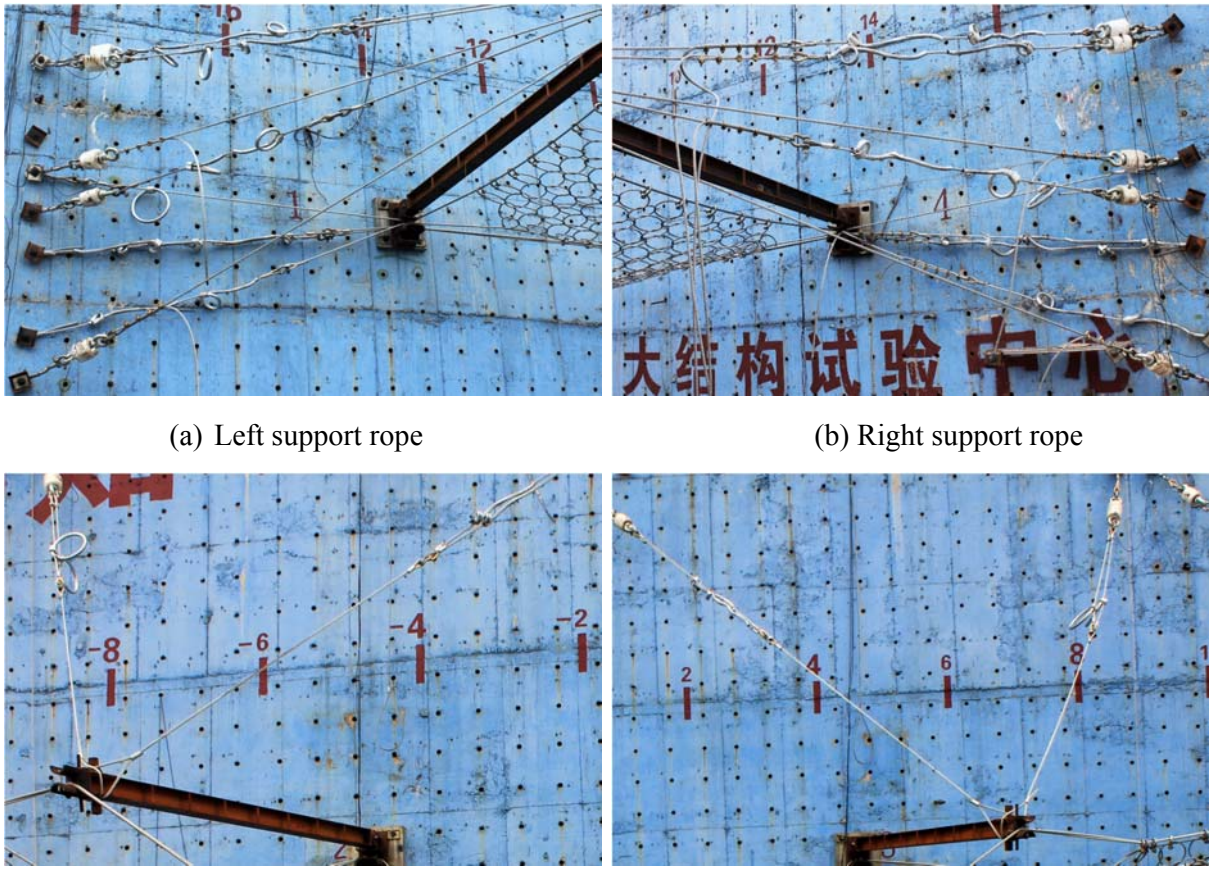

(a) Left support rope (b) Right support rope

(c) Upslope anchor ropes 4,5 (d) Upslope anchor ropes 6,7

Figure 15. Elongations of Energy Dissipating Devices

Table 3. Comparison of Key Parameters between Test and Simulation

Impact	Nominal height h_N (m)	Residual height h_R (m)	h_R/h_N	Maximum impact deflection (m)
Test	5.245	2.905	55.39%	8.426
Simulation	5.186	2.718	52.41%	8.084
Difference	1.12%	6.44%	5.38%	4.06%

Note: h_N is the nominal height and h_R is the residual height.

It can be seen from Table 3 that the difference between full-scale test and numerical simulation is small. Both the results of test and simulation show that $h_R/h_N > 50\%$, reaching the class A for the standard [17]. The results show that the deflection-control-based flexible rockfall barrier system has the good performance under the impact load. In addition, the impact deflection of the system is 7.720 m and 8.426 m obtained from analytical solution and full-scale test respectively. The difference between them is 9.1% and therefore the proposed method in the companion paper is good for engineering practice. The error may be from the approximate behavior of energy dissipating devices assumed in the analytical solution.

After the test, the inner posts swing laterally, while the edge posts were slightly upturned. No buckling and damage were found in all steel posts, seen in Figure 15. Figure 16 shows the time-history curves of internal force of rope obtained in full-scale test and numerical simulation, as well as the nominal breaking force of the steel wire rope [23]. Figure 16(a-c) shows the curves of force versus time of support ropes. It can be seen that, from 0 second to 0.1 second, the system was rapidly changed from loose state to tighten state. The internal force of the support ropes increased very fast and approaching to the activation force of the energy dissipating devices. After 0.1 second, the energy dissipating devices mounted on the support ropes are activated and the plastic tensile deformation was developed. The support ropes began to slide along the ends of the post and the internal force increased steadily. The funnel-shaped deflection was finally developed.

Figure 16(d-g) shows the curves of force versus time of anchor ropes. It can be seen that, after 0.3 second, the energy dissipating devices mounted on the upslope anchor ropes were activated and the plastic tensile deformation was generated, making the steel post swing downward. At the same time, the internal forces of support ropes increased steadily, and the system continued to dissipate energy. At 0.4 second, the energy dissipating devices mounted on the upslope anchor rope L5, L6 stopped working after reaching the ultimate elongation and as a result, the corresponding internal force on the upslope anchor ropes increased sharply to a peak force, seen in Figure 16(e, f). However, the internal forces of upslope anchor ropes L4 and L7 in the non-impact zone were small, as seen in Figure 16(d, g). After 0.4 second, the internal force of support ropes kept increasing steadily, and the maximum value of the internal force appeared at about 0.45 second. After that, all the ropes were unloaded and the rockfall rebounded. During the first impact process, the working time of the energy dissipating devices were about 0.35 second. Under the impact load, the dynamic response of the ropes was small and the peak internal force was low. Thus, no breaking of the components was found and the system shows good performance with safety reserve.

For the support ropes, as mentioned above, since the load cells were mounted near the anchorages of support ropes, the results obtained by the load cells were the internal forces of ropes at the anchorages. However, due to the friction effect, the internal force of the support rope is attenuated from the impact zone to both sides. It means that the internal force at the anchorages was less than the internal force in the impact zone. Thus, the support ropes in the impact zone have larger safety reserve larger than other ropes.

The curves of force versus time of ropes obtained by the numerical simulation agree well with results of the full-scale test. The numerical simulation reproduces the entire impact process well. It should be noted that the lateral anchor ropes are used to prevent large lateral swing of the steel post and maintain the stability of the posts and therefore, the energy dissipating devices are not required. In Figure 16h, the difference between the curves of the internal force of lateral anchor rope may essentially be caused by the slack of the rope due to the blemish of the model installation.

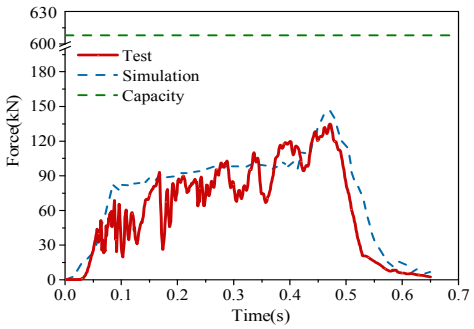

(a) Upper primary support rope L1

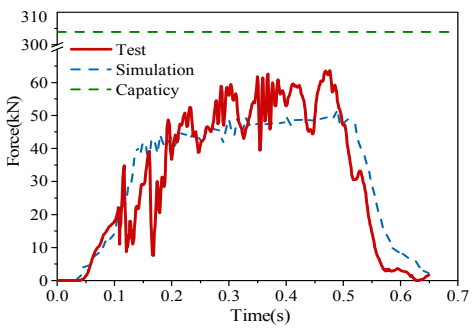

(b) Upper secondary support rope L2

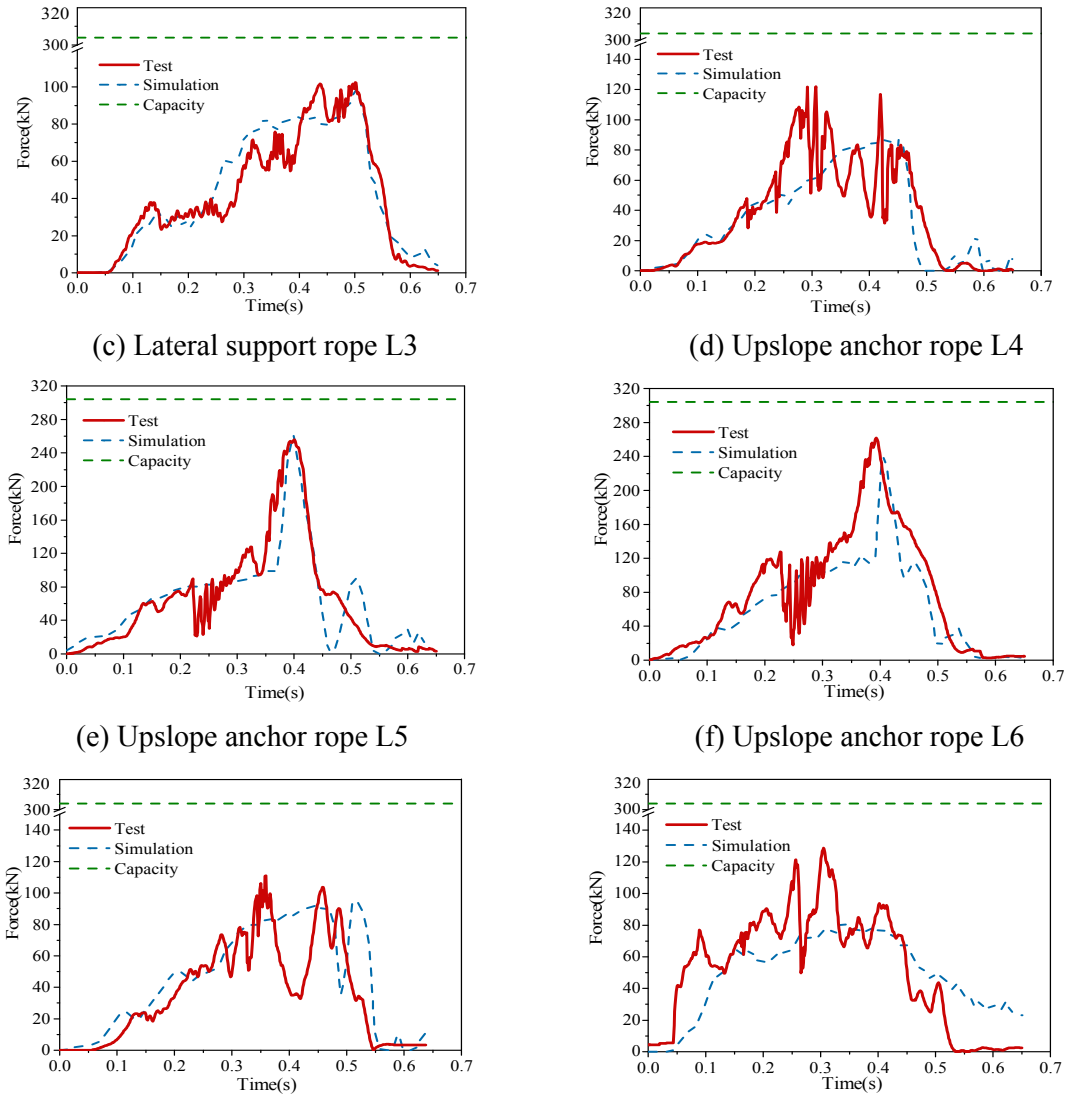

(c) Lateral support rope L3

(d) Upslope anchor rope L4

(e) Upslope anchor rope L5

(f) Upslope anchor rope L6

(g) Upslope anchor rope L7

(h) Lateral anchor rope L8

Figure 16. Comparison of Force Responses between Test and Simulation

4. PARAMETRIC STUDY FOR BUFFER PERFORMANCE CONTROL

As mentioned above, the plastic deformation of the energy dissipating devices is vital to realize the buffer mechanics and achieve the structural performance of the system. In order to further investigate the influence of plastic deformation of energy dissipating devices on the system response, eight different numerical models for parametric study are built with different force-displacement relationships of the energy dissipating devices on support ropes. As the difference between P_a and P_s is small, the working force of the energy dissipating device will be simplified as $P_a = P_s$. Taking the energy dissipating devices on primary support ropes as an example, the P-δ curve is shown in Figure 17. Due to the same capacity of energy dissipation of the eight groups of energy dissipating devices, the envelope areas all curves are equal. The parameters of the energy dissipating devices in Table 4 are summarized for practical engineering. The parameters associated with the energy dissipating devices on the lateral support ropes and the upslope anchor

ropes are same as shown in Table 2. According to the results of the numerical simulation, the eight groups of models successfully intercepted the rockfall, and the processes of impact deflection are similar to that in Figure 14. The difference is only the system deflection, the response of internal force and the efficiency of the energy dissipating devices, which will be discussed in detail later.

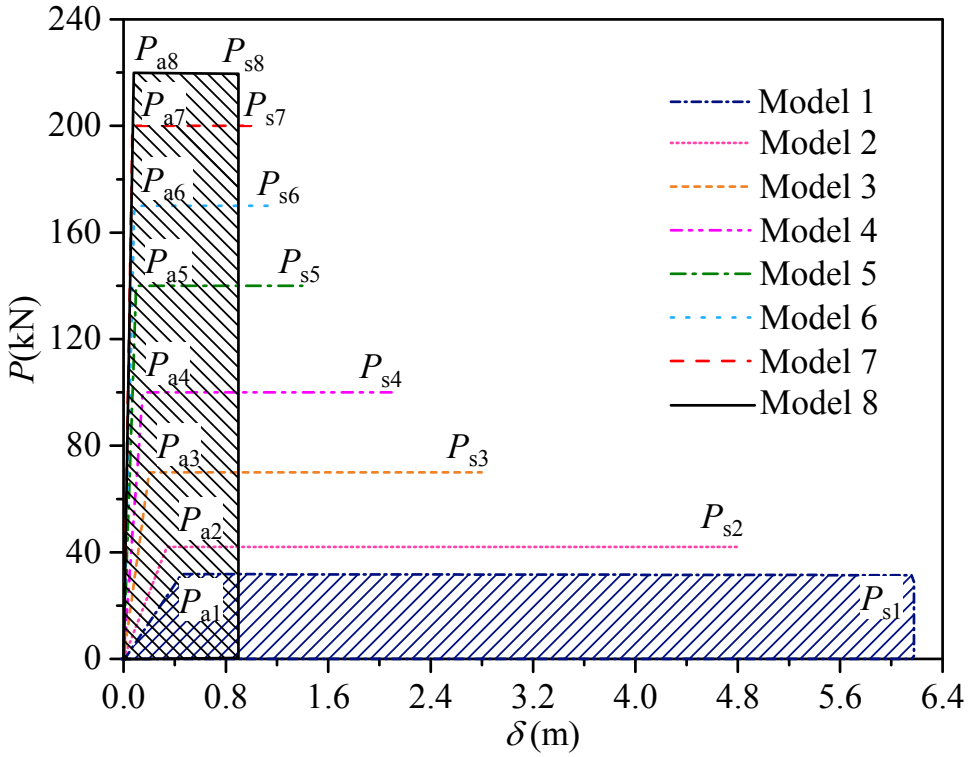

Figure 17. Performance Parameters of Energy Dissipating Devices

Table 4. The Parameters of Energy Dissipating Devices

Model	Upper primary support rope		Lower primary support rope		Upper secondary support rope		Lower secondary support rope	
	P_a~P_s(kN)	δ (m)	P_a~P_s(kN)	δ (m)	P_a~P_s(kN)	δ (m)	P_a~P_s(kN)	δ (m)
1	32~32	6.20	32~32	6.20	16~16	6.20	16~16	6.20
2	42~42	4.80	42~42	4.80	21~21	4.80	21~21	4.80
3	70~70	2.80	70~70	2.80	35~35	2.80	35~35	2.80
4	100~100	2.10	100~100	2.10	50~50	2.10	50~50	2.10
5	140~140	1.40	140~140	1.40	70~70	1.40	70~70	1.40
6	170~170	1.20	170~170	1.20	85~85	1.20	85~85	1.20
7	200~200	1.00	200~200	1.00	100~100	1.00	100~100	1.00
8	220~220	0.90	220~220	0.9	110~110	0.90	105~105	0.90

4.1 Discussion on Deflection

In order to investigate the influence of the performance parameters of the energy dissipating devices on the system response, the deflection of support structure (Δ_{1a}), sliding movement of support rope (Δ_{2s}), puncturing deflection of ring net (Δ_{3n}) and the overall system deflection (s) are extracted from numerical simulation, compared with the analytical solutions as shown in Table 5. In general, with the increase of working force of the energy dissipating devices, s decreased significantly. For example, s in model 8 is about 50% of that in model 1, and the deflection decreased is more than 5 meters. Therefore, in practical application, the performance parameters of the energy dissipating devices can be adjusted to control the buffer deformation of the system to meet the design limit. It can be seen from Table 5 that the analytical solution of s is in good agreement with the numerical solution. However, the difference between the analytical solution Δ_{1a} and the numerical solution Δ_{1a} of the model 1 is up to 20.5%. It is because the working force of the energy dissipating devices on support ropes in model 1 is small and the elongation of energy dissipating devices and the sliding of support ropes are large, which leads to the buffer deformation of the system is very large and the corresponding impact force is small. The overload protection provided by the energy dissipating devices causes the vertical component of the impact load is not enough to make the energy dissipating devices on the upslope anchor rope fully work. In other words, when using the analytical method to calculate Δ_{1a}, the empirical coefficient of the stretching efficiency used in the energy dissipating devices is greater than that in the numerical model. Thus, the analytical solution Δ_{1a} is larger than that in numerical simulation. It should be noted that, in the models 1 and 2, as the elongation of the energy dissipating devices on secondary support ropes is restricted by the ultimate stretching length (Δ_{trans}) of the ring net along the bypassed length, the development of Δ_{2s} is limited. However, the primary support ropes and secondary support ropes are forced together and mutually restrain in the deflection-control-based system. For this reason, it is recommended to take the average elongation of energy dissipating devices mounted on primary support ropes and secondary support ropes when using the analytical method to calculate Δ_{2s}. The detailed calculation can be referred to Eq. 9 of the companion paper.

Table 5. Comparison of Deflections

Results	$\angle_{1a}$ (m)	$\angle_{2s}$ (m)	$\angle_{3n}$ (m)	s (m)	Relative error (%)			
Model 1/ Analytical	0.39/0.47	7.55/7.39	3.17/3.06	11.11/10.92	20.5	2.1	3.5	1.7
Model 2/ Analytical	0.44/0.47	6.82/6.54	3.18/3.06	10.44/10.07	6.8	4.1	3.5	3.5
Model 3/ Analytical	0.52/0.47	5.22/5.03	3.01/3.06	8.79/8.56	9.6	3.6	1.7	2.6
Model 4/ Analytical	0.49/0.47	4.45/4.10	3.15/3.06	8.09/7.63	4.1	7.9	2.9	5.7
Model 5/ Analytical	0.45/0.47	3.55/3.05	3.02/3.06	7.02/6.58	4.4	14.1	1.3	6.3
Model 6/ Analytical	0.46/0.47	3.16/2.72	3.01/3.06	6.63/6.25	2.2	13.9	1.7	5.7
Model 7/ Analytical	0.48/0.47	2.58/2.35	2.91/3.06	5.97/5.88	2.1	8.9	5.2	1.5
Model 8/ Analytical	0.52/0.47	2.38/2.16	2.88/3.06	5.78/5.69	9.6	9.26	6.3	1.6

4.2 Discussion on Rope Force

To investigate the influence of the performance parameters of the energy dissipating devices on the internal force of ropes, the time-history curves of internal force of the ropes are extracted from the numerical simulation, as shown in Figure 18. As the models are symmetrically arranged, only the results of the upper primary support rope L1, the upper secondary support rope L2, the upslope anchor rope L4 and the upslope anchor rope L5 are extracted from the numerical simulation, and the number of ropes is shown in Figure 8. As the ropes are affected by the overload protection provided by the energy dissipating devices, the development of internal force on the ropes and the working force of the energy dissipating devices is similar. The internal force of ropes has clear yield stage which is positive correlation with the working force of the energy dissipating devices, as shown in Figure 18(a, b). Meantime, with the increase of elongation of energy dissipating devices, the duration of the yield stage also increases significantly, leading to effectively reduce the impact force on the system.

For the support ropes, the peak internal force of the primary support ropes in the model 3 and model 4 appears after 0.4 second. The reason is that the designed elongation of energy dissipating devices is slightly short which can be improved by increasing the potential elongation of the energy dissipating devices. In model 3, there are similar characteristics in internal force of secondary support ropes with the same reason. In the other models, the internal forces of support ropes are stable, indicating that the corresponding parameters of energy dissipating devices in these models are more favorable for the overload protection of the system.

For the upslope anchor ropes, the rope L4 in the non-impact zone and the rope L5 in the impact zone show a significantly different dynamic response. The internal force of the upslope anchor rope L4 is generally small because it is not directly subjected to impact load, and the maximum value of force is the same, as shown in Figure 18c. The change regulation of force response of anchor rope L5 in the impact zone can be analyzed in combination with Table 5. With the reduction of the working force of the energy dissipating devices on support ropes, the buffer deformation of system increase while the impact force will be reduced. Thus, the internal force of the anchor rope and the elongation of the energy dissipating devices on anchor ropes will also be reduced. When the actual elongation of the energy dissipating devices is less than the designed elongation, the rope will be in the state of overload protection.

In models 1 to 4, the yielding stage of upslope anchor rope L5 remains stable, seen in Figure 18d. In contrast, the internal force of the anchor rope L5 in model 5-8 shows significant peak value. It is because the increase of impact force on the system causes more significant elongation of energy dissipating devices, and therefore the designed elongation should be increased. In practical design, the increase of the working force of energy dissipating devices will improve the overload protection capacity for both the components and the system, by appropriately increasing the design elongation.

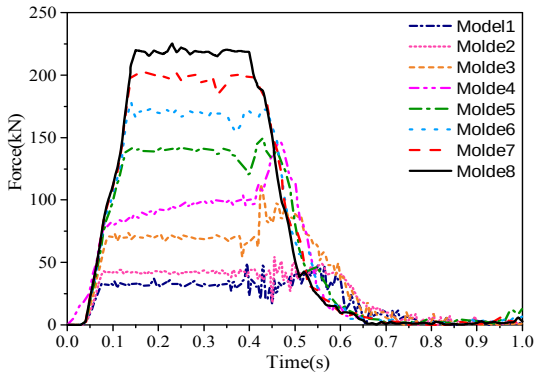

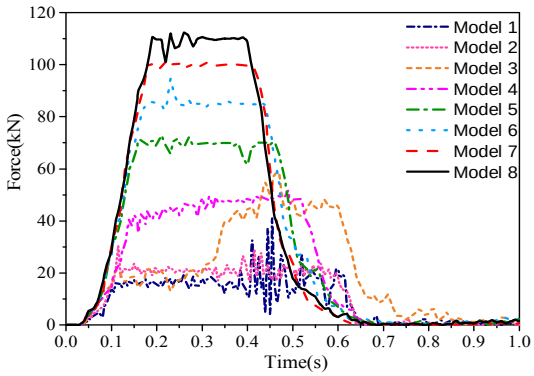

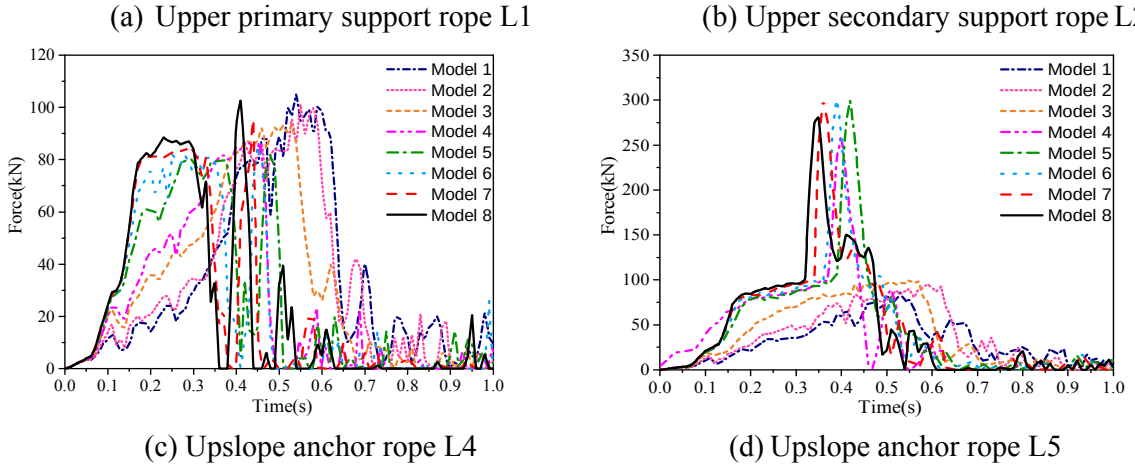

Figure 18. Time-History Curves of Ropes

4.3 Energy Dissipation and Control

To investigate the influence of the performance parameters of the energy dissipating devices on the energy dissipation of system, the analysis results of energy dissipation of the energy dissipating devices on the support ropes and the upslope anchor ropes are extracted from the numerical simulation, as shown in Table 6. In the table, the contribution ratio is obtained from the actual energy dissipation of the energy dissipating devices over the nominal energy of the system. The utilization ratio is calculated from the actual energy dissipation of the energy dissipating devices over the designed energy dissipation. Taking model 3 as an example, with the decreasing of the working force of the energy dissipating devices, the contribution ratio and the utilization ratio of the energy dissipating devices are reduced. Meanwhile, with the increasing of the working force of the energy dissipating devices, the contribution ratio and the utilization ratio are also reduced. The parameters of energy dissipating devices in model 3 show relatively superior characteristics. As mentioned above, the energy dissipation ratio of the energy dissipating devices keeps as 80% in the design stage. Hence, if the working force decreases, the allowable elongation of the energy dissipating devices should be increased. Taking model 1 and model 4 as examples, the designed elongation of energy dissipating device in model 1 is 6.2 meters, an increase of about 200% compared to model 4, which directly leads to the increase of Δ_{2s}. However, as mentioned in the companion paper, the actual elongation of energy dissipating devices on the support ropes is also restricted by Δ_{trans}, which inhibits the internal force from transmitting to the anchorages of support ropes. Thus, it is impossible for the energy dissipating devices on the support ropes to be fully stretched, resulting in the decrease in contribution ratio and utilization ratio. At the same time, the development of Δ_{2s} is also restricted. Taking models 4 to 8 as the examples, as the nominal energy levels of the systems are identical, the increase of the designed elongation of the energy dissipating devices is difficult due to increase of the working force simultaneously. As a result, the energy dissipating devices cannot be fully stretched and the contribution ratio and utilization of energy dissipating device are also decreased. The results of the parametric analysis show that the optimal elongation and corresponding working force can be determined in energy dissipating devices to obtain the best buffering performance of the system. Combined with the designed parameters in Table 4 and analysis results in Table 6 for the models 3 and 4, the optimal elongation of the energy dissipating devices can be determined by trial-and-error calculation. The upper limit of elongation is Δ_{trans} as mentioned in the companion paper.

Table 6. Results of Numerical Simulation of Energy Dissipating Device

Model	Nominal energy levels	Energy dissipating device			
		Design energy dissipating	Actual energy dissipating	Contribution ratio	Utilization ratio
1	2000 kJ	1685 kJ	1285 kJ	64.3%	76.3%
2	2000 kJ	1705 kJ	1400 kJ	70.0%	82.1%
3	2000 kJ	1671 kJ	1520 kJ	76.0%	91.0%
4	2000 kJ	1755 kJ	1442 kJ	72.1%	82.2%
5	2000 kJ	1671 kJ	1377 kJ	68.9%	82.4%
6	2000 kJ	1719 kJ	1354 kJ	67.7%	78.8%
7	2000 kJ	1695 kJ	1309 kJ	65.5%	77.3%
8	2000 kJ	1683 kJ	1288 kJ	64.4%	76.5%

In addition, the correlation between the impact force (F) and buffer deflection (s) is further studied. As the energy dissipating capacity of the barrier system is identical, with the increase of the working force of energy dissipating devices on the support ropes, s gradually decreases while F increases. Thus, the slope of F-s curves also increases gradually, which indicates that the stiffness of system increases gradually, as shown in Figure 19a. However, when the working force of energy dissipating device on support ropes increases to a certain limit, e.g. models 7 and 8, F tends to be stable and the change of s is small. According to the companion paper, Δ_{2s} accounts for more than half of the s and plays a controlling role in the buffer deformation of the system when the buffer mechanism is functioned properly. However, with the increase of working force of the energy dissipating devices, the elongation of the energy dissipating devices decreases significantly, which makes Δ_{2s} decrease significantly. Therefore, s will depend on Δ_{1a} and Δ_{3n}. However, Δ_{1a} is smaller than other deflection components, while Δ_{3n} is almost constant. As a result, the total deflection s tends to be stable when the working tension of the energy dissipating devices on support ropes increases to a certain value. This rule can be used to determine the upper limit threshold of the working force of energy dissipating devices in the actual design.

Figure 19b shows the correlation between the working force of the energy dissipating devices on the support ropes and the elongation of the system, and the numbers in parentheses indicate the design elongation of the energy dissipating devices. According to the previous analysis, it is not beneficial to enhance the buffer performance of the system when working force of energy dissipating devices is too large or too small. Hence, the parameters of energy dissipating devices on the support ropes in models 3 to 6 can be used as the control interval. Taking the point A in Figure 19b as an example, when the working force of energy dissipating devices on the support ropes is the same as that in model 5, the designed elongation may range from 1.4 m to 2.8 m. In other words, when s does not allow to exceed 8.0 m due to the protection requirement within a limit, the working force of energy dissipating devices on the support ropes can be 150 to 255 kN. Apparently, this provides a practical approach for selection or design of flexible barrier product.

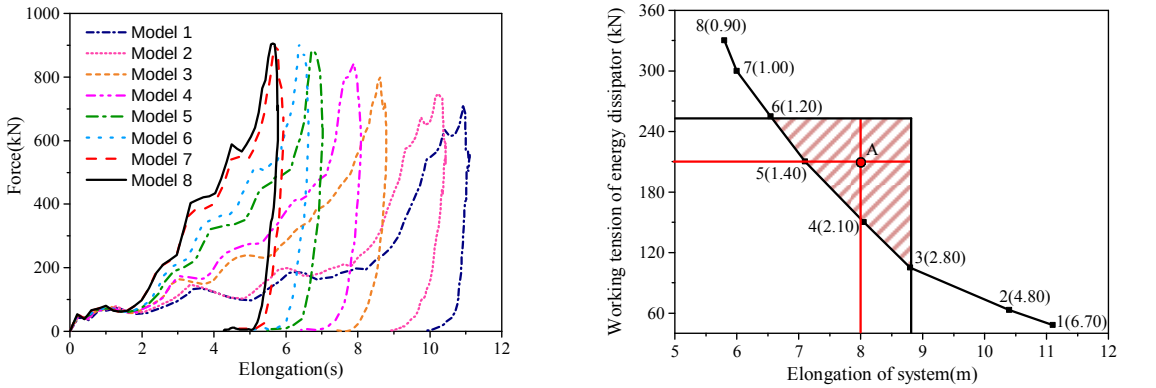

(a)*F-s* curves of System (b) Performance Control and Parameters Interval

Figure 19. Results of Parametric Analysis

5. CONCLUSIONS

This paper establishes a deflection-control-based mechanical model with improved buffer performance. A prototype model with a nominal energy level of 2000 kJ was designed using the analytical method introduced in part one of the paper. Both full-scale test and numerical simulation were carried out to investigate the response of the prototype model under impact load. The results show that the motion interference and the braking effect during impact test are effectively controlled by the proposed deflection-control-based mechanical model, leading to an optimized design regarding system buffer performance. In summary, the following conclusions can be made:
The motion interference in the flexible barrier system can be effectively avoided by using the proposed structural form, with improvement of sliding movement and buffer mechanism.

(1) The deflection-control-based flexible rockfall barrier system has no clear “braking effect” when it is impacted by the rockfall, which reduces the possibility of damage and improves the buffer performance of the system.

(2) The working force of the energy dissipating devices is a negative correlation with the elongation of the system. However, when the working force is too large, the system deflection does not relate to it. The parametric study on the energy dissipating devices provides a practical solution for the optimal design of buffer performance of flexible barrier system.

Based on the proposed *F-s* correlation curve, a hierarchical design standard related to the requirements of performance object can be established by controlling the energy dissipating devices on the support ropes. However, the hierarchical design of performance requires a statistical analysis with large amount of full-scale tests and numerical simulation, which needs more research work in the future.

ACKNOWLEDGMENTS

The authors are grateful for financial support from the National Natural Science Foundation of China under Grant No. 51678504 and No. 51408498, Department of Science and Technology of Sichuan Province under Grant No. 2018JY0029, Open Fund of National Engineering Laboratory

for Bridge Structure Safety Technology under Grant No.310821151102, and the Fund of State Key Laboratory of Geohazard Prevention and Geoenvironment Protection under Grant No.SKLGP2016K013. The last author is grateful for financial support the Innovation and Technology Fund of the Hong Kong SAR Government for the project “Development of an Energy Absorbing Device for Flexible Rock-Fall Barriers (ITS/059/16FP)”.

REFERENCES

[1] Peila D, Pelizza S, Sassudelli F. “Evaluation of Behaviour of Rockfall Restraining Nets by Full Scale Tests”. Journal of Rock Mechanics & Rock Engineering, 1998, Vol. 31, No. 1, pp. 1-24.

[2] Escallón J P, Boetticher V, Wendeler C, et al. “Mechanics of chain-link wire nets with loose connections”. Engineering Structures, 2015, Vol. 101, pp. 68-87.

[3] Zhao Shichun, Yu Zhixiang, Zhao Lei, et al. “Damage mechanism of rockfall barriers under strong impact loading”, Journal of Engineering Mechanics, 2016, Vol. 33, No. 10, pp. 24-34.

[4] Zhao Shichun, Yu Zhixiang, Wei Tao, et al. “Test study of force mechanism and numerical calculation of safety netting system”. Journal of China Civil Engineering Journal, 2013, Vol.46, No. 5, pp. 122-128.

[5] Gottardi G, Govoni L. “Full-scale Modelling of Falling Rock Protection Barriers”. Journal of Rock Mechanics & Rock Engineering, 2010, Vol. 43, No. 3, pp. 261-274.

[6] Escallón J P, Wendeler C, Chatzi E, et al. “Parameter identification of rockfall protection barrier components through an inverse formulation”. Journal of Engineering Structures, 2014, Vol. 77, pp. 1-16.

[7] Grassl H, Bartelt P A, Volkwein A, et al. “Experimental and numerical modeling of highly flexible rockfall protection barriers” Proceedings of 12th Panamerican Conference on Soil Mechanics and Geotechnical Engineering, Cambridge, Massachusetts, USA, 2003, Vol. 2589—2594.

[8] Qi Xin. “The Mechanics Performance of Passive Flexible Protection Structure”. Southwest Jiaotong University, 2014.

[9] Kwan J S H,Chan S L, Cheuk J C Y, et al. “A case study on an open hillside landslide impacting on a flexible rockfall barrier at Jordan Valley”, Journal of Hong Kong. Landslides, 2014, Vol. 11, No. 6, pp. 1-14.

[10] Gentilini C, Govoni L, Miranda S D, et al. “Three-dimensional numerical modelling of falling rock protection barriers”. Journal of Computers & Geotechnics, 2012, Vol. 44, No. 44, pp. 58-72.

[11] Bertrand D, Trad A, Limam A, et al. “Full-Scale Dynamic Analysis of an Innovative Rockfall Fence Under Impact Using the Discrete Element Method: from the Local Scale to the Structure Scale”. Journal of Rock Mechanics & Rock Engineering, 2012, Vol. 45, No. 5, pp. 885-900.

[12] Volkwein A. “Numerical modelling of flexible rockfall protection systems”. Journal of American Society of Civil Engineers, 2013, Vol. 11, No. 179, pp. 1-11.

[13] Moon T, Oh J, Mun B. “Practical design of rockfall catchfence at urban area from a numerical analysis approach”. Journal of Engineering Geology, 2014, Vol. 172, No. 5, pp. 41-56.

[14] Gentilini C, Gottardi G, Govoni L, et al. “Design of falling rock protection barriers using

numerical models". Journal of Engineering Structures, 2013, Vol.50, No. 3, pp. 96-106.
[15] Muhunthan, B.,H. Radhakrishnan.,"Finite Element Analysis of Hybrid Barrier for Rock Fall Slope Protection", Final Report, Department of Civil and Environmental Engineering, Washington State University, 2007.
[16] Miranda S D, Gentilini C, Gottardi G, et al. "Virtual testing of existing semi-rigid rockfall protection barriers", Journal of Engineering Structures, 2015, Vol. 85, pp. 83-94.
[17] Gentilini C, Ubertini F, Govoni L, et al. "Modelling of falling rock protection barriers", Journal of Physical Modelling in Geotechnics, 2011, Vol. 11, No. 4, pp. 126-137.
[18] Miranda S D, Gentilini C, Gottardi G, et al. "A simple model to simulate the full-scale behaviour of falling rock protection barriers", Physical Modelling in Geotechnics, 2010.
[19] Geobrugg.https://www.geobrugg.com/zh/Rockfall-protection-barriers-RXE-77708, 7859.html.
[20] Livermore software technology corporation (LSTC), LS-DYNA keyword user's manual volume I, 2007.
[21] EOTA. Guideline for European technical approval of falling rock protection kits (ETAG 027), 2012, Brussels.
[22] Castanon-Jano L, Blanco-Fernandez E., "Castro-Fresno D, et al Energy Dissipating Devices in Falling Rock Protection Barriers", Journal of Rock Mechanics & Rock Engineering, 2017, Vol 50, pp. 1-17.
[23] GB/T 20118-2006, Steel wire ropes for general purpose, Standardization Administration of the People's Republic of China, Beijing, 2006.
[24] Higgins J D, "Recommended procedure for the testing of rockfall barriers", AASHTO Technical Report, Washington, 2003.
[25] Peila D, Ronco C, "Technical Note: Design of rockfall net fences and the new ETAG 027 European guideline", Journal of Natural Hazards and Earth System Sciences, 2009, Vol. 9, No. 4, pp. 1291-1298.
[26] Muhunthan B, Shu S, Sasiharan N, "Analysis and design of wire mesh/cable net slope protection", Washington State Transportation Center (TRAC) Report, 2005.
[27] Qiao Wentao, An Qi, Zhao Mingshan, et al., "Experimental study on the fundamental mechanical features of cable-supported ribbed beam composite slab structure", Advanced Steel Construction, 2017, Vol. 13, No. 2, pp. 96-116.
[28] Guo Jiamin, Yuan Xingfei, Xiong Zhixin, et al., "Force finding of suspended-domes using back propagation (BP) algorithm", Advanced Steel Construction, 2016, Vol. 12, No. 1, pp. 17-31.
[29] Luo Bin, Guo Zhengxing, Chen Xiangnan, et al., "Static equilibrium form-finding analysis of cable-strut system based on nonlinear dynamic finite element method", Advanced Steel Construction, 2015, Vol. 11, No. 4, pp. 452-468.

INVESTIGATING THE EFFECT OF JOINT BEHAVIOR ON THE OPTIMUM DESIGN OF STEEL FRAMES VIA HUNTING SEARCH ALGORITHM

Erkan Doğan[1], Soner Şeker[2*], M. Polat Saka[3] and Celalettin Kozanoğlu[1]

[1] *Celal Bayar University , Department of Civil Engineering , 45140 , Manisa , Turkey*
[2] *Uşak University , Department of Civil Engineering , 64200 , Uşak , Turkey*
[3]*University of Bahrain, Department of Civil Engineering, Isa Town, Bahrain*
**(Corresponding author: E-mail: soner.seker@usak.edu.tr)*

Received: 21 April 2016; Revised: 13 April 2017; Accepted: 21 April 2017

ABSTRACT: This study aims to carry out the effect of beam-to-column connections on the minimum weight design of steel plane frames. In the practical analysis of steel frames, end connections are assumed to be either fully restrained or pin-connected. However, experiments reveal that the real behavior is between these extremes and should be taken into account for the realistic design of structures. Hunting search algorithm is used for the automation of optimum design process. It is a numerical optimization method inspired by group hunting of animals such as wolves and lions. It is proven that it is a reliable and efficient technique for obtaining the solution of discrete structural optimization problems. Present design algorithm developed on the basis of hunting search algorithm selects w- sections for the members of semi rigid steel frame from the complete list of w- sections given in LRFD- AISC (Load and Resistance Factor Design, American Institute of Steel Construction). The design constraints are implemented from the specifications of the same code which covers serviceability and strength limitations. The selection of w-sections is carried out such that the design limitations are satisfied and the weight of semi- rigid frame is the minimum. In order to demonstrate its efficiency, three different steel frames are designed by the optimum design algorithm presented. The designs obtained by use of this algorithm are also compared with the ones produced by particle swarm optimization method.

Keywords: Stochastic Search techniques; hunting search algorithm; optimization problems; semi-rigid steel frames, end plate connections

DOI: 10.18057/IJASC.2018.14.2.3

1. INTRODUCTION

In the analysis and design of steel frames, the realistic modeling of beam-to-column connections provides an accurate response of the frame under the external loads. In practice, these connections are assumed to be either fully rigid or perfectly pinned. In the former assumption, it is implied that there is no relative rotation of connection and the column takes the whole end moment of the beam. On the other hand, the pinned connection assumes that the moment of connection is always zero and there is no existing restraint for the rotation of connection. However, experiments have revealed that the real behavior of beam-to-column connections is between these extremes. Namely, all these practically used connections possess some stiffness falling between two cases mentioned above. Moreover, it is found that there exists a nonlinear relation of relative beam-to-column rotation when a moment is applied to a flexible connection [11]. These partially restrained connections influence the drift (P-Δ effect) of whole structure as well as the moment distribution in beams and columns. Use of a direct nonlinear inelastic analysis is one way to account for all these effects in frame design [1]. To be able to implement such analysis, beam-to-column connections should be assumed and modeled as semi-rigid connections. The semi-rigid connection flexibility depends on the geometric parameters of the elements used in beam-to-column connection, such as dimensions of end plates and bolt size.

This study presents a hunting search method based optimum design algorithm for unbraced steel frames with semi rigid end connections. Hunting search algorithm is one of the recent additions to meta-heuristic search methods, which is inspired by group hunting of animals such as lions, wolves, and dolphins. Hunters involved in the hunting group encircle and catch their prey abiding by the certain strategies. For instance, wolves can hunt animals bigger or faster than themselves by relying on this kind of hunt. One prey is selected and the hunting group gradually moves toward it. The hunters avoid standing in the wind such that the prey senses their smell. This concept is used in the constrained problem to avoid prohibited regions. In the optimization process, each of the hunters indicates one solution for a particular problem. Similar to animals cooperate to find and catch the prey, the optimum design process seeks to find the optimum solution. Originally, hunting search algorithm produces continuous numbers. As made in some previously developed optimum design algorithms, this assumption can be used for the solution of many structural optimization problems [2]. However, such an assumption cannot be used in the optimum design problem of steel frames where the steel sections for its beams and columns are to be selected from a steel profile list, which consists of discrete values. Hence, discrete variables should be used in the hunting search algorithm. In literature, two approaches exist to obtain integer numbers from continuous ones. The first was suggested by Kennedy and Eberhart where binary numbers are used in the optimization algorithm to achieve a discrete set [16]. The second method is to round off the real numbers to the nearest integer numbers, which is suggested by Liu et al. [17]. In this study, discrete solution is accomplished by using rounding off technique due to its ease in the implementation of computer code.

Optimum design problem is formulated according to the specifications of LRFD-AISC [21]. The design constraints; displacement limitations, inter-storey drift restrictions of multi-storey frames, strength requirements for beam-columns are included in the formulation of the design problem. Furthermore, additional constraints namely geometric constraints are also considered to satisfy the practical requirements. The design problem formulated turns out to be a discrete nonlinear programming problem. The design algorithm developed selects W sections for beams and columns of an unbraced frame from discrete steel section list such that the design constraints imposed by LRFD-AISC are satisfied and the frame has the minimum weight.

2. ANALYSIS OF UNBRACED STEEL FRAMES WITH SEMI-RIGID CONNECTIONS

Various semi-rigid connection modeling and their moment-rotation relationships exist in the literature. The most well-known ones are linear, polynomial, cubic B spline, power and exponential models [12]. In the analysis and design of semi-rigid steel frames connections can be represented by discrete, inelastic rotational springs. The effect of connection flexibility is modeled by attaching rotational springs with stiffness moduli K_A and K_B to the first and second ends of a member as shown in Figure 1.

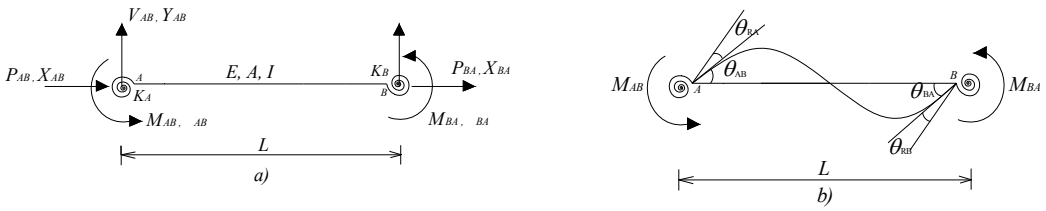

Figure 1. Semi-rigid Plane Beam Member with Rotational Springs
(a) End forces and end displacements (b) end rotations

A beam member with semi-rigid end connections has the nonlinear stiffness matrix form shown in the following. (Eq. 1)

Where;

$$[ST]=\left[\begin{array}{ccc|ccc} A & & & & & \\ B & D & & & & \\ C1 & E1 & F1 & & & \\ \hline -A & -B & -C1 & A & & \\ -B & -D & -E1 & B & D & \\ -C2 & -E2 & F2 & C2 & E2 & G \end{array}\right] \tag{1}$$

$$A=\frac{EA}{L}+\frac{12EI}{L^3}f_{x1}\phi_5 \qquad E_1=\frac{6EI}{L^2}f_{x2}\phi_2$$
$$B=\frac{EA}{L}-\frac{12EI}{L^3}f_{x1}\phi_5 \qquad E_2=\frac{6EI}{L^2}f_{x3}\phi_2$$
$$D=\frac{EA}{L}-\frac{12EI}{L^3}f_{x1}\phi_5 \qquad F_1=\frac{4EI}{L}f_{x6}\phi_3$$
$$C_1=-\frac{6EI}{L^2}f_{x2}\phi_2 \qquad F_2=\frac{2EI}{L}f_{x5}\phi_3$$
$$C_2=-\frac{6EI}{L^2}f_{x3}\phi_2 \qquad G=\frac{4EI}{L}f_{x6}\phi_4$$

$$KK = K_A K_B + 4(K_A + K_B) + 12 \qquad f_{x4} = K_A(K_B + 3) / KK \tag{2}$$
$$f_{x1} = (K_A K_B + K_A + K_B) / KK \qquad f_{x5} = K_A K_B / KK$$
$$f_{x2} = K_A(K_B + 2) / KK \qquad f_{x6} = K_B(K_A + 3) / KK$$
$$f_{x3} = K_B(K_A + 2) / KK$$

in which E represents the modulus of elasticity, L, I, A are the length, moment of inertia and area of beam, respectively. Above stiffness matrix includes the effect of the flexible connections. To be able to modify the stiffness matrix of a rigid beam, modification coefficients are used. These coefficients are calculated by use of the following equations.

In Eq. 2, K_A and K_B symbolize the stiffness moduli of the flexible connections at first and second end of the member. In addition, stability functions are included in the stiffness matrix to consider the effect of axial forces on the deformed shape. To calculate the values of stability functions, power series approximation is used. However, this method needs the trigonometric functions and one of which is $\alpha\cot\alpha$ gives singular values at some α values. For this reason, Livesely's approximation which is the sum of a power series in Euler critical load factor ρ and a rotational function Eq. 3 is implemented [10]. These stability functions are given as follows;

$$\phi_1 = \alpha\cot\alpha = \frac{64-60\rho+5\rho^2}{(16-\rho)(4-\rho)} - \sum_{n=1}^{7}\frac{a_n\rho^n}{2^{3n}} \tag{3}$$

in which, the constants take the values as;

$$a_1 = 1.57973627, \quad a_2 = 0.15858587, \quad a_3 = 0.02748899, \quad a_4 = 0.00547540,$$
$$a_5 = 0.00115281, \quad a_6 = 0.00024908, \quad a_7 = 0.00005452 \tag{4}$$

$$\phi_2 = \alpha^2/(3-3\phi_1) \qquad \alpha = 0.5\pi\sqrt{\rho} \qquad \rho = P / P_{cr} = Pl^2/(\pi^2 EI)$$
$$\phi_3 = (3\phi_2 + \phi_1)/4$$
$$\phi_4 = (3\phi_2 - \phi_1)/2$$
$$\phi_5 = \phi_2\phi_1$$

Where; P is the axial force in beam member, P_{cr} is the Euler critical load of beam member.

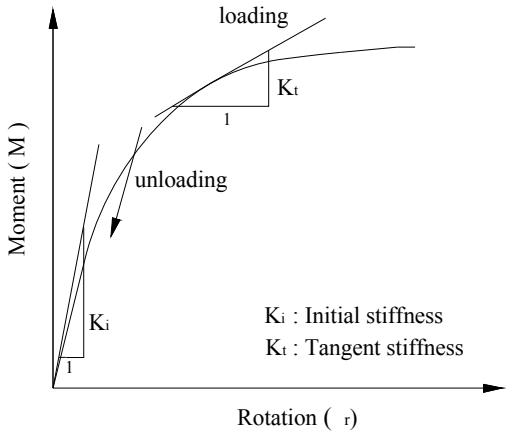

Figure 2. Moment Rotation Behavior of Semi–rigid Connection

In practice, curve-fitting the experimental data with simple expressions is the most commonly used approach to describe the M-θ_r curve of flexible connection. There are several analytical models to represent connection flexibility using available experimental test data. A polynomial model where M-θ_r behavior is represented by an odd power polynomial, proposed by Frye and Morris is adopted in present study due to its easy implementation [11]. The Frye and Morris model uses the method of least square to determine the constants of the polynomial and has the following form. (Eq. 5)

$$\theta_r = C_1(KM)^1 + C_2(KM)^3 + C_3(KM)^5 \tag{5}$$

in which C_1, C_2, C_3 are the curve-fitting constants and K symbolizes the standardization constant dependent on the connection type and geometry. The values of these constants vary for each connection type and are given in the literature [13]. K_A and K_B, called as the rotational stiffness of the springs at each end of the flexible frame member, are calculated as a tangent stiffness using above given nonlinear standardized function. (Eq. 5) To achieve this, first flexibility of connection is determined as $d\theta/dM$. Then, the stiffness of the connection, which is to be used in the modification of general stiffness matrix, is obtained as a reciprocal of the connection flexibility calculated for a certain value of a moment, when connection is loaded. If the state is unloading, the stiffness of the connection is assumed as its initial stiffness. These two states are shown in Figure 2. The size parameters of the end plate without column stiffeners connection, modeled in this study, are shown schematically in Figure 3. For the end plate without column stiffeners connection model, curve-fitting and standardization constants are given as in the following. (Eq. 6)

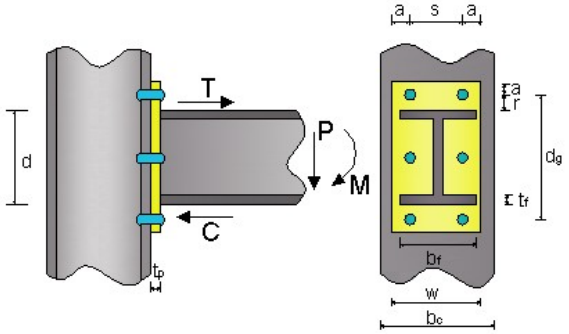

Figure 3. End Plate without Column Stiffeners Connection

$$C_1=1.83\text{x}10^{-3} \quad C_2=1.04\text{x}10^{-4} \quad C_3=6.38\text{x}10^{-6} \quad \text{and } K = d_g^{-2.4}\, t_p^{-0.4}\, d_b^{1.5} \tag{6}$$

where d_g, t_p, d_b are; the distance between two bolts at the top and bottom of plate, the thickness of plate, and the diameter of bolts, respectively.

An increase in lateral displacements occurs in the analysis of steel frames with semi-rigid connections. Hence, consideration of the effect of axial forces in the response of semi-rigid frame becomes a necessity. The following steps give details about the algorithm, which accounts for *P*-Δ effect in the analysis of frame.

1. In the beginning of the procedure, axial forces in the frame members are assumed to be zero.
2. Overall stiffness matrix is constructed. Then the frame is analyzed under the external loads. Joint displacements and member forces are calculated.
3. Corresponding stability functions are determined using the axial forces obtained for the members.

The steps from 2 are repeated until the difference between two successive sets of axial forces is smaller than a specific tolerance.

The determinant of overall stiffness matrix is calculated and the loss of stability is checked during these iterations. If no loss of stability occurs and the convergence in the axial forces is obtained, the joint displacements and member forces determined in this nonlinear response are used in the computation of fitness values for this particle. During the analysis, the design load is applied immediately and the iterations are carried out at this load. It should be pointed out that the fixed end moments change in each iteration due to the rotational springs. The modified fixed end moments are determined by considering the flexible end connection.

3. HUNTING SEARCH OPTIMIZATION FOR DISCRETE DESIGN VARIABLES

The optimum design problem with discrete variables can be expressed as follows:

$$Min.\, f(x) \qquad i = 1, ..., n \tag{7}$$

Subject to;

$$\begin{aligned} & g_j(x) \le 0 \qquad j = 1, ..., m \\ & x_i \in X \quad , \quad X = \{x_1, x_2, ...x_n\} \end{aligned} \tag{8}$$

where x_i represents the discrete design variable *i,* which is to be selected from the set ***X*** that contains *q* number of discrete values for these variables. *n* is the total number of design variables. $f(x_i)$ defines the objective function and $g_j(x_i)$ shows the design constraint *j*. *m* is the total number of these constraints in the design problem.

Hunting search algorithm is one of the recent additions to the meta-heuristic search techniques of combinatorial optimization problems, introduced by Oftadeh et al [7]. This approach is based on the group hunting of animals such as lions, wolves and dolphins. The common part in the way of hunting of these animals is that, they all hunt in a group. They encircle the prey and gradually tighten the ring of siege until they catch the prey. Each member of the group corrects its position based on its own position and the position of other members during this action. If a prey escapes from the ring, hunters reorganize the group to siege the prey again. The hunting search algorithm is based on the way as wolves hunt. The procedure involves a number of hunters, which represents

the hunting group are initialized randomly in the search space of an objective function. Each hunter represents a candidate solution of the optimum design problem. Originally hunting search algorithm produces continuous design variables. To be able to use the method for discrete design variables, some adjustments are required to be carried out. Firstly, the discrete values, among which the values of design variables x_i are to be selected in set {X}, are arranged in ascending sequence. The sequence number of these values is then treated as design variable instead of x_i itself. For example in a design set, which consists of 272 values, the sequence numbers from 1 to 272 are the main design variables. At any stage of design cycle, once a sequence number is generated by the algorithm, then the real value of the design variable, which corresponds to this sequence number, is easily taken from the discrete set. The steps of the algorithm are given in the following:

1. ***Initialize the parameters:*** These are hunting group size (number of solution vectors in hunting group, *HGS*), maximum movement toward the leader (*MML*) and hunting group consideration rate (*HGCR*), which varies between 0 and 1. The parameters *MML* and *HGCR* are used to improvise the hunter position (solution vector).

2. ***Initialize the hunting group:*** Based on the number of hunters (*HGS*), the hunting group matrix is filled with feasible randomly generated solution vectors. The values of objective function are computed for each solution vector and the leader is defined depending on these values.

3. ***Generate new hunters' positions:*** New solution vectors $x' = \{x'_1, x'_2, ..., x'_n\}$ are generated by moving toward the leader (the hunter that has the best position in the group) as follows;

$$x_i^j = x_i + rand.MML.(x_i^j - x_i) \tag{9}$$

where *rand* is a uniform random number [0,1] and x'_i is the position value of the leader for the i^{th} variable.

For each hunter, if the movement toward the leader is successful, the hunter stays in its new position. However, if the movement is not successful (its previous position is better than its new position) it comes back to the previous position. This provides two advantages. First, the hunter is not compared with the worst hunter in the group to allow the weak members to search for other solutions. They may find better solutions. Secondly, for prevention from rapid convergence of the group, the hunter compares its current position with its previous position; therefore, good positions will not be eliminated. The value of *MML* varies depending on the problem under consideration.

4. ***Position correction- cooperation between members*****:** The cooperation among the hunters is required to be modeled in order to conduct the hunt more efficiently. After moving toward the leader, hunters (based on other hunter positions and some random factors) choose another position to find better solutions. Hunters correct their position either following "*real value correction"* or "*digital value correction"*. In real value correction, the new hunter's position $x' = \{x'_1, x'_2, ..., x'_n\}$ is generated from *HG*, based on hunting group considerations or position corrections. For instance, the value of the first design variable for the j^{th} hunter x_1^j for the new vector, can be selected as a real number from the specified $HG(x_i^1, x_i^2, ..., x_i^{HGS})$ or corrected using *HGCR* parameter (chosen between 0 and 1). The variable is updated as follows:

$$x_i^j = \begin{cases} x_i^j \in (x_i^1, x_i^2, ..., x_i^{HGS}) & with\ probability\ HGCR \\ x_i^j = x_i^j \pm Ra & with\ probability\ (1 - HGCR) \end{cases} \qquad i:1,...,n, \quad j:1,...,HGS \tag{10}$$

The parameter *HGCR* is the probability of choosing one value from the hunting group stored in the *HG*. It is reported that selecting values between 0.1 and 0.4 produces better results. *Ra* is an arbitrary distance radius for the continuous design variable. It can be fixed or reduced during the optimization process. Several functions can be selected for reducing *Ra.* Eq. 11.

$$\mathrm{R}a(it) = \mathrm{R}a_{\min}(x_i^{\max} - x_i^{\min}) \exp\left(\frac{1n\left(\frac{Ra_{max}}{Ra_{min}}\right) \times it}{itm}\right) \tag{11}$$

Where; *it* is the iteration number. $x_i^{\max}$ and $x_i^{\min}$ are the maximum and minimum possible values for x_i. Ra_{max} and Ra_{min} are the maximum and minimum of relative search radius of the hunter, respectively, and *itm* is the maximum number of iterations in the optimization process.

In digital value correction, instead of using real values of each variable, hunters communicate with each other by the digits of each solution variable. For example, the solution variable with the value of 23.4356 has six meaningful digits. For this solution variable, the hunter chooses a value for the first digit *(i.e.2)* based on hunting group considerations or position correction. After the quality of the new hunter position is determined by evaluating the objective function, the hunter moves to this new position; otherwise it keeps its previous position.

5. Reorganizing the hunting group: In order to prevent being trapped in a local optimum, they must reorganize themselves to get another opportunity to find the optimum point. The algorithm does this in two independent conditions. If the difference between the values of the objective function for the leader and the worst hunter in the group becomes smaller than a preset constant ε_1 and the termination criterion is not satisfied, then the algorithm reorganizes the hunting group for each hunter. Alternatively, after a certain number of searches, the hunters reorganize themselves. The reorganization is carried out as follows: the leader keeps its position and the other hunters randomly choose their position in the design space

$$x_i^j = x_i^1 \pm rand_i \cdot (x_i^{max} - x_i^{min}) \cdot \alpha \cdot \exp(-\beta \cdot EN) \tag{12}$$

where x_i^1 is the position value of the leader for the i^{th} variable. *rand* is a uniform random number between [0,1]. $x_i^{\max}$ and $x_i^{\min}$ are the maximum and minimum possible values of variable x_i, respectively. *EN* counts the number of times that the group has been trapped until this step. As the algorithm goes on, the solution gradually converges to the optimum point. Parameters α and β are positive real values.

6. Termination: **S**teps 3-5 are repeated until maximum number of iterations is satisfied.

Constraint handling: In this study fly-back mechanism is used for handling the design constraints, which is proven to be effective in the literature [2]. Once all hunter positions x_i are generated, the objective functions are evaluated for each of these and the constraints in the problem are then computed with these values to find out whether they violate the design constraints. If one or a number of the hunter gives infeasible solutions, these are discarded and new ones are re-generated. If some hunters are slightly infeasible, then such hunters are kept in the solution. These hunters, having one or more constraints slightly infeasible, are utilized in the design process that might provide a new hunter that may be feasible. This is achieved by using larger error values initially for the acceptability of the new design vectors and then reduce this value gradually during the design cycles and uses finally an error value of 0.001 or whatever necessary value that is required to be selected for the permissible error term towards the end of iterations. This adaptive error strategy is found quite effective in handling the design constraints in large design problems.

The pseudo code of the algorithm is given in Figure 4.

```
begin;
    Initialize optimization problem and parameters:
        HGS: number of hunters- hunting group size
        MML: maximum movement toward leader
        HGCR: hunting group consideration rate
        EN: number of epochs
        Ra: distance radius
        α and β : reorganization parameters
    Initialize the hunting group- generate random population of HGS
    solutions (hunters);
    Calculate the fitness values of initial members: fitness(i)= f (xi);
    Set leader as the best fitness of all hunters
    while (the termination conditions are not met)
        for each hunter i ;
            Change the position- move toward leader in view of
    MML
            Calculate fitness(i)
            if fitness(i) is better than leader; leader = fitness(i)
        end for;
        for each hunter i ;
            Correct position on the basis of group consideration
            (HGCR) and local search
            Calculate fitness(i)
            if fitness(i) is better than leader; leader = fitness(i)
        end for;
        for each hunter i ;
            Update the position- reorganize the hunting group
            Calculate fitness(i)
            if fitness(i) is better than leader; leader = fitness(i)
        end for;
    end while
end procedure;
```

Figure 4. Pseudo Code for Hunting Search Algorithm

4. DISCRETE OPTIMUM DESIGN OF UNBRACED STEEL FRAMES WITH SEMI-RIGID CONNECTIONS TO LRFD-AISC

In the design of unbraced steel frames, the main concept is to select the readymade steel sections for its columns and beams from standard steel section tables. This design can be valid only if the serviceability and strength requirements specified by the code of practice are satisfied. In order to obtain an accurate response of the frame under the external loading, beam-to-column connections are assumed to be partially restrained. Hence, the stability analysis is included in the formulation of the design problem.

When the constraints are implemented from LRFD–AISC in the formulation of the design problem, the discrete optimum design problem of unbraced steel frames with semi-rigid beam-to-column connections, where the objective is the minimum weight can be expressed as follows:
Minimize;

$$W = \sum_{k=1}^{ng} m_k \sum_{i=1}^{nk} L_i \tag{13}$$

Subject to

$$(\delta_j - \delta_{j-1}) / h_j \le \delta_{ju} \qquad j = 1,...., ns \tag{14}$$

$$\delta_i \le \delta_{iu} \qquad i = 1,...., nd \tag{15}$$

$$V_u \le \phi V_n \tag{16}$$

$$\left(\frac{P_u}{\phi_c P_n}\right)_{il} + \left(\frac{8}{9}\left(\frac{M_{ux}}{\phi_b M_{nx}}\right)\right)_{il} \le 1.0 \qquad for \quad \frac{P_u}{\phi_c P_n} \ge 0.2$$
$$\left(\frac{P_u}{2\phi_c P_n}\right)_{il} + \left(\frac{M_{ux}}{\phi_b M_{nx}}\right)_{il} \le 1.0 \qquad for \quad \frac{P_u}{\phi_c P_n} \le 0.2 \tag{17}$$

$$B_{sb} \le B_{sc} \qquad s = 1,...., nu \tag{18}$$

$$D_s \le D_{s-1} \tag{19}$$

$$m_s \le m_{s-1} \tag{20}$$

where Eq. 13 defines the weight of the frame, *ng* is total numbers of groups in the structural system, m_k is the unit weight of the steel section selected from the standard steel sections table that is to be adopted for group k, L_i is the length of member i that belongs to group k, n_k is total number of members in group k. Eq. 14 represents the inter-storey drift of the multi-storey frame. δ_j and δ_{j-1} are lateral deflections of two adjacent storey levels and h_j is the storey height. *ns* is the total number of storeys in the frame. Eq. 15 defines the displacement restrictions that may be required to include other than drift constraints such as deflections in beams. *nd* is the total number of restricted displacements in the frame. δ_{ju} is the allowable lateral displacement. The horizontal deflection of columns is limited due to unfactored imposed load and wind loads to height of column / 300 in each storey of a building with more than one storey. δ_{iu} is the upper bound on the deflection of beams which is given as *span*/300 if they carry plaster or other brittle finish. Eq. 16 represents the shear capacity check for beam-columns. ϕ is resistance factor in shear, V_u required shear strength, V_n is nominal shear strength. Eq. 17 defines the local capacity check for beam-columns. *nm* is number of members, *nl* is number of load cases, M_{nx} is nominal flexural strength, M_{ux} is applied moment, P_n is nominal axial strength, P_u is applied axial load, ϕ_c is resistance factor for columns if the axial force is in compression, ϕ_b is resistance factor in bending. It is apparent that computation of compressive strength $\phi_c P_n$ of a compression member requires its effective length. The computation of the effective length of a compression member in a frame can be automated by using Jackson and Moreland monograph [9]. Eq. 18 is included in the design problem to ensure that the flange width of the beam section at each beam-column connection of storey s should be less than or equal to the flange width of column section. Eqs. 19-20 are required to be included to make sure that the depth and the mass per meter of column section at storey s at each beam-column connection are less than or equal to width and mass of the column section at the lower storey *s-1*. *nu* is the total number of these constraints Figure 5.

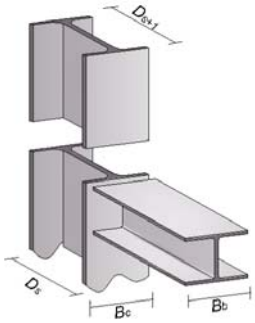

Figure 5. Geometry of Beam-column Connection

4.1 Optimum Design Algorithm

Solution of the discrete design problem given in Eqs. 13-20 is obtained using hunting search algorithm.

Hunting search method based optimum design algorithm treats the sequence number of the steel sections in the standard W-section list as a design variable. Once a sequence number is selected, then the sectional designation and properties of that section becomes available for the algorithm. Therefore, the design vector consists of integer numbers that corresponds to the sequence numbers of W-sections in the discrete set given in LRFD–AISC, which are selected for each group in the steel frame. The design algorithm consists of the following steps.

1. Select the values of parameters namely, hunting group size *HGS,* maximum movement towards leader *MML*, hunting group consideration rate *HGCR*, maximum and minimum of relative search radius of the hunter Ra_{max} and Ra_{min}, maximum iteration number *itm,* reorganization parameters α and β, number of epochs *EN*.
2. Generate hunter's positions. Select randomly sequence number of steel sections from the discrete list for each group in the frame.
3. Carry out the analysis of the steel frame with these sections, under the consideration of the stiffness matrix modified in such a way that the corresponding terms represent the flexibility of the beam-to-column connections. Check whether the design limitations are satisfied or not. If the hunter violates the design constraints severely, discard this hunter and repeat the selection of a new one. If it is slightly infeasible consider it for the hunting group.
4. Check whether the newly selected hunter is acceptable. If not, go to step 3.
5. After the selection of acceptable hunters, calculate the objective function value for each hunter. Determine the one which has the best objective function value.

5. DESIGN EXAMPLES

Three unbraced semi-rigid steel frames are designed using hunting search method based optimum design algorithm presented in the previous section. Effect of connection modeling on the minimum weight of frames is investigated. In addition, to demonstrate the efficiency of hunting search algorithm, the same examples are also solved with particle swarm optimizer which is proven to be robust and efficient in the solution of structural optimization problems. The discrete set, from which the design algorithm selects the sectional designations for frame members, is considered to be the complete set of 272 W-sections starting from W100x19.3 to W1100x499mm as given in LRFD-AISC. For this study, hunting search algorithm parameters; *MML, HGCR,* Ra_{max}, Ra_{min}, α, β,

EN are chosen to be 0.005, 0.3, 0.01, 0.001, 1.2, 0.02, 25, respectively. These values are decided after carrying out several trials in the design examples. Each example is solved with each method ten times with different seed values in order to inquire the effect of random numbers to optimum solutions. Algorithms perform this by producing different random number in each iteration by using call random_seed(*i*), where i is the iteration number. Then the best one amongst them, which has the minimum frame weight, is accepted as the optimum design.

5.1 Eight Storey- Six Bay Steel Frame

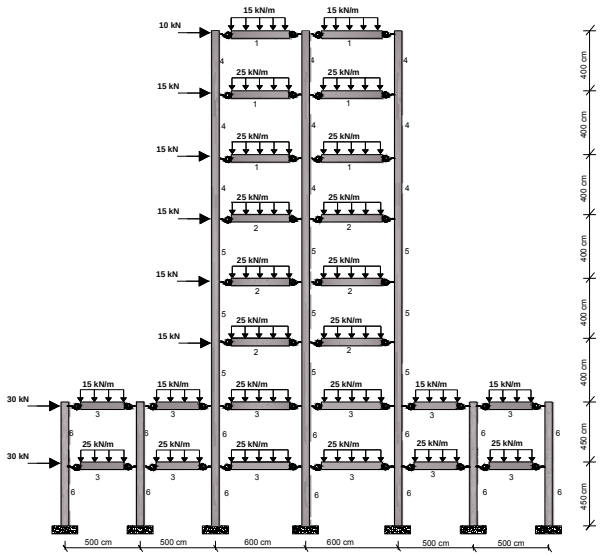

Figure 6. Eight-storey, Six-bay Steel Frame

The eight storey six bay steel frame shown in Figure 6 is considered as first design example. The frame consists of fifty six members that are collected in six groups as shown in Figure6. The allowable inter-storey drift is 1/300 cm of storey height while the lateral displacement of the top storey is limited to 1/300 cm of total height of the frame, which corresponds to 1.33cm and 11cm, respectively. The modulus of elasticity is 200kN/mm^2.

At first, frame is designed ten times assuming the beam-to-column connections to be end plate without column stiffeners. Then, ten different designs are produced assuming the end connections to be fully restrained. Best, worst and average runs obtained by each method are given in Table 1. The optimum W-sections designations obtained by the hunting search and particle swarm method are given in Table 2. Results obtained by the consideration of both end connection assumptions are tabulated.

Table 1. Minimum Weights (kg) obtained for Eight Storey Six Bay Frame

	PSO		**HuS**	
	Rigid	**Semi Rigid**	**Rigid**	**Semi Rigid**
Best Design **(kg)**	13186,81	16313,780	13186,81	15423,360
Average Design **(kg)**	15687,68	18220,35	14574,45	16281,440
Worst Design **(kg)**	20293,76	29514,25	17561,62	17732,93

Table 2. Optimum Designs for Eight-storey, Six-bay Steel Frame

		PSO		**HuS**	
Group No	**Member Type**	**Rigid**	**Semi Rigid**	**Rigid**	**Semi Rigid**
1	Beam	W410X46,1	W410X38,8	W410X46,1	W410X38,8
2	Beam	W460X52	W530X74	W460X52	W530X74
3	Beam	W460X52	W530X66	W460X52	W460X52
4	Column	W250X32,7	W310X38,7	W250X32,7	W410X38,8
5	Column	W310X52	W410X67	W310X52	W410X67
6	Column	W460X52	W410X67	W460X52	W410X67
Maximum inter storey drift ratio		0,98	1,00	0,98	0,99
Maximum Strength Ratio		0,99	0,96	0,99	0,98
Top storey drift **(cm)**		8,79	9,37	8,79	9,77
Minimum Weight **(kg)**		**13186,810**	**16313,780**	**13186,810**	**15423,360**

Convergence rate graphs of the optimum designs are shown Figure 7. The lightest design where the former assumption is made, weighs 13186.81kg. Hunting search algorithm and particle swarm optimizer produce the same design. However, it can be clearly seen from the figure that particle swarm optimizer shows better convergence in finding the optimum solution. On the other hand, it is noticed that the weight of the optimum design becomes 15423.36 kg in the case of latter assumption, which is obtained by hunting search algorithm. The one attained with particle swarm optimizer is 16313.78 kg, which is 6% heavier than this design. This implies that the frames with semi-rigid end connections (end plate without column stiffeners) are heavier than the ones with rigid end connections.

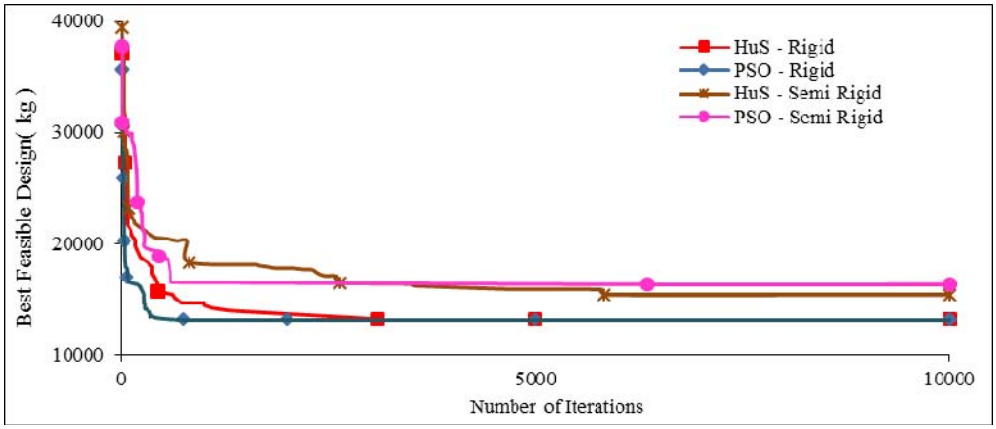

Figure 7. Design history graph for eight-storey, six -bay steel frame

5.2 Ten Storey Four Bay Steel Frame

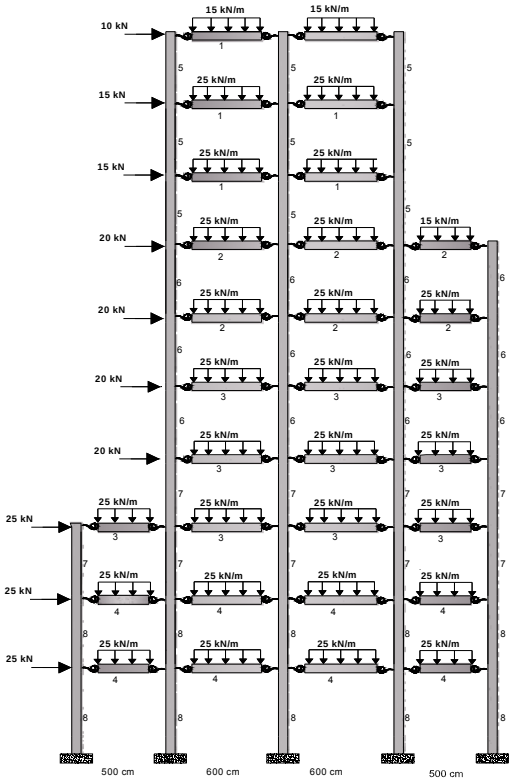

Figure 8. Ten-storey, Four-bay Steel Frame

Ten-storey, four-bay frame shown in Figure 8 is considered as second design example. The frame configuration dimensions, loading, joint numbering and member grouping are shown in the same figure. The frame consists of seventy members that are collected in eight groups as shown in the figure. Top storey drift is limited to 13.67cm, which is again 1/300 cm of total height of frame and inter-storey drift is restricted to 1.33cm i.e. 1/300 cm of storey height of frame. The modulus of elasticity is 200kN/mm^2. Roof beams are loaded by uniform gravity loads of 15kN/m while the others are loaded by those of 25kN/m. There are also lateral point loads acting on the joints at each story level. Material properties of steel profiles remain the same with the previous example.

This frame is also designed by use of both algorithms. Best, worst and average runs obtained by each method are given in Table 3. Optimum section designations for each design are given in Table 4. It is observed that maximum strength ratio of the optimum designs, obtained with hunting search and particle swarm methods, are 1.00 for rigid frames.

Table 3. Minimum Weights (kg) obtained for Ten-storey, Four-bay Steel Frame

	PSO		**HuS**	
	Rigid	**Semi Rigid**	**Rigid**	**Semi Rigid**
Best Design **(kg)**	18121,55	22469,73	17663,79	21700,77
Average Design **(kg)**	22282,53	28752,45	18311,73	23499,09
Worst Design **(kg)**	35100,40	41649,03	23749,28	25472,10

Table 4. Optimum Designs for Ten-storey, Four-bay Steel Frame

		PSO		HuS	
Group No	**Member Type**	**Rigid**	**Semi Rigid**	**Rigid**	**Semi Rigid**
1	Beam	W410X46,1	W410X38,8	W410X46,1	W360X44
2	Beam	W460X52	W410X38,8	W410X46,1	W410X46,1
3	Beam	W460X52	W460X60	W460X52	W530X66
4	Beam	W460X52	W610X82	W460X52	W610X82
5	Column	W250X38,5	W310X38,7	W360X44	W360X44
6	Column	W460X60	W530X66	W360X51	W360X51
7	Column	W460X60	W530X74	W460X52	W530X74
8	Column	W460X68	W530X123	W460X74	W530X101
Maximum inter storey drift ratio		0,96	0,99	0,99	0,98
Maximum Strength Ratio		1,00	0,89	1,00	0,99
Top storey drift **(cm)**		10,39	10,65	10,81	10,36
Minimum Weight **(kg)**		**18121,550**	**22469,730**	**17663,790**	**21700,770**

Besides, it is noticed that maximum inter-storey drift ratios are 0.99 and 0.96 for the same frames, respectively. This clearly indicates that the designs attained with fully restrained connection assumption are dominated by strength constraints. Hunting search produces rigid frame with the weight of 17663.79 kg and semi-rigid frame with the weight of 21700772 kg, while the optimum designs of rigid and semi-rigid frames obtained with particle swarm weigh 18121.55kg and 22469.73 kg, respectively. This means that similar to first example, semi-rigid connection modeling gives heavier design for this frame configuration. Convergence rate graphs are shown in Figure 9.

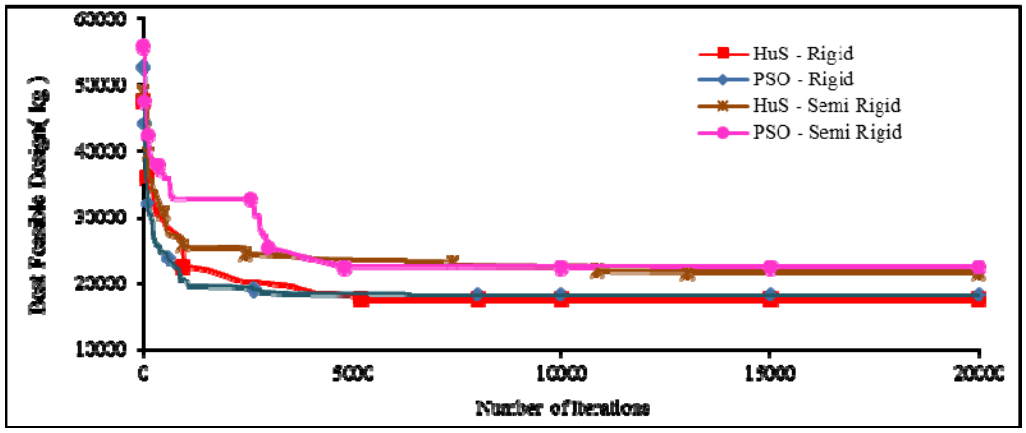

Figure 9. Design History Graph for Ten-storey, Four-bay Steel Frame

5.3 Twelve Storey Four Bay Steel Frame

Twelve-storey, four-bay frame shown in Figure 10 is considered to be the third design example. The same figure shows the frame configuration dimensions, loading, joint numbering and member grouping. Frame is composed of 108 members, 60 of which is column and 48 of which is beam. These frame members are collected in ten groups. Roof beams are loaded by uniform gravity loads of 15kN/m while the others are loaded by those of 25kN/m. There are also lateral point loads acting on the joints at each story level.

Frame is separately designed ten times using both methods. Best, worst and average runs are given in Table 5. Results reveal that hunting search technique attains lighter frame for both end connection assumptions. Optimum designs for rigidly connected frames achieved by HuS and PSO methods weight 39478,25kg and 42220,05kg, respectively. On the other hand, semi rigid frames produced by the same methods weigh 61124,64kg and 71699,77kg, respectively. These four designs are tabulated in Table 6 with section designations attained for each member group. This table also includes the maximum values of design constraints, reached in each design. According to these results, while the strength constraints dominate the rigid frames, inter-story drift constraints are effective in the solution of semi-rigid frames. Convergence rate graphs are given in Figure 11.

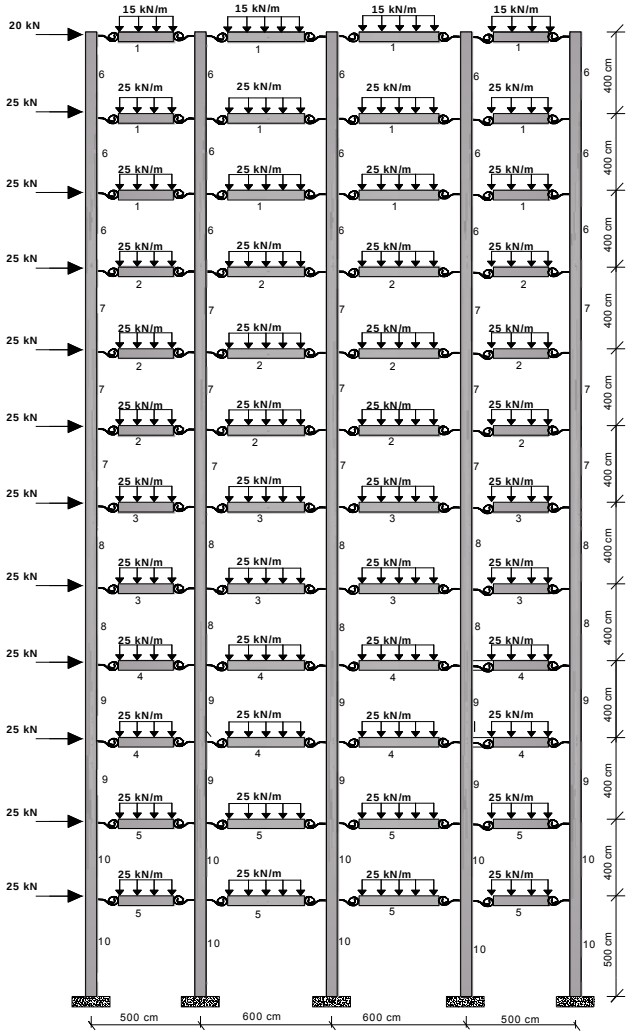

Figure 10. Twelve-storey, Four-bay Steel Frame

Table 5. Minimum Weights (kg) obtained for Twelve-storey, Four-bay Steel Frame

	PSO		**HuS**	
	Rigid	**Semi Rigid**	**Rigid**	**Semi Rigid**
Best Design **(kg)**	42220,05	55089,580	39478,25	46451,310
Average Design **(kg)**	53221,63	59680,44	47029,48	50605,04
Worst Design **(kg)**	75877,34	79454,82	57512,21	59764,62

Table 6. Optimum Designs for Twelve-storey, Four-bay Steel Frame

		PSO		HuS	
Group No	**Member Type**	**Rigid**	**Semi Rigid**	**Rigid**	**Semi Rigid**
1	Beam	W410X46,1	W360X60	W410X46,1	W410X38,8
2	Beam	W460X60	W530X66	W410X67	W460X52
3	Beam	W460X52	W460X60	W410X60	W460X74
4	Beam	W460X60	W530X74	W460X68	W460X52
5	Beam	W460X74	W610X82	W410X53	W690X170
6	Column	W250X38,5	W360X79	W310X38,7	W410X53
7	Column	W360X134	W460X89	W410X75	W460X60
8	Column	W360X134	W610X113	W410X85	W530X92
9	Column	W760X134	W760X196	W610X101	W610X153
10	Column	W760X134	W840X329	W610X217	W610X241
Maximum inter storey drift ratio		0,96	0,95	0,97	0,93
Maximum Strength Ratio		0,99	0,82	0,99	0,88
Top storey drift **(cm)**		11,97	11,24	12,60	11,23
Minimum Weight **(kg)**		**42220,050**	**55089,580**	**39478,250**	**46451,310**

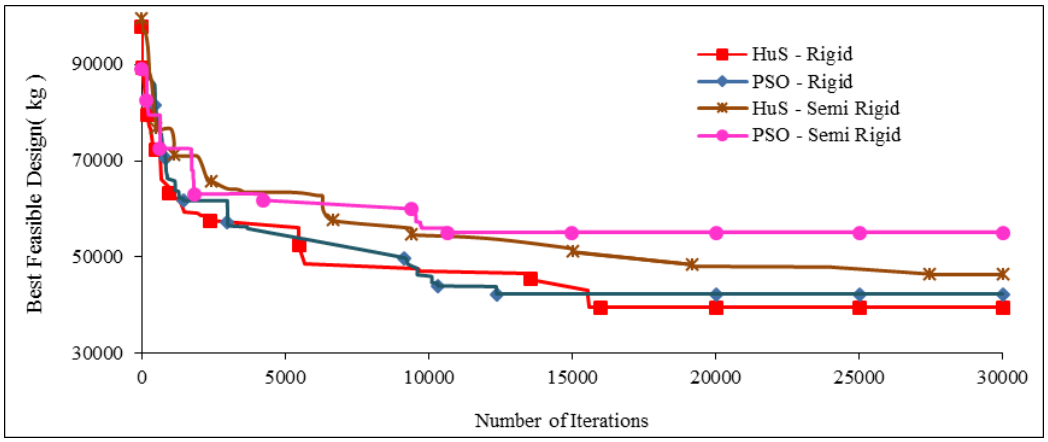

Figure 11. Design History Graph for Twelve-storey, Four-bay Steel Frame

6. CONCLUSIONS

In this study, a hunting search optimization based optimum design algorithm is presented for unbraced steel frames with semi-rigid connections. Developed computer program analyzes the nonlinear steel frame with flexible connections, taking into account the LRFD-AISC specifications and selects W sections from ready section lists available in the literature. Experimental studies in the literature declare that the connection flexibility affects the distribution of forces in the frame and leads to an increase in the drift of whole structure. This makes it necessary to consider P-Δ effect in the frame analysis. There are several connection models in the literature. Among them end plate without column stiffeners connection model is carried out in the present study. Analysis and design routine is modified in such a way that it includes the flexibility and geometry of end-plate connection. For the determination of the effect of joint flexibility on the behavior of whole structure,

example problems are also designed as rigid frames. This way, a comparison between both assumptions is carried out and it is noticed that semi-rigid connection assumption results in heavier frames. According to the observations, since great amount of horizontal displacement exist in the flexible connections, displacement constraints become dominant in the design. Therefore, algorithm selects stronger sections to satisfy these constraints. As a result, the weight of the whole structure designed with partially restrained connection assumption becomes greater than the one designed with fully restrained connection assumption. The second part of the study is devoted to the demonstration of the efficiency of presented hunting search-based design algorithm. To do this, the same analysis and design routine is automated with particle swarm optimizer. The same numerical problems are solved by this algorithm, once again. Results show that hunting search produces better designs compared to particle swarm optimizer.

REFERENCES

[1] Kameshki, E.S. and Saka, M.P., "Optimum Design of Nonlinear Steel Frames with Semi-rigid Connections using a Genetic Algorithm", Computers and Structures, 2001, Vol. 79, pp. 1593-1604.

[2] He, S., Prempain, E. and Wu, Q.H., "An Improved Particle Swarm Optimizer for Mechanical Design Optimization Problems", Engineering Optimization, 2004, Vol. 36, No. 5, pp. 585-605.

[3] Saka, M.P., "Optimum Design of Steel Frames using Stochastic Search Techniques based on Natural Phenomena: A Review", Civil Engineering Computations: Tools and Techniques, Ed. B. H. V. Topping, Saxe-Coburgh Publications, 2007, Chapter 6: pp. 105-147.

[4] Hasançebi, O., Çarbaş, S., Doğan, E., Erdal, F. and Saka, M.P., "Performance Evaluation of Metaheuristic Search Techniques in the Optimum Design of Real Size Pin Jointed Structures", Computers and Structures, 2009, Vol. 87, No. 5-6, pp. 284-302.

[5] Hasançebi, O., Çarbaş, S. and Saka, M.P., “Improving the Performance of Simulated Annealing in Structural Optimization”, Journal of Structural and Multidisiplinary Optimization, 2010, Vol. 41, pp: 189–203.

[6] Degertekin, S.O. and Hayalioglu, M.S., “Harmony Search Algorithm for Minimum Cost Design of Steel Frames with Semi-rigid Connections and Column Bases”, Journal of Structural and Multidisiplinary Optimization, 2010, Vol. 42, pp. 755–768.

[7] Oftadeh, R., Mahjoob, M.J. and Shariatpanahi, M., "A Novel Meta-heuristic Optimization Algorithm Inspired by Group Hunting of Animals: Hunting Search", Computers Mathematics with Applications, 2010, Vol. 60, pp. 2087-2098.

[8] Doğan, E. and Saka, M.P. “Optimum Design of Steel Frames to LRFD- AISC Using Particle Swarm Optimization”, Advances in Engineering Software, 2012, Vol. 46, No.1, 27-34.

[9] McGuire, W., “Steel Structures”, Prentice-Hall, 1968.

[10] Majid, K.I., “Nonlinear Structures”, London Butterworth, 1972.

[11] Chen, W.F.,“Practical Analysis for Semi-Rigid Frame Design”, World Scientific Pub Co Inc., 1999.

[12] Chan, S.L. and Chui, P.P.T., “Non-Linear Static and Cyclic Analysis of Steel Frames with Semi-Rigid Connections”, Elsevier, 2000.

[13] Faella, C., Piluso, V. and Rizzano, G., “Structural Steel Semirigid Connection”s, CRC Press LLC, Boca Raton, 2000.

[14] Kochenberger, G.A. and Glover, F., “Handbook of Meta-Heuristics”, Kluwer Academic Publishers, 2003.

[15] Christensen, P.W., “An Introduction to Structural Optimization”, Springer, Linköping, Sweden, 179-200, 2008.

[16] Kennedy, J. and Eberhartm, R.C., “Particle Swarm Optimization”, Proceedings of IEEE International Conference on Neural Networks, NJ, 1995, Piscataway.

[17] Liu, H., Shichang, S. and Ajith, A., “Particle Swarm approach to Scheduling Work-flow Applications in Distributed Data-intensive Computing Environments”, Proceedings of the 6th International Conference on Intelligent Systems Design and Applications, 2006, (ISDA'06) : 0-7695-2528-8/06.

[18] Doğan, E. and Saka, M.P., “Optimum Design of Steel Frames to LRFD- AISC using Particle Swarm Optimization”, Proceedings of The 9th International Conference on Computational Structures Technology, 2-5 September, Athens, Greece, 2008.

[19] Doğan, E. and Saka, M.P., “Particle Swarm Optimization Design of Moment Resisting Steel Frames with Semi-rigid Connections to LRFD-AISC”, Proceedings of the 8th World Congress on Structural and Multidisciplinary Optimization, 2009.

[20] Hasançebi, O. and Azad, K.S., “A Comparison of Metaheuristics in Structural Optimization" Intl. Conf. on Advances in Civil, Structural and Mechanical Engineering, 2013, CSM 2013, pp. 18-22.

[21] “LRFD-AISC”, Manual of Steel Construction - Load and Resistance Factor Design, SA, 1986.

FLEXURAL BUCKLING DESIGN OF FABRICATED AUSTENITIC AND DUPLEX STAINLESS STEEL COLUMNS

Yang-Lu[1,*], Zhao-Menghan[1], Chan-Takming[2] and Shang-Fan[1]

[1] *The College of Architecture and Civil Engineering; Beijing University of Technology, Beijing 100124, China*
[2] *Department of Civil and Environmental Engineering, The Hong Kong Polytechnic University, Hung Hom, Kowloon, Hong Kong SAR*
**(Corresponding author: E-mail: lyang@bjut.edu.cn)*

Received: 29 September 2016; Revised: 13 February 2017; Accepted: 16 April 2017

ABSTRACT: This paper presents a numerical investigation on the flexural buckling design of fabricated austenitic and duplex stainless steel columns. Complementary experimental investigation was conducted and the numerical modelling methodology was validated against the complementary experimental database. The target parametric study was carried out to assess the influence of initial geometric imperfections, residual stress patterns, mechanical properties, local cross-section slenderness and global slenderness on the structural behaviour. A total of 968 FEA results were developed which included 301 welded box-section and 667 welded I-section columns. The resulting structural performance data were collated to assess the reliability of the current design provisions - EN 1993-1-4 and ASCE 8-02. Results indicate the conservatism on current practices. Improved design provisions were proposed based on the Direct Strength Method, ASCE 8-02 and Perry formulae.

Keywords: Flexural buckling design, parametric analysis, reliability analysis, stainless steel, columns

DOI: 10.18057/IJASC.2018.14.2.4

1. INTRODUCTION

In recent years, stainless steel has been widely used for construction because of their favorable material properties and the corrosion resistance [1]. Corresponding stainless steel design specifications have also been developed and adopted in Europe [2], the United States [3] and China [4] which promotes the further acceptance by the engineers. These days, research on stainless steel focuses on material characterization, residual stress patterns, local and global stability behaviours. Over the research on the material characterization, Mirambell and Real [5] proposed a two-stage Ramberg-Osgood model which was subsequently modified by Quach [6] to a three-stage model. Research on residual stress measurements were conducted by Gardner [7], Quach [8] and Yuan [9]. Wang [10] and Yang [11], on the other hand, developed an overall stability calculation method for welded I-section stainless steel beams through experimental and theoretical investigations. Yuan [12] studied the local-overall interaction buckling of welded stainless steel columns experimentally and proposed a new design method. Research on stability loading capacity of cold-formed stainless steel columns was also carried out by Shu [13, 14]. Two modified design methods for lean duplex stainless steel beam-columns was also proposed in Huang and Young [15]. A new design method – Continuous strength method, which can further exploit the strain-hardening benefits of the stainless steel materials, has been developed in the last two decades by Gardner and Nethercot [16-18].

Current design specifications for stainless steel include EN 1993-1-4 (for cold-formed and welded members), SEI/ASCE 8-02 and AS/NZS 4673-2001 (for cold-formed members) [19]. The design methodologies in EN 1993-1-4 and AS/NZS 4673-2001 are fundamentally the same as their carbon steel design counterparts.

To expand the current stainless steel research to welded/fabricated sections, the objective of this paper is to develop an efficient method for flexural buckling design on fabricated austenitic and duplex stainless steel columns. Experimental programme, followed by the numerical investigation, was discussed in two companion papers [20, 21]. Experimental investigation on twenty-two austenitic and duplex stainless steel welded I-section compression members were conducted by Yang *et al.* [20] while twelve austenitic and duplex welded stainless steel box-section columns were tested by Yang *et al.* [21]. A corresponding numerical model was developed to replicate the experimental procedure. The load-displacement curves and buckling strength of experiments and finite element simulations were compared, indicating that the finite element methodology is applicable for parametric studies.

Considering the conservatism of existing codified approaches during the stage prior to the yield stress, the focus of the present paper was the development of new efficient methods, i.e. a three-segment model, for the design of welded stainless steel cross-sections under compressive loading, based on the experimental results from the companion papers and parametric studies conducted herein. The reliability of the proposed design method will be assessed by comparing the design proposal with generated structural performance data.

2. NUMERICAL MODELING

2.1 Introduction

In conjunction with the previously conducted experimental studies [20, 21], a numerical modeling programme was performed using the general-purpose finite element analysis package ANSYS. The aims of the numerical investigations were initially to replicate the full experimental load–deformation curves and to assess the sensitivity of the FE models to extensive input parameters, and subsequently to conduct parametric studies to generate further structural performance data to supplement the experimental results. The accuracy of the FE models was assessed in the companion paper [20, 21] by comparing the key results, full load–deformation histories and failure modes obtained from tests with those derived from the numerical simulations.

2.2 Parametric Analysis

Having verified the general ability of the FE models to replicate the column test behaviour, a series of parametric studies were conducted. The basic FE model took $0.001L$ as initial geometric imperfection factor, where L is the length of the member. Residual stress distribution model proposed by Yuan Huanxin [9], the measured material properties and geometric dimensions were used as based modelling parameters. The primary aim of the parametric studies was to investigate the influence of initial global geometric imperfection, residual stress, material properties, local width-to-thickness ratio and non-dimensional global slenderness on the column load carrying capacity. The obtained results were also used to assess column buckling design curves.

2.3 Global Geometric Imperfection

Three different amplitudes of the global geometric imperfection, including $0.0005L$, $0.001L$, and $0.002L$, in the shape of a half-sine wave, were used. Table 1 and Table 2 show the FE results of column loading capacity with different geometric imperfections. The comparison of buckling resistance by using different amplitudes is also presented in Figure 1. It illustrates that:

Table 1. FE Results with Different Geometric Imperfections (Box-section)

Austenitic stainless steel						Duplex stainless steel					
$\bar{\lambda}$	$F_{0.001}$ (kN)	$F_{0.002}$ (kN)	$F_{0.0005}$ (kN)	$F_{0.002}/F_{0.001}$	$F_{0.0005}/F_{0.001}$	$\bar{\lambda}$	$F_{0.001}$ (kN)	$F_{0.002}$ (kN)	$F_{0.0005}$ (kN)	$F_{0.002}/F_{0.001}$	$F_{0.0005}/F_{0.001}$
0.49	771	739	795	0.96	1.03	0.74	1362	1287	1402	0.94	1.03
0.74	627	589	653	0.94	1.04	0.94	1132	1054	1176	0.93	1.04
0.99	491	457	515	0.93	1.04	1.15	907	842	946	0.93	1.04
1.24	378	348	398	0.92	1.05	1.35	722	670	748	0.93	1.04
1.48	290	266	308	0.92	1.06	1.55	576	537	597	0.93	1.04
1.73	225	207	239	0.92	1.06	1.75	466	436	482	0.93	1.03
1.98	178	164	188	0.92	1.06	1.96	382	359	395	0.94	1.03
2.23	143	132	151	0.92	1.06	2.16	318	300	329	0.94	1.03
2.47	117	109	124	0.93	1.05	2.36	269	254	278	0.94	1.03

Table 2. FE Results with Different Geometric Imperfections (I-section)

	Austenitic stainless steel						Duplex stainless steel					
	$\bar{\lambda}$	$F_{0.001}$ (kN)	$F_{0.0005}$ (kN)	$F_{0.002}$ (kN)	$F_{0.0005}/F_{0.001}$	$F_{0.002}/F_{0.001}$	$\bar{\lambda}$	$F_{0.001}$ (kN)	$F_{0.0005}$ (kN)	$F_{0.002}$ (kN)	$F_{0.0005}/F_{0.001}$	$F_{0.002}/F_{0.001}$
Major axis	0.39	905	937	855	1.04	0.94	0.50	1763	1830	1672	1.04	0.95
	0.59	764	788	713	1.03	0.93	0.71	1471	1530	1380	1.04	0.94
	0.79	640	663	586	1.04	0.92	0.92	1182	1240	1103	1.05	0.93
	0.99	523	550	478	1.05	0.92	1.13	938	980	874	1.04	0.93
	1.18	429	451	390	1.05	0.91	1.34	746	778	697	1.04	0.93
	1.38	353	370	321	1.05	0.91	1.56	601	623	564	1.04	0.94
	1.58	292	305	266	1.04	0.91	1.77	491	506	463	1.03	0.94
	1.77	244	253	223	1.04	0.92	1.98	408	418	386	1.03	0.94
	1.97	203	213	189	1.05	0.93	2.19	343	351	326	1.02	0.95
Minor axis	0.53	923	942	884	1.02	0.96	0.66	1795	1866	1707	1.04	0.95
	0.73	759	780	711	1.03	0.94	0.84	1539	1604	1443	1.04	0.94
	0.92	611	636	566	1.04	0.93	1.01	1292	1359	1199	1.05	0.93
	1.12	487	511	450	1.05	0.92	1.19	1064	1120	986	1.05	0.93
	1.32	394	416	362	1.06	0.92	1.37	874	918	811	1.05	0.93
	1.52	323	342	297	1.06	0.92	1.54	722	760	672	1.054	0.93
	1.72	269	285	247	1.06	0.92	1.72	605	635	563	1.05	0.93
	1.91	228	240	208	1.05	0.91	1.90	511	534	476	1.04	0.93
	2.11	194	204	178	1.05	0.92	2.07	436	455	408	1.04	0.93
	2.31	168	175	154	1.05	0.92	2.25	376	391	352	1.04	0.94

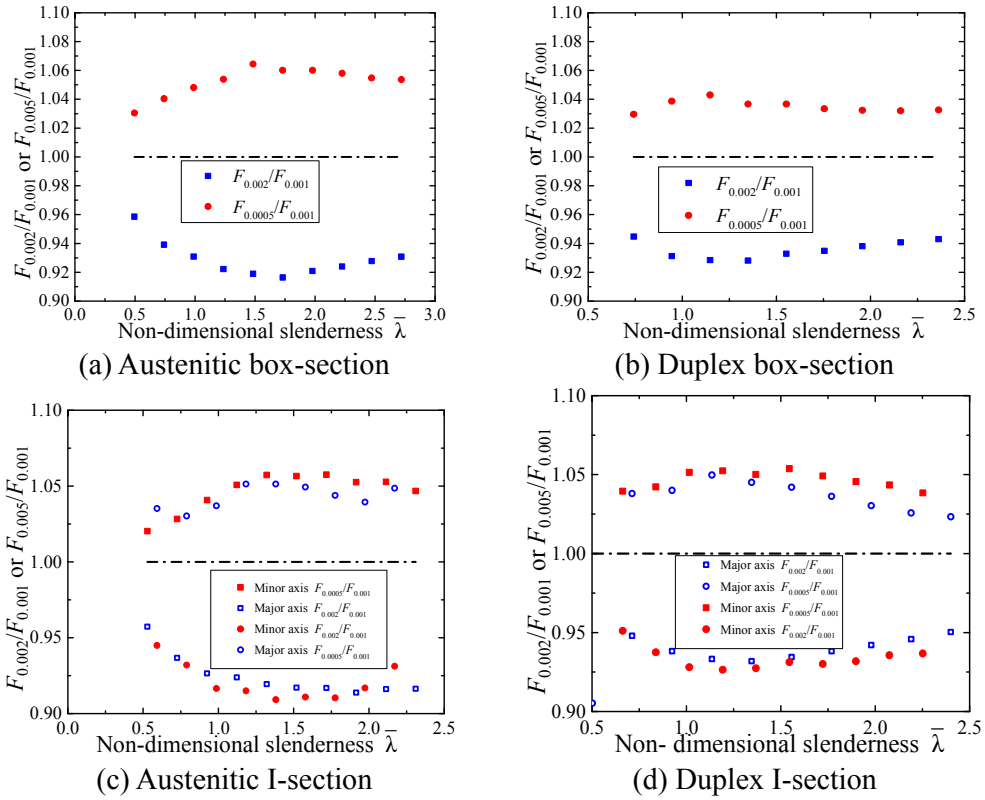

(a) Austenitic box-section (b) Duplex box-section

(c) Austenitic I-section (d) Duplex I-section

Figure 1. The Influence of Initial Imperfection

- The influence of column geometric imperfections on the loading capacity is related to column slenderness. Columns with medium lengths, as anticipated, are more sensitive to different geometric imperfections;
- $F_{0.0005}$ is generally 5% higher than $F_{0.001}$, while $F_{0.001}$ is generally 7% higher than $F_{0.002}$. And the ultimate load is slightly fluctuated with the change of non-dimensional slenderness ratio;
- For columns buckling about minor axis, the influence of geometric imperfections on loading capacity is slightly more obvious.

2.4 Residual Stress

The residual stress measurements were conducted in [20, 21] and the corresponding models were proposed as shown in Figure 2. This section compares the FE results with and without the consideration of residual stress and the results are summarized in Table 3 and Table 4 respectively. All data are also compared in Figure 3. In Figure 3, the horizontal axis is the non-dimensional slenderness ratio and the vertical axis is the ratio of ultimate load F_w to F_y. F_w and F_y represent the loading capacity with and without considering the residual stress respectively. It shows that

- The influence of residual stress upon the loading capacity is related to column slenderness. Box-section columns with larger slenderness are more sensitive to residual stress. For columns buckling about major axis, residual stress affects slender columns more than stub counterparts. While for columns buckling about minor axis, residual stress affects medium-length columns the most.
- Columns buckling about minor axis are more sensitive to residual stress.

Therefore, residual stress was considered in all models in the subsequent parametric analysis.

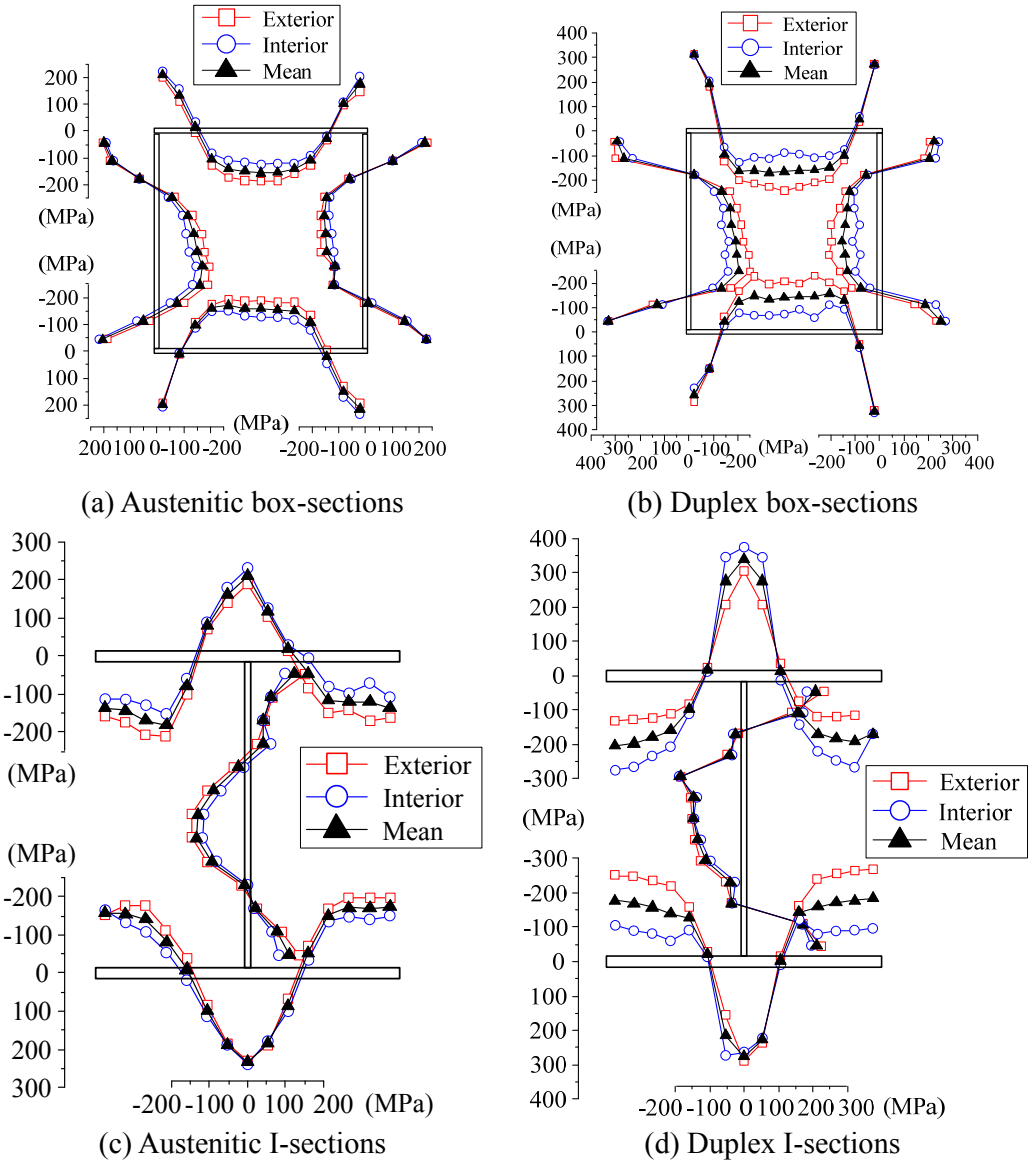

Figure 2. Residual Stress Distribution in [9]

Table 3. FE Results with (Fy) and without (Fw) Residual Stress (Box-section)

Austenitic stainless steel				Duplex stainless steel			
$\bar{\lambda}$	F_y (kN)	F_w (kN)	F_w/F_y	$\bar{\lambda}$	F_y (kN)	F_w (kN)	F_w/F_y
0.49	771	759	0.98	0.74	1564	1561	1.00
0.74	627	618	0.98	0.94	1362	1362	1.00
0.99	491	494	1.01	1.15	1132	1139	1.01
1.24	378	390	1.03	1.35	907	922	1.02
1.48	289	307	1.06	1.55	722	738	1.02
1.73	225	242	1.07	1.75	575	594	1.03
1.98	177	193	1.09	1.96	466	484	1.04
2.22	143	157	1.10	2.14	382	399	1.04
2.47	117	130	1.11	2.36	318	333	1.05

Table 4. FE Results with (Fy) and without (Fw) Residual Stress (I-section)

	Austenitic stainless steel				Duplex stainless steel			
	$\bar{\lambda}$	F_w (kN)	F_y (kN)	F_w/F_y	$\bar{\lambda}$	F_w (kN)	F_y (kN)	F_w/F_y
Major axis	0.39	1045	1044	1.00	0.50	0	2280	0.00
	0.59	899	905	0.99	0.71	1779	1763	1.01
	0.79	760	764	0.99	0.92	1482	1471	1.01
	0.99	642	640	1.00	1.13	1193	1181	1.01
	1.18	537	523	1.03	1.34	946	938	1.01
	1.38	445	429	1.04	1.56	758	746	1.01
	1.58	367	352	1.04	1.77	612	601	1.02
	1.77	305	292	1.04	1.98	500	491	1.02
	1.97	256	243	1.05	2.19	414	408	1.01
	2.17	217	203	1.07	2.40	348	343	1.01
Minor axis	0.53	962	923	1.04	0.66	1843	1795	1.03
	0.73	820	759	1.08	0.84	1582	1539	1.03
	0.92	679	611	1.11	1.01	1328	1292	1.03
	1.12	559	487	1.15	1.19	1093	1064	1.03
	1.32	460	393	1.17	1.37	897	874	1.02
	1.52	379	323	1.17	1.54	740	722	1.02
	1.72	314	269	1.16	1.72	617	605	1.02
	1.91	262	228	1.15	1.90	520	511	1.02
	2.11	221	194	1.14	2.07	443	436	1.02
	2.31	189	168	1.12	2.25	381	376	1.01

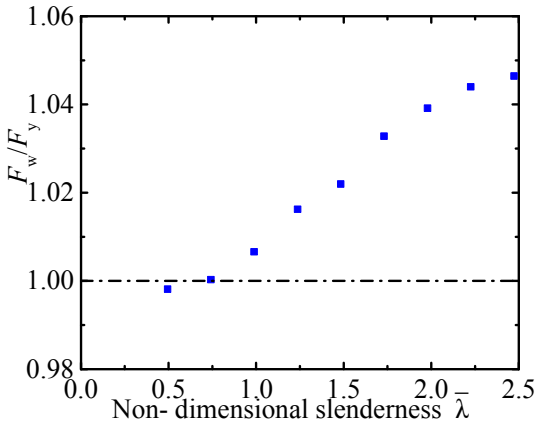

(a) Austenitic box-section

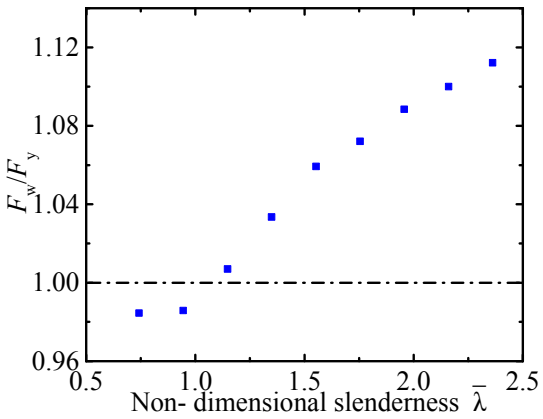

(b) Duplex box-section

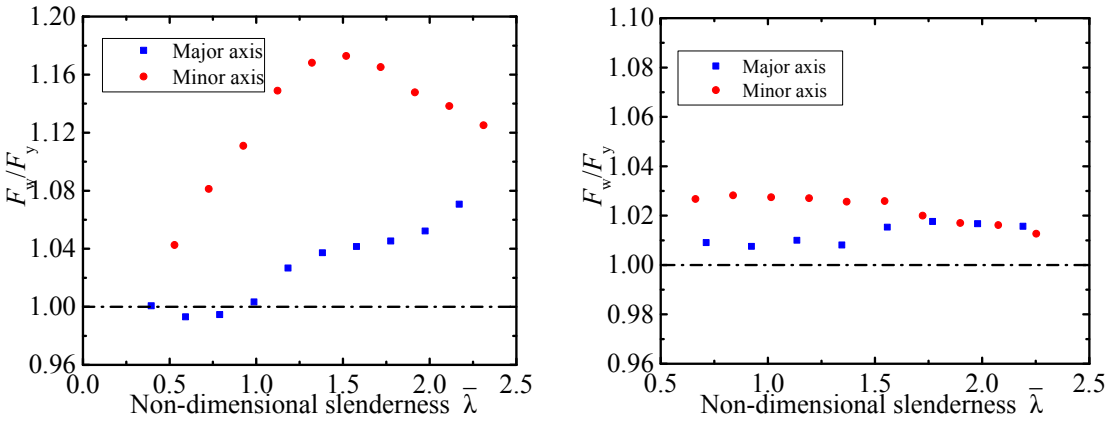

(c) Austenitic I-section (d) Duplex I-section

Figure 3. The Influence of Residual Stress

2.5 Material Properties

Material curves of 6 mm and 10 mm stainless steel plates are used for numerical analysis to assess the influence of material properties. The two based material curves are shown in Figure 4. The parametric results are shown in Table 5-6 and Figure 5. In Figure 5, the horizontal axis is the non-dimensional slenderness ratio, the vertical axis is the ratio of ultimate load of two different materials F_1 (for 6 mm), F_2 (for 10 mm). It can be observed that:

- The influence of material properties on the loading capacity is related to column slenderness, i.e. columns with smaller slenderness are more sensitive to material properties;
- Columns buckling about minor axis are more sensitive to material properties;
- The influence of material properties on duplex stainless steel columns is more obvious than that of austenitic stainless steel.

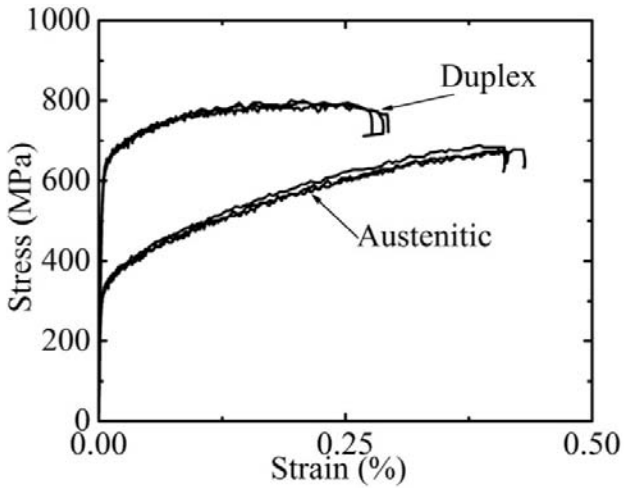

(a) 6 mm plates

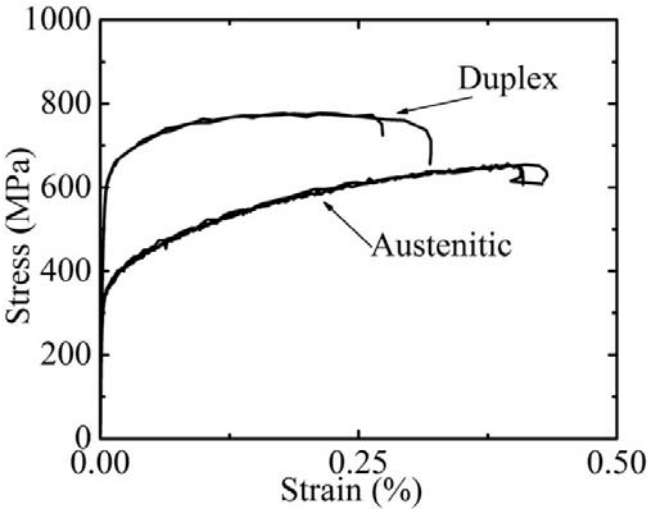

(b) 10 mm plates

Figure 4. Material Curves of 6 mm and 10 mm Plates

Table 5. FE Results with Different Material Properties – F_1 for 6 mm and F_2 for 10 mm (Box-section)

Austenitic stainless steel				Duplex stainless steel			
$\bar{\lambda}$	F_1 (kN)	F_2 (kN)	F_2/F_1	$\bar{\lambda}$	F_1 (kN)	F_2 (kN)	F_2/F_1
0.49	775	813	1.05	0.54	1564	1500	1.04
0.74	638	675	1.06	0.74	1362	1298	1.05
0.99	502	528	1.05	0.94	1132	1079	1.05
1.24	387	401	1.03	1.15	907	878	1.03
1.48	295	303	1.02	1.35	722	701	1.03
1.73	229	232	1.01	1.55	575	565	1.02
1.98	180	182	1.01	1.75	466	458	1.02
2.22	145	146	1.01	1.96	382	378	1.01
2.47	119	120	1.01	2.16	318	315	1.01
2.72	99	100	1.01	2.36	269	266	1.01

Table 6. FE Results with Different Material Properties – F1 for 6 mm and F2 for 10 mm (I-section)

Buckling axis	Austenitic stainless steel				Duplex stainless steel			
	$\bar{\lambda}$	F_1 (kN)	F_2 (kN)	F_1/F_2	$\bar{\lambda}$	F_1 (kN)	F_2 (kN)	F_1/F_2
Major axis	0.39	1044	1088	1.04	0.39	2257	2059	1.10
	0.49	976	1022	1.05	0.66	1835	1735	1.06
	0.59	905	954	1.05	0.92	1471	1372	1.07
	0.69	832	885	1.06	1.18	1115	1037	1.07
	0.79	764	815	1.07	1.45	833	786	1.06
	0.89	701	744	1.06	1.71	631	601	1.05
	0.99	640	676	1.06	1.97	491	468	1.05
	1.18	523	548	1.05	2.24	388	374	1.04
	1.30	474	494	1.04	2.50	316	304	1.04

	1.43	429	444	1.03	2.76	259	252	1.03
Minor axis	0.85	682	700	1.03	0.57	1926	1747	1.10
	1.22	467	486	1.04	0.84	1539	1322	1.16
	1.65	332	346	1.04	1.11	1173	988	1.19
	1.88	285	296	1.04	1.37	874	749	1.17
	2.12	247	256	1.03	1.64	661	579	1.14
	2.37	214	223	1.04	1.90	511	458	1.11
	2.62	188	195	1.04	2.17	405	368	1.10
	2.89	168	172	1.03	2.57	296	275	1.08

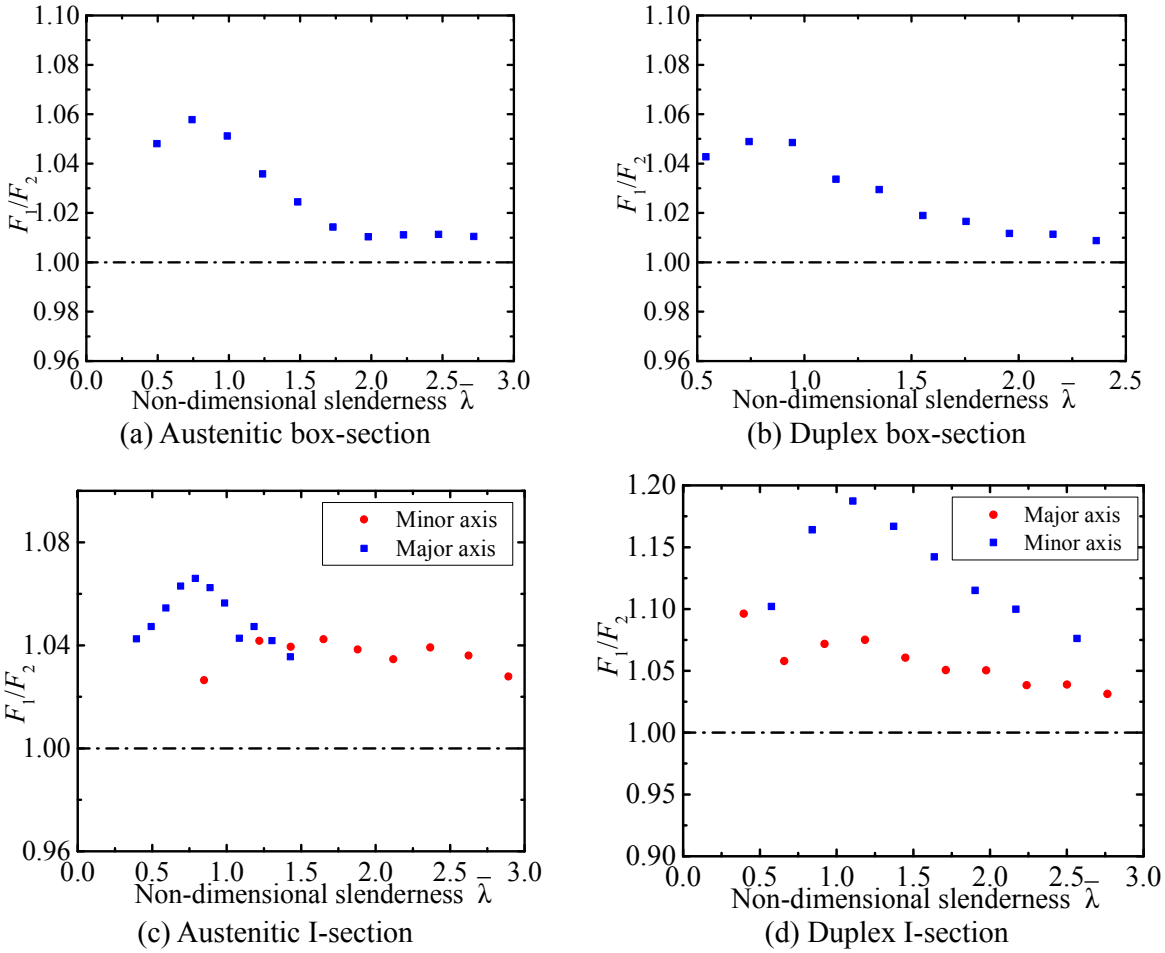

(a) Austenitic box-section (b) Duplex box-section

(c) Austenitic I-section (d) Duplex I-section

Figure 5. The Influence of Material Properties

2.6 Local width-to-thickness Ratio

The width-to-thickness ratios ranged from 9 to 40 were adopted for the parametric analysis and the results are shown in Table 7-8. The ultimate load was obtained by numerical analysis, based on which the stability coefficient was calculated. Afterwards the calculated coefficients based on simulation and EN 1993-1-4 are compared and graphically shown in Figure 6, where the stability coefficient φ is defined as the ratio of simulated force to normal force (Af_y). It can be seen from the diagrams that the width-to-thickness ratio barely affects the stability coefficient for both box and I-section members.

Table 7. FE Results with Different Width-to-thickness Ratio (Box-section)

Austenitic stainless steel			Duplex stainless steel		
B/t	F (kN)	φ	B/t	F (kN)	φ
10	168	0.46	10	220	0.31
13	230	0.46	13	302	0.31
17	292	0.46	17	384	0.31
20	355	0.46	20	465	0.31
23	417	0.46	23	547	0.31
27	479	0.46	27	629	0.31
30	542	0.46	30	710	0.31
33	604	0.46	33	792	0.31
37	666	0.46	37	874	0.31
40	728	0.46	40	955	0.31

Table 8. FE Results with Different Width-to-thickness Ratio (I-section)

Buckling form	Section position	Austenitic stainless			Duplex stainless		
		B/t	F(kN)	φ	B/t	F(kN)	φ
Major axis	Web	15	697	0.79	15	1198	0.70
		20	736	0.80	20	1265	0.70
		25	775	0.80	25	1330	0.70
Major axis	Flange	15	775	0.80	15	1330	0.70
		18	896	0.80	18	1540	0.70
		21	1017	0.80	21	1749	0.70
Minor axis	Web	15	372	0.42	15	559	0.32
		20	391	0.42	20	587	0.32
		25	411	0.42	25	615	0.32
		30	430	0.42	30	642	0.32
		35	450	0.42	35	670	0.32
Minor axis	Flange	9	280	0.42	9	416	0.32
		12	345	0.42	12	516	0.32
		15	411	0.42	15	615	0.32
		18	476	0.42	18	714	0.32
		21	542	0.42	21	812	0.32

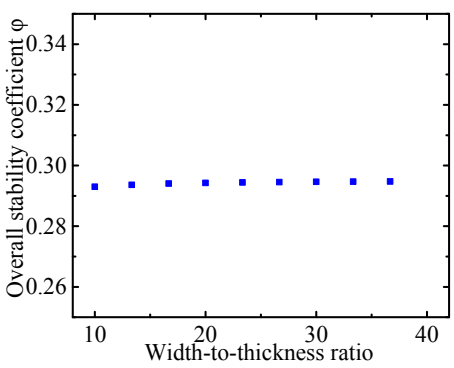

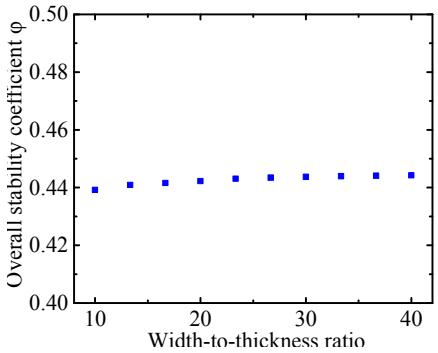

(a) Austenitic box-section (b) Duplex box-section

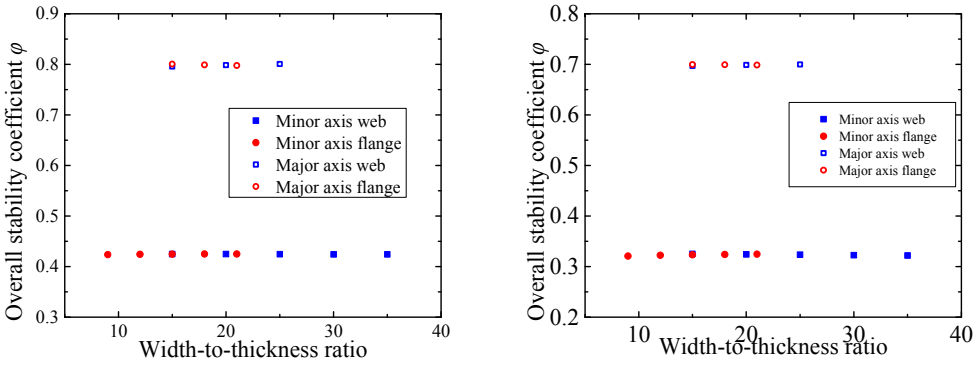

(c) Austenitic I-section (d) Duplex I-section

Figure 6. The Influence of width-to-thickness ratio

2.7 Global Slenderness Ratio

Columns with a wide range of global non-dimensional slenderness ratio have been analyzed using ANSYS and the results are summarized in Table 9-10. The stability coefficients of varying slenderness are depicted in Figure 7. It is obviously illustrated that the coefficient decreases with the increase of non-dimensional slenderness ratio.

Table 9. FE Results with Different Global Non-dimensional Slenderness (Box-section)

Austenitic stainless steel			Duplex stainless steel		
$\bar{\lambda}$	F(kN)	φ	$\bar{\lambda}$	F(kN)	φ
0.37	829	0.99	0.54	1564	0.95
0.49	775	0.92	0.64	1467	0.89
0.62	707	0.84	0.74	1362	0.83
0.74	638	0.76	0.84	1249	0.76
0.86	571	0.68	0.94	1132	0.69
0.99	502	0.60	1.05	1017	0.62
1.11	441	0.53	1.15	907	0.55
1.24	387	0.46	1.25	808	0.49
1.36	338	0.40	1.35	722	0.44
1.48	295	0.35	1.45	645	0.39
1.61	259	0.31	1.55	575	0.35
1.73	229	0.27	1.65	518	0.31
1.85	202	0.24	1.75	466	0.28
1.98	180	0.21	1.85	421	0.25
2.10	161	0.19	1.96	382	0.23
2.22	146	0.17	2.06	348	0.21
2.35	131	0.16	2.16	318	0.19
2.47	119	0.14	2.26	292	0.18
2.59	108	0.13	2.36	269	0.16

Table 10. FE Results with Different Global Non-dimensional Slenderness (I-section)

Buckling form	Austenitic stainless steel			Duplex stainless steel			Buckling form	Austenitic stainless steel			Duplex stainless steel		
	$\bar{\lambda}$	F (kN)	φ	$\bar{\lambda}$	F (kN)	φ		$\bar{\lambda}$	F (kN)	φ	$\bar{\lambda}$	F (kN)	φ
Major axis	0.28	1102	1.03	0.40	2257	1.01	Minor axis	0.40	1013	1.05	0.57	1013	0.95
	0.37	1044	0.98	0.51	1896	1.02		0.49	923	0.86	0.66	923	0.86
	0.46	976	0.92	0.61	1763	0.85		0.59	839	0.78	0.75	839	0.78
	0.55	905	0.85	0.72	1620	0.79		0.68	759	0.71	0.84	759	0.71
	0.65	832	0.78	0.83	1471	0.73		0.77	682	0.64	0.93	682	0.64
	0.74	764	0.71	0.93	1324	0.66		0.87	611	0.57	1.01	611	0.57
	0.83	701	0.65	1.04	1181	0.59		0.96	544	0.51	1.10	544	0.51
	0.92	640	0.59	1.15	1054	0.53		1.05	488	0.45	1.19	487	0.45
	1.01	580	0.54	1.25	938	0.47		1.14	437	0.41	1.28	437	0.41
	1.11	523	0.49	1.36	833	0.42		1.24	393	0.37	1.37	393	0.37
	1.20	474	0.44	1.47	746	0.37		1.33	356	0.33	1.46	356	0.33
	1.29	429	0.40	1.58	668	0.33		1.42	323	0.30	1.54	323	0.30
	1.38	388	0.36	1.68	601	0.30		1.52	295	0.28	1.63	295	0.28
	1.48	352	0.33	1.79	542	0.27		1.61	269	0.25	1.72	269	0.25
	1.57	320	0.30	1.90	491	0.24		1.70	247	0.23	1.81	247	0.23
	1.66	292	0.27	2.00	446	0.22		1.79	228	0.21	1.90	228	0.21
	1.75	266	0.25	2.11	408	0.20		1.89	210	0.20	1.99	210	0.20
	1.84	243	0.23	2.22	373	0.18		1.98	194	0.18	2.07	194	0.18
	1.94	223	0.21	2.32	343	0.17		2.07	180	0.17	2.16	180	0.17
	2.12	189	0.18	2.43	314	0.15		2.17	168	0.16	2.25	168	0.16

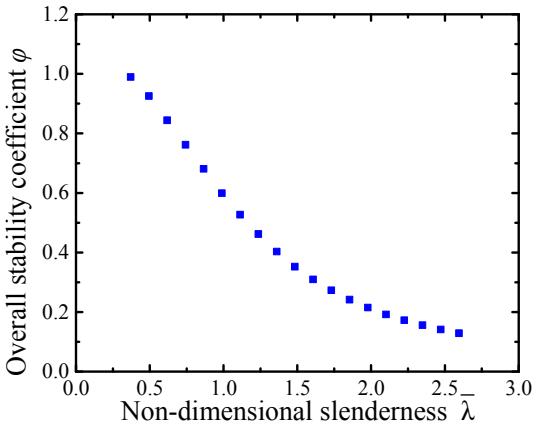

(a) Austenitic box-section

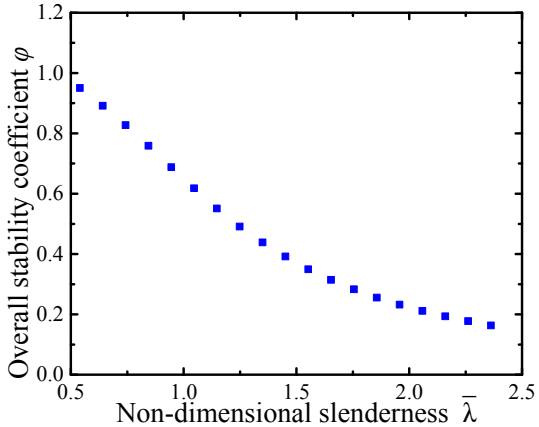

(b) Duplex box-section

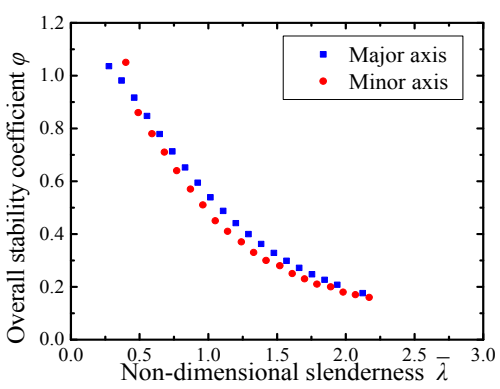

(c) Austenitic I-section

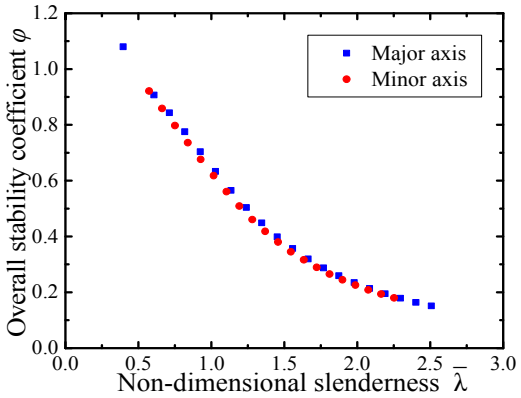

(d) Duplex I-section

Figure 7. The Influence of Non-dimensional Slenderness Ratio

2.8 Discussion

It can be concluded that the global non-dimensional slenderness ratio is the most sensitive parameter for the loading capacity of welded stainless steel columns while the effect of the local width-to-thickness ratio can be neglected. The influence of residual stress, initial geometric imperfections and material characteristics is moderate. The results from the parametric analysis identify an appropriate global imperfection level and the necessity of taking residual stress into consideration. These vital parameters would be considered in the new method for flexural design of stainless steel column in the following sections.

3. DESIGN PROPOSAL OF STAINLESS STEEL WELDED-SECTION COLUMNS

3.1 Data from Parametric Analysis

This section focuses on the investigation on the influence of slenderness on loading capacity of stainless steel columns.

Austenitic and duplex stainless steel columns with 6 mm and 10 mm plates are studied. Material properties of the samples are shown in Table 11. Geometric dimensions of stainless steel box-section samples and I-section samples are shown in Table 12 and Table 13 respectively.

Table 11. Material Properties along the Rolling Direction

Grade	t (mm)	E_0 (MPa)	f_y (MPa)	f_u (MPa)	Elongation at fracture (%)	n
Austenitic	6.00	182300	282	696	58.1	6.5
	10.00	198700	321	660		6.0
Duplex	6.00	191900	553	798	35.0	7.0
	10.20	190400	547	775		6.4

Table 12. Geometric Dimensions of Stainless Steel Box-section Samples

Designation	B	t	B/t	A
B1	130	6	21.7	2976
B2	180	10	18	6800
B3	200	12	16.7	9024
B4	240	16	15	14336
B5	270	12	22.5	12348
B6	360	16	24.6	22016

Table 13. Geometric Dimensions of Stainless Steel I-section Samples

Designation	H	B	t_w	t_f	H/t_w	B/t_f	A
H1	150	150	6	10	21.7	15	3780
H2	180	150	8	10	20	15	4280
H3	200	180	10	12	17.6	15	6080
H4	200	200	8	12	22	17	6208
H5	180	160	12	14	12.7	11.4	6304
H6	200	200	14	18	11.7	11.1	9496
H7	180	220	16	18	9	12.2	10224

In total, 968 columns, including 153 austenitic stainless steel box-section columns, 148 duplex stainless steel box-section columns, 161 austenitic stainless steel I-section columns buckling about minor axis, 176 austenitic stainless steel I-section columns buckling about major axis, 161 duplex stainless steel I-section columns buckling about minor axis and 169 duplex stainless steel I-section columns buckling about major axis were analyzed.

Comparisons between sample data and specification column curves are in Figure 8. It can be observed that section types have no influence on column curves. Besides, when slenderness is greater, calculated curves and EN 1993-1-4 curves fit well while calculated curves and ASCE 8-02 curves fit well for medium-length columns.

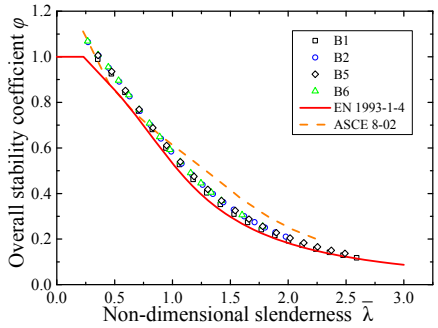

(a) Austenitic box-section

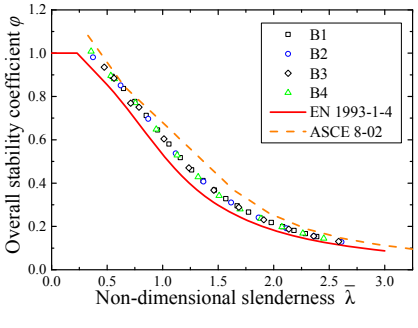

(b) Duplex box-section

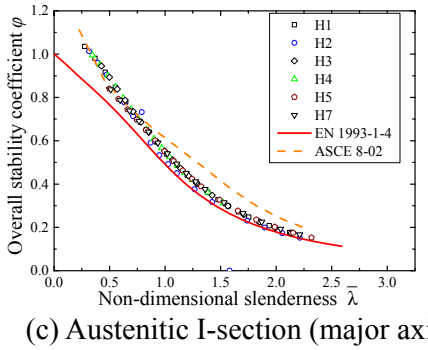

(c) Austenitic I-section (major axis)

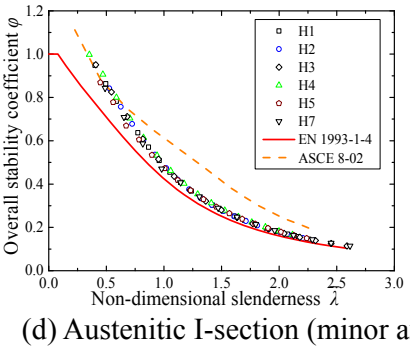

(d) Austenitic I-section (minor axis)

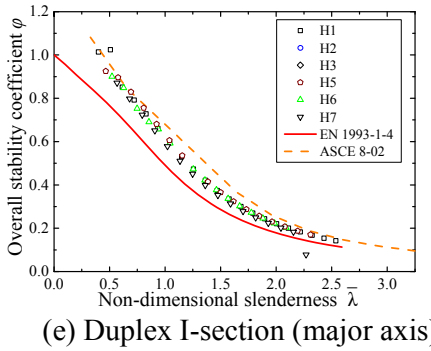

(e) Duplex I-section (major axis)

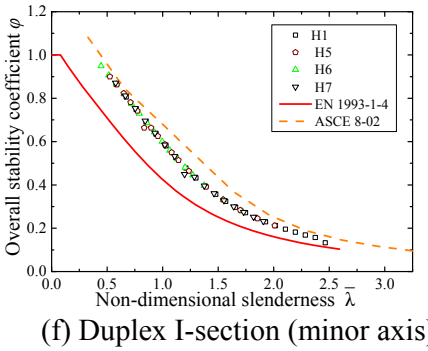

(f) Duplex I-section (minor axis)

Figure 8. Comparisons between Sample Data and Specification Column Curves

3.2 Proposed Three-segment Model

EN 1993-1-4 and ASCE 8-02 are commonly used for stainless steel structural design. Considering the limitations of the two design specifications, including conservatism and iteration, a three-segment column curve is proposed based on the test and numerical results. For the 1-segment of the curve, continuous strength method (DSM) proposed by Gardner [18] could be used to capture the beneficial effect of strain-hardening for stocky sections. For the 2-segment, the American cold-formed stainless steel specification could be used considering the nonlinear properties of materials and plastic buckling occurred for intermediate slenderness. For the 3-segment (final segment), Perry formula, based on the edge yield criterion, could be used for large slenderness and the occurred elastic buckling.

Overall stability coefficient formula of welded stainless steel columns can now be expressed as:

$$\varphi=\begin{cases} a_1+a_2*\lambda^2 & \lambda\le a \\ a_3*a_4{}^{\lambda^2} & a<\lambda\le b \\ \dfrac{1}{2\lambda^2}\left[(a_5+a_6\lambda+\lambda^2)-\sqrt{\left((a_5+a_6\lambda+\lambda^2\right)^2-4\lambda^2}\right] & b<\lambda \end{cases} \quad (1)$$

Schematic diagram of this formula is illustrated in Figure 9.

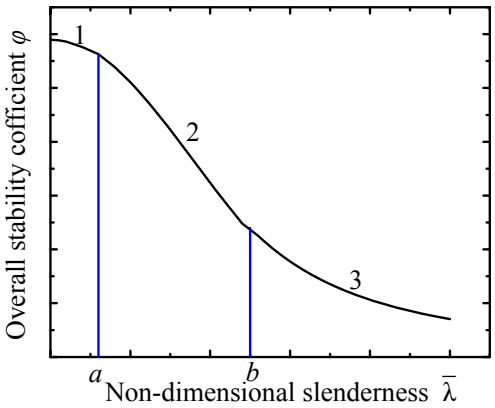

Figure 9. Proposed buckling curves

The first graphical critical point, *a*, can be determined by buckling stress σ obtained according to ASCE:

$$\sigma = \frac{\pi^2 E_t}{(KL/r)^2} = \frac{\pi^2}{(KL/r)^2} * \frac{E_0 f_y}{f_y + 0.002 n E_0 \left(\frac{\sigma}{f_y}\right)^{n-1}} \tag{2}$$

Section buckling stress is regarded as the critical stress.

The slenderness ratio when $\sigma = f_y$ is:

$$(KL/r)^2 = \frac{\pi^2 E_0}{f_y + 0.002 n E_0} \tag{3}$$

The first critical point was evaluated as 0.25 and 0.4 for austenite and duplex stainless steel respectively. The second critical limit, *b*, was determined by curve-fitting, for stainless steel. Values of the second critical limit *b* and the parameters of a_1-a_6 in Eq. 1 are summarized in Table 14.

Table 14. Second Critical Limit for Proposed 3-segement Design Curve

Material	Section	Value type	Second critical limit	a_1	a_2	a_3	a_4	a_5	a_6
Austenitic	Box-section	Fitted value	1.1	1.245	-2.936	1.058	0.5428	0.8845	0.4438
		Suggested value	1.1	1.2	-2.94	1.06	0.54	0.88	0.44
	I-section major axis	Fitted value	1.3	1.111	-0.9412	1.011	0.6044	0.8983	0.3405
		Suggested value	1.3	1.1	-0.94	1.01	0.6	0.9	0.34
	I-section minor axis	Fitted value	1	1.222	-2.932	1.033	0.5113	0.8494	0.5288
		Suggested value	1	1.2	-2.93	1.03	0.51	0.85	0.53
Duplex	Box-section	Fitted value	1.0	1.203	-1.85	1.052	0.432	0.836	0.7279
		Suggested	1.0	1.2	-1.85	1.05	0.43	0.84	0.73

I-section major axis	value							
	Fitted value	1.1	1.106	0.7688	1.062	0.5657	1.029	0.2247
	Suggested value	1.1	1.1	-0.77	1.06	0.57	1.03	0.23
I-section minor axis	Fitted value	1.2	1.088	-1.044	0.9964	0.5426	1.039	0.3772
	Suggested value	1.2	1.1	-1.04	1	0.54	1.04	0.38

3.3 Reliability Analysis

Each parameter of the proposed equation has been fitted using MATLAB. In order to verify the accuracy of the design method, the ratio of FE stability coefficient φ_1 to calculated stability coefficient φ_2 is illustrated in Figure 10. In Figure 9, φ_1/φ_2 fluctuates between 0.95 and 1.05, which shows the reliability of the design proposal.

The proposed design curve and the design curves from EN1993-1-4 and ASCE8-02 are compared in Figure 11. It can be observed that the proposed column curve is in-between the EN 1993-1-4 and the ASCE 8-02 curves. It also indicates that the discrepancies between the calculated overall stability coefficient and the EN 1993-1-4 curve for austenitic stainless steel member are smaller than that of duplex stainless steel. It indicates that different material grades significantly impact the overall stability loading capacity and therefore separated design curves are needed. Also the discrepancies of the major-axis buckling are less than that of the minor-axis buckling in terms of I-section members and thus separated design curves are needed. It can also be seen that the EN 1993-1-4 produced an evidently conservative design for welded stainless steel columns. The design loading capacity to test and simulated data ratio are approximately 1 for both box-section and I-section members, verifying the rationality of the proposed formula. The mean value, COV and reliability index of tests and FEA to the design predictions ratio are shown in Tables 15-17. The mean value of the experimental and numerical axial strengths over the modified design strengths is nearer to 1.0, while the COV of which is much lower. And the reliability index of the proposed method is generally higher than other provisions. In general, the test and numerical results on welded stainless steel columns can be accurately predicted by the proposed column curves. It should also be noted that the modified design proposal does not require iterative process in calculating the column strength as shown in ASCE's provisions.

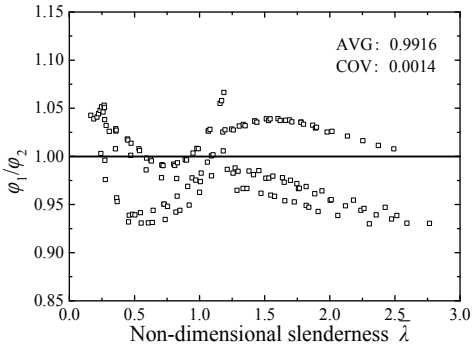

(a) Austenitic box-section

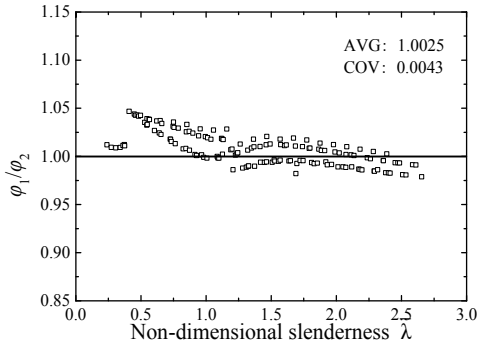

(b) Duplex box-section

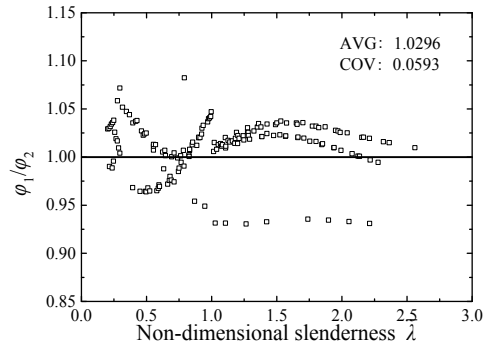

(c) Austenitic I-section (major axis)

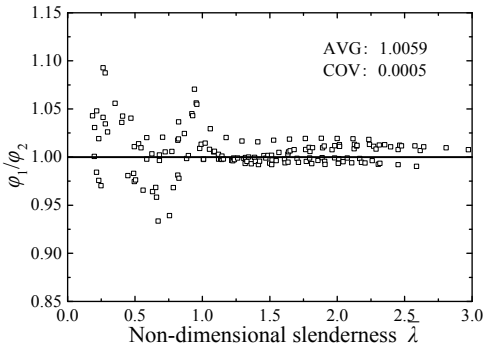

(d) Austenitic I-section (minor axis)

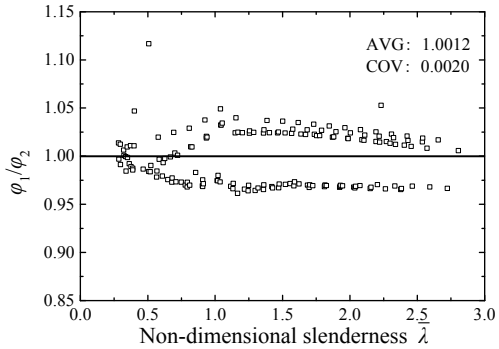

(e) Duplex I-section (major axis)

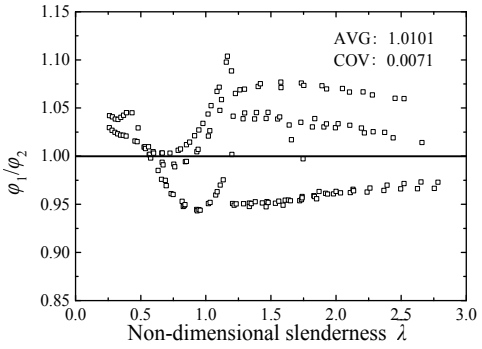

(f) Duplex I-section (minor axis)

Figure 10. Comparison of FE and Calculated Stability Coefficient

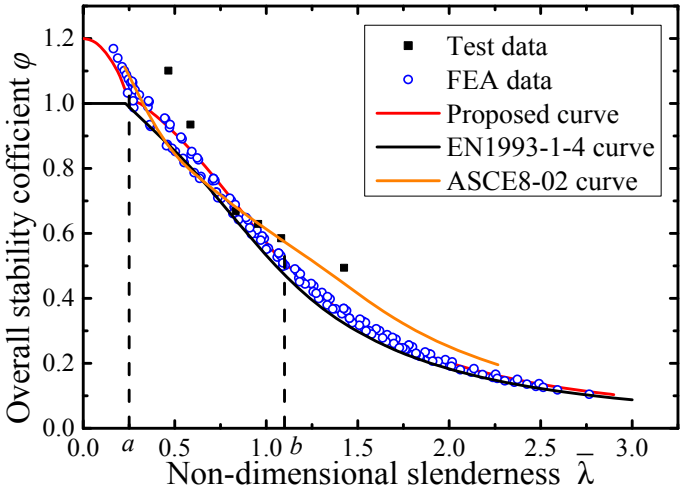

(a) Austenitic box-section

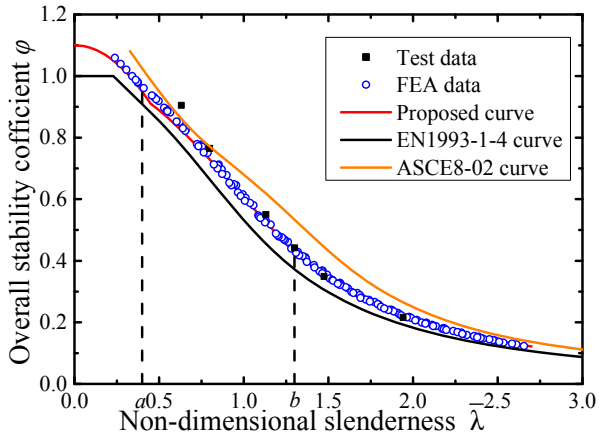

(b) Duplex box-section

Table 15. Comparison of Test and FEA Results with Design Predictions (Box-section)

Parameters	Austenitic stainless steel			Duplex stainless steel		
	Current design rules		Modified design rules	Current design rules		Modified design rules
	$\frac{P_{exp} \text{ and } P_{FE}}{P_{EC3}}$	$\frac{P_{exp} \text{ and } P_{FE}}{P_{ASCE}}$	$\frac{P_{exp} \text{ and } P_{FE}}{P_{MO}}$	$\frac{P_{exp} \text{ and } P_{FE}}{P_{EC3}}$	$\frac{P_{exp} \text{ and } P_{FE}}{P_{ASCE}}$	$\frac{P_{exp} \text{ and } P_{FE}}{P_{MO}}$
Number of data	159	12	159	152	12	152
AVG	0.9911	1.3574	0.9962	0.9816	1.3402	1.0012
COV	0.0039	0.0402	0.0026	0.0045	0.0414	0.0025
Reliability index	15.89	6.48	19.30	7.87	6.31	20.53

Table 16. Comparison of Test and FEA Results with Design Predictions (I-section buckling around major axis)

Parameters	Austenitic stainless steel			Duplex stainless steel		
	Current design rules		Modified design rules	Current design rules		Modified design rules
	$\frac{P_{exp} \text{ and } P_{FE}}{P_{EC3}}$	$\frac{P_{exp} \text{ and } P_{FE}}{P_{ASCE}}$	$\frac{P_{exp} \text{ and } P_{FE}}{P_{MO}}$	$\frac{P_{exp} \text{ and } P_{FE}}{P_{EC3}}$	$\frac{P_{exp} \text{ and } P_{FE}}{P_{ASCE}}$	$\frac{P_{exp} \text{ and } P_{FE}}{P_{MO}}$
Number of data	167	22	167	172	21	172
AVG	1.1051	1.2815	0.9987	1.0520	1.0933	0.9998
COV	0.1057	0.0864	0.2189	0.0032	0.0028	0.0009
Reliability index	3.24	12.28	12.06	18.57	19.45	33.38

Table 17. Comparison of Test and FEA Results with Design Predictions
(I-section buckling around minor axis)

Parameters	Austenitic stainless steel			Duplex stainless steel		
	Current design rules		Modified design rules	Current design rules		Modified design rules
	P_{exp} and P_{FE} / P_{EC3}	P_{exp} and P_{FE} / P_{ASCE}	P_{exp} and P_{FE} / P_{MO}	P_{exp} and P_{FE} / P_{EC3}	P_{exp} and P_{FE} / P_{ASCE}	P_{exp} and P_{FE} / P_{MO}
Number of data	167	22	167	172	21	172
AVG	1.0527	1.1841	0.9905	1.2227	1.0896	1.0824
COV	0.0046	0.0312	0.0019	0.0037	0.0115	0.0022
Reliability index	14.59	6.42	12.85	20.02	9.73	23.00

4. CONCLUSIONS

This paper has presented an extensive parametric investigation with an aim to proposing a new design method for flexural design of fabricated austenitic and duplex stainless steel columns. Complementary experimental programme were conducted and the corresponding finite element modelling methodologies were validated in early investigations [20, 21]. The key parameters, including initial global geometric imperfections, residual stress, local width-to-thickness ratio, material properties and non-dimensional slenderness ratio were assessed. A total of 301 welded box-section and 667 welded I-section columns were simulated, which were used to evaluate the current design provisions and the calculation method proposed in this paper. The design curves provided in EN 1993-1-4 were confirmed to give conservative predictions while ASCE 8-02 give slightly overestimated predictions.

Based on the complementary tests and simulated results, a three-segment design curve was proposed for the flexural design of fabricated austenitic and duplex stainless steel columns and demonstrated reliable predictions.

ACKNOWLEDGEMENT

This study is supported by the National Natural Science Foundation of China (Grant NO. 51478019) and Beijing NOVA programme 2016.

REFERENCES

[1] Baddoo, N. R., “Stainless Steel in Construction: A Review of Research, Applications, Challenges and Opportunities”, Journal of Constructional Steel Research, 2008, Vol. 64, No. 11, pp. 1199-1206.

[2] EN 1993-1-4, Eurocode 3: “Design of Steel Structures Part 1-4: General Rules-Supplementary Rules for Stainless Steels”, Brussels: European Committee for Standardization, 2006.

[3] SEI/ASCE 8-02, “Specification for the Design of Cold-Formed Stainless Steel Structural Members, Virginia: American Society of Civil Engineers”, 2002.

[4] CECS 410:2015, “Technical Code of Stainless Steel Structures”, Nanjing: Ministry of Industry and Information Technology of the People's Republic of China, 2015.

[5] Mirambell, E. and Real, E., "On the Calculation of Deflections in Structural Stainless Steel Beams: An Experimental and Numerical Investigation", Journal of Constructional Steel Research, 2000, Vol. 54, No. 1, pp. 109-133.

[6] Quach, W. M., Teng, J. G. and Chung, K. F., "Three-stage Full-range Stress-strain Model for Stainless Steels", Journal of Structural Engineering, 2008, Vol. 134, No. 9, pp. 1518-1527.

[7] Gardner, L. and Cruise, R. B., "Modeling of Residual Stresses in Structural Stainless Steel Sections", Journal of Structural Engineering, 2009, Vol. 135, No. 1, pp. 42-53.

[8] Quach, W. M., Teng, J. G. and Chung, K. F., "Residual Stresses in Press-braked Stainless Steel Sections, I: Coiling and Uncoiling of Sheets", Journal of Constructional Steel Research, 2009, Vol. 65, No. 8, pp. 1803-1815.

[9] Yuan, H. X., Wang, Y. Q., Shi, Y. J. and Gardner, L., "Residual Stress Distributions in Welded Stainless Steel Sections", Thin-Walled Structures, 2014, Vol. 79, pp. 38-51.

[10] Wang, Y. Q., Yang, L., Gao, B., Shi, Y. J. and Yuan, H. X., "Experimental Study of Lateral-torsional Buckling Behaviour of Stainless Steel Welded I-section Beams", International Journal of Steel Structures, 2014, Vol. 14, No. 2, pp. 411-420.

[11] Yang, L., Wang, Y. Q., Gao, B., Shi, Y. J. and Yuan, H. X., "Two Calculation Methods for Buckling Reduction Factors of Stainless Steel Welded I-section Beams", Thin-Walled Structures, 2014, Vol. 83, pp. 128-136.

[12] Yuan, H. X., Wang, Y. Q., Gardner, L. and Shi, Y. J., "Local–overall Interactive Buckling of Welded Stainless Steel Box Section Compression Members", Engineering Structures, 2014, Vol. 67, No. 4, pp. 62-76.

[13] Shu, G., Zheng, B. and Xin, L., "A New Design Method for Stainless Steel Columns Subjected to Flexural Buckling", Thin-Walled Structures, 2014, Vol. 83, pp. 43–51.

[14] Shu, G., Zheng, B. and Shen, X., "Experimental and Theoretical Study on the Behaviour of Cold-formed Stainless Steel Stub Columns", International Journal of Steel Structures, 2013, Vol. 13, No. 1, pp. 141-153.

[15] Huang, Y. and Young, B., "Design of Cold-formed Lean Duplex Stainless Steel Members in Combined Compression and Bending", Journal of Structural Engineering, 2014, Vol. 141, No. 5, pp. 04014138.

[16] Gardner, L. and Nethercot, D. A., "Experiments on Stainless Steel Hollow Sections—Part 1: Material and Cross-sectional Behaviour", Journal of Constructional Steel Research, 2004, Vol. 60, No. 9, pp. 1291-1318.

[17] Gardner, L. and Nethercot, D. A., "Experiments on Stainless Steel Hollow Sections—Part 2: Member Behaviour of Columns and Beams", Journal of Constructional Steel Research, 2004, Vol. 60, No. 9, pp. 1319–1332.

[18] Gardner, L., "The Continuous Strength Method", Proceedings of the Institution of Civil Engineers-structures and Buildings, 2008, Vol. 161, No. 3, pp. 127-133.

[19] AS/NZS 4673: "Cold- formed Stainless Steel Structures", Sydney: Joint Technical Committee, 2001.

[20] Yang, L., Zhao, M. H., Xu, D., Shang, F., Yuan, H. X., Wang, Y. Q. and Zhang, Y., "Flexural Buckling Behaviour of Welded Stainless Steel Box-section Columns", Thin-Walled Structures, 2016, Vol. 104, pp. 185-197.

[21] Yang, L., Zhao, M. H., Chan, T. M., Shang, F. and Xu, D. C., "Flexural Buckling of Welded Austenitic and Duplex Stainless Steel I-section Columns", Journal of Constructional Steel Research, 2016, Vol. 122, pp. 339-353.

NOTATION

The following symbols are used in this paper:

A= the section area;
B = the width of the member section;
E_0= the initial elasticity modulus;
F_y= bearing capacity;
F_w= bearing capacity with residual stress considered;
$F_{0.001}$= the ultimate load of the members with 0.001L geometric imperfection;
$F_{0.002}$= the ultimate load of the members with 0.002L geometric imperfection;
$F_{0.0005}$= the ultimate load of the members with 0.005L geometric imperfection;
f_y = the 0.2% proof stress;
H = the height of the member section;
P_{EC3} = the ultimate buckling load calculated according to EN1993-1-4;
P_{ASCE} = the ultimate buckling load calculated according to ASCE-8-02;
P_{exp} = the tested ultimate buckling load;
P_{FE}= the simulated ultimate load with the residual stress considered;
n = the strain-hardening exponent;
t = the thickness of the member section;
t_f = the thickness of the flange;
t_w = the thickness of the web;
δ_0 = the initial geometric imperfection;
$\bar{\lambda}$ = the non-dimensional slenderness ratio;
σ = buckling stress;
φ = overall stability coefficient.

PRE-TENSIONED STEEL CABLES EXPOSED TO LOCALISED FIRES

Yong Du[1,2,3], J.Y. Richard Liew[1,3], Hao Zhang[1] and Guoqiang-Li[2]

[1]*Nanjing Tech University, College of Civil Engineering, Jiangsu, 211800, China*
[2]*Civil Engineering Disaster Prevention National Key Laboratory, Shanghai, 200092, China*
[3]*National University of Singapore, Department of Civil & Environmental Engineering, 117576, Singapore*
**(Corresponding author: E-mail: yongdu_mail@njtech.edu.cn)*

Received: 30 November 2016; Revised: 23 May 2017; Accepted: 13 June 2017

ABSTRACT: Pre-tensioned steel cables are often used in hybrid string structures, suspended roofs and cable suspended bridges. When subjected to localised fire, the tensile force in the steel cables reduces due to thermal expansion, and thus, the geometry of the structure and the internal force distribution in the cable-tensioned structure will be affected. The mechanical behavior of pre-tensioned steel cables is sensitive to the elevated temperature history. In this paper, a set of analytical formulation has been proposed to determine the transient tension force in a cable subjected to localised heating considering the mechanical properties at elevated temperature and the effects of loading configuration, pre-tensioned force level, and thermal expansion at elevated temperature. The fire resistance of a pre-tensioned steel cable can be determined when the cable tension force is equal to its effective yield strength at elevated temperature. Meanwhile, the proposed method is able to capture the relationship between the transient tension forces with each influence parameter in order to study the behavior of steel cables subjected to localised fire. The mechanical responses predicted by the proposed analytical method of pre-tensioned cables exposed to localised fires are validated against the numerical results obtained from nonlinear finite element software. Finally, a design flow chart is proposed for fire resistant design of pre-tensioned steel cables and the calculations can be implemented using a spreadsheet program.

Keywords: Cable-tensioned structure, fire resistance, localised fire, pre-tensioned structure, steel cable

DOI: 10.18057/IJASC.2018.14.2.5

1. INTRODUCTION

Pre-tensioned structures, such as beam string structures and suspension domes, are applicable for large space buildings or long span bridges. Typical pre-tensioned members are steel cables, steel rods or chains and they are generally named as ‘string’ in hybrid string structures. The steel cable is the most commonly used as a pre-tensioned member in hybrid string structures because of its high strength and the ease of applying tension force [1]. Fire induced high temperature can cause damage to pre-tensioned structures. For example, an aircraft warehouse with pre-tensioned truss in Brussels International airport collapsed in fire, shown in Figure 1, just as the roof of Ji’nan Olympic Stadium in China with cable suspension dome damaged in fire, as shown in Figure 2.

There is an abundance of research on behaviour of tensioned structures at ambient temperature [1]~[3]. As shown in Figure 3 and 4, a large number of cases has been located in China. Zhou [4] studied the fire resistance of cable suspended structures exposed to standard ISO fire, and determined that a cable suspended structure under ISO fire hold similar displacement as a pre-tensioned cable. Sheng [5] and Fan [6] studied the mechanical behaviours of beam string structures and suspension domes exposed to localised fire respectively. In the work by Wang et al. [7] and the manual for post-tensioned concrete[8], the Young’s Modulus and yield strength of steel wires at elevated temperature have been reported based on experimental investigation. It should be noted that analysis of fire resistance of tension structures is mainly done by numerical method, and there are limited data for pre-tensioned steel cable or tensioned structure tested at elevated

temperature. Although the final aim of the study is to determine the fire resistance capability of tension structures, the first step is to determine the mechanical response of pre-tensioned cables exposed to localised fire. The fire resistance of a pre-tensioned cable can be established by comparing the transient horizontal tension force in cables throughout the whole fire history with the effective yield strength of the cable. The analytical method proposed in this paper would be useful for analysing the structural response of cable suspended buildings, beam string structures or suspension bridges exposed to localized fires.

Figure 1. Collapse of the Aircraft Warehouse of Brussels International Airport after Fire

Figure 2. Ji'nan Olympic Stadium in China Damaged in Fire

Figure 3. Pudong International Airport in Shanghai, China

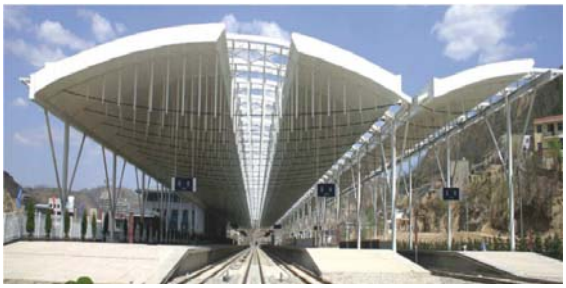

Figure 4. Train Station Platform, in Yan-an City, China

There is an abundance of research on behaviour of tensioned structures at ambient temperature [1]~[3]. As shown in Figure 3 and 4, a large number of cases has been located in China. Zhou [4] studied the fire resistance of cable suspended structures exposed to standard ISO fire, and determined that a cable suspended structure under ISO fire hold similar displacement as a pre-tensioned cable. Sheng [5] and Fan [6] studied the mechanical behaviours of beam string structures and suspension domes exposed to localised fire respectively. In the work by Wang et al. [7] and the manual for post-tensioned concrete [8], the Young's Modulus and yield strength of steel wires at elevated temperature have been reported based on experimental investigation. It should be noted that analysis of fire resistance of tension structures is mainly done by numerical method, and there are limited data for pre-tensioned steel cable or tensioned structure tested at elevated temperature. Although the final aim of the study is to determine the fire resistance capability of tension structures, the first step is to determine the mechanical response of pre-tensioned cables exposed to localised fire. The fire resistance of a pre-tensioned cable can be established by comparing the transient horizontal tension force in cables throughout the whole fire history with the effective yield strength of the cable. The analytical method proposed in this paper would be useful for analysing the structural response of cable suspended buildings, beam string structures or suspension bridges exposed to localized fires.

2. MODELLING OF PRE-TENSIONED CABLES IN FIRES

2.1 Modelling of Localised Fires

Figure 5 shows a steel cable, simply supported at both ends, is exposed to a localized fire. The temperature distribution in the cable is non-uniform in nature with hot smoke tends to accumulate at the ceiling level and the temperature distribution varies in accordance with the flame radiation which is related to the distance of the cable with respect to the fire source, as shown in Figure 5. From the vertical axis of plume centre, the temperature reduces symmetrically following the distance '*x*' from the fire source, as shown in Figure 6, which is generated from a CFD fire simulation[13].

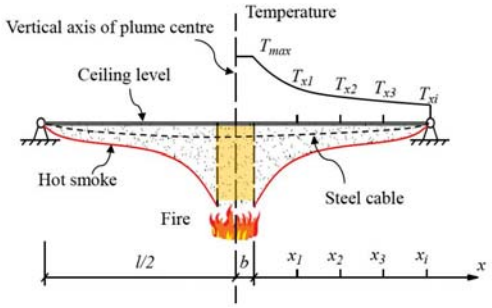

Figure 5. Effects of Hot Smoke and Flame on the Steel Cable

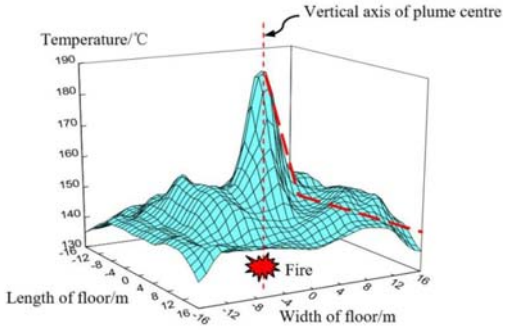

Figure 6. Typical Transient Temperature Distribution in Localized Fire

There are many models to predict the temperature distribution in localised fires, e.g. localised fires in EN 1991-1-2 [9], ASTM Standard E119-05 [10] and large space fires in NFPA 92B [11]. CECS200:2006[12] and Du et al.[13] describe the temperature distribution based on the field model given as:

$$T = T_{\max} f(x) = T_{\max}\left[\eta + (1-\eta)\exp\left(\frac{b-x}{7}\right)\right] \quad (1)$$

where b is the effective radius of fire source, taken as $b = \sqrt{A_q/\pi}$; A_q is the area of the fire source; $T_{\max}$ is the maximum temperature above the fire source, as shown in Figure 7; x is the distance from the vertical axis of plume centerline as shown in Figure 6; $f(x)$ is the regressing function of temperature shown in Figure 7 with a range of factor η which is the reduction factor of temperature depending on the floor area, Asp, and ceiling height, *H*, given in Table 1 [13].

There are three cases that the area of the fire source cannot be ignored. One is short spanning cable in which the size of the fire source "*b*" is relatively important as it affects the temperature distribution in the cable. The second is the area of the fire source becomes much larger from 9m^2 up to 50m^2. The third is the cable is far away from the fire source. If the area of the fire source cannot

be ignored, the length of the cable right above the fire source of size "*b*" will be subjected to the maximum temperature during the fire history. In most cases, the length of the cable is much longer than the size of the fire resource as the cables are usually employed by long span buildings.

Table 1. Reduction Factor η with Volumes of Large Space Buildings

A_{sp} (m^2)	H (m)				
	6	9	12	15	20
500	0.60	0.65	0.70	0.80	0.85
1000	0.50	0.55	0.60	0.70	0.75
3000	0.40	0.45	0.50	0.55	0.60
6000	0.25	0.30	0.40	0.45	0.50

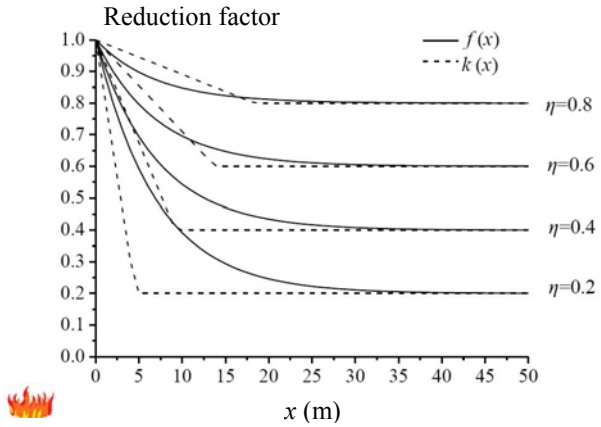

Figure 7. Regression Function Versus the Distance from the Vertical Axis of Plume Centerline with Varying η

Function $f(x)$ is a complex equation in which integration cannot be performed. *A* simplified bi-linear model $k(x)$ is proposed to replace $f(x)$ as follow:

$$k(x)=\begin{cases}\gamma x+1 & x<23\eta \\ \eta & x\geq 23\eta\end{cases} \tag{2}$$

in which $\gamma=(\eta-1)/23\eta$

The temperature reduction factor T/T_{max} predicted by Eq. 1 and Eq. 2 are plotted in Figure 5 with respect to the distance x from the fire source. It is worth noting that Eq. 1 can just predict the hot smoke temperature distribution under localised fire. As the flame radiation is taken into account the maximum temperature, T_{max}, will be improved significantly under lower η value [14]. Thus, the simplified model tends to predict more non-uniform temperature distribution with more sharply gradient of η value. But it provides an overall good fit for higher η value as the flame radiation influences on the maximum temperature slightly under less non-uniform temperature distribution.

2.2 Young's Modulus of Cable at Elevated Temperature

Wang et al. [7] experimentally proposed the value of the Young's Modulus of steel cables at elevated temperature and can be fitted by the following equation. Eq. 3 is compared with test data and a good fit is observed as shown in Figure 9.

$$E_T=\frac{E}{0.975+0.007\exp(T/90)} \qquad (20\text{□}\leq T\leq 60\text{□}) \tag{3}$$

where E_T is the Young's Modulus of steel cable at elevated temperature; E is the Young's Modulus of steel cable at ambient temperature (20°C), taken as 1.89×105N/mm^2.

2.3 Stress-strain Relationship of Steel Cable at Elevated Temperature

Wang et al. [7] conducted tests on high tensile steel wires to obtain the mechanical properties at elevated temperature. In this paper, the nonlinear stress strain curves from tests [7] may be approximated using a bi-linear model as shown in Figure 10. The Young's Modulus, E_T, is defined as the slope of linear elastic range. The cable proof stress $f_{y,0.02}^{T}$ is defined as the effective yield strength with proof strain of 0.02, in accordance with EC3 [9]. The yield strength of cables, f_y, is taken as 1690MPa at ambient temperature, and the reduction factor of yield strength for cables at elevated temperature, T, is obtained [7] as:

$$f_{y,0.02}^{T} / f_y = 1.013 - 1.3\times10^{-3}T + 6.179\times10^{-6}T^2 - 2.468\times10^{-8}T^3 + 2.279\times10^{-11}T^4 \quad (4)$$

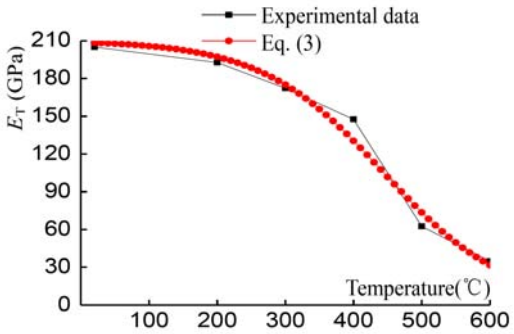

Figure 8. Young's Modulus of Cables at Elevated Temperature - Tests Versus Predicted Formula

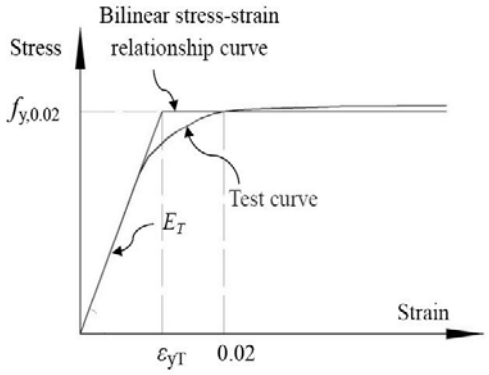

Figure 9. Bi-linear Model to Predict the Stress-strain Relationship of Cable at Elevated Temperature

3. CACULATION OF CABLE TENSILE FORCE UNDER LOCALISED FIRE

When a cable is subjected to a horizontal pre-tensioned force, H_0', its initially curved configuration will change to a straight configuration as shown in Figure 10(a). When the cable is subjected to uniformly distributed load, q_0, along its length, the cable is deformed to a new configuration and cable horizontal tension force changes to H_0, as shown in Figure 10(b). Under a fire situation, the cable will deform further due to the reduction of Young's modulus at elevated temperature. The horizontal tension force in the cable changes to H_{1T} as shown in Figure 10(c).

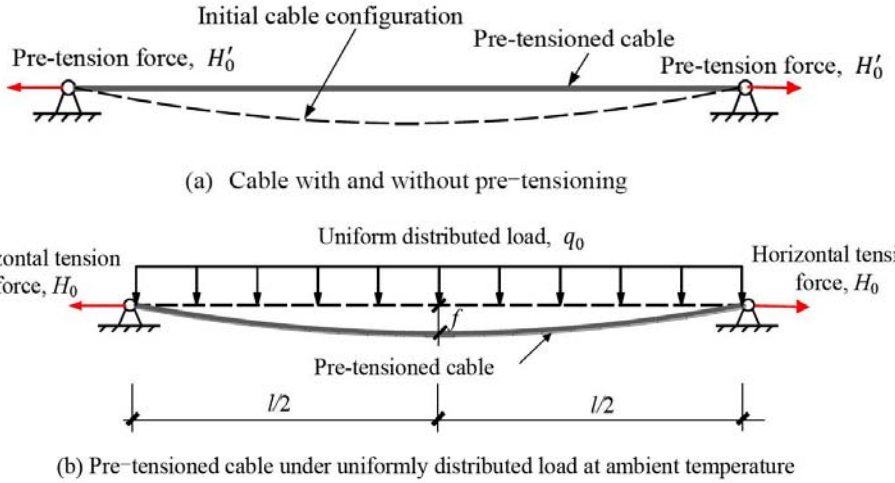

Figure 10. Response of a Pre-tensioned Cable before and during Fire

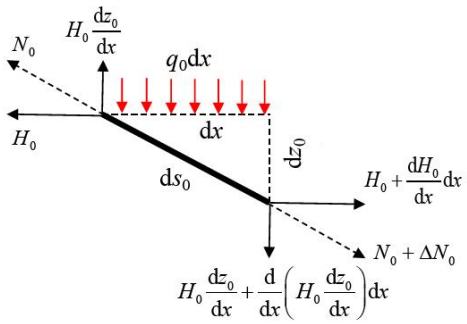

Figure 11. Force Equilibrium of a Differential Element at Ambient Temperature

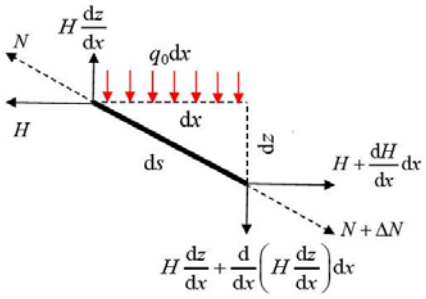

Figure 12. Force Equilibrium of a Differential Element at Elevated Temperature

In order to capture the transient tension force, which is temperature dependent, the force equilibrium equation of a differential cable element can be established at ambient temperature and at elevated temperature as shown in Figure 11 and 12, respectively. The temperature increases from T_0 to T_n given as $\Delta T = T_n - T_0$. If the differential cable element is small enough, the material properties which are temperature dependent will be kept at the same within acable element even though the non-uniform temperature along the length of a cable.

The transient tension force of a cable under uniform distributed load and subject to fire has been derived based on an analytical method proposed in the following sections.

3.1 Cables Subject to Uniform Distributed Loads

A pre-tensioned cable with span, l, and hinged at ends A and B at the same level, is subject to the uniform distributed load, q_0 as shown in Figure 10(b). The cable deflects under a uniformly distributed load, q_0, and the maximum deflection, f, occurs at the mid-span of the cable. The horizontal tension force, H_0, in the cable at ambient temperature can be obtained as reference [2]. At an elevated temperature, the horizontal tensile force changes from H_0 to $H = H_0 + \Delta H$ and the following equation can be obtained based on force equilibrium of a differential element as shown in Figure 13.

$$H\frac{\mathrm{d}^2 z}{\mathrm{d}x^2}+q_0=0 \tag{6}$$

integrating Eq. 6, the following equation can be obtained as:

$$\frac{\mathrm{d}z}{\mathrm{d}x}=\frac{q_0(l-2x)}{2H} \tag{7}$$

as shown in Figure 13, the length of the differential element of a cable can be described as:

$$\mathrm{d}s=\sqrt{\mathrm{d}x^2+\mathrm{d}z^2}=\sqrt{1+\left(\frac{\mathrm{d}z}{\mathrm{d}x}\right)^2}\,\mathrm{d}x \tag{8}$$

similar to Eq. 7, the vertical displacement of the differential element of a cable at ambient temperature as shown in Figure 12 can be written as:

$$\frac{\mathrm{d}z_0}{\mathrm{d}x}=\frac{q_0(l-2x)}{2H_0} \tag{9}$$

thus, the thermal elongation of the differential element for a pre-tensioned cable can be derived as:

$$\mathrm{d}s-\mathrm{d}s_0=\sqrt{1+\left(\frac{\mathrm{d}z}{\mathrm{d}x}\right)^2}\,\mathrm{d}x-\sqrt{1+\left(\frac{\mathrm{d}z_0}{\mathrm{d}x}\right)^2}\,\mathrm{d}x \tag{10}$$

expanding the square root term in Eq. 10 by Taylor series and neglecting the second term, Eq. 10 can be approximated as:

$$\mathrm{d}s-\mathrm{d}s_0=\frac{1}{2}\left[\left(\frac{\mathrm{d}z}{\mathrm{d}x}\right)^2-\left(\frac{\mathrm{d}z_0}{\mathrm{d}x}\right)^2\right]\mathrm{d}x \tag{11}$$

The total thermal elongation of a pre-tensioned cable can then be obtained by integrating Eq. 11 along the length of the cable as

$$\Delta s=\int_l(\mathrm{d}s-\mathrm{d}s_0)\,\mathrm{d}x=\frac{1}{2}\int_l\left[\left(\frac{\mathrm{d}z}{\mathrm{d}x}\right)^2-\left(\frac{\mathrm{d}z_0}{\mathrm{d}x}\right)^2\right]\mathrm{d}x \tag{12}$$

The total strain of a pre-tensioned cable at elevated temperature is the sum of the strain of a cable due to thermal elongation, $\Delta\varepsilon_{\mathrm{th}}$, and that due to the increment of internal tensile force, $\Delta\varepsilon_{\mathrm{N}}$, as:

$$\Delta\varepsilon=\Delta\varepsilon_{\mathrm{th}}+\Delta\varepsilon_{\mathrm{N}}=\alpha\Delta T+\frac{\Delta N}{E_{\mathrm{T}}A} \tag{13}$$

where ΔN is the variation of internal tension force given as $\Delta N=\Delta H\frac{\mathrm{d}s}{\mathrm{d}x}$, α is the coefficient of thermal expansion, and A is the cross section size of a cable.

Integrating Eq. 13 along the cable length, the change of cable length can be obtained as

$$\Delta s=\int_l\left\{\frac{\Delta H}{E_T A}\left[1+\left(\frac{\mathrm{d}z}{\mathrm{d}x}\right)^2\right]\right\}\mathrm{d}x+\int_l\left[\alpha\Delta T\sqrt{1+\left(\frac{\mathrm{d}z}{\mathrm{d}x}\right)^2}\right]\mathrm{d}x \tag{14}$$

Neglecting the higher order term, $\left(\frac{\mathrm{d}z}{\mathrm{d}x}\right)^2$, the above equation can be rewritten as

$$\Delta s=\int_l\frac{\Delta H}{E_T A}\mathrm{d}x+\int_l\alpha\Delta T\,\mathrm{d}x \tag{15}$$

Substituting Δs from Eq. 12 into Eq. 15, and expressing ΔH as

$$\int_l\frac{\Delta H}{E_{\mathrm{T}}A}\mathrm{d}x+\int_l\alpha\Delta T\,\mathrm{d}x=\frac{1}{2}\int_l\left[\left(\frac{\mathrm{d}z}{\mathrm{d}x}\right)^2-\left(\frac{\mathrm{d}z_0}{\mathrm{d}x}\right)^2\right]\mathrm{d}x \tag{16}$$

In the following sections, two fire scenarios will be adopted to analyze the cable: (1) the fire engulfs the entire cable and thus the cable is uniformly heated along its length, and (2) the cable is subject to localized fire and thus the cable is only partially heated at certain portion of the cable length.

Cables subject to Uniform Heating and under uniformly Distributed Load

Substituting Eq. 7 and Eq. 9 into Eq. 16, and integrating the transient horizontal tension force ΔH by assuming uniform heating along the cable length in which the factor of η equals to 1.0 and the cable Young's Modulus remains the same along the length, the cable tensile force can be obtained as:

$$H^2 = \frac{q_0^2 l^2 H_0^2 E_T A}{24H_0^2 H - 24H_0^3 + 24H_0^2 E_T A\alpha\Delta T + q_0^2 l^2 E_T A} \tag{17}$$

The transient horizontal force H in Eq. 17 can be solved by assuming a value of H on the right-hand term and search for the final solution by an iterative process till the right-hand term equal to the left-hand term.

3.2.1 Cables subject to partial heating under uniformly distributed load

When the cable is partially heated under localized fire, the Young's Modulus is varied along the length of cables, depending on it location with respect to fire source. If the area of the fire source is small relative to the length of the cable, the effective radius of fire source, b, in Eq. 1 can be ignored. Substituting Eq. 2 and Eq. 3 into the left side of Eq. 16, we can obtain

$$\int_l \frac{\Delta H\left(975 + 7\exp\left(\frac{T_{\max}k(x)}{90}\right)\right)}{EA\times 10^3}\mathrm{d}x + \int_l \alpha\Delta T k(x)\,\mathrm{d}x = \frac{1}{2}\int_l \left[\left(\frac{\mathrm{d}z}{\mathrm{d}x}\right)^2 - \left(\frac{\mathrm{d}z_0}{\mathrm{d}x}\right)^2\right]\mathrm{d}x \tag{18}$$

The integration zone is shown in Figure 12, while the fire source is right below the cable mid-span, which is dependent on the temperature distribution given by Eq. 2. Since the temperature distribution function is dependent on the length of a cable, the integration zone under centre fire will be classified into two models, that is whether the distance from the vertical axis of plume centre to the end of the cable is over the value of 23η or not. Then, The integration zone of Eq. 18 can be defined as, $0 \le x < \frac{l}{2} - 23\eta$, $\frac{l}{2} - 23\eta \le x \le \frac{l}{2}$, $\frac{l}{2} \le x \le \frac{l}{2} + 23\eta$ and $\frac{l}{2} + 23\eta < x \le l$, as the half length of a cable is not smaller than the value of 23η, shown in Figure 14(a). Otherwise, Eq. 18 will be integrated within the zone, $0 \le x < \frac{l}{2}$ and $\frac{l}{2} \le x < l$, as the half length of a cable is smaller than 23η, as shown in Figure 13(b).

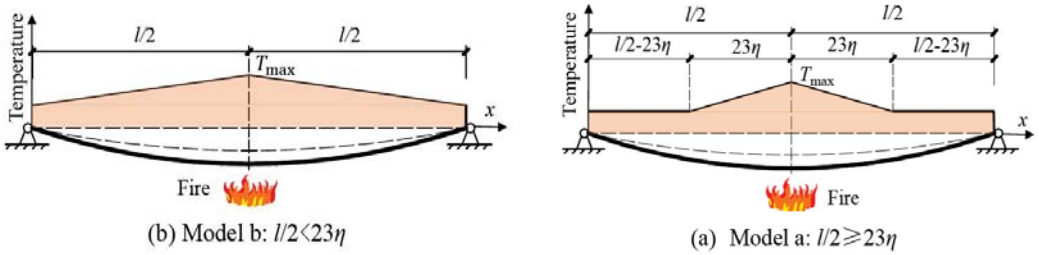

Figure 13. Integration Models along a Cable Dependent of Temperature distribution under Centre Fire

Then, substituting Eq. 7 and Eq. 9 into the right-hand of Eq. 18, the equation of the transient horizontal tension force, which is due to the fire scenario shown in Figure 12, can be obtained as:

$$H^2 = \frac{q_0^2 l^3 H_0^2 EA}{12H_0^2 HB_{nd} - 12H_0^3 B_{nd} + 12H_0^2 EA\alpha\Delta TC_{nd} + q_0^2 l^3 EA} \tag{19}$$

where

if $l/2 \geq 23\eta$, then

$$B_{nd} = \frac{39l}{20} + \frac{63}{25T_{\max}\gamma}\exp\left(\frac{T_{\max}}{90}\right)\left[\exp\left(\frac{T_{\max}\gamma(25-24\eta)}{90}\right)-1\right] + \frac{7}{250}\exp\left(\frac{T_{\max}\eta}{90}\right)\left(\frac{l}{2}-23\eta\right)$$

$$C_{nd} = 2\eta l + 46\eta(1-\eta)$$

if $l/2 < 23\eta$, then

$$B_{nd} = \frac{39l}{20} + \frac{63}{25T_{\max}\gamma}\exp\left(\frac{T_{\max}}{90}\right)\left[\exp\left(\frac{T_{\max}\gamma l}{180}\right)-1\right]$$

$$C_{nd} = 2l + \gamma l^2/2$$

3.3 Pre-tensioned Cables Subject to Point Loads

As shown in Figure 14, a pre-tensioned cable is with the nonlinear geometry shape, s_b, due to gravity load, q_b, at ambient temperature. The horizontal tension force, H_b, can be calculated by Eq. 20.

$$H_b = \frac{q_b l^2}{8f} \tag{20}$$

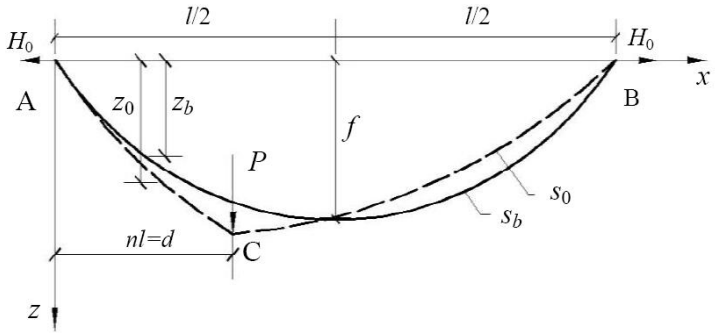

Figure 14. Nonlinear Response of a Pre-tensioned Cable under Point Load at Ambient Temperature

When the cable is subject to a point load, P, at a distance nl from the left support A, the cable geometry changes from the original configuration 's_0' to the deformed geometry 's_b'. The new cable geometry consists of two parabolic segments, AC and CB, with a slope discontinuity at Point C. The following equations can be derived based on the force equilibrium of the cable segments AC and CB [3]

for $0 \leq x \leq d$

$$z_0 = \frac{q_b(l-x) + 2P(1-n)x}{2H_0} \tag{21}$$

for $d < x \leq l$

$$z_0 = \frac{(q_b x + 2Pn)(l-x)}{2H_0} \tag{22}$$

At ambient temperature, Eq. 16 can be rewritten as below

$$\int_l \frac{H_0 - H_b}{EA} dx + = \frac{1}{2}\int_l \left[\left(\frac{dz_0}{dx} \right)^2 - \left(\frac{dz_b}{dx} \right)^2 \right] dx \tag{23}$$

Substituting Eq. 21 and Eq. 22 into Eq. 23, and integrating along the length of a cable, it can be written as:

$$\frac{2(H_0 - H_b)l}{EA} = \frac{12Pq_b d(l-d) + 12P^2 d(1-2n) + 12P^2 n^2 l + q_b^2 l^3}{12H_0^2} - \frac{q_b^2 l^3}{12H_b^2} \tag{24}$$

Let $\xi = 12Pq_b d(l-d) + 12P^2 d(1-2n) + 12P^2 n^2 l + q_b^2 l^3$, the transient horizontal tension force of a pre-tensioned cable under point load at ambient temperature can be derived from Eq. 24 as

$$H_0^2 = \frac{EA\xi H_b^2}{24H_0 H_b^2 l - 24H_b^3 l + q_b^2 l^3 EA} \tag{25}$$

3.3.1 Cables subject to uniform heating along its length under point load

At uniform elevated temperature distribution along the length of the cable, the transient horizontal tensile force in cable increases to $H=H_0+\Delta H$, and induces the nonlinear deformation, z, in a pre-tensioned cable described by as below:

for $0 \le x \le d$

$$z = \frac{q_b(l-x) + 2P(1-n)x}{2H} \tag{26}$$

for $d < x \le l$

$$z = \frac{(q_b x + 2Pn)(l-x)}{2H} \tag{27}$$

Substituting Eq. 21, Eq. 22, Eq. 26 and Eq. 27 into Eq. 16, and integrating along the length of cable, the transient horizontal tensile force of cable under point load with uniform temperature distribution can be obtained as below:

$$H^2 = \frac{H_0^2 D_{ud} E_T A}{8H_0^2 Hl - 8H_0^3 l + 8H_0^2 E_T A\alpha\Delta Tl + D_{ud} E_T A} \tag{28}$$

with $D_{ud} = q_b^2 l^3 / 3 + 4Pq_b d(l-d) + 4P^2(1-2n)d + 4P^2 n^2 l$

3.3.2 Cables subject to non-uniform heating along its length under point load

The regions for integrating Eq. 16 is taken as $0 \le x < l/2 - 23\eta$, $l/2 - 23\eta < x < nl$, $nl < x < l/2$, $nl < x < l/2 + 23\eta$ and $l/2 + 23\eta < x < l$ if the half length of cable is greater than the value of 23η, as shown in Figure 15(a). Otherwise, Eq. 16 shall be integrated within the zone of $0 \le x < l/2$ and $l/2 \le x < l$ as the half length of cable is smaller than 23η, as shown in Figure 15(b). The horizontal tensile force in the cable under point load exposed to non-uniform heating distribution can be obtained as:

$$H^2 = \frac{H_0^2 D_{ud} E_{20} A}{4H_0^2 HB_{nd} - 4H_0^3 B_{nd} + 4H_0^2 E_{20} A\alpha\Delta TC_{nd} + D_{ud} E_{20} A} \tag{29}$$

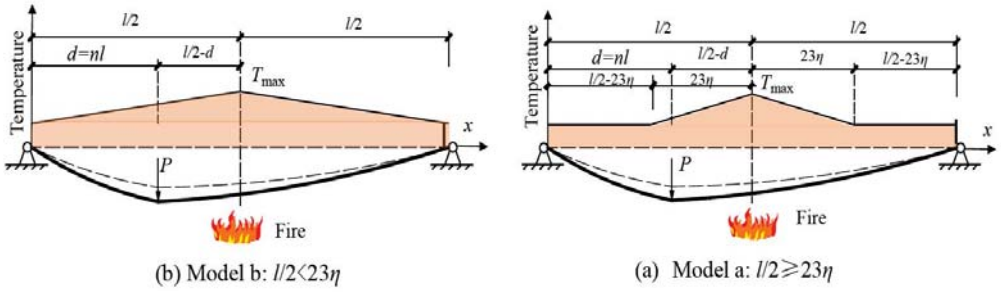

Figure 15. Integration Model along a Cable dependent of Non-uniform Temperature distribution under Centre Fire with Point Load, P

4 CASE STUDY

As shown in Figure 10(b), the cable is subject to a pre-tensile force of H_0=19.1 kN and under the uniformly distributed load of q_0=0.5 kN/m. The length of the cable is 8m, and the cable cross sectional area is 0.674 cm^2. Young's Modulus, E, at ambient temperature is 1.89×105 MPa. Assuming the cable is fully engulfed in fire and it is subjected to uniform heating along its entire length, the transient horizontal tension force in the exposed to uniform heating can be obtained as follow.

Assuming a temperature of 250℃, the Young's Modulus of the cable can be calculated from Eq. 3 as $E_T = 1.78\times10^5$MPa. Substituting the values of H_0, A, l, q_0, E_T, into Eq. 17 and obtain:

$$H^2 = \frac{7975}{H + 44.6} \tag{30}$$

The transient horizontal tension force, H, from Eq. 30 can be calculated using an iterative method and a final value of H = 11.9kN is obtained. A similar method is then repeated to calculate H for cable subject to another temperature and the relationship between H and temperature, T, is plotted as shown in Figure 16.

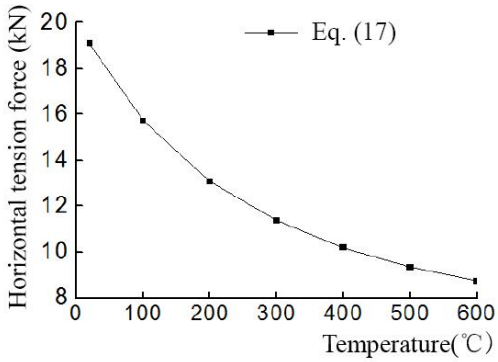

Figure16. Horizontal Tension Force against Temperature

For other loading configuration and temperature distributions, the transient horizontal tension force in the cable can be obtained from Eq. 19, Eq. 28 or Eq. 29, respectively.

5. LOAD RESISTANCE OF PRE-TENSIONED STEEL CABLES UNDER FIRE

The transient horizontal tension force of pre-tensioned cables under uniform distributed load or point load exposed to local fire scenarios can be calculated by the proposed equations while the effective yield strength of cables dependent on the elevated temperature can be obtained from Eq. 4. The fire resistance or critical temperature of a pre-tensioned cable can be determined when the tension force is equal to the yield load of the cable. The following example illustrates the procedure of calculating the fire resistance of pre-tensioned cable subjected to localized fire.

At fire limit state, the load resistance of a pre-tensioned cable is dependent on the maximum temperature according to Eq. 1 and temperature distribution as shown in Figure 5. For long span cable, if the vertical displacement of a cable is small enough, the tension force in cables will be similar to the horizontal tensile force. Then, the stress of a pre-tensioned cable should be satisfied by the equation as:

$$\sigma_{\mathrm{T}}=\frac{H}{A}\leq f_{y,0.02}^{T} \tag{31}$$

where σ_{T} is the stress of a pre-tensioned cable at elevated temperature; A is the size of cross section of a cable; H is the transient horizontal tensile force at elevated temperature, obtained by Eq. 17, Eq. 19, Eq.28 or Eq. 29 respectively; $f_{y,0.02}^{T}$ is the yield strength of a cable dependent on temperature, obtained by Eq. 4.

For example, a pre-tensioned cable with the size of cross section, A=0.674 cm^2; and Young's Modulus as E =1.89×105MPa. The span length of the cable is l = 20m; horizontal tension force at ambient temperature is H_{b} = 11.53kN; uniformly distributed dead load is q_0=0.2 kN/m; point force P =1kN is acting at 0.5l from the support. The temperature reduction factor is taken as η=0.6 .A numerical model of pre-tensioned cable mentioned above has been established by using ANSYS software shown in Figure 17. The 'Link8' element has been employed to simulate the pre-tensioned cable. As Shown in Figure 18, the numerical model of pre-tensioned cable designed as above is modelled by the Link 8 elements and cut into one hundred elements along its length. The horizontal tension force and the tensile stress in the cables computed by the numerical analyses and from Eq. 29 are compared as shown in Figure. 20 and 21, respectively.

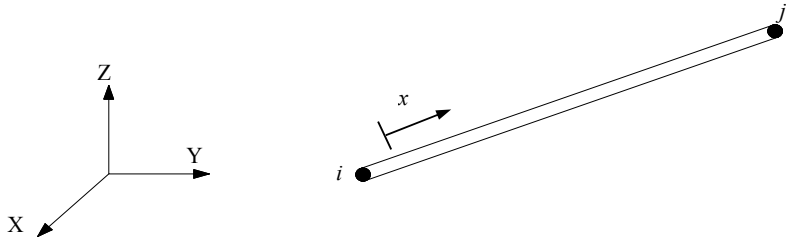

Figure 17. Numerical Model of Link 8 Element

Figure 18. Numerical Model of a Pre-tensioned Cable

According to the Eq. 1, the temperature distribution along the pre-tensioned cable can be updated by tracing the maximum temperature, T_{max}, with 10℃ interval. Under each temperature distribution, the tension force, H, can be calculated by Eq. 17, Eq. 19, Eq. 28 or Eq. 29, and then, checked by Eq. 31 step by step.

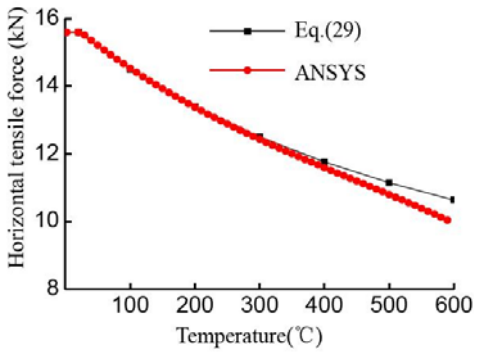

Figure 19. Horizontal Tension Force of the Pre-tensioned Cable at Elevated Temperature

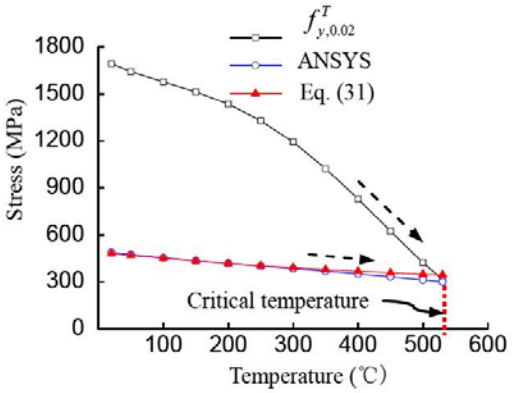

Figure 20. Mechanical Response of the Pre-tensioned Cable at Elevated Temperature

Figure 16 shows that the horizontal tension force calculated from Eq. 29 decreases with the temperature rise and fits the numerical result well in lower temperature range. Above 400℃, there is somewhat a difference between Eq. 29 and numerical results. The maximum amount of deviation reaches 7% at 600℃ because the higher order term, $(dz/dx)^2$, is ignored in Eq. 14.

The yield strength of the steel cable at elevated temperature is also plotted in Figure 20. When the tensile stress of the steel cable meets the yield strength, the fire resistance temperature or critical temperature is attained. Figure 20 also shows that the tensile stress in the cable obtained from the numerical simulation and a good fit with the analytical result is observed. It indicates that the equations of the transient horizontal force developed in the present studies can provide a good estimate of the mechanical response of pre-tensioned steel cable subjected to localized fire.

The following section investigates the key parameters that influence the mechanical behavior of pre-tensioned cables under localized fire.

6. FACTORS AFFECTING THE CABLE TENSILE FORCE UNDER FIRES

Tension force in cables represents the key mechanical characterizes of pre-tensioned cables. The initial tension force level, load ratio, span of cables and the degree of non-uniform temperature distribution along the length of the cable are involved in Eq. 17, Eq. 19, Eq. 28 and Eq. 29, which determines the transient tension force in cables.

Firstly, the pre-tension level, P_r, is defined as the pre-tension force, H_0', forming the nonlinear geometric shape before loading, shown in Figure 9(a), to yield strength at ambient temperature as:

$$P_r = \frac{H_0'}{f_y A} \tag{32}$$

In Eq. 32, the pre-tension force is always designed as lower than 30% yield strength at ambient temperature [2].

Load ratio, R, is the horizontal tension force of cables due to load, shown in Figure 10(b), to yield strength at ambient temperature as below.

$$R = \frac{H_0}{f_y A} \tag{33}$$

6.1 Effects of Pre-tensioned Force Level

To study the effects of pre-tensioned force level on the horizontal tension force of cables at elevated temperature, an example has been designed as below.

The pre-tensioned steel cable under uniform distributed load, shown in Figure 10(c), with the cross section of 0.674 cm^2;Young's Modulus of 1.89 × 105 MPa; cable span of 20m; load level of 0.4;the non-uniform temperature distribution with the reduction factor, $\eta = 0.6$;the initial pre-tension force level, P_r , ranged of 0.1 to 0.18.

At ambient temperature, the initial geometrical configuration of a cable is significantly dependent on the pre-tension force before loading. The cable will be stretched more tightly and induced the less displacement at the mid-span with higher pre-tension force level.

As shown in Figure 10(a) and 10(b), the horizontal tension force, H_0' , can be updated to H_0, due to uniform distribution load, that is, the horizontal tension force, H_0, is affected by pre-tension force, H_0' , and uniform distribution load, q_0. In order for parametric analysis to keep the given load level, R=0.4, constant, the horizontal tension force, H_0, should be kept constant according to the Eq. 33. Meanwhile, the pre-tension force level increases as listed in table 2 to analyze its effect on the mechanical behaviors of pre-tensioned cables under localized fire. According to the Eq. 32, the pre-tension force, H_0' , increases while the pre-tension force level increasing. Thus, the uniform distribution load, q_0, should be decreased while the pre-tension force increases to keep the horizontal tension force constant.

Table 2. Pre-tension Force Level under the Uniform Distribution Load

Pre-tension force level, P_r	0.10	0.12	0.14	0.16	0.18
Uniform distribution load, q_0 (kN/m)	2.130	1.788	1.540	1.355	1.215

Resulting from the Eq. 19, at each elevated temperature level, the horizontal tension force of the cable decreases with the increase of the pre-tensioned force level at each temperature level, as shown in Figure 21. When comparing with the horizontal tension forces in the cable which resulted from numerical analysis and Eq. 19 at elevated temperature, it is discovered that they hold the same tendency, that is, with the tension force level increasing, the horizontal tension force decreases more sharply under localized fire.

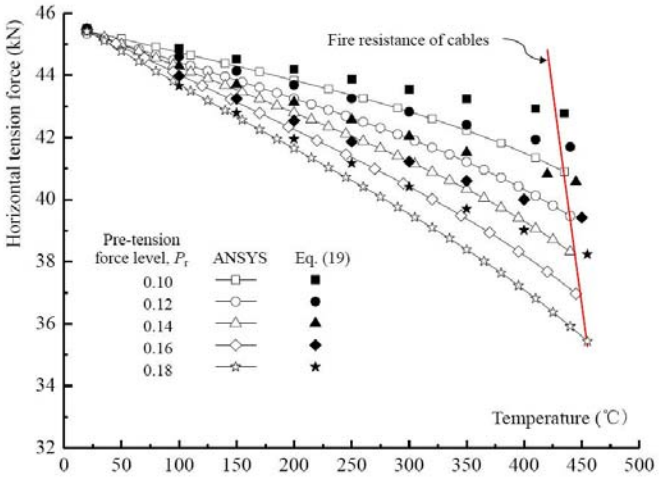

Figure 21. Horizontal Tension Force vs. Temperature in a Range of Pre-tensioned Force Level

As shown in Figure 21, the maximum deviation of the horizontal tensile force is 7.3% between the curves resulted from Eq. 19 and numerical simulation using by ANSYS software. It proves that the numerical analysis can simulate the mechanical behaviors of cables under localized fires enough. It should be noted that the critical temperature of the pre-tensioned steel cable is dependent on the pre-tension force level, temperature distribution and the fire resistance of cables together under the same load ratio. Hence, according to the same failure state which is shown in Figure 21, when the curve of horizontal tension force drops more sharply, it meets the fire resistance curve, which decreases through the whole temperature history, more lately and led to the higher critical temperature as the pre-tensioned force level increasing.

6.2 Effects of Load Ratio

In order to study the effects of load ratio on the horizontal tensile force of cables at elevated temperature, the cable with the same geometric properties given in the 5.1 section of this paper is with the pre-tensioned force level, $P_r = 0.1$; the reduction factor of the temperature distribution is taken as $\eta = 0.6$;the load ratio, R, in a range of 0.2 to 0.7.

A range of horizontal tension force at ambient temperature, H_0, can be obtained by Eq. 33 under each load ratio. It should be noted that the horizontal tension force, H_0, increases with the increasing of the load ratio at ambient temperature. In order to keep the increasing of the horizontal tension force, the uniform distribution load should be increased as listed in table 3.

Table 3. Load Ratio under the Uniform Distribution Load

Load ratio, R	0.2	0.3	0.4	0.5	0.6	0.7
Uniform distribution load, q_0 (kN/m)	1.03	1.575	2.13	2.71	3.28	3.88

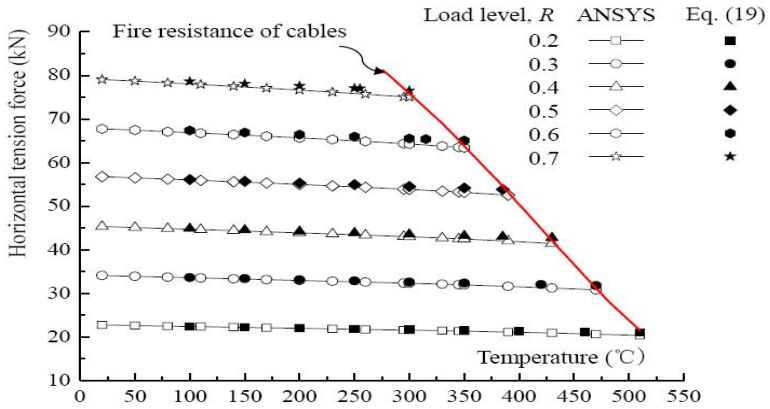

Figure 22. Horizontal Tension Force Versus Temperature History in a Range of Load Ratio

Resulting from the Eq. 19, at each elevated temperature level, the horizontal tension force in the cable is increasing dramatically with the increasing of load ratio at each temperature level, shown in Figure 22. Comparing with the horizontal tension forces in the cable resulted from numerical analysis and Eq. 19 at elevated temperature, they fit well together with 3.2% deviation between the curves resulted from Eq. 19 and numerical simulation using by ANSYS software, and the horizontal tension force is decreasing slightly at the same gradient through the whole temperature history.

Checking with Eq. 31, the curve of the horizontal tension force met the fire resistance curve earlier and led to the lower critical temperature as the load ratio increasing.

6.3 Effects of Non-uniform Heating Along the Length of Cables

In order to study the effects of the non-uniform temperature distribution on the horizontal tension force in cables at elevated temperature, the cable with the same geometric properties given in the 5.1 section of this paper is with the pre-tension force level, $P_r = 0.1$; the load ratio, $R = 0.3$; uniform distribution load, $q_0 = 1.575\text{kN/m}$; and the non-uniform heating along the length of the cable with the reduction factors in a range of, η=0.2~1.0.

Resulting from the Eq. 19, at each elevated temperature level, the horizontal tension force in the cable is decreased with the increasing of temperature reduction factor, shown in Figure 23. The comparison with the horizontal tension forces in the cable resulted from numerical analysis and Eq. 19 at elevated temperature, the maximum deviation of the horizontal tension force is 5.3%.

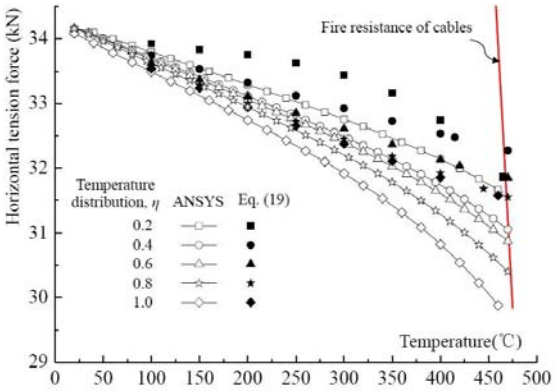

Figure 23. Horizontal Tension Force Versus Temperature History in a Range of Temperature Distribution

The horizontal tension force is decreasing more sharply with the larger temperature reduction factor, that is, the more uniform temperature distribution can lead to the horizontal tension force dropping more sharply and meeting the fire resistance curve more lately. Checking with Eq. 31, the curve of the horizontal tension force met the fire resistance curve more early with the more non-uniform temperature distribution and led to the lower critical temperature. As the uniform temperature distribution with $\eta = 1.0$, the element at the end of a cable may fall to failure much earlier than that with a little lower tension force at the mid-span of a cable.

6.4 Effects of the Cable Span Length

As shown in Figure 24, a longer cable will be exposed to the more concentrate heated zone along its length. Therefore, the cable length should be one of the key factors which would influence the horizontal tension force in cables at elevated temperature.

In order to study effects of the cable span length on the horizontal tension force in a cable at elevated temperature, the cable with the same geometric properties given in the 5.1 section of this paper is with the pre-tension force level, $P_r = 0.1$; the load ratio, $R = 0.5$; the non-uniform heating along the length of the cable with the reduction factors, $\eta = 0.6$, and the span length of the cable in a range of 12m ~ 32m.

In order to keep the constant value of the horizontal tension force, H_0, the load, q_0, should be updated with the length of the cable increasing as listed in table 4.

Table 4. Pre-tension Force Level against the Uniform Distribution Load

Length of the cable, l (m)	12	16	20	24	28	32
Uniform distribution load, q_0 (kN/m)	2.87	2.75	2.705	2.69	2.71	2.73

Resulting from the Eq. 19, at each elevated temperature level, the horizontal tension force in the cable decreases with a decrease of the length of cables at each temperature level, as shown in Figure 24. Comparing with the horizontal tension forces in the cable resulted from numerical analysis and Eq. 19 at elevated temperature, the maximum deviation of the horizontal tension force is 6.6%.

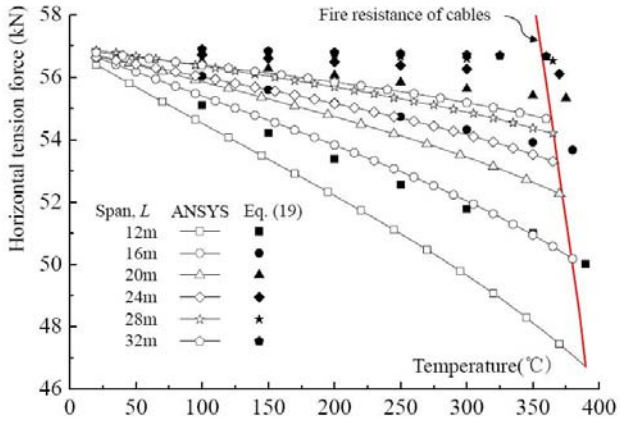

Figure 24. Horizontal Tension Force under Temperature History in a Range of Span

The horizontal tension force decreases more sharply with the shorter span of cables, that is, the localized fire will influence the horizontal tension force in the shorter span cables more greatly. Checking with Eq. 31, the curve of the horizontal tension force met the fire resistance curve more early with the larger span and led to the lower critical temperature.

6.5 Effects of the Moving Fire

Movement of fire is one of the typical features of localized fires in nature. As shown in Figure 25, as the fire moves away from the center, the non-uniform temperature distribution with factor, η=0.6, is no longer symmetrical to the mid-span of cables. When the fire moved from point A to point B, as shown in the insert of Figure 25, the tension force distribution along the length of a cable kept symmetrical to the mid-span of cables, and the value of the tension force increased slightly. It should be worth noting that the tension force at the mid-span of the cable decreases only by about 10% from that at the end of cable. The gradient of tension force along the large span of cable is rather low. It can be assumed that the tension force is almost uniform distribution along the cable. On the other hand, the fire resistance of cable decreases significantly as temperature increases, as shown in Figure 20. Thus, the centre fire scenario is considered to be more critical and can be used to evaluate the fire safety of a pre-tensioned cable.

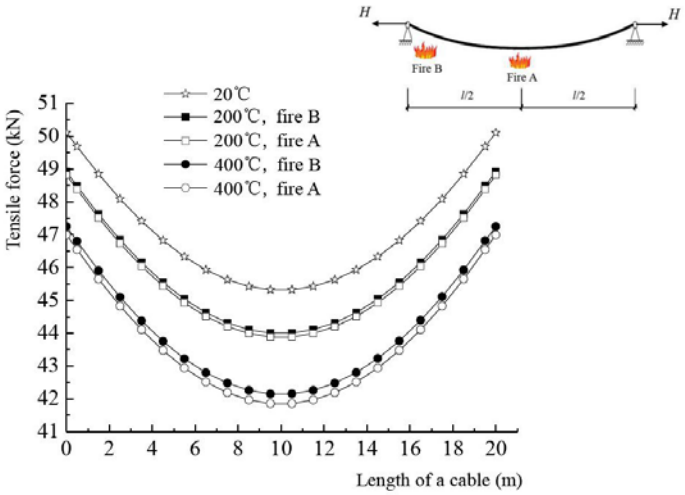

Figure 25. Tension Force Distribution along the Length of a Cable under Moving Fire

7. DESIGN OF PRE-TENSIONED CABLES FOR FIRE SAFETY

Figure 26 outlines a design flow chart without using sophisticated numerical software to determine the fire safety of a pre-tensioned cable subject to localised fire. The ability of a pre-tensioned cable to sustain the applied load under localised fires is considered the yield strength and Young's modulus of cables dependent on the non-uniform temperature distribution along the length of the cable. Two design strategies have been proposed to improve the fire resistance for pre-tensioned cables based on the influence parameters analysis illustrated above and thermal transfer respectively.

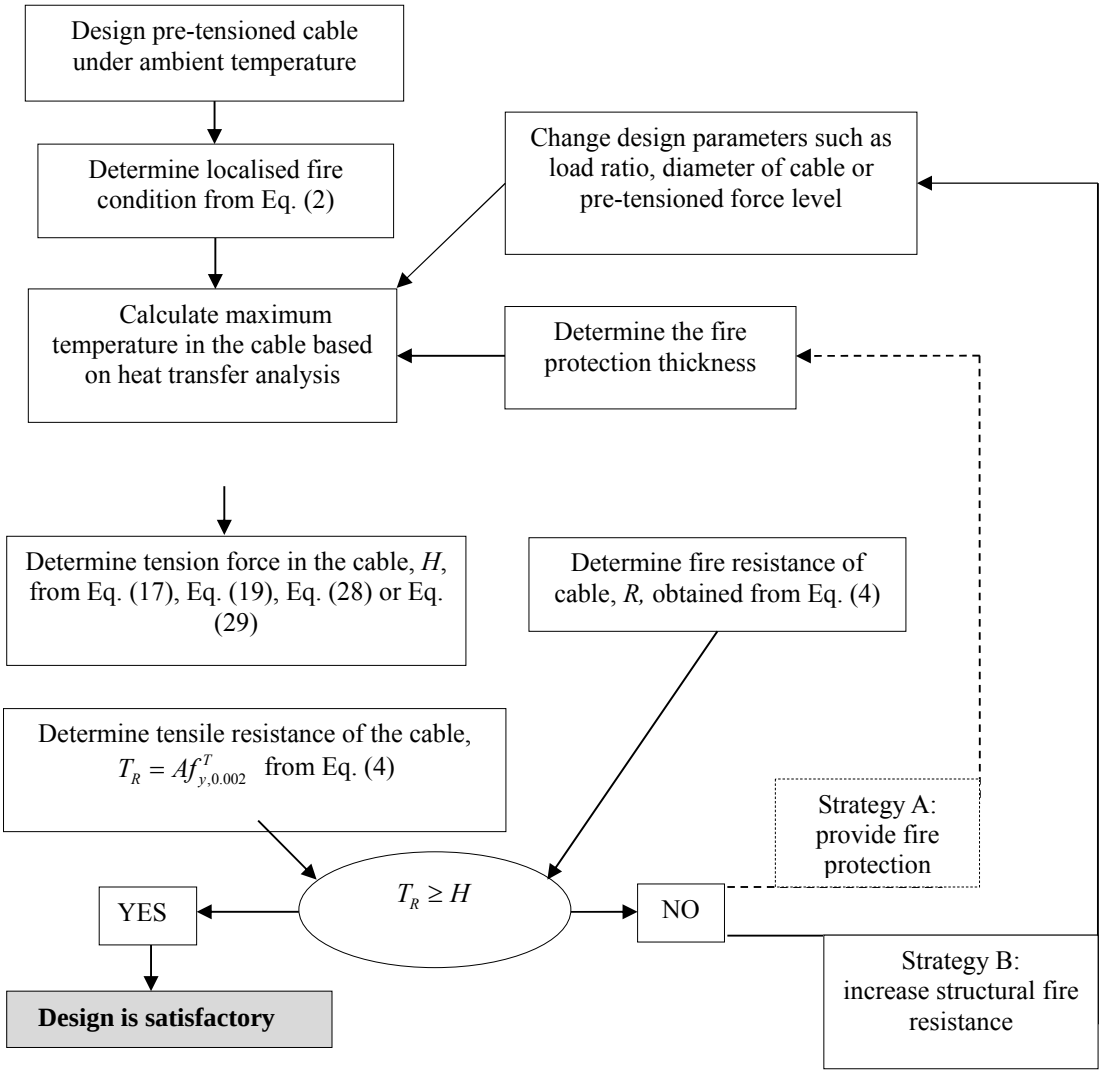

Figure 26. Design Flow Chart for Pre-tensioned Cables at Localised Fire

7. CONCLUSIONS

In this study, an analytical method has been proposed to determine the mechanical behaviour of pre-tensioned steel cables subjected to localised fire. The horizontal tensile force subjected to localised fire is influenced by the load ratio, pre-tensile force level, length of cables, temperature distribution along the cable length and material properties at elevated temperature. Analytical methods have been developed to predict the horizontal tensile force in cable under different fire scenarios which consider uniform or non-uniform heating along the cable length with point load or uniform distributed load.

The critical temperature of the cable can be determined when the horizontal tensile stress reaches the effective yield strength of the cable at elevated temperature. The accuracy of the proposed analytical method is verified against the results obtained by nonlinear finite element analysis. Parametric studies have been conducted and the results show that:

- The horizontal tension force in cables decreased more sharply as the pre-tensioned force level increases.
- The horizontal tensile force in cables increases with the increase of load ratio and decreases with the increase in temperature.
- The horizontal tension force decreases more sharply with the degree of the non-uniform temperature distribution along the length of a cable.
- The horizontal tensile force decreases more sharply with the shorter span of cables in the same temperature distribution in localised fire.
- The horizontal tension force in cables is not affected significantly by the location of the fire. The critical location of the fire source is identified to be the one located just below the mid-length of the cable.

Finally, the design flow chart for pre-tensioned cables at localized fire has been proposed to estimate the fire safety of cables. The results from parametric analyses are useful to formulate design guide to evaluate the fire safety of pre-tensioned structures.

ACKNOWLEDGE

The authors gratefully acknowledge the financial support of the Civil Engineering Disaster Prevention National Key Laboratory in China, and the International Structural Fire Research Laboratory (ISFRL) in Nanjing Tech University, China.

REFERENCES

[1] Saitoh, M. and Okada, A., “The Role of String in Hybrid String Structure”, Engineering Structures, 1999, Vol.21, pp.756–769.
[2] Shen, S.Z., Xu, C.B. and Zhao, C., “Design of Cable Structures”, China Architecture & Technology Press”, 2006. (in Chinese)
[3] Krishna, P. “Cable Suspension Roofs”, Kingsport Press, USA, 1978.
[4] Zhou, H.T., “Study on Fire Resistance Performance of Saddle Cable Net Structures”, Ph.D thesis, Tongji University, Shanghai, China, 2006. (in Chinese)
[5] Sheng, H.M., “Research on Mechanics Behaviors with Analytical Solutions and Numerical Simulation for Beam String Structures under Localized Fire”, Ms.D thesis, Nanjing Tech University, Nanjing, China, 2014. (in Chinese)

[6] Fan, D.H., “Research on Failure Modes of Kiewitt-Lamella Suspension Domes under Localized Fire”, Ms.D thesis, Nanjing Tech University, Nanjing, China, 2015. (in Chinese)
[7] Wang, Y., Shen, Z. and Li, Y., “Experimental Study of the Mechanical Properties of Pre-stressed Steel Wire at Elevated Temperatures”, International Conference on Structures in Fire, USA, 2010.
[8] Society of American Post-tensioned Concrete, East China Technology Development Center of Pre-stressed Concrete. Pre-tensioned Concrete Manual. Southeast University Press, Nanjing, 1989.
[9] EN 1991-1-2 (1992), Eurocode 1–Actions on Structures. Part 1-2. General Actions – Actions on structures exposed to fire. European Committee for Standardization, Brussels, 2013.
[10] ASTM (2005), Standard methods of fire tests of building construction and materials, ASTM Standard E119-05, American Society for Testing and Materials, West Conshohocken, PA.
[11] NFPA (2006), Standard methods of tests of fire Endurance of Building Construction and Materials. NFPA 251. National Fire Protection Association, Quincy, MA.
[12] National Institute of Standards for Engineering. Technical Code for Fire Safety of Steel Structures in Buildings. CECS 200：2006, China.
[13] Du, Y. and Li, G.Q., “A New Temperature Curve for Analysis of Structural Fire-resistance”, Fire Safety Journal, 2012, Vol. 54, No. 11, pp.113-120.
[14] Du, Y. and Li, G.Q., “Effects of Flame Radiation on Temperature Elevation of Steel Members in Large Space Building Fire”, International Conference on Application of Structure Fire Engineering, Prague, Czech Republic, 2009, pp.356-361.

DYNAMIC RESPONSE ANALYSIS OF WIND TURBINE TUBULAR TOWERS UNDER LONG-PERIOD GROUND MOTIONS WITH THE CONSIDERATION OF SOIL-STRUCTURE INTERACTION

Tao Huo[1,2], Lewei Tong[1, 2,*] and Yunfeng Zhang[2, 3]

[1]*State Key Laboratory of Disaster Reduction in Civil engineering , Tongji University，Shanghai, 200092, China*
[2]*College of Civil Engineering, Tongji University, Shanghai 200092, China*
[3]*Department of Civil & Environmental Engineering, University of Maryland, College Park, MD 20742, US*
** (Corresponding author: E-mail: tonglw@tongji.edu.cn)*

Received: 13 July 2016; Revised: 24 May 2017; Accepted: 25 June 2017

ABSTRACT: Existing research in the seismic response of wind turbine tubular towers subjected to long-period ground motions is lacking, especially when soil-structure interaction (SSI) is considered. This paper discusses the seismic performance of typical pitch-controlled 1.25MW wind turbine systems, with particular focus on the influences of SSI effect and ground-motion characteristics. Modal analysis and resonance analysis are carried out first, ensuring that resonance does not occur when the tower is in operation. Two long-period waves and a bedrock wave are selected from the worldwide earthquake record database, followed by detailed dynamic time history analysis. The results indicate that the maximum displacement, acceleration, stress level and internal force responses of the tower subjected to the long-period ground motions are significantly larger than the corresponding values induced by the bedrock wave. Some responses can be further amplified due to the SSI effect, and this highlights the importance of incorporating the SSI effect into seismic design of wind turbine towers, especially for those located in soft soil regions. Furthermore, neglecting the vertical seismic action could lead to unsafe design. Other important issues, including the risk of pounding, stress concentration near the door regions, spindle shear fracture, and foundation failure, are also discussed, and summarized as references or comments for design and analysis of such structures.

Keywords: Soil-structure interaction (SSI), Long-period ground motion, Wind turbine tubular towers, Time history analysis, Design and analysis comments

DOI: 10.18057/IJASC.2018.14.2.6

1. INTRODUCTION

Since the 20th century, traditional energy source has been exhaustingly consumed, leading to global energy crisis. After the 1970s, the concept of sustainable energy became prevalent, and wind power, which is a renewable source of energy, has been extensively developed [1]. Modern commercial wind turbine system originated in Northern Europe which is not a seismically active region; therefore engineers were more concerned about the wind-induced dynamic response at that time. However, with an increasing number of wind turbine systems being constructed in the seismically active region all over the world [2], it is essential to revisit the dynamic performance of these systems against seismic action.

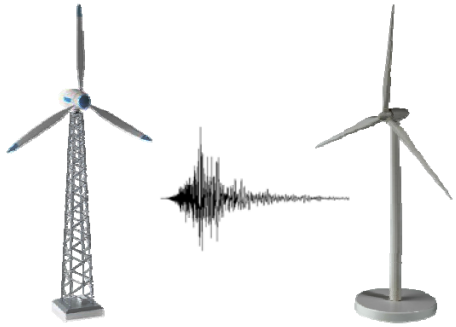

Figure 1 Typical Wind Turbine Lattice Tower and Wind Turbine Tubular Tower

There are two common types of the horizontal-axis wind turbine towers, namely, lattice tower and tubular tower, as shown in Figure 1 [2, 3]. Lattice towers, which are widely used in small and medium-sized wind turbine systems, have their merits of low cost and convenient transportation, but turbulence issues for blade along the downwind direction may be caused. On the other hand, tubular towers have the advantages of elegant appearance, good vibration performance, and convenient maintenance. Therefore, tubular towers, which are the focus of the current study, are widely employed in large-scale wind turbine systems [2].

Some researchers have conducted a series of modeling and dynamic analysis on wind turbine tubular towers. Lobitz [4] proposed a mass-damping-spring model for wind turbine towers and carried out dynamic time history wind analysis; however, no seismic analysis was conducted. Through using mass-damping-spring model in seismic dynamic time history analysis, Bazeos et al. [5] found that the soil-structure interaction (SSI) effect has a significant influence on the dynamic response of tubular towers. Lavasas et al. [6] presented a finite element model containing both the tubular tower and the foundation, where the SSI effect was considered through introducing contact elements. However, in that study, only static analysis was performed without considering any dynamic effects. It is noted that in their studies [5, 6], the blades and nacelle were not directly built in the models. Witcher [7] used both time domain and response spectrum methods to study the seismic response of a 2 MW wind turbine tower. The results showed that the time domain method is more accurate. Based on a shear transfer mechanism, Murtagh et al. [8, 9] developed a coupling finite element model for connecting the tower and blades. The coupling mechanism was defined in detail and dynamic time history analysis was conducted to investigate the wind load effect. Taking SSI effect into account through introducing springs and dampers, Zhao and Maißer [10,11] established multi-body dynamic models for the wind turbine towers to investigate the seismic behavior in time domain and confirmed that the SSI effect plays more significant roles in higher mode vibrations. Through adopting a combined modal and multi-body dynamic formulation, Prowell et al. [12] examined the seismic behavior of a typical 5MW wind turbine system and concluded that the bending vibrations of the towers induced by earthquake loading need to receive sufficient attention in the design. Díaz et al. [13] presented an analytical model of an operating wind turbine subjected to three components base accelerations. The results indicated that in strong earthquake regions, the wind turbine design, especially the tubular tower section, can be controlled by the combined action of the earthquake and wind load. Based on a simplified soil spring model and Boundary Element Method, Taddei et al. [14] established a simplified finite element model of wind turbine towers and adopted a spectrum-compatible synthetic acceleration method to evaluate the applicability of the simplified soil representation in the practical seismic design. The results showed that with increasing thickness of the soil layer, their natural frequencies decrease, and the simplified soil spring model could have better agreement with more sophisticated and accurate soil models. Alati et al. [15] inveatigated the seismic behaviour of fully coupled offshore wind turbine models with fixed and flexible foundations under some typical load cases, and it was concluded that the fully coupled models can provide better prediction on the dynamic responses of the blades,

which are more sensitive to the foundation flexibility. More recently, some innovative vibration reduction solutions, adoping smart materials such as shape memory alloys [16, 17], were also proposed for wind turbine towers[18, 19].

While continuous progress has been made looking into the seismic performance of wind turbine towers, relevant investigations on the influences of long-period ground motions and the SSI effect are generally lacking. Far field, long-period seismic ground motions could bring serious damage to flexible structures [20]. So far, long-period ground motion characteristics and response spectrums have been investigated by various researchers [21, 22], with the main focus on high-rise buildings [23, 24]. However, relevant studies on wind turbine tubular towers subjected to long-period ground motions are still insufficient, and in addition, the long-period range of the response spectrum in major codes [25,26] may not fully meet the design requirement for long-period structures including wind turbine systems. Pounding between the blades and the tower under certain circumstances can be another issue which needs to be carefully addressed. Therefore, it is necessary to take an in-depth look into the seismic response of wind turbine tubular towers subjected to long-period ground motions, taking the SSI effect into account.

In light of the above, a detailed finite element model, consisting of rotor, nacelle, tower and foundation, is established and discussed in this study. The study starts with the introduction of the prototype wind turbine system and the modeling strategy, followed by the discussions of modal analysis and resonance analysis results. A set of dynamic time history analysis are then conducted, where different types of seismic ground motions are considered and the structural responses under long-period seismic ground motions (waves) and bedrock seismic ground motion (wave) are discussed in detail. Based on the numerical results, some preliminary design and analysis recommendations are finally made.

2. INTEGRATED FINITE ELEMENT MODEL

2.1 Description of Prototype Wind Turbine System

This study considers a typical pitch-controlled 1.25MW wind turbine system, based on which an integrated finite element model was built. The key material properties of the blade, nacelle and tower body are listed in Table 1. In the current study, the material was assumed to remain elastic under the considered design earthquakes; in other words, only elastic time-history analysis was performed for the tower. In addition, the three blades were simplified as cantilever beams with a rectangular cross section. The length, width and depth of each blade are 32.175m, 1.5m and 0.3m, respectively. The mass of the rotor (including the blades and hub) is 27470kg. The nacelle and its internal components were treated as an integrated part in the model. The length, width and height of the nacelle are 9.8m, 3.22m and 3.01m, respectively. The mass of the whole nacelle is 52000kg. The main body of the tower is comprised of three segments with varying cross section properties, and the height of each segment is 10.14m, 21.486m and 30.211m (from bottom to top), making a total height of 61.837m. The corresponding tube wall thicknesses for the three segments are 20mm, 16mm and 12mm, respectively. The diameter of the tower increases linearly from 4.2m at the bottom to 2.58m at the top. In order to facilitate maintenance and testing, a door is opened near the bottom of the tower. The height and width of the door is 1.8m and 0.8m respectively in the vertical projection plane. In order to avoid local shell buckling, a doorframe is also installed, as shown in Figure 2b. A 10m×10m×1.8m reinforced concrete raft foundation is located at the bottom of the tower, and the yaw angle of the tower is 0 degree. As defined in Figure 2a, the blades rotational plane is perpendicular to X-Direction, the direction along the tower height is labeled as Z-axis, and the location where the blade is parallel to the positive direction of Z-axis is defined as 0^o azimuth

angle. Murtagh et al. [9] observed that the most unfavourable location of the blades is 0°. In addition, Alati et al. [15] found that the influences of different spatial positions of the blades on the seismic responses are not notable. Therefore, this study only considers the critical location (0°) of the blades to investigate the seismic performance of wind turbine systems, as shown in Figure 2a.

Table 1. Material Properties of Structural Components used in ANSYS

Components	Material	Modulus of elasticity (GPa)	Poisson's ratio
Blade	Glass Reinforced Plastic	42.60	0.22
Nacelle	Steel(Q345D)	206	0.30
Tower	Steel(Q345D)	206	0.30

(a) Integrated finite element model (b) Doorframe

Figure 2. Integrated Finite Element Model and Doorframe

2.2 Modeling

Using the commercial software ANSYS [27], an integrated finite element model was established (see Figure 2a). Eight-node shell elements (SHELL181) were adopted to model both the blades and the tower. The nacelle including inner components was simulated by beam elements (BEAM 189). Following the GL Guideline [28], solid elements (SOLID 95) were used to simulate the doorframe. The foundation section was modeled using reinforced concrete solid elements (SOLID 65). Due to the differences of element types and mesh densities among components, constraint equations and coupling interactions were applied to connect different types of elements. In particular, Rigid Zone connections using the CERIG command were employed between the tower top circular nodes and nacelle beam nodes. Rigid Zone connections were also used between the central nodes of the three blades and the end nodes of the nacelle beam, as shown in Figure 3a. Apart from that, coupling interactions were utilized between the tubular tower nodes along the thick direction and the doorframe nodes through the CPINTF command (see Figure 3b). Constraint equation connections were applied between the tower bottom circular nodes and the foundation top nodes using the CEINTF command (see Figure 3c).

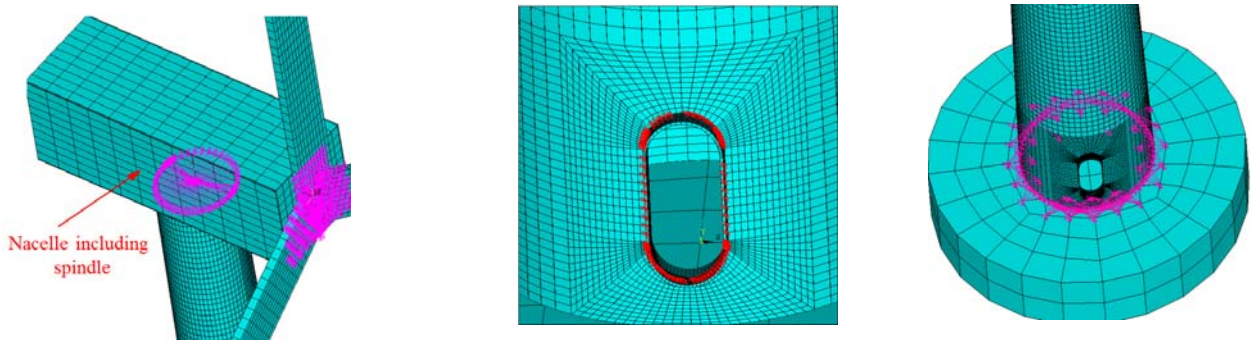

(a) Rigid Zone connection

(b) Coupling connection between tubular tower and doorframe

(c) Constraint equation connection between tubular tower and foundation

Figure 3. Constraint Equations and Coupling Interactions between Different Types of Elements

In order to examine the influence of the SSI effect on the dynamic behavior of the wind turbine system, two models were compared in this study: one model taking account of the SSI effect and the other one excluding this effect. Wolf [29] and Richart et al. [30] suggested that the influence of SSI effect on structural dynamic performance could be achieved by introducing a series of discrete springs and dampers between the soil and the foundation. Using this strategy, a series of discrete springs and dampers were incorporated into the soil-foundation interface. Elements COMBIN14 were applied to simulate the interaction between the foundation and soil in ANSYS. The details of the mechanical model considering the SSI effect are shown in Figure 4, and the values of the foundation soil parameters are provided in Table 2.

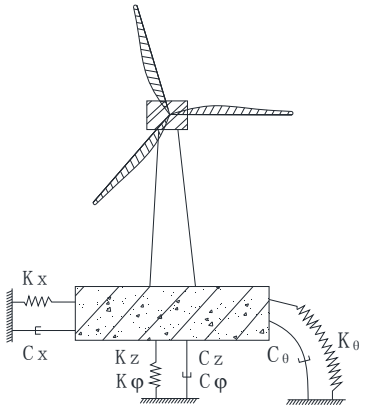

Figure 4. Mechanical Model Considering SSI Effect

Table 2. Parameters of Foundation Soil

Density (Kg/m^3)	Cohesive stress (Pa)	Poisson's ratio	Shear modulus (Pa)	Shear wave velocity (m/s)	Internal friction angle (°)	Dilatancy angle (°)
1900	19000	0.333	5.60E+06	150	25	29

As can be seen in Figure 4, the soil-structure interaction can be modeled with two-dimensional soil spring stiffness coefficients, damping coefficients and mass of springs [29-32]. The basic properties of the springs and dampers were determined from the following equations[29, 30]:

$$K_x = K_y = \frac{8G_sR_s}{2-\nu_s} \qquad K_z = \frac{4G_sR_s}{1-\nu_s} \qquad K_\theta = \frac{8G_sR_s^3}{3(1-\nu_s)} \qquad K_\varphi = \frac{16}{3}G_sR_s^3 \tag{1}$$

$$C_x = C_y = \frac{4.6R_s^2}{2-\nu_s}\sqrt{G_s\rho_s} \quad C_z = \frac{3.4R_s^2}{1-\nu_s}\sqrt{G_s\rho_s} \quad C_\theta = \frac{0.745R_s^4}{1-\nu_s}\sqrt{G_s\rho_s} \quad C_\varphi = 0.815R_s^4\sqrt{G_s\rho_s} \tag{2}$$

$$M_x = M_y = \frac{0.76\rho_s R_s^3}{2-\nu_s} \quad M_z = \frac{1.08\rho_s R_s^3}{1-\nu_s} \quad M_\theta = \frac{0.64\rho_s R_s^5}{(1-\nu_s)} \quad M_\varphi = 0.24\rho_s R_s^5 \tag{3}$$

Where K_x and K_y are the horizontal stiffness coefficients; K_z is the vertical stiffness coefficient; K_θ is the rotational stiffness coefficient; K_φ is the torsional stiffness coefficient. Similarly, $C_i, M_i (i = x, y, z, \theta, \varphi)$ are the corresponding damping coefficients and mass of springs, respectively; R_s is the radius of the circular foundation; G_s, ν_s and ρ_s are the shear modulus, Poisson ratio and density of the soil, respectively.

Substituting the considered soil parameters given in Table 2 into Eq. 1 through Eq. 3, the spring and damper parameters used in ANSYS are calculated and given in Table 3.

Table 3. Property of Springs and Dampers

Directions of degree of freedom	Stiffness coefficients	Damping coefficients	Mass of springs
Horizontal direction	1.34E+08 N/m	7.12E+06 N·s/m	1.08E+05 Kg
Vertical direction	1.68E+08 N/m	1.31E+07 N·s/m	3.85E+05 Kg
Rotational direction	2.80E+09 N·m	7.20E+07 N·s·m	5.70E+06 Kg·m^2
Torsional direction	3.73E+09 N·m	5.25E+07 N·s·m	1.43E+06 Kg·m^2

3. SEISMIC ANALYSIS PROCEDURES

3.1 Modal Analysis

The basic vibration characteristics of the wind turbine system are first determined through modal analysis, where the Lanczos Block method was adopted. The comparisons of the natural frequencies of the wind turbine system with and without considering the SSI effect are given in Table 4. As shown in Figure 5, the first mode vibration is governed by flexural deformation of the tower along with the blades flap-wise motion (in X-Direction), and the second mode vibration is featured by the lateral bending vibration (in Y-Direction) of the tower along with the blades flap-wise motion. The third and fourth mode shapes mainly involve local vibration of the blades. The modal analysis results imply that a coupling model including the blades and tower should be adopted in the dynamic analysis of wind turbine systems in order to obtain accurate results. In general, the natural frequencies considering the SSI effect are smaller than the corresponding values without considering the SSI effect.

Table 4. Comparison of Frequencies of Models with &without Considering SSI Effect

Mode number	Frequency (Hz)		Difference /%
	Without considering SSI effect	Considering SSI effect	
1	0.345	0.328	2.27
2	0.402	0.380	3.43
3	0.411	0.403	1.95
4	0.425	0.410	3.53
5	0.994	0.971	2.31
6	1.472	1.342	8.83
7	2.032	1.353	33.3
8	2.063	1.362	33.9
9	2.446	1.381	43.4
10	2.502	1.417	43.3

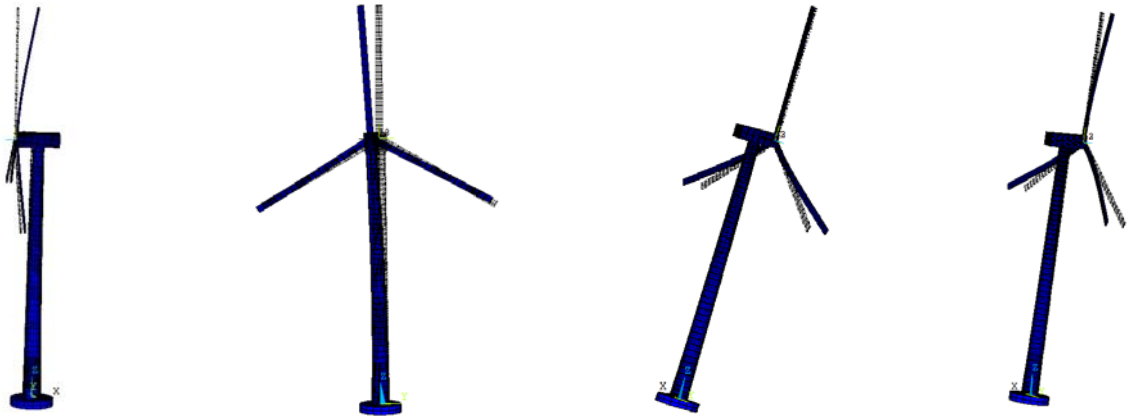

(a) (b) (c) (d)

Figure 5. The First Four Modal Shapes of the Wind Turbine Towers:
a) The first-order modal shape; b) The second-order modal shape;
c) The third-order modal shape; d) The fourth-order modal shape

3.2 Resonance Analysis

The purpose of performing resonance analysis is to avoid resonance when the tower is in operation. This requires that the structural natural frequencies should be sufficiently 'far away' from the external excitation frequency to ensure that structural dynamic response is within the controlled range. A common practice is that for wind turbine systems, all the natural frequencies f must stay away from the blade rotational frequency f_{1p} and blade passing frequency f_{np} (The subscript n is the number of blade), with the required differences larger than 10%. The number of the blade in this study is three, thus the blade-passing frequency f_{3p} is three times of the blade rotating frequency, namely, $f_{3p} = 3 f_{1p}$.

For the 1.25MW wind turbine system studied here, the working speed of the rotor is 9.6~17.8 r/min, and therefore the corresponding rotational frequency range is 0.16~0.29 Hz and the passing frequency range of the blade is 0.48~0.87 Hz. It is seen from Table 4 that these frequencies ranges stay away from the natural frequencies of the structure, and therefore, it can be concluded that no resonance will happen whether the SSI effect is taken into account or not. The comparisons of the natural frequencies against the rotating frequencies can also be done via the Campbell diagram shown in Figure 6.

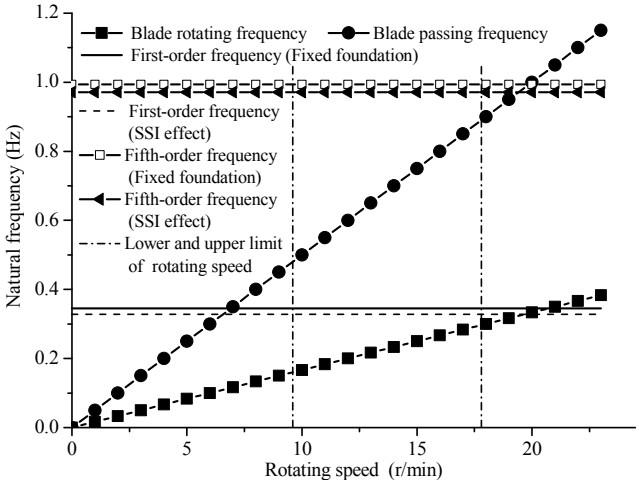

Figure 6. Campbell Diagram of Vibration in Wind Turbine System

3.3 Seismic Ground Motion Selection and Characteristic Comparisons

3.3.1 *Ground Motion Records Selection*

The EI-Centro (NS) wave, a typical bedrock wave which is widely used for seismic analysis, was chosen and two additional long-period seismic waves, namely, the HKD054 (EW) wave recorded in the Tokachi Oki earthquake in Japan in 2003 [20] and the CDAO (EW) wave recorded in the Mexico City of Mexico in 1985, were selected from the worldwide earthquake record database. The basic information of the three seismic waves is given in Table 5, and the acceleration time history curves of the three seismic waves are plotted in Figure 7. Hereafter, for ease of discussion, 'bedrock wave' stands for the EI-Centro (NS) wave, and the HKD054 (EW) wave and CDAO (EW) wave are referred as 'long-period waves'.

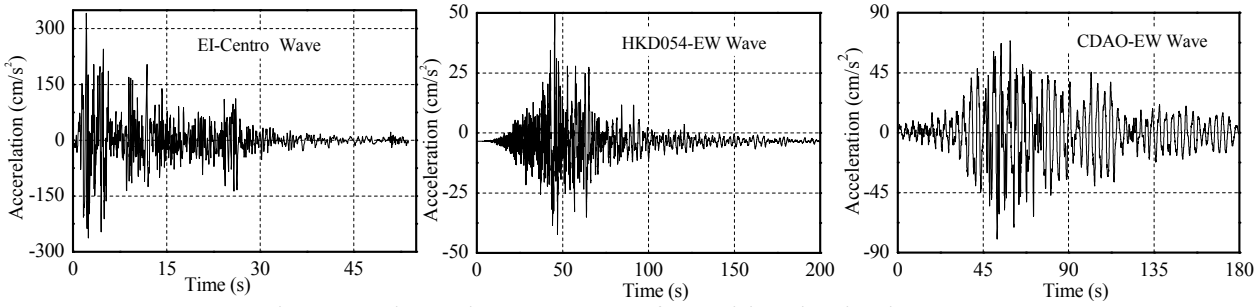

Figure 7. Time History Curves of Considered Seismic Waves

Table 5. Basic Information of Considered Seismic Waves

Earthquake wave	Magnitude	Date	Original record time (s)	Peak ground acceleration (gal)	Site classification
EI-Cento(NS)	6.4	6-Jun-1938	53.76	341.7	Ⅲ
HKD054(EW)	8.0	25-Sep-2003	213	50.53	Ⅳ
CDAO(EW)	8.1	19-Sep-1985	180	79.98	Ⅳ

It was considered that the site soil classification for the construction site of the wind turbine system is Ⅳ and the fortification intensity is Ⅶ [26]. For comparison purposes, the PGA of all the seismic waves was scaled to 35gal. For each seismic wave, three components were considered in the elastic time history analysis, and the accelerations along the horizontal principal direction (X-Direction), the lateral direction (Y-Direction) and the vertical direction were proportioned with the scaling coefficients of 1.0:0.85:0.65, respectively [26]. Raleigh damping was adopted in the structural model. The Rayleigh damping factor was calculated based on assigning 2% damping ratio to the first two modal frequencies. Due to the relatively long durations of the long-period seismic waves, a reduced duration of each wave was taken, starting from the time when 0.3PGA (peak ground acceleration) is first reached and ending when 0.3PGA last appears [33]. The main purpose of using reduced periods of seismic wave was to reduce the computational time, noting that the selected duration of seismic waves meets the relevant requirement for time history analysis [26]. No such reduction was made for the EI-Centro (NS) wave because the duration of the bedrock seismic waves is reasonably short. The time intervals and durations, for the analysis using, of the three seismic waves are illustrated in Table 6.

Table 6. Time Interval and Duration for Analysis of Considered Seismic Waves

Seismic Wave	EI-Centro(NS)	HKD054(EW)	CDAO(EW)
Time internal (s)	0.02	0.01	0.005
Duration (s)	53.76	42.20	79.72

Apart from the seismic excitation, gravity load and wind load were also taken into account in the analysis. It was assumed that the wind turbine system is in shutdown state when earthquake happens, and therefore the dynamic effect of rotating blade was not considered. The gust loading factor (GLF) method [34] was used to obtain the equivalent static wind load, i.e. mean wind load multiplied by a gust loading factor. It is worth mentioning that the gust-loading factor was obtained by a spectrum analysis method adopting the wind-induced random vibration theory along the wind direction. The calculated results of GLF and equivalent static wind load are detailed in Appendix A. In this study, the wind load was only applied in the X-direction, and therefore the modeling results obtained from the X-direction are used to reflect an extreme structural response where the maximum wind load and the earthquake occur concurrently. No wind load is applied in the Y-direction, and therefore the Y-direction response can be used to discuss the sole influences of earthquake characteristics. Multi-core parallel computing technology was adopted in the computing process.

3.3.2 *Basic Characteristics of Selected Ground Motions*

The frequency characteristics of the selected ground motion records can be shown with Fourier spectrums using the fast Fourier transform (FFT) method, as shown in Figure 8.

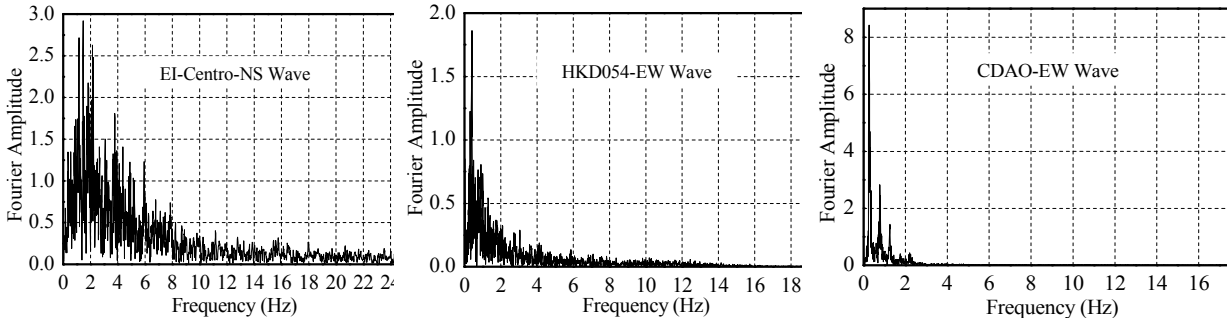

Figure 8. Fourier Frequency Spectrums

It can be seen that dominating frequency components are approximately distributed in 0.4-6 Hz for the EI-Centro (NS) wave. However, the dominating frequency ranges of the HKD054 (EW) and CDAO (EW) waves are approximately 0.2-1.3Hz and 0.22-0.8Hz, respectively. It is worth noting that the basis for determining the dominating frequency ranges for three seismic waves is that the ratio of area covered by the dominating frequency ranges to the total area of the Fourier amplitude spectrum reaches 80% in this study. Being different from the bedrock wave which involves significant high frequency components, the long-period waves are mainly governed by low frequency components. This may cause more significant seismic response for structures with long periods.

The response spectrums, as shown in Figure 9 in a normalized manner, can further reflect such dynamic characteristics of the selected seismic waves [22]. Here, the dynamic magnification factor is defined as the acceleration response spectrum normalized by the peak ground acceleration (PGA) value.

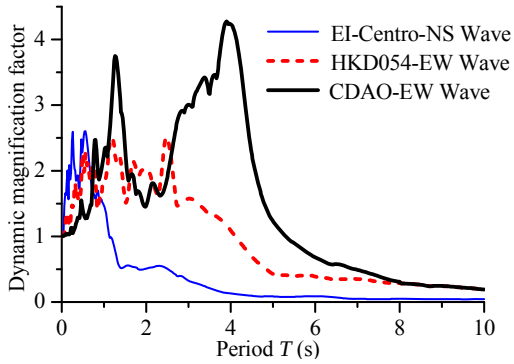

Figure 9. Acceleration Response Spectrums (ξ=0.02)

4. SEISMIC ANALYSIS RESULTS

4.1 Displacement Response

Considering both cases of fixed (rigid) foundation and that considering the SSI effect, the comparisons of the maximum height-wise displacements (in three directions) of the towers under the excitation of the bedrock and long-period seismic waves are shown in Figure 10. Some key response values are provided in Table 7. For ease of discussion, F model denotes the one with fixed (rigid) foundation, and S model refers to the one with 'elastic foundation', i.e. considering the SSI effect.

Table 7. Comparison of Maximum Displacements in Three Directions

Seismic Wave	The maximum displacement in X-Direction (mm)	The maximum displacement in Y-Direction (mm)	The maximum displacement in Z-Direction (mm)
EI-Centro-NS	890.36	25.53	32.01
HKD054-EW(F Model)	920.41	124.67	33.32
CDAO-EW(F Model)	984.14	65.64	35.76
HKD054-EW(S Model)	1170.95	111.72	38.46
CDAO-EW(S Model)	1239.53	147.31	40.89

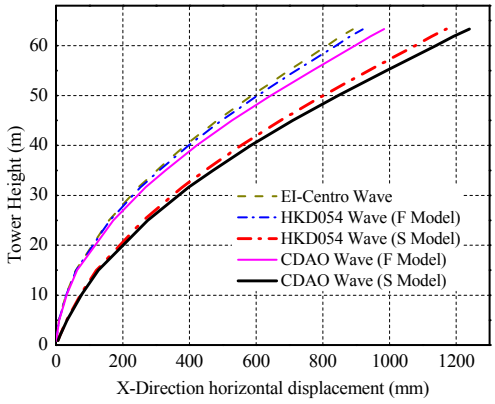

(a)

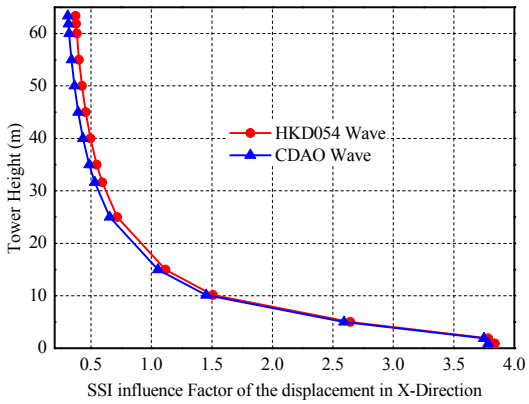

(b)

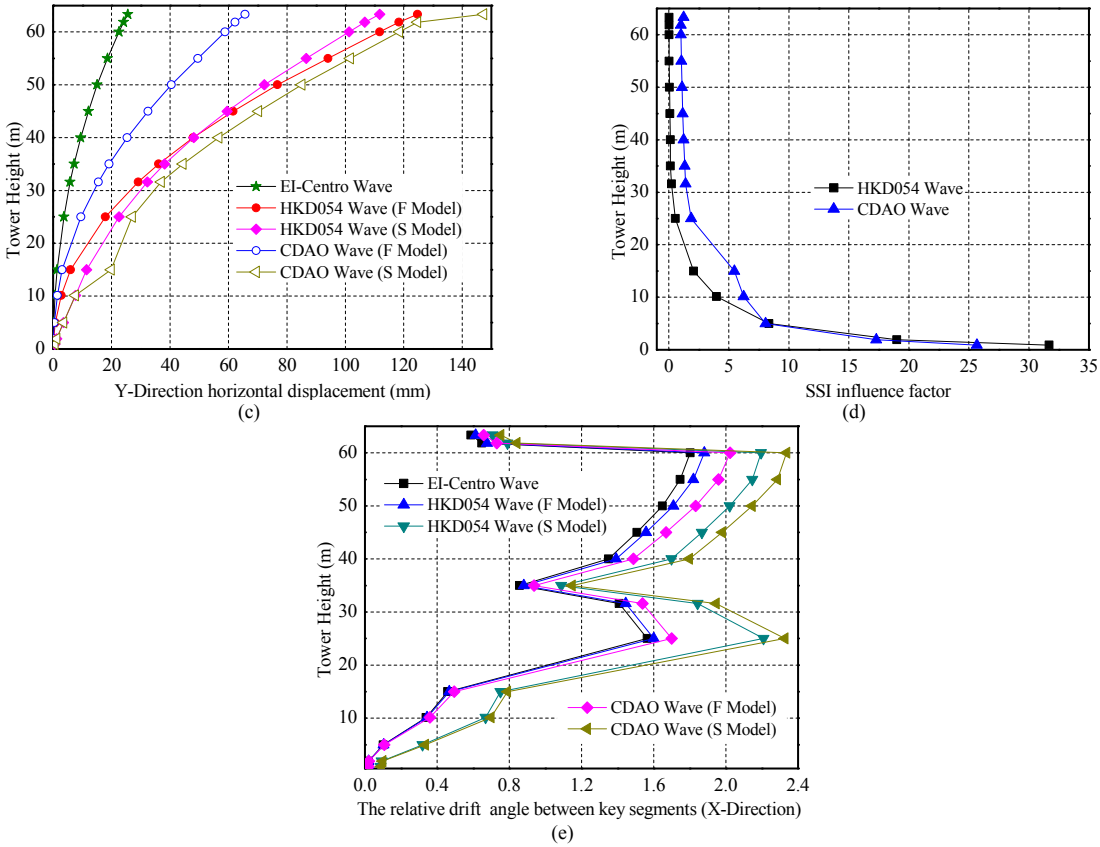

Figure 10. Nodal Displacement Analysis Results: a) Envelope Diagram of Horizontal Displacement in X-Direction; b) Variation of SSI Influence Factor (X-Direction); c) Envelope Diagram of Horizontal Displacement in Y-Direction; d) Variation of SSI Influence Factor (Y-Direction); e) Distribution of Drift Angle between Segments along Tower Height

It can be seen from Figure 10a and Figure 10c that with increase in height, the maximum nodal displacements in the two directions gradually increase, where the maximum displacement is observed at the tower top. Moreover, the displacement responses induced by the long-period seismic waves are obviously greater than the corresponding values caused by the bedrock seismic wave, especially at the top of the tower (see Table 7). Taking the deformation response along the Y-Direction for instance (F models), the maximum displacements induced by the long-period seismic waves can be 4.9 times of the corresponding values caused by the bedrock seismic wave. Due to the presence of the equivalent wind load applied along the X-Direction, the influence of the seismic wave types on the maximum nodal displacement in the X-Direction seems to be less pronounced. In general, the maximum top displacement (in X-Direction) under the combined wind and seismic action can reach nearly 1.0 m (see Figure 10a) when the tower is subjected to long-period seismic waves. Another issue that needs to be carefully addressed is the risk of pounding (between the blades and the tower) which can severely damage the entire wind turbine system (see Figure 11a), especially when the tower is in operation during an earthquake. Figure 11b and Figure 11c show the minimum gap between the blades and the tower during the considered earthquakes, taking account of the wind effect. It is clearly seen that the long-period waves lead to more noticeable vibrations of the blades and thus smaller minimum blade-tower gaps. In particular, HKD054 wave (F Model) leads to a minimum gap of -0.08 m, indicating that pounding would occur when the tower is hit by the considered wind and seismic loads. No such risk is observed for the case of bedrock wave.

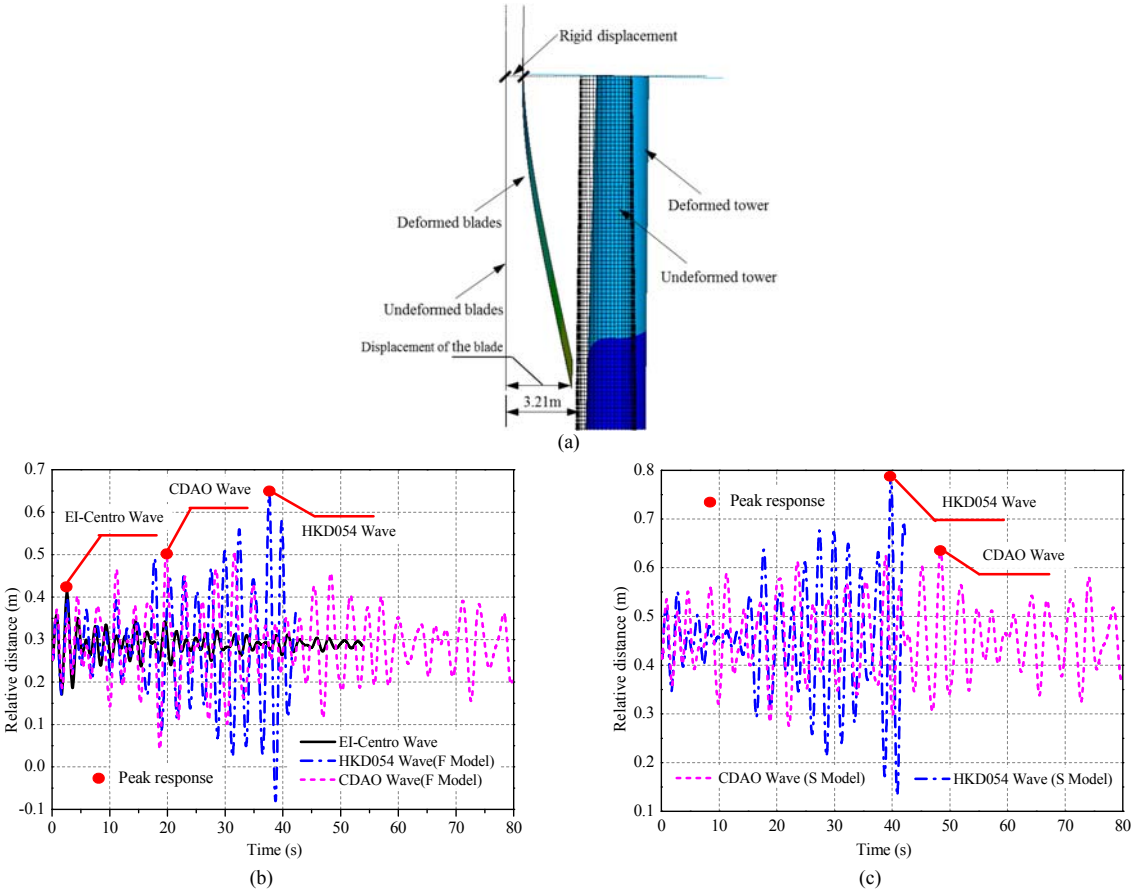

Figure 11. Relative Distance between the Blade Tip and the Tower: a) Illustration of Pounding between the Blades and the Tower; b) F Model Response; c) S Model Response

The displacement response is also affected by the SSI effect. In general, the nodal displacements of the towers including the SSI effect are larger than those without considering the SSI effect (see Figure 10a). When the SSI effect is considered, the maximum tower top displacement can achieve more than 1.2 m, corresponding to a drift level of approximately 2%. This drift level may cause failure of the foundation, leading to overturn of the tower. This effect should receive sufficient attention in future studies. In addition, the inclusion of the SSI effect may further exacerbate the influence of the long-period waves. As can be seen in Table 7, for the S-models, the maximum displacements induced by the long-period seismic waves can be 5.8 times that of the corresponding values caused by the bedrock seismic wave. This level of amplification is larger than that found in the F-models. This highlights the importance of considering the SSI effect for predicting the maximum deformation of the towers, especially when long-period seismic waves are considered. It is worth noting that the SSI effect seems to reduce the risk of pounding, as shown in Figure 11c. This is possibly due to the fact that the soil can help dissipate some input energy, leading to decreased vibration effect of the blades themselves. It is also of interest to see that some parts of the tower could have slightly decreased maximum deformation in Y-Direction when the SSI effect is included (under the HKD054-EW wave). This is because that the predominant frequency of the HKD054-EW record is closer to the second modal frequency of the F-model (compared with the S-model).

In order to more clearly show the influence of the SSI effect, a SSI influence factor, η, is defined by:

$$\eta = \frac{\text{Elastic foundation response value-Fixed foundation response value}}{\text{Fixed foundation response value}} \tag{4}$$

As indicated in Figure 10b and Figure 10d, for all the considered seismic waves, the influence of the SSI effect on the maximum nodal horizontal displacements at the lower part of the tower are significant. With increasing height, the influences of the SSI effect become less remarkable.

It can be observed in Figure 10e that the drift angle of key segments induced by the long-period waves are greater than the corresponding values for the case of bedrock wave, although a certain level of fluctuations can be observed. These fluctuations correspond to the stepped tube wall thickness variation locations as well as the locations where flexural stiffness change abruptly.

4.2 Acceleration Response

Apart from the displacement response, it is also necessary to investigate the acceleration response which may affect the functionality of electro-mechanical equipment. In this study, the structural acceleration response is presented by acceleration amplification coefficients, i.e. the ratio of maximum structural acceleration over the peak ground acceleration (PGA). The maximum acceleration amplification coefficients of the towers with and without considering the SSI effect are provided in Figure 12a through Figure 12c.

Table 8. Comparison of Maximum Acceleration Responses in Three Directions

Seismic Wave	The maximum acceleration in X-Direction (cm/s^2)	The maximum acceleration in Y-Direction (cm/s^2)	The maximum acceleration in Z-Direction (cm/s^2)
EI-Centro-NS	236.95	29.75	332.61
HKD054-EW(F Model)	275.66	88.36	614.02
CDAO-EW(F Model)	323.58	46.11	740.29
HKD054-EW(S Model)	268.38	64.86	612.66
CDAO-EW(S Model)	313.53	75.27	738.92

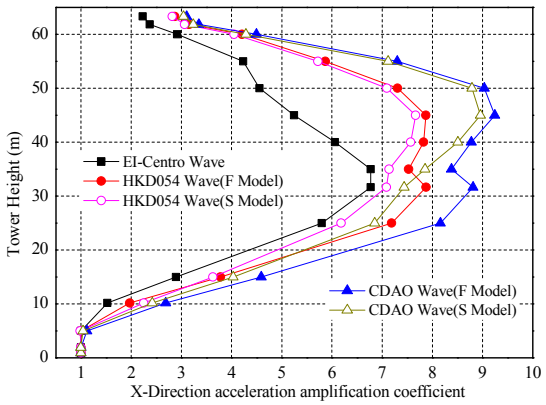

(a)

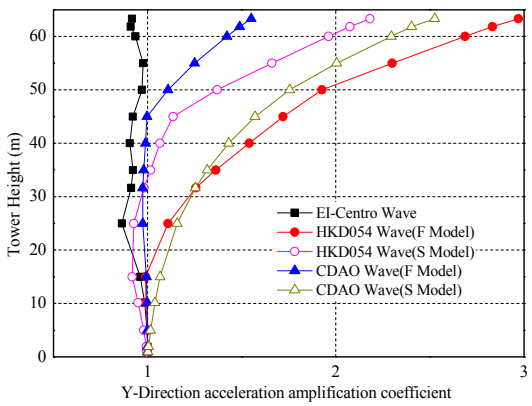

(b)

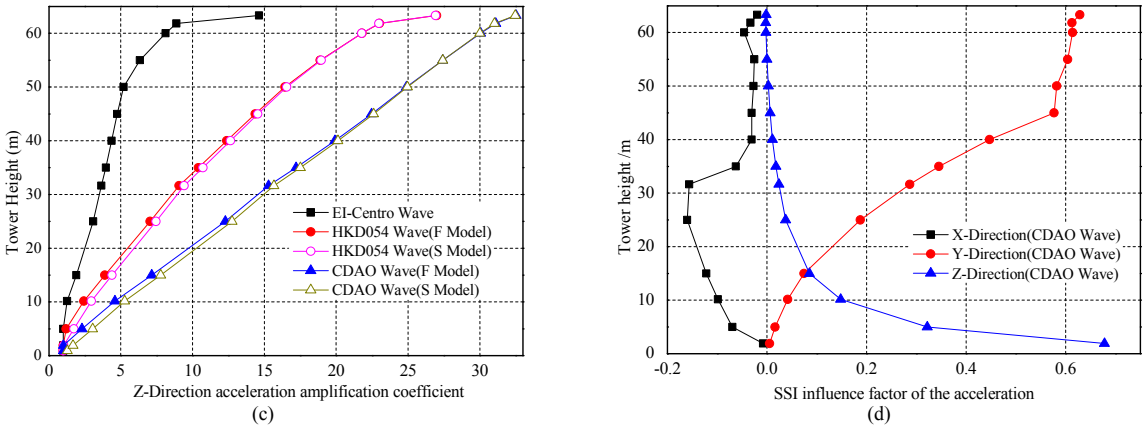

Figure 12. Acceleration Response Analysis Results: a) Envelope Diagram of Acceleration Amplification Coefficient (X-Direction); b) Envelope Diagram of Acceleration Amplification Coefficient (Y-Direction); c) Envelope Diagram of Acceleration Amplification Coefficient (Z-Direction); d) Variation of SSI Influence Factor (CDAO Wave)

It can be seen that the structural acceleration amplification coefficients induced by the long-period seismic waves are clearly larger than the corresponding values caused by the bedrock seismic wave, as detailed in Table 8. Taking the acceleration response along the Y-Direction for instance, the maximum acceleration response of the towers subjected to the long-period waves can be nearly 3 times that of the corresponding value for the case of the bedrock wave. In the X-Direction, at approximately 1/2-2/3 height of the tower, the acceleration amplification factor reaches its peak, and beyond this height the amplification coefficient starts to decrease. Similar behaviors were also reported by other researchers [15]. It is noted that at the top of the tower, the location of particular interest in terms of electric machine functionality, the maximum acceleration response (in the X-Direction) is not substantially increased when the long-period waves are considered instead of the bedrock wave. In the Y-Direction, the maximum acceleration response is slightly increased when the long-period waves are considered. This indicates that the maximum horizontal accelerations that the electric machines experience are not significantly influenced by the long-period waves. More attention needs to be paid for the acceleration in the vertical direction (i.e. Z-Direction), as the maximum height-wise accelerations in the Z-Direction increase apparently and the associated acceleration amplification is greater than those in the X and Y-Directions. At the top of the tower, the peak acceleration is 30 times more than the PGA under the long-period waves. This implies that the vertical earthquake action needs to receive sufficient attention in the design of wind turbine systems, especially when the tower is subjected to the long-period waves and the vertical acceleration at the tower top is of critical importance in design. Neglecting the vertical seismic action may lead to unsafe design.

The SSI effect tends to have inconsistent influence on the structural acceleration responses, as typically shown in Figure 12d. However, compared with the influence on nodal displacement (see Figure 10d), the influence of the SSI effect on acceleration is much less significant. Under certain conditions (e.g. HKD054-EW in X-Direction), the SSI effect tends to decrease the acceleration, and this is because that the soil could help dissipate some energy and thus to decrease the responses of the superstructure. It is noted that the maximum structural acceleration response is also affected by the relationship between the predominant frequency of the earthquake record and the critical modal frequencies of the structure, which explains the inconsistency of the SSI influence factors.

4.3 Stress Response

The height-wise maximum von Mises stresses (excluding the stress concentration effect near the door frame) of the tubular tower under the combined action of seismic load and wind load are shown in Figure 13a through Figure13c.

Table 9. Comparison of Height-wise Maximum Von Mises Stresses

Seismic Wave	The maximum von Mises stress (MPa)
EI-Centro-NS	209.77
HKD054-EW(F Model)	213.74
CDAO-EW (F Model)	226.65
HKD054-EW(S Model)	209.38
CDAO-EW (S Model)	224.47

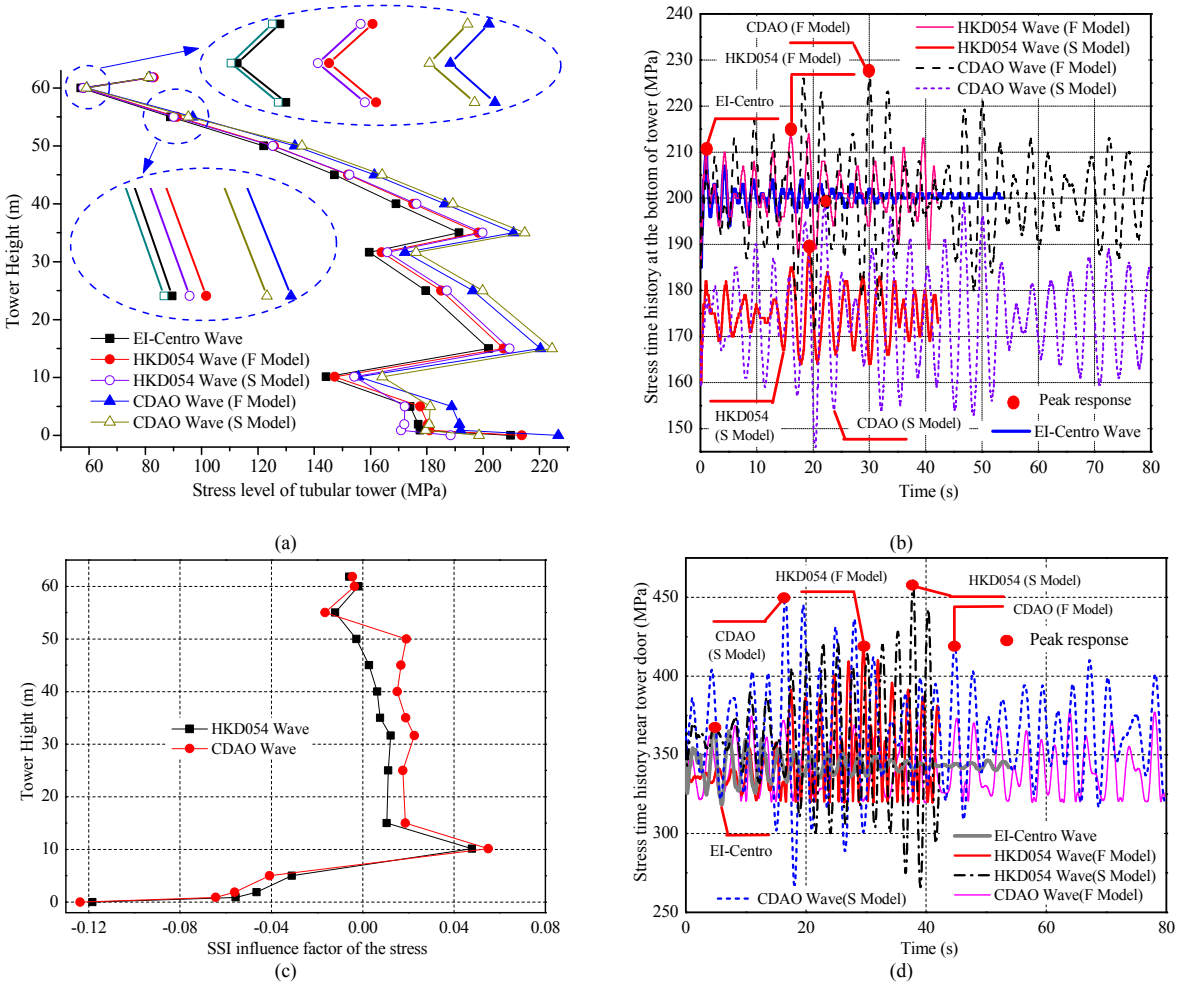

Figure 13. Stress Level Analysis Results: a) Stress Envelope Diagram of Tower along Height; b) Stress Time History at the Bottom of Tower; c) Variation of SSI Influence Factor on Stress; d) Stress Time History Near Tower Door

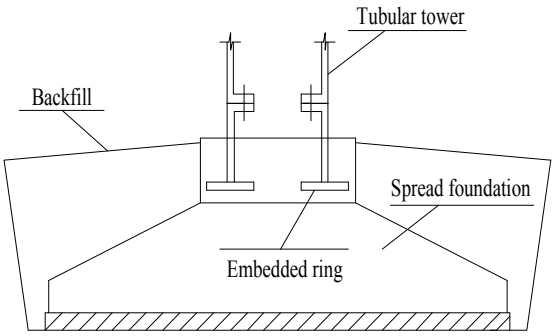

Figure 14. Typical Foundation of Wind Turbine Towers

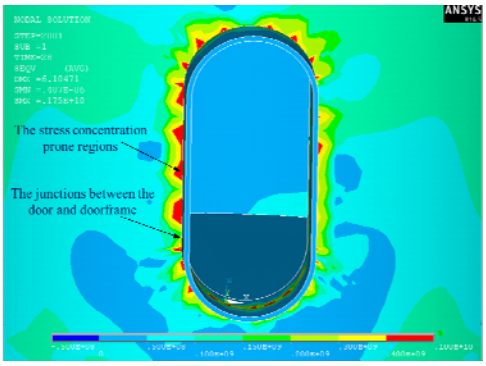

Figure 15. Stress Contour at the Junctions between Tower and Doorframe

Compared with the bedrock seismic wave, the long-period seismic waves could lead to higher stresses in the tower, as shown in Table 9.

In addition, as shown in Figure13a, compared with the case of fixed foundation, SSI effect could lead to slight decrease of the stress level near the foundation. As mentioned previously, this could be due to the extra energy dissipated by the surrounding soil. On the other hand, within the range between 15m and 50m of the tower height, the SSI effect can slightly increase the stress level. Moreover, with increase in height, the influence of the SSI effect on stress level decreases (see Figure 13c). In general, compared with the displacement and acceleration response, the influence of the SSI effect on stress response is much less significant.

For all the considered cases, the maximum von Mises stresses generally follow a decreasing trend with the increase of the tower height, although a certain level of fluctuations are observed. These fluctuations correspond to the stepped tube wall thickness variation locations as well as locations where the bending stiffness changes obviously. In general, the stress level along the height of the main body of the tower is within 230MPa, which is within the elastic range for normal constructional steel, and the stress distribution shows that the tapering design of the tower is quite economical in terms of material strength utilization.

Another important finding is that the local stress variation condition is more sensitive to the seismic waves and the SSI effect. The results given in Figure 13d show that the long-period waves could lead to increased level of stress concentration near the doorframe (see Figure 15). When the SSI effect is considered, the local stress near the doorframe is further increased, and the peak value could achieve nearly 460MPa. This indicates that the junctions between the tower and doorframe could experience significant stress concentration due to geometric discontinuity, and special attention needs to be paid to address this issue, especially when the long-period waves are considered.

4.4 Internal Forces

Based on the stress distributions, the internal forces, including base moment, base shear force, and axial force, of the tower can be extracted from the model.

Table 10. Comparison of Maximum Internal Force Responses

Seismic Wave	Shear force in X-Direction (kN)	Shear force in Y-Direction (kN)	Axial force in Z-Direction (kN)	Bending moment about X-axis (kN·m)	Bending moment about Y-axis (kN·m)	Torsion about Z-axis (kN·m)
EI-Centro	915.16	21.05	662.95	1107.51	44890.50	34.99
HKD054 (F Model)	928.64	91.74	924.32	5611.71	45761.25	125.35
CDAO (F Model)	976.68	52.77	1114.51	3012.01	48814.91	76.06
HKD054 (S Model)	927.27	64.50	933.81	3950.30	44142.22	137.20
CDAO (S Model)	971.31	80.50	1126.40	4750.53	46516.37	133.17

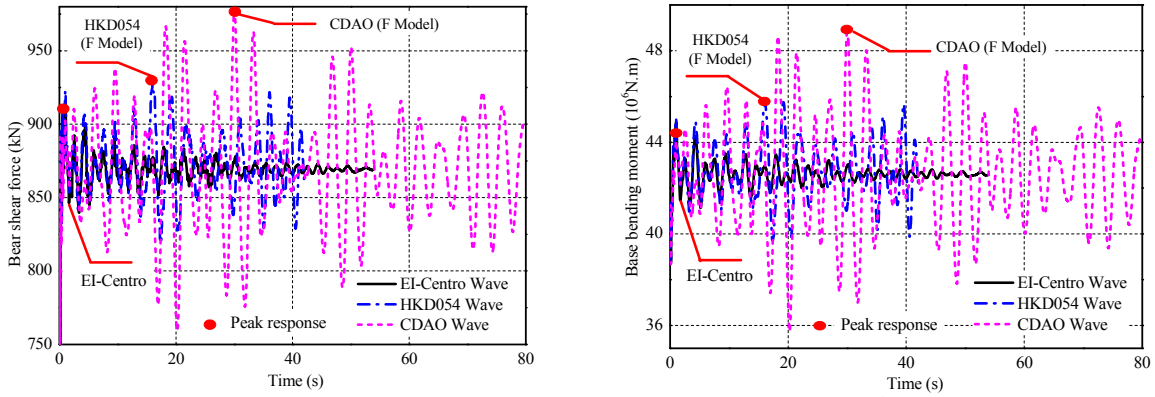

Figure 16. Base Internal Force Analysis Results: a) Base Shear Force Time History in X-Direction; b) Base Bending Moment Time History (about Y-axis)

Table 11. Comparison of spindle shear force responses

Seismic Wave	Shear force in Z-Direction (kN)	Shear force in Y-Direction (kN)	Resultant shear force (kN)
EI-Centro	634.24	14.28	634.41
HKD054(F Model)	781.07	67.33	783.97
CDAO(F Model)	864.15	35.85	864.89
HKD054(S Model)	797.56	47.09	798.95
CDAO(S Model)	884.15	57.29	886.01

According to Table 10 and Figure 16a through Figure 16b, the base shear forces, bending moments and torsions of the towers subjected to the long-period waves are greater than the results from the case of the bedrock wave. Taking the internal force responses along the Y-Direction for instance, the shear forces and bending moments (about X-axis) of the towers when subjected to the long-period waves are 2~5 times of the responses caused by the bedrock wave. It is noted that a similar degree of the increase in the displacement response is also observed. Due to the presence of the equivalent wind load applied along the X-Direction, the bending moment about Y-axis and the shear force along the X-Direction are quite significant. The combined moment and shear action may cause collapse of the towers if the foundation or the foundation embedded ring of the tower is not strong enough.

Another issue that needs to receive attention is the shear capacity of the spindle that links the blades to the nacelle (see Figure 3a). The vertical and horizontal vibrations of the tower in conjunction with the torsional effects could cause significant shear force at the spindle of the rotor. As can be seen in Table 11, the maximum shear force at the spindle generally exceeds 600 kN. The long-period seismic waves cause larger shear forces onto the spindle of the rotor, and the SSI effect could further increase this shear effect. It is worth mentioning that if the tower is in operation

during the earthquake, the rotating blades could cause an even larger dynamic shear force applied onto the spindle of the rotor. This cautions that if the shear force is too large, fracture of the spindle could happen.

5. PRELIMINARY DESIGN AND ANALYSIS ADVICE

Based on the information obtained from the finite element analysis, the fundamental seismic performances of the wind turbine tubular towers under long-period ground motions with the consideration of the SSI effect are understood, and some issues are also identified. Based on the research findings, some preliminary design comments are given as follows.

5.1 Door Frame

It can be seen from the analysis results that the junctions between the doorframe and tower door experience high stress levels (due to stress concentration). As a result, the weld of the doorframe may experience low-cycle fatigue failure during earthquakes and also potentially high-cycle fatigue failure under the wind action [35]. These areas may need to be strengthened locally if the tower is required to behave elastically during a design earthquake. Alternatively, an optimization study, examining the influences of varying geometric configurations of the door, may be performed to minimize the stress concentration effect near the doorframe. This is worth future investigations.

5.2 Foundations

The current study reveals that under a combined strong wind and seismic action, especially when the long-period waves are considered, considerably large displacement response can be induced at the top of the tower, noting that this is the location where the mass is concentrated. This displacement is further enlarged due to the SSI effect. This warns that overturn failure is a potential risk for towers located at soft soil regions. In recent years, the majority of the manufacturers adopt the embedded ring to connect the tubular tower and the foundation (see Figure 14). Although the peak stress for the current model is within the elastic range, a more severe earthquake may cause failure of the foundation, originating from the embedded ring. In fact, a number of overturn failures of such wind turbine towers have been reported [36]. Considering this, appropriate construction detailing may need to be applied to strengthen this “weak area”. To fix this problem, the recently developed prestressed-anchor foundation and prefabricated prestressed cylinder foundation, as shown in Figure 18, may be used, noting that the latter foundation form was specifically developed for soft soil regions.

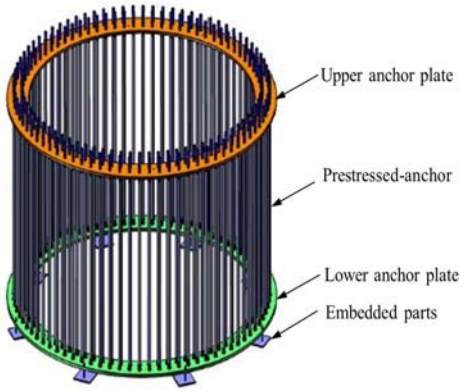

(a) A beam-slab prestressed-anchor foundation

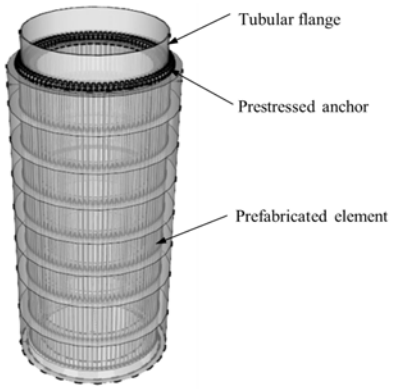

(b) A prefabricated prestressed cylinder foundation

Figure 18. New-type Foundation Forms for Wind Tubular Towers (http://www.goldenocean.cc/index.asp)

5.3 Ground Motion Selection and SSI Effect

Based on the current analysis results, SSI effect can amplify the structural responses (e.g. displacement, torsion effect, and axial force) under certain circumstances. With numerous wind turbine systems constructed in the soft soil regions, simplifying the foundation as a fixed constraint may be unsafe. In addition, the long-period seismic waves in the far field soft soil regions can also significantly increase the structural responses and the risk of pounding between the blades and the tower. In view of this, long-period seismic waves in conjunction with the SSI effect should be considered in the seismic design of the wind turbine systems in soft soil regions.

6. SUMMARY AND CONCLUSIONS

In this paper, an integrated finite element model consisting of rotor, nacelle, tower and foundation was established. To investigate the influence of long-period seismic waves and SSI effect on structural dynamic performances, two comparative models were built, and modal analysis, resonance analysis, and seismic time history analysis were conducted. Based on the numerical simulation results, the main conclusions are drawn as follows:

1) Considering the SSI effect can reduce the natural frequency of the wind turbine system. Therefore, the SSI effect should receive sufficient attention, especially when the towers are located in soft soil regions. Moreover, in order to capture some key responses including shear forces of the spindle and the risk of pounding, it is recommended that a coupling model including both the blades and tower is adopted in dynamic analysis of wind turbine towers.
2) The maximum displacement, acceleration, stress level and internal force responses of the tower subjected to the long-period seismic waves are significantly larger than the values obtained from the bedrock seismic wave. The long-period waves can also increase the risk of pounding between the blades and the tower. Therefore, long-period seismic waves are suggested to be considered in seismic design of such towers.
3) The influence of the SSI effect depends on a number of factors including the fundamental characteristic of the seismic wave and the modal frequencies of the tower itself. In general, the influences of the SSI effect on the maximum acceleration, stress level, and internal forces are not significant, whereas the maximum displacement response is much more sensitive to the SSI effect.
4) The acceleration amplification coefficients in the vertical direction are quite large, especially when the tower is subjected to long-period waves. As a result, neglecting the vertical seismic action

in seismic dynamic response analysis may lead to unsafe design, especially for electro-mechanical equipment functionality.

5) Adequate attention should be paid to the bottom part of the tower as well as the door regions. When the long-period waves are considered, the bending moment, shear force and von Mises stresses at the tower base section are apparently increased, and significant stress concentration effect can be observed near the doorframe. Appropriate strengthening approaches may be needed to decrease the stress demand at these critical locations, and thus to avoid extensive yielding as well as potential fatigue issues.

Finally, it is worth mentioning that the effect of the rotating blades is not considered in this paper. With the rotating blades disturbing the air flow, the wind field can be more complex. In future studies, a more accurate rotating wind speed spectrum model may be established for the dynamic response and fatigue analysis. Moreover, refined models should be established for the nacelle and flange plates to understand the dynamic response at these connection locations of the different components.

ACKNOWLEDGEMENTS

The authors wish to thank the Ministry of Science and Technology of China for financially supporting the research in the study through the Grant No. SLDRCE14-B-04. The authors would also like to thank Pacific Earthquake Engineering Research Center (PEER), National Research Institute for Earth Science and Disaster Prevention (NIED), Center for Engineering Strong Motion Data (CESMD) and U.S. Geological Survey (USGS) for their earthquake records provided.

REFERENCES

[1] Bilgili, M., Yasar, A. and Simsek, E., “Offshore Wind Power Development in Europe and its Comparison with Onshore Counterpart”, Renewable and Sustainable Energy Reviews, 2011, Vol.15, No.2, pp.905-915.

[2] Burton, T., Sharpe, D. and Jenkins, N., “Wind Energy Handbook”, New York: John Wiley & Sons, 2011, 2nd Section, pp. 1-7.

[3] Zhu, L., “Seismic Response of Wind Turbine in the Parked and Operating Conditions”, Departing of Civil Engineering, the University of Tokyo, Ph.D. Dissertation, 2007, pp.1-4.

[4] Lobitz, D. W., “A nastran-based Computer Program for Structural Dynamic Analysis of Horizontal Axis Wind Turbine”, Proceedings of the Horizontal Axis Wind Turbine Technology Workshop, Ohio, USA, 1984, Vol. 13, pp. 1-10.

[5] Bazeos, N., Hatzigeorgion, G. D., Hondros, I. D.,et al, “Static, Seismic and Stability Analyses of a Prototype Wind turbine Steel Tower”, Engineering Structures, 2002, Vol. 24, No. 8, pp. 1015-1025.

[6] Lavassas, I., Nikolaidis, G., Zervas, P., et al, “Analysis and Design of the Prototype of a Steel 1-MW Wind Turbine Tower”, Engineering Structures, 2003, Vol. 25, No. 8, pp. 1097-1106.

[7] Witcher, D., “Seismic Analysis of Wind Turbine in the Time Domain”, Wind Energy, 2005, Vol. 8, No.1, pp. 81-91.

[8] Murtagh, P. J., Collins, R., Basu, B., et al, “Dynamic Response and Vibration Control ofWind Turbine Towers”, Irish Engineers Journal, 2004, Vol. 58, No. 7, pp. 1-7.

[9] Murtagh, P. J., Basu, B. and Broderick, B. M., “Along-wind Response of a Wind Turbine Tower with Blade Coupling subjected to Rotationally Sampled Wind Loading”, Engineering Structures, 2005, Vol. 27, No. 8, pp. 1209-1219.

[10] Zhao, X. and Maißer, P., "Seismic Response Analysis of Wind Turbine Towers Including Soil-structure Interaction", Proceeding of the Institution of Mechanical Engineers, Part K: Journal of Multi-body Dynamics, 2006, Vol. 220,No. 1, pp.53-61.

[11] Zhao, X., Maißer, P. and Wu, J., "A New Multibody Modelling Methodology for Wind Turbine Structures using a Cardanic Joint Beam Element", Renewable Energy, 2007. Vol. 32, No. 3, pp. 532-546.

[12] Prowell ,I., Elgamal, A., Uang, C. and Jonkman, J., "Estimation of Seimic Load Demand for a Wind Turbine in the Time Domain", Proceeding of European Wind Energy Conference, Brussels, Belgium, 2010, Report No. NREL/CP 500, 47536.

[13] Díaz, O. and Suárez, L. E., "Seismic Analysis of Wind Turbines", Earthquake Spectra, 2014, Vol. 30, No. 2, pp. 743-765.

[14] Taddei, F. and Meskouris, K., "Seismic Analysis of Onshore Wind Turbine including Soil-structure Interaction Effects", Seismic Design of Industrial Facilities, 2014, pp. 511-522.

[15] Alati, N., Failla, G. and Arena, F., "Seismic Analysis of Offshore Wind Turbines on Bottom-fixed support Structures", Phil. Trans. R. Soc. A, 2015,Vol. 373, No. 2035, doi: 10.1098/rsta.2014.0086.

[16] Fang, C., Yam, M.C.H., Lam, A.C.C. and Xie, L., "Cyclic Performance of Extended End-plate Connections Equipped with Shape Memory Alloy Bolts", Journal of Constructional Steel Research, 2014, Vol. 94, pp. 122-136.

[17] Yam, M.C.H., Fang, C., Lam, A.C.C. and Zhang, Y.Y., "Numerical Study and Practical Design of Beam-to-column Connections with Shape Memory Alloys", Journal of Constructional Steel Research, 2015, Vol. 104, pp. 177-192.

[18] Karakalas, A.，Machairas, T.，Solomou, A.，Riziotis, V. and Saravanos, D., "Morphing Airfoil with Shape Memory Alloy Wire Actuators for Active Aerodynamic Load Control in Large Wind-Turbine Blades", EWEA 2015 Annual Event Conference, Paris, France, 2015.

[19] Yan, S., Yu, J. Y., Niu, J., and Wang, W., "Wind-induced Vibration Control of Wind Turbine Tower Structures based on Shape Memory Alloys", Journal of Disaster Prevention and Mitigation Engineering, 2016, Vol. 36, No. 1, pp. 159-164.

[20] Koketsu, K., Hatayama, K., Furumura, T., et al, "Damaging Long-period Ground Motions from the 2003 Mw 8.3 Tokachi-oki, Japan Earthquake", Seismological Research Letters, 2005, Vol. 76, No.1, pp. 67-73.

[21] Faccioli, E., Paolucci, R. and Rey, J., "Displacement Spectra for Long Periods", Earthquake Spectra, 2004, Vol. 20, No. 2 , pp. 347-376.

[22] Faccioli, E., Cauzzi, C., Paolucci, R., et al, "Long Period Strong Ground Motion and its Use as Input to Displacement Based Design", Earthquake Geotechnical Engineering, 2007, Vol. 6, pp. 23-51.

[23] Chung, Y. L., Nagae, T., Hitaka, T., et al, "Seismic Resistance Capacity of High-Rise Buildings Subjected to Long-Period Ground Motions: E-Defense Shaking Table Test", Journal of Structural Engineering, ASCE, 2012, Vol. 136, No. 6, doi:10.1061/(ASCE)ST.1943-541X.0000161.

[24] Ariga, T., Kanno, Y. and Takewaki, I., "Resonant Behaviour of Base-isolated High-Rise Building under Long-period Ground motions", The Structural Design of Tall and Special Buildings, 2005,Vol. 15,No. 3, pp. 325-338.

[25] BS EN 1998-1, "Eurocode 8: Design of Structures for Earthquake Resistance: Part 1: General Rules Seismic Actions and Rules for Buildings", Brussels: European Committee for Standardization, 2011.

[26] GB 50011-2010, "Code for Seismic Design of Buildings", Beijing: Ministry of Construction of the People's Republic of China, 2010.[in Chinese].

[27] ANSYS, Release 14.5, User's Manual, "Structural Analysis Guide", ANSYS Inc., 2012.

[28] Germanischer Lloyd (GL), “Guideline for the Certification of Wind Turbines: Part 5: Strength Analyses”, Hamburg, Germany, 2003.

[29] Wolf, J. P., “Spring-dashpot-mass models for foundationvibrations”, Journal of Earthqake Engineering and Structural Dynamics, 1997, Vol. 26, No. 9, pp. 931-949.

[30] Richart, F. E., Hall, J. R. and Woods, R. D., “Vibration of Soils and Foundations”, New York: Prentice-Hall, 1970, pp. 191-243.

[31] Ma, H.W., “Seismic Analysis for Wind Turbines including Soilstructure Interaction Combining Vertical and Horizontal Earthquake”, Proceedings of 15th World Conference on Earthquake Engineering, Lisbon, Portugal, 2012, pp. 336-345.

[32] Mulliken, J. S. and Karabalis, D.L., “ Discrete Model for Dynamic through-the-soil Coupling of 3-D Foundations and Structures”, Earthquake Engineering & Structural Dynamics, 1998, Vol. 27,No. 7, pp. 687-710.

[33] Watson, J. A. and Abrahamson, N. A., “Selection of Ground Motion Time Series and Limits on Scaling”, Soil Dynamics and Earthquake Engineering, 2006, Vol. 6 , No. 5, pp. 477-482.

[34] Davenport, A. G., “Gust Loading Factors”, Journal of the Structural Division, ASCE, 1967, Vol. 93, No.3, pp. 11-34.

[35] DIN EN 50308 Berichtigung 1 and VDE 0127-100 Berichtigung 1, “Wind Turbines-Protective Measures-Requirements for Design, Operation and Maintenance”, Berlin: Deutsches Institut für Normung, 2008.

[36] Agbayani, N. A., “Defects, Damage, and Repairs subject to High Cycle Fatigue: Examples from Wind Farm Tower Design”, Forensic Engineering Congress 2009: Pathology of the Built Environment, ASCE, 2009, pp. 546-555.

[37] GB 50009-2012, “Load Code for the Design of Building Structures”, Beijing: Ministry of Construction of the People’s Republic of China, 2012.[in Chinese].

Appendix A.

The calculated results of the gust loading factor (GLF) and the Equivalent static wind load

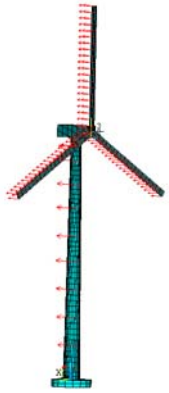

Figure 19. Wind Load on Wind Turbine Towers

According to the load code for the design of building structures [37], the basic wind pressure for the construction site of the wind turbine towers is 0.55 kN/m^2. In addition, the surface roughness classification is A. Moreover, the Simiu spectrum is adopted to obtain the wind-induced response in this study and the peak value factor is 2.2. Here, the blade parallel to the Z-axis is defined as blade 1, the other two blades are called blade 2 and blade 3 along the counter-clockwise direction. It is noted that the GLF values and the equivalent static wind load of the blade 2 are the same as those of the blade 3.

Table 12. GLF Value and Equivalent Static Wind Load of the Tower Body

Height (m)	3.32	9.95	16.59	23.22	29.89	36.50	43.13	49.76	56.40	59.72
GLF	2.114	2.128	2.141	2.153	2.165	2.177	2.191	2.204	2.221	2.238
the equivalent static wind load (kN)	31.256	39.243	42.643	44.342	45.069	45.137	44.752	43.973	42.903	42.429

Table 13. GLF Value and Equivalent Static Wind Load of the Blade 1

Height (m)	GLF	The equivalent static wind load (kN/m^2)
64.95	2.244	3.228
66.56	2.248	3.253
68.17	2.251	3.277
69.78	2.256	3.301
71.39	2.259	3.325
72.99	2.264	3.349
74.60	2.267	3.372
76.21	2.271	3.395
77.82	2.276	3.418
79.43	2.280	3.441
81.04	2.283	3.464
82.65	2.288	3.487
84.26	2.292	3.509
85.86	2.297	3.532
87.47	2.301	3.554
89.08	2.304	3.576
90.69	2.308	3.598
92.30	2.313	3.620
93.91	2.317	3.641
95.52	2.322	3.663

Table 14. GLF Value and Equivalent Static Wind Load of the Blade 2 and Blade 3

Height (m)	GLF	The equivalent static wind load (kN/m^2)
62.54	2.238	3.191
61.73	2.237	3.178
60.93	2.235	3.166
60.12	2.233	3.153
59.32	2.231	3.140
58.52	2.229	3.127
57.71	2.227	3.114
56.91	2.225	3.101
56.10	2.223	3.088
55.30	2.222	3.075
54.49	2.220	3.061
53.69	2.218	3.048
52.89	2.216	3.034
52.08	2.214	3.021
51.28	2.212	3.007
50.47	2.211	2.993
49.67	2.209	2.979
48.86	2.207	2.965
48.06	2.205	2.951
47.25	2.203	2.937

USE OF DIFFERENT SHAPED STEEL SLIT DAMPERS IN BEAM TO COLUMN CONNECTIONS OF STEEL FRAMES UNDER CYCLING LOADING

Mehmet Alpaslan Köroğlu[1,*], Ali Köken[2] and Yunus Dere[1]

[1] *Dept. of Civil Engineering, Necmettin Erbakan Univ., Konya 42060, Turkey*
[2] *Dept. of Civil Engineering, Selcuk Univ., Konya 42075, Turkey*
**(Corresponding author: E-mail: makoroglu@konya.edu.tr)*

Received: 21 August 2017; Revised: 29 September 2017; Accepted: 1 November 2017

ABSTRACT: Following the Northridge and Kobe earthquakes, extensive research was conducted on the use of various materials and systems that will absorb the earthquake effects within the structure itself in order to improve the behavior of the steel structures under seismic effects. In this study, the use of seismic dampers at beam-column joints of steel-framed structures to prevent damage to the structural members by absorbing the energy of the lateral loads was investigated. Thus, it will be possible for the steel-framed structures to be put into service right after a damaging earthquake by only replacing the dampers attached to the joints as no damage will occur to the beams and columns. For this purpose, as a first step, dampers with ductile behavior were chosen through preliminary tests. Consistent with the results of the preliminary tests, a total of six full-scale corner beam-column joint test specimens were produced. Five specimens were attached various types of dampers in different sizes and one reference specimen was designed with regular end-plate connection.

After the evaluation of the test results, valuable data on the load carrying and energy consumption capacities, stiffness characteristics and the general behavior of the specimens were obtained. In the analytical part of the study, analyses of the selected specimens were performed through ANSYS finite elements software package. The analytical and experimental results were compared and have been found very consistent with each other.

Keywords: Beam-column joint, steel slit damper, steel frame, seismic damper, finite element

DOI: 10.18057/IJASC.2018.4.2.7

1. INTRODUCTION

Structures built throughout history were damaged by the earthquakes that caused devastating property damage and loss of lives. Therefore, different solutions to minimize the destructive effects of earthquakes were proposed with the impact of technological advances of the last century. Structural control mechanisms based on the principle of damping the seismic energy through non-structural members were developed. Among these members, metallic dampers are economical, easy-to-produce, and can effectively dissipate seismic energy through hysteretic behavior. The use of metallic dampers attracted the attention of researchers, especially after the unexpected damages to the joints of the steel framed structures in the Northridge (1994) and Kobe (1995) earthquakes [1]
Many types of metallic dampers have been developed so far. The most popular among these are stiff dampers which are called ADAS (Added Damping and Stiffness) [2]. These members are made of high ductility steel and usually attached to steel frames. When built in triangular shape and produced from mild steel, they are called TADAS (Triangular Added Damping and Stiffness) [3]. They are welded at the bottom and bolted at the top and attached to the beam-column joints. In addition to these, honeycomb dampers [4], buckling restrained braces [5], bell shaped metallic dampers, lead-added metallic dampers and pi dampers are also available [6]. Passive energy steel dampers which are created by opening holes on steel plates are called slit dampers [7]. Recently, these metallic dampers have become increasingly popular. Especially following the Northridge (1994) and Kobe

(1995) earthquakes, the use of passive energy dampers at different regions of steel structures became quite common. A variety of dampers in different shapes and sizes were used for this purpose.
Oh et al. [1], used slit dampers at steel beam-column joints for the first time in the literature. Performing four full scale beam-column joint experiments, the researchers managed to dissipate the energy of the applied cyclic loads without causing any damage to the columns and beams. They investigated the behavior of the steel dampers of different geometric shapes in IPE type steel beams under cyclic loadings, different from other researchers.

Steel slit dampers were used by many researchers in moment resisting frames and in the center of X bracings (Lee et al., [7], Chan and Albermani [8]). And slit dampers have been used at beam-column joints recently [1, 9-14].

In this study, the use of dampers attached to the beam-column joint of a moment resisting frame that provides resistance to earthquakes preventing damage to the column or beam by damping the effects of lateral loads was investigated. Dampers are welded plates having bolt holes at their top and bottom edges for easy installation. They are attached to the beam-column joint by bolting both to the bottom flange of the beam and to the gusset plate (lower split-T) of the column. Therefore, they can be easily replaced when they get damaged during an extensive earthquake. The slit dampers with lower split-T can also be replaced easily [1]. However, in this study, changing only the damper will be sufficient. Moreover, one damper was used for narrow flanged beams as opposed to using two dampers as in [1].

A two stage experimental research was conducted for the use of dampers at beam-column joints. First, preliminary tests were performed in order to determine the appropriate type of damper. Thus, nine dampers with different geometric shapes previously used at different locations of steel frames in the literature were considered and experimentally evaluated. In line with the test results, three types of dampers were selected to be used in the full scale steel beam-column joint tests which constitute the core of this study. The behavior of dampers with different geometric shapes was compared with each other and the experiments were modeled using finite element method.

2. MATERIAL AND METHOD

In this study, the use of dampers at beam-column joints of steel frames was investigated. The experimental part of the study was composed of two stages. In the first stage, a test system to apply shear force to the dampers was developed in order to investigate the behavior of the dampers having nine different geometric shapes subjected to cyclic loading. These experiments were referred to as preliminary tests in this study. In the second stage, based on the preliminary test results, the feasible damper types were determined. Afterwards, an experimental system for the tests of the full scale beam-column joints was created. The full scale tests were performed in order to investigate the use of dampers at beam-column joints.

3. TEST SPECIMENS USED IN THE PRELIMINARY TESTS AND THEIR PROPERTIES

In this section, the geometric shapes of the produced dampers were determined based on the dampers from the literature that were used at different locations of steel structures. In the preliminary tests, damper shapes were chosen based on the ones available in the literature that are located either at the joints where x-bracings meet the column and beams or at the foundation joints of columns. The dampers with the most suitable geometry for the full-scale beam-column joint tests were selected

regardless of their load bearing capacities. A rigid loading frame that can apply reversed-cyclic loads was developed as the testing apparatus of the preliminary tests.

One edge of the damper was fixed to one of the columns of the rigid frame by bolts whereas the other edge of the damper was bolted to the connector plate attached to the load cell and the hydraulic pump that can apply reversed-cyclic loading. (Figure 1).

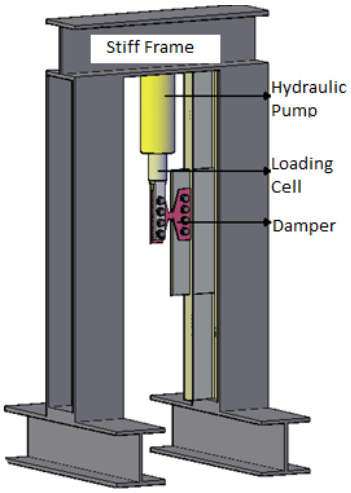

Figure 1. Test Apparatus used in the Preliminary Tests

Three steel specimens made of St-37 type steel material and complying with the European standards were tested. The results obtained from the tensile tests are listed in Table 1. In Figure 2, various types of dampers considered during the preliminary tests are presented. At the end of the tests, considering the ductility, loading bearing capacity and stability of these geometric shapes, the decision was made for the use of three dampers displayed in Figure 3 which are called slit, L-shaped and round-hole type dampers.

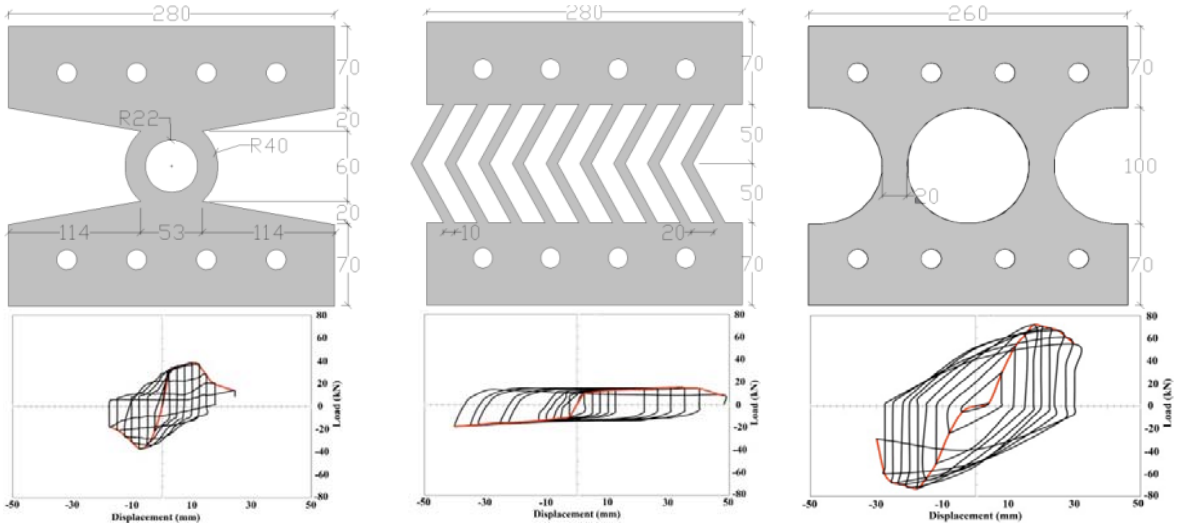

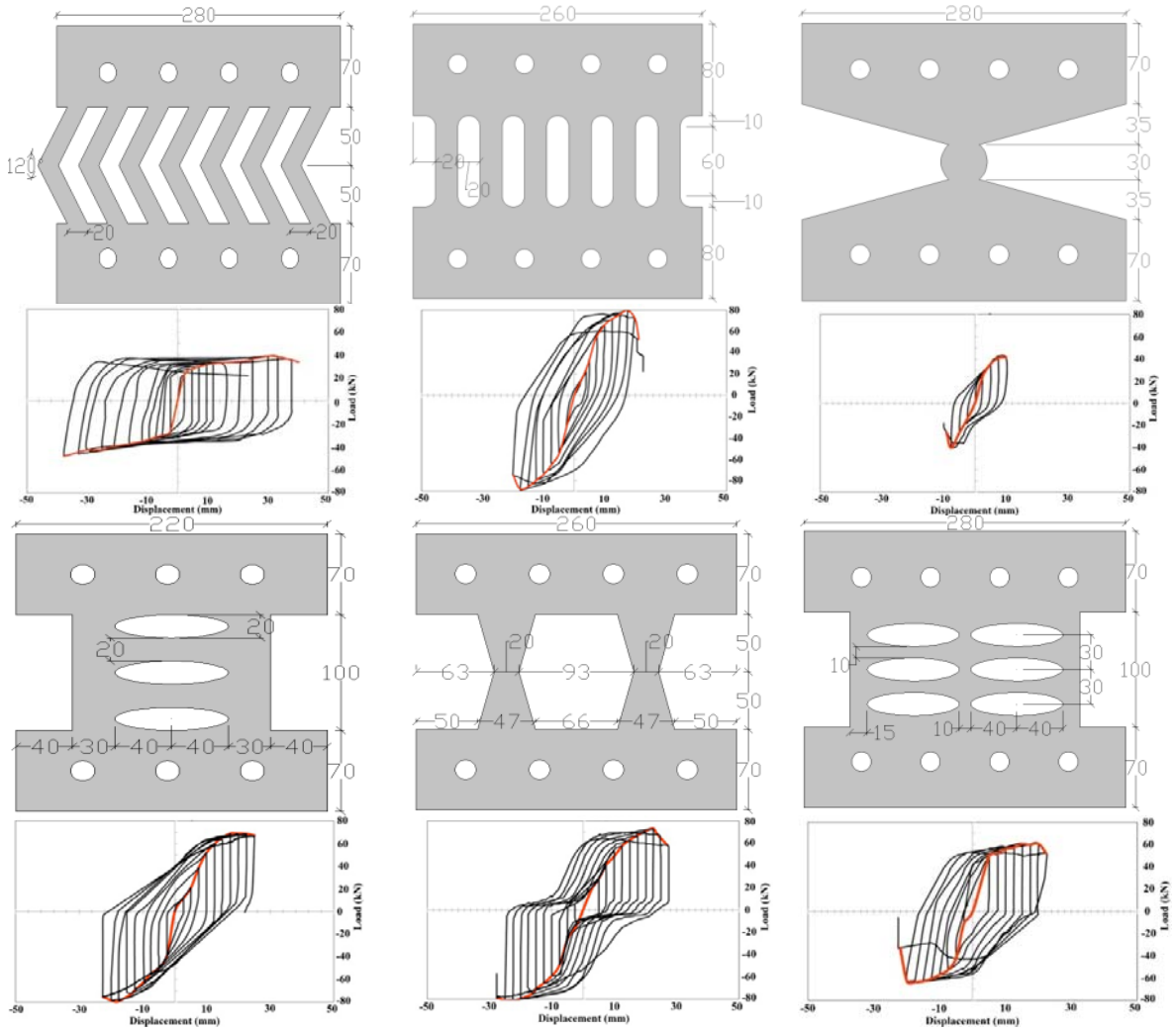

Figure 2. Various Types of Dampers Considered during the Preliminary Tests (Koroglu 2011,2012)

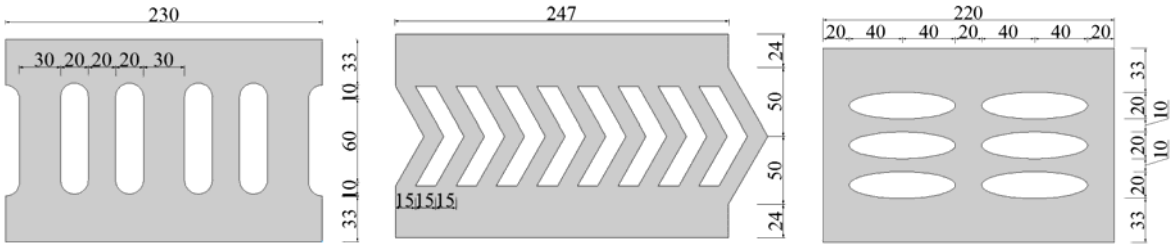

slit damper L-shaped round hole

Figure 3. Damper Types Determined after the Preliminary Tests

Table 1. Tensile Test Results of Steel Material used in the Preliminary Tests

Test No	**Width** (mm)	**Thickness** (mm)	**Elasticity Module** (MPa)	**Yielding Stress** (MPa)	**Max Stress** (MPa)	**Failure Stress** (MPa)	**Failure Strain** (%)
1	24.90	10.00	210,6	302.40	414.60	312.40	33.20
2	25.10	10.05	209,9	301.70	411.40	321.30	34.60
3	24.90	10.00	209,4	303.40	421.30	304.80	35.10
		Average	209976	302.50	415.77	312.83	34.30

4. FULL SCALE TESTS OF THE BEAM-COLUMN JOINTS OF STEEL FRAMES

In the literature, there are two different test configurations available for the full scale beam-column joint tests. These test configurations are different for the corner and middle columns.

In this study, the test configuration for the corner columns is selected for the full scale tests. Test specimens were pin-supported at the zero moment points, i.e. at the center points of the upper and lower floor columns in order to reflect the real frame behavior. The beam at floor level was subjected to reversed-cyclic loading right at the center point (Figure 4).

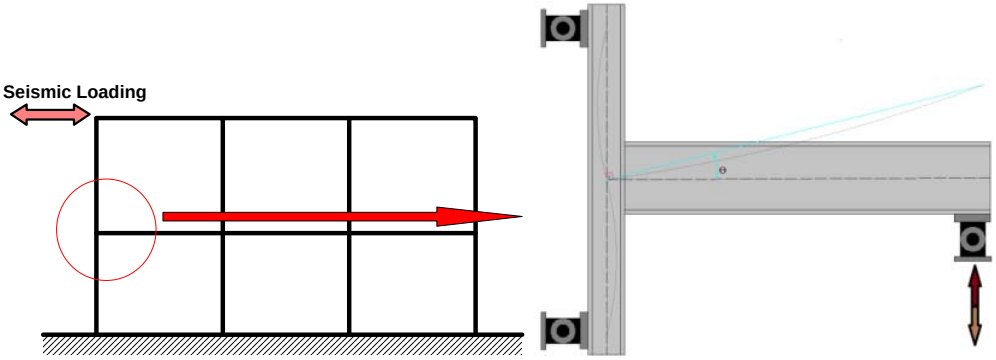

Figure 4. Idealization of the Beam-column Joint.

The target with this damper-attached connection system was to absorb the energy during a severe earthquake by having the steel slit damper damaged without causing any damage to the column or beam. Afterwards, the damaged steel slit damper can be rapidly and easily replaced so that the structure could be put back into service safely. For this purpose, in this joint configuration, a plate is welded at the top and bottom edges of the slit damper. One plate is bolted to the beam's lower flange by high strength bolts, and the other to a rigid split-T gusset plate attached to the column. To constitute the beam support allowing rotations, the beam's upper flange is bolted to a split-T member attached to the column (Figure 5).

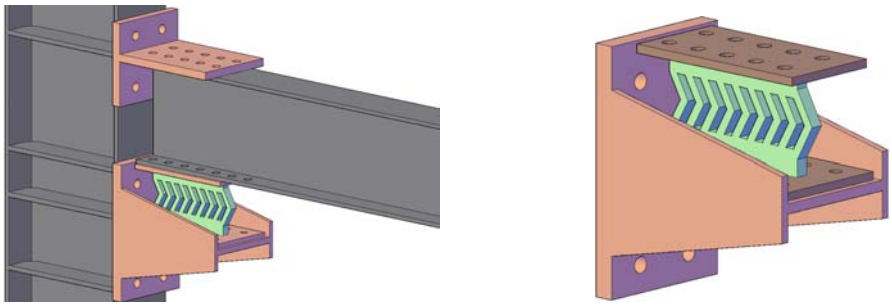

Figure 5. The Details of Beam-column Joint Utilizing a Slit Damper.

Unlike in the study by Oh et al. [1], in order to ease the use of narrow flange beams and also to allow damper edges to be welded at both sides, single damper was used instead of two. The welded plates will allow easy installation and replacing of damper.

5. TEST PROGRAM

Six full scale beam-column joint tests were carried out in an adaptive manner. First, a specimen with rigid end-plate connection was created as a reference. Then, a 12 mm thick steel slit damper (12D) without reinforcing the beam and a 15 mm thick steel slit damper (15D) with beam stiffeners

were tested. Later, a 22 mm thick L-shaped steel damper (22E) was tested without reinforcing the beam. This damper was found to be weak at one direction and therefore a 15 mm thick double-skewed L-shaped (15E) damper was designed and tested (Figure 6.c). Finally, a 15 mm thick round holed damper was tested (15Y).

5.1 Test Specimens

In the full scale experiments, IPE 400 and IPE 270 type sections were chosen for columns and beams, respectively. The height of the column measured from the lower hinge to the upper hinge was 3m. The beam length measured from the point of load application up to the column's face was 2m. In the full scale tests, the damper-attached beam-column joint was detailed a little differently from the commonly used end plate connection. A "T- plate" connecting the beam to the column from the upper beam flange was manufactured by cutting a HEA 600 type profile while the gusset that transfers forces from the lower flange of the beam to the columns through the damper was manufactured from HEA 800 type profile. The gusset was stiffened with members welded at the top and bottom corners. Two types of steel material namely, St-37 and St-44, were used in the full scale tests. The material of IPE 270 and IPE 400 type profiles, the gusset and the upper T-plate was of St-44 standard. On the other hand, St-37 type material was used for the continuity plate, the end plate and the dampers. Joint details of the test specimens are presented in Figure 6. The mechanical properties of the materials obtained from the tension tests are provided in Table 2.

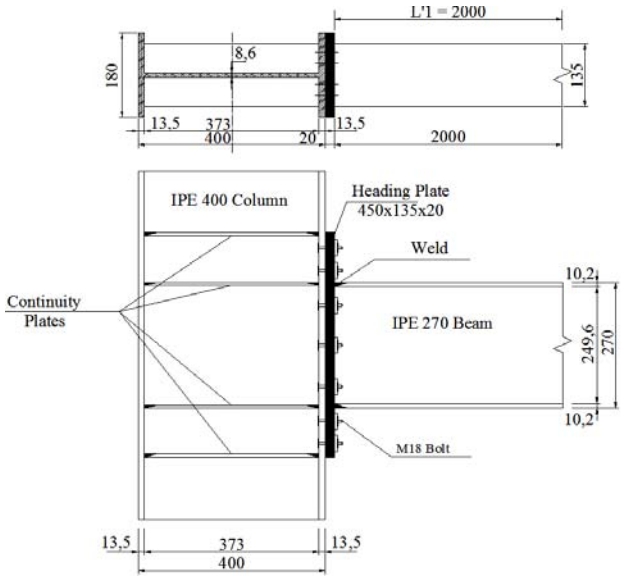

(a) Connection detail with end plate

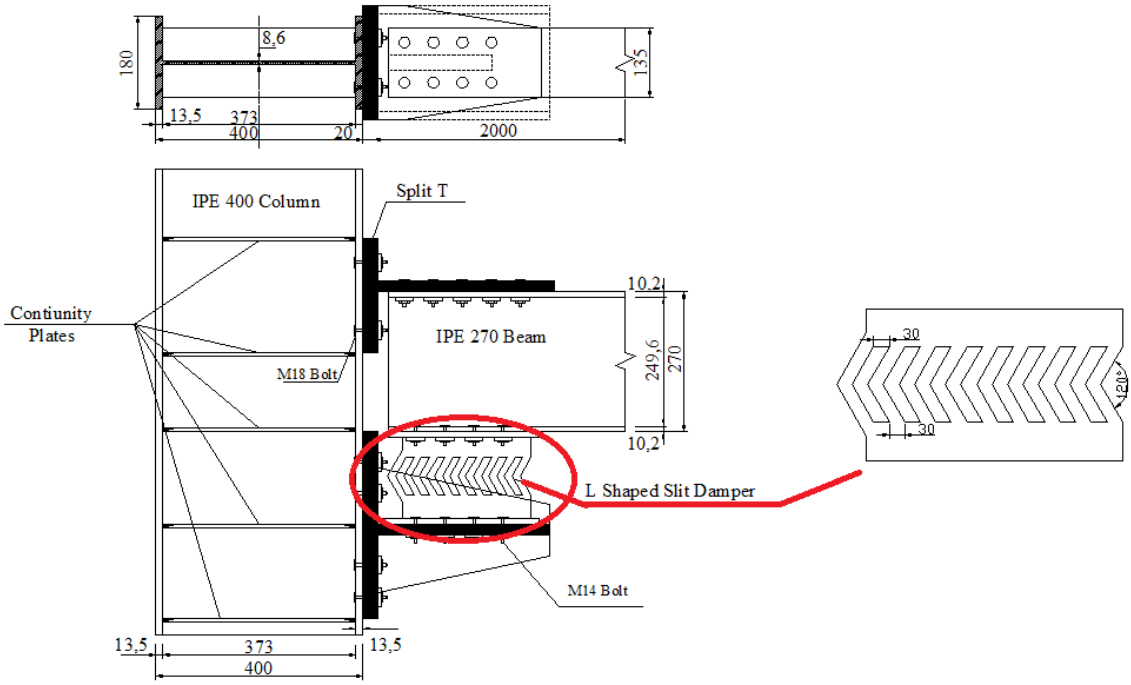

(b) Connection detail with damper

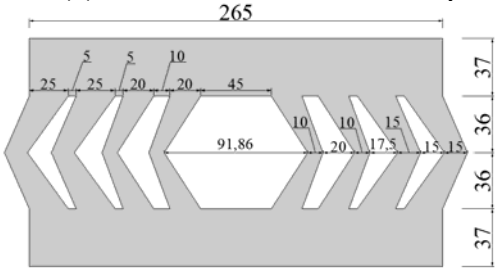

c) Geometric details of 15E damper

Figure 6. Joint Details of the Test Specimens

Table 2. Mechanical Properties of the Steel

Test Specimen		Steel grade	σ_y (MPa)	σ_u (MPa)	Ɛ (%)
Beam		St-44	319.40	458.22	27.4
Column		St-44	308.40	443.50	29.4
Split T	Gusset	St-44	322.40	457.45	26.3
	Upper T	St-44	329.35	465.10	25.9
Damper	(t=22 mm)	St-37	314.00	407.00	33
	(t=12 mm)	St-37	314.10	402.20	31
	(t=15 mm)	St-37	315.20	403.00	32

Welded and bolted connections were both utilized in the test specimens. All bolts were of high strength type bolts with a minimum failure stress of 800 MPa and a minimum yield strength of 640 MPa. The type of welding applied at the test specimens was gas metal arc welding and only fillet welds were performed. The diameter of the bolts and the thickness of welds were at their maximum allowed values so that no damage would occur in these members. Thus, no damage was detected at the welds and bolts during the tests.

Displacements were checked in all the tests carried out. Load control was enforced based on the load cycles presented in the study by Pachoumis et al. [15], which complies with FEMA-351 [16] and the regarding values are provided in Figure 7.

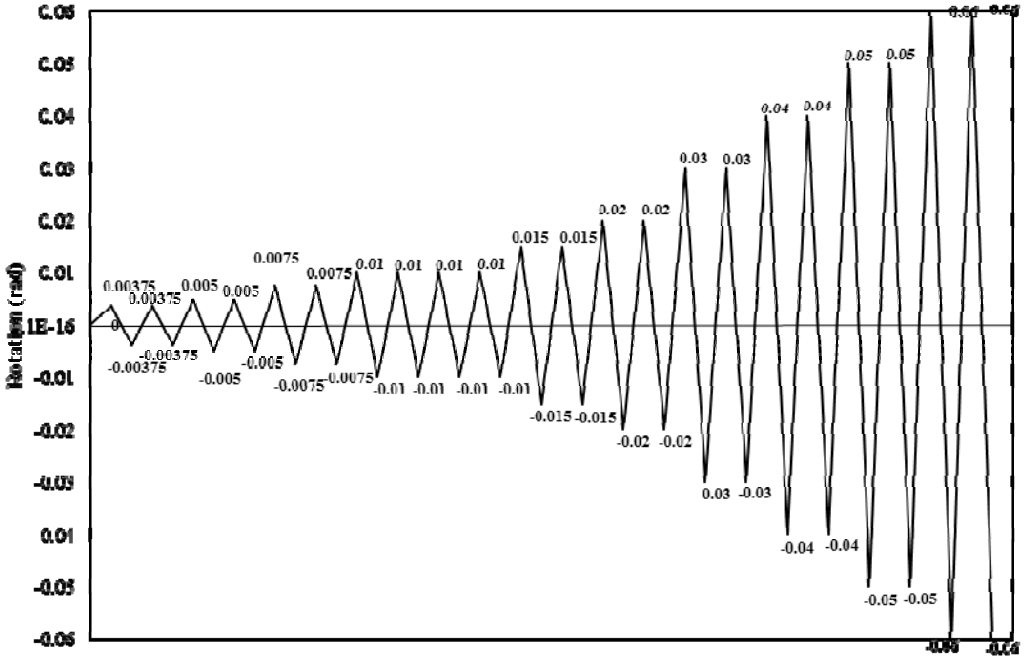

Figure 7. The load pattern applied during the tests

6. RESULTS OF THE RESEARCH

The full scale tests of six beam-column joint specimens, two with slit dampers, two with L-shaped dampers, one with round hole dampers and one with regular extended end plate, were performed. From the specimens with slit dampers, one specimen with a 12 mm thick slit damper was connected to the unreinforced beam, while the other specimen with a 15 mm thick damper was connected to the beam reinforced with two stiffeners. From the specimens with L-shaped damper, the specimen with 22 mm thick damper was connected to the unreinforced beam, whereas the other with 15 mm thick damper was connected to the beam reinforced with two stiffeners. On the other hand, 15 mm thick round-hole damper was connected to the beam reinforced with two stiffeners. The model drawings of test specimens can be seen in Figure 8.

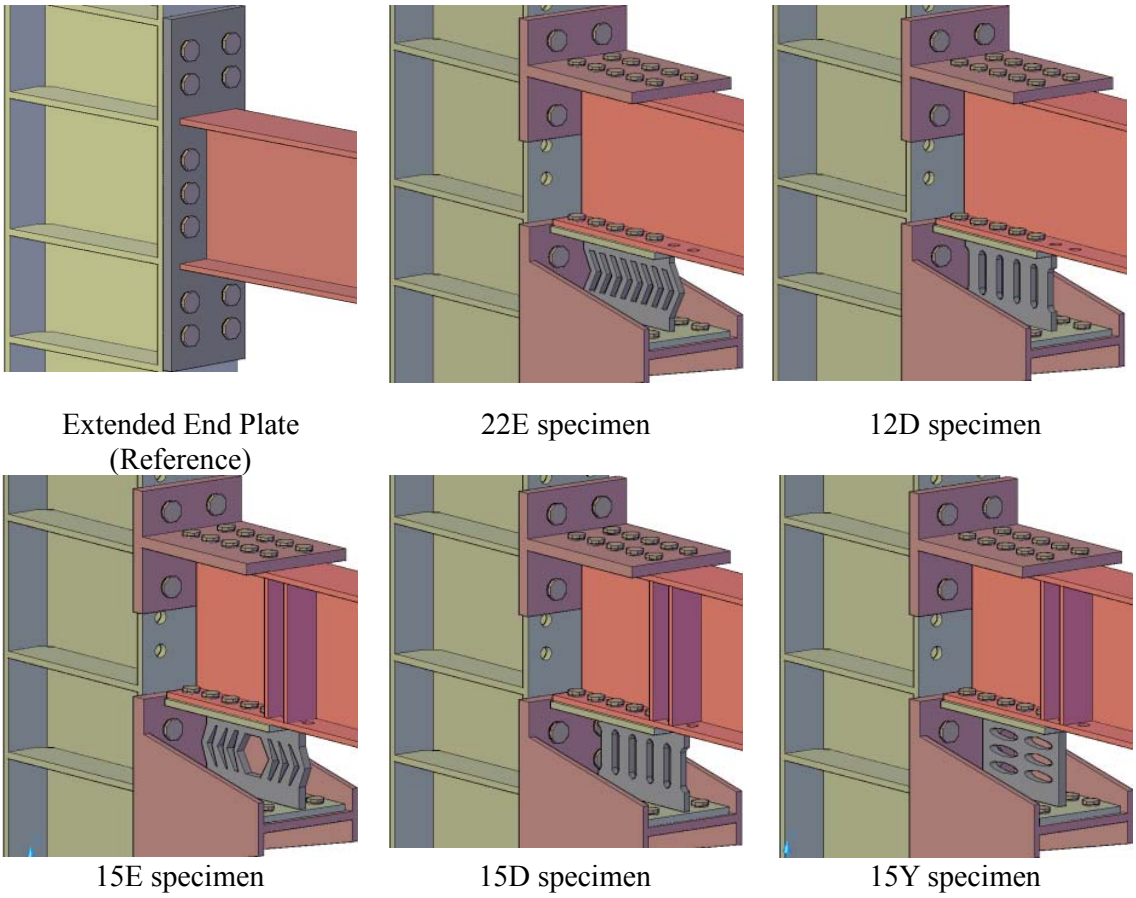

Figure 8. Test Specimens

The purpose of the experiment with the unreinforced beam under cycling loading was to concentrate the damage on the damper by preventing any damage to the beam, before reaching the beam's theoretical moment capacity i.e. staying within the elastic range. On the other hand, the aim with the reinforced beam specimen was to dissipate the energy by damaging the damper and having no damage on the beam although the theoretical moment capacity of the beam would be exceeded. The theoretical yield moment for the IPE 270 section was calculated as 132.8 kNm. This limit value was marked on the moment-rotation graph with dashed lines in Figure 9-14.

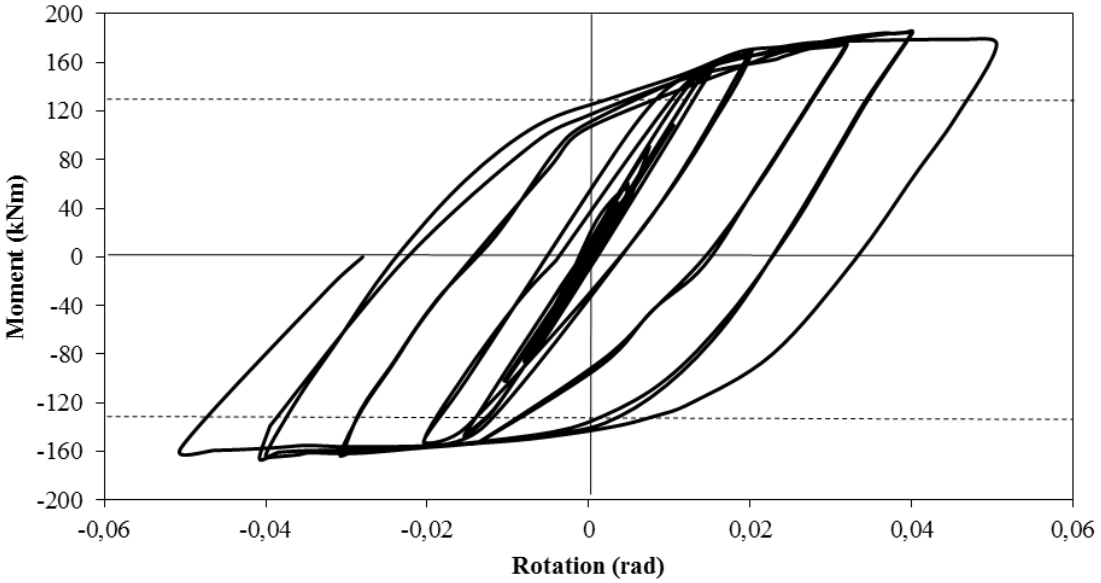

Figure 9. Moment-Rotation Diagram of the Reference Specimen

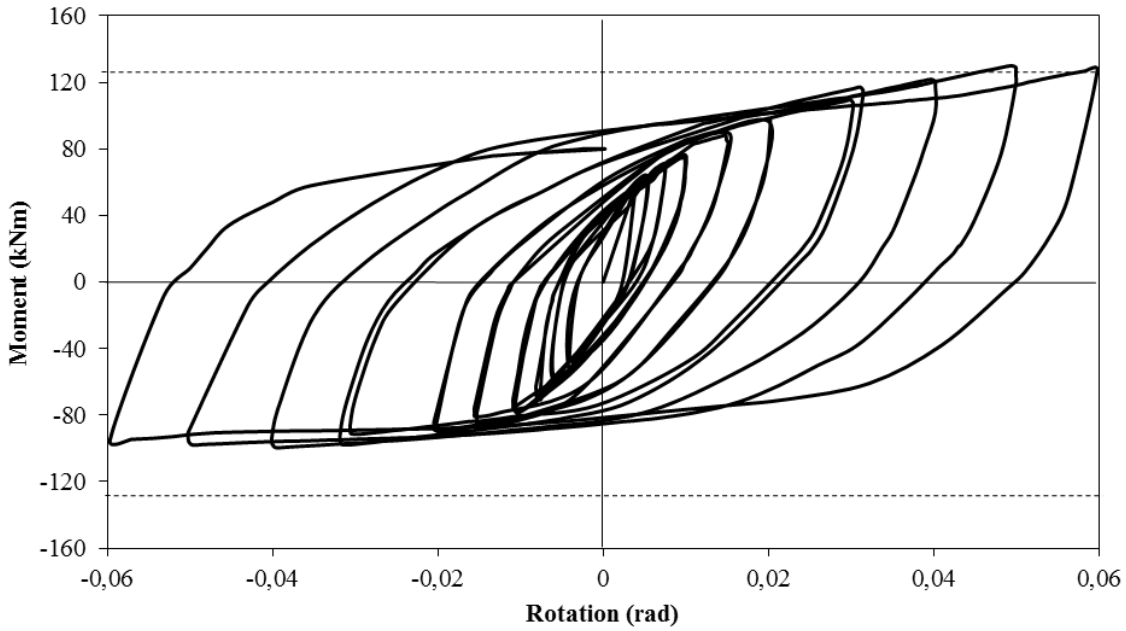

Figure 10. Moment-Rotation Diagram of Specimen 22E

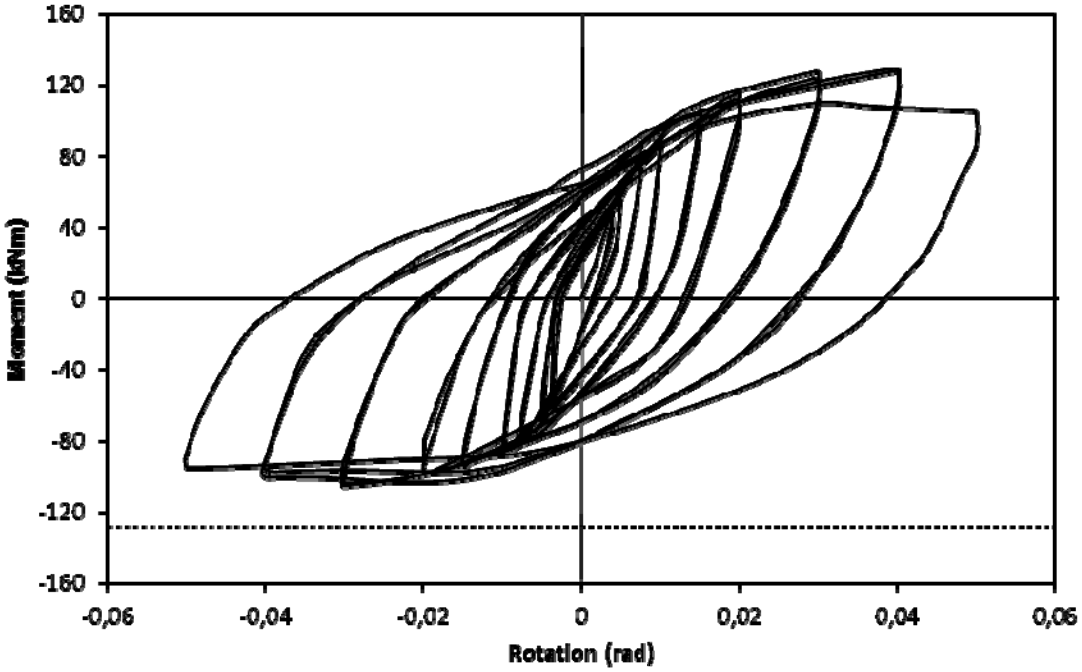

Figure 11. Moment-Rotation Diagram of Specimen 12D

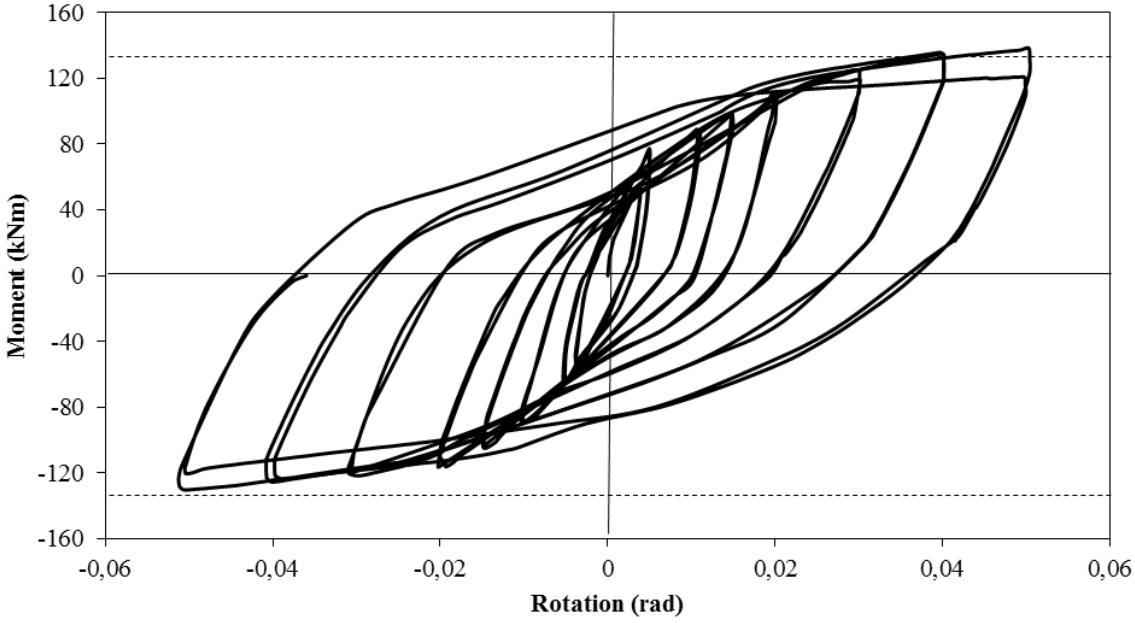

Figure 12. Moment-Rotation Diagram of Specimen 15E

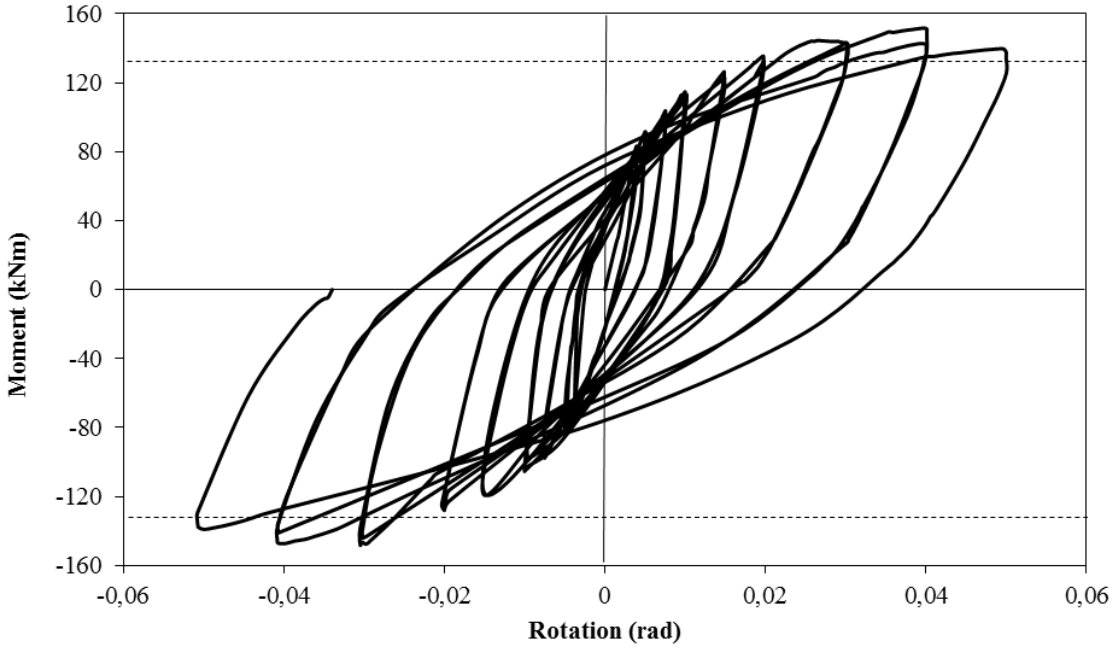

Figure 13. Moment-Rotation Diagram of Specimen 15D

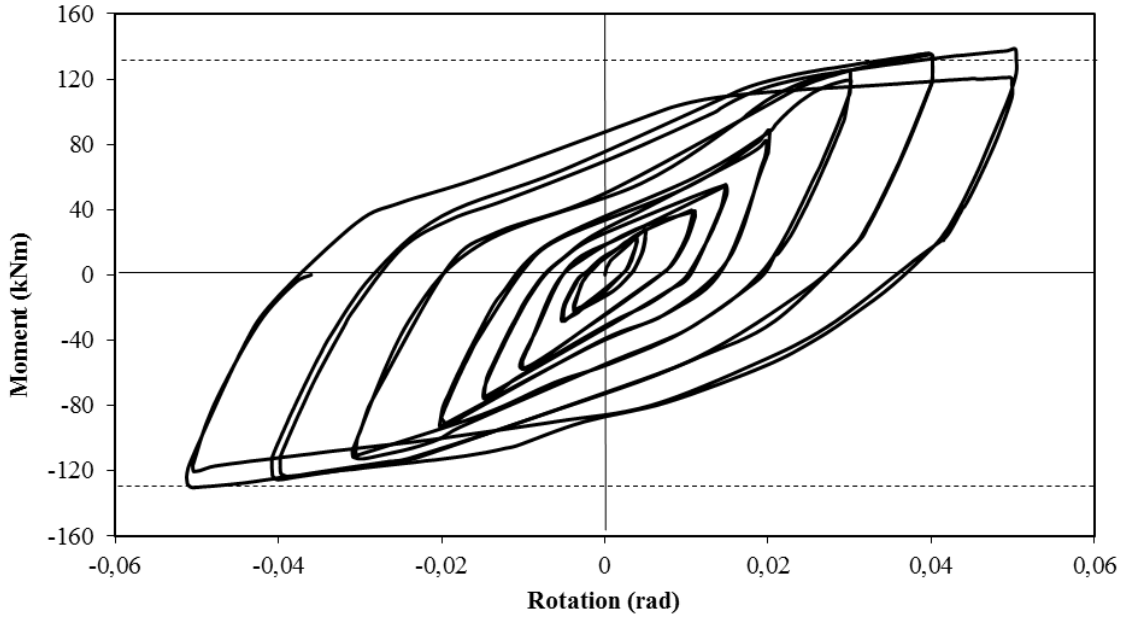

Figure 14. Moment-Rotation Diagram of Specimen 15Y

No permanent damage was observed during loading in any of the test specimens until a rotation value of 0.02 radians. After this rotation value, local buckling started to occur in the lower flange of the specimen with the extended end plate. Moreover, the plastic deformations in the test specimens with dampers occurred only on the dampers with no sign of damage on the beams. In further load steps, particularly above 0.02 radians of rotation, the local buckling of the lower flange of the beam was obvious in the reference specimen and excessive deformations and damage occurred at the dampers of the test specimens (Figure 15). Some cracks were observed at the upper part of the damper's end stud at 0.04 radians rotation in the specimen 12D. For the specimen 15D with thicker stud, the cracks at the damper occurred at 0.06 radians rotation. The deformation was

apparent at 0.02 radians rotation and micro cracks were detected at the elliptical ends in the specimen 15Y. In the specimen 22E, it is observed that the studs of the L-shaped damper extended and elongated at positive loads and folded down and shortened in negative loads starting from the first load cycles. Micro cracks were detected at the tip of the damper studs at 0.03 radians rotation. Due to single skewedness of L-shaped dampers, the stability of the compression side of the damper could be lost in a short time irrespective of the load direction and thus, the double-skewed damper 15E which has studs skewed in two opposite directions was designed and produced. Since the cracks concentrated at the tips of the damper studs for the rest of the dampers, the thickness of the damper studs was increased in order to prevent damage at the ends due to stress concentration at the sharp stud corners. The double-skewed L-shaped damper achieved similar load carrying capacities for positive and negative load cycles. Micro cracks were detected at the end of the damper studs at 0.02 radians rotation. The specimen 12D carried 3% less moment than the beam's theoretical plastic moment capacity and the theoretical elastic limit was not exceed. Therefore, no damage on the beam was observed. Although the specimen 15D carried 11% more moment than the theoretical plastic moment capacity of the beam, no damage was observed on the beam owing to the stiffeners welded on the potential plastic hinge location. It was determined that the specimens 15Y carried 2% more, 22E carried 4% less and 15E carried %5 more moment than the beam's plastic moment capacity.

As expected, the panel zone reinforced with stiffeners remained within the elastic range and exhibited a strong panel zone behavior. Figure 9-14 shows that 0.03 radians plastic rotation was exceed at all joints.

The hysteresis curves of the load and the displacement values measured at the free-end of the beam for every test specimen are provided in Figure 16.

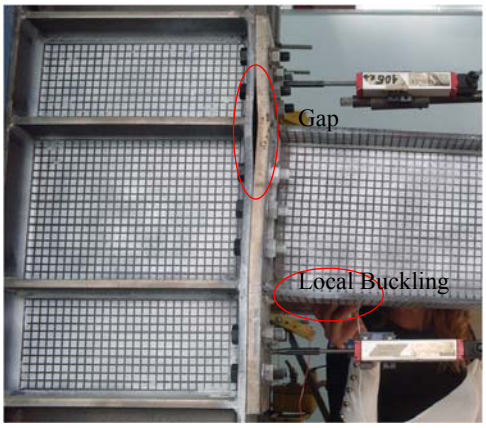

Buckling of the reference specimen

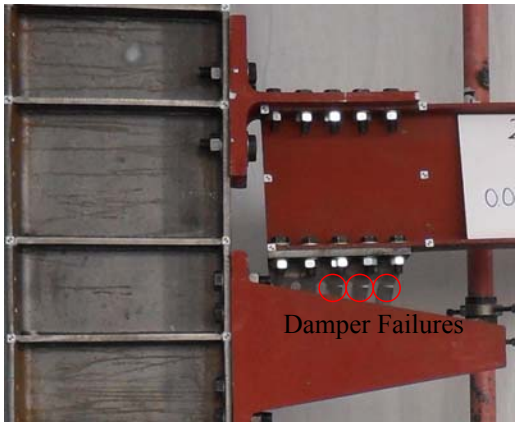

Failure of the damper studs of specimen 12D

Damper deformation of specimen 15D

Failure of the studs of specimen 15E

Failure of the damper studs of specimen 15Y Failure of the damper studs of specimen 22E

Figure 15. Damage Photos from the Tests

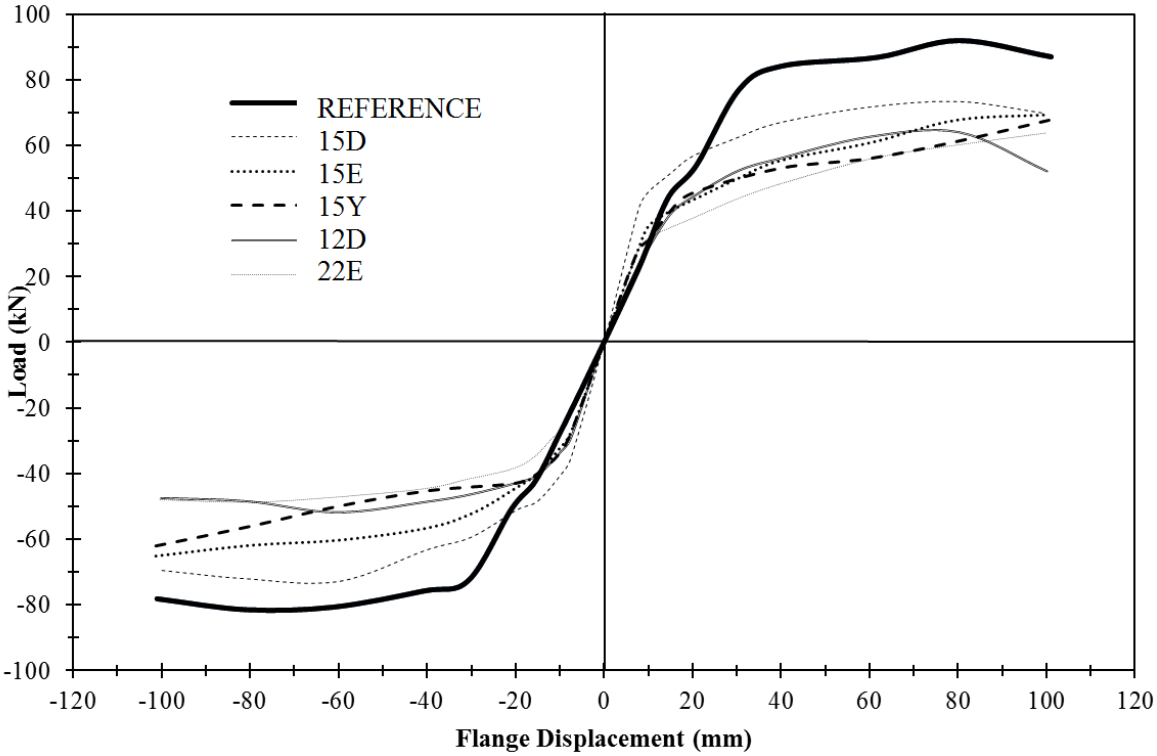

Figure 16. Load-displacement Hysteresis Curve of all Specimens

The plastic hinge formation caused the stiffness of the specimens to reduce during cyclic loading. The slope of the load-displacement curve at each load cycle is determined and the stiffness reduction graph was generated (Figure 17).

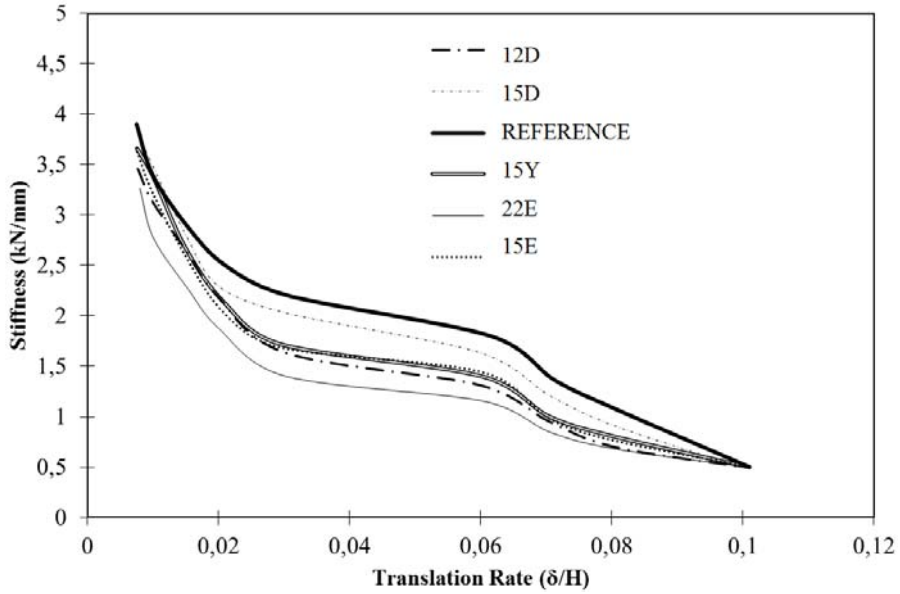

Figure 17. Stiffness Reduction Graph

Frame systems subjected to lateral cyclic loads consume a part of the produced energy by deformations. Amount of the consumed energy is quite important particularly in the case of dynamic loads such as earthquakes. Energy is equal to the work done, while the work is equal to force multiplied by distance. Therefore, the energy consumed by the test specimen is equal to the area under the load-displacement curve for each cycle. In this study, as seen in Figure 18, test specimens 12D, 15D, 15E, 15Y consumed 9%, 4%, 10%, and 13% less energy than the reference specimen, respectively. The specimen 22E, however, exhibited quite a ductile behavior and consumed 8% more energy than the reference specimen (Figure 18).

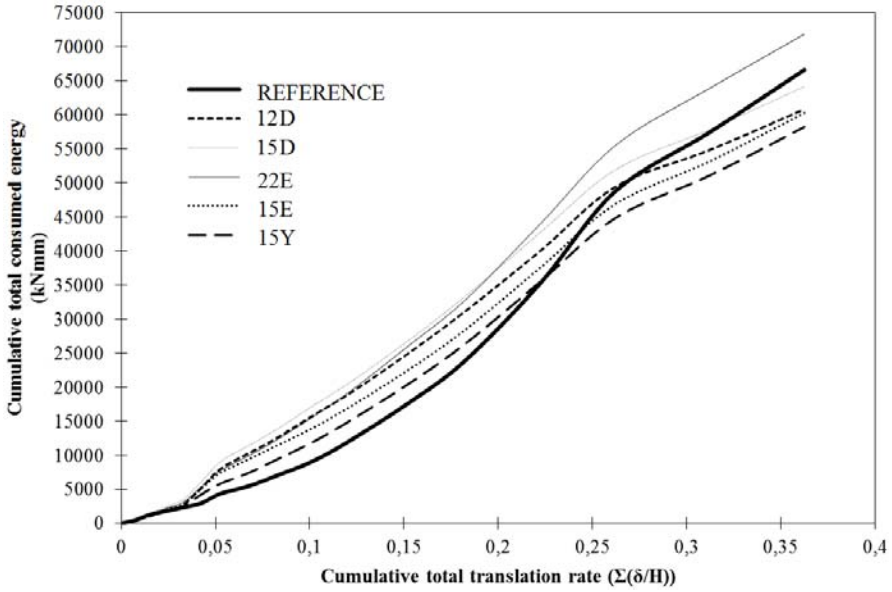

Figure 18. The graph of Total Consumed Energy

Considering the stiffness and the consumed energy, the specimen 15D with 15 mm thick damper performed best among the tested dampers. It has the highest stiffness and carried 11% more moment than the theoretical plastic moment of the beam. Although specimen 22E has higher energy consumption than 15D, its stiffness was the lowest of all dampers.

7. ANALYTICAL STUDY

In this section, the nonlinear model of the beam-column joint of a steel frame subjected to cyclic loading was created by using finite element method (FEM) so that the results of the experiments and of the numerical analysis could be compared. Hysteretic behavior of the considered beam-column joint was obtained by determining the stresses and deformations at various stages of the loading. For the nonlinear analyses, the required material models for each material type were obtained. Each material model was numbered and the numbers were assigned to the elements. The stress-strain curves obtained from the tensile tests of St-44 and St-37 type steel specimens were used for the column, beam, gusset and top T members, and for dampers, respectively.

3D model geometry was meshed using Solid 187 element type available in ANSYS library. Solid 187 is a 3D, 10-node tetrahedral solid element with mid-nodes. It has quadratic displacement behavior and is widely used in modeling irregular meshes. It has three translational degrees of freedom at each node in x, y and z directions (Figure 19). The average element size near beam-column connection was 12 mm. Coarser meshing was applied away from the joint where the average element size became 20 mm. The contacting surfaces between steel plates were assumed to be perfectly bonded. In order to see the stress concentrations around the bolt holes, they were included in the model. However, the bolts were not modeled. The column was fixed at top and bottom surfaces through 70 mm distance from the free edges. The load was applied at the centerline of the beam section at 2 m away from the face of the column connection plate.

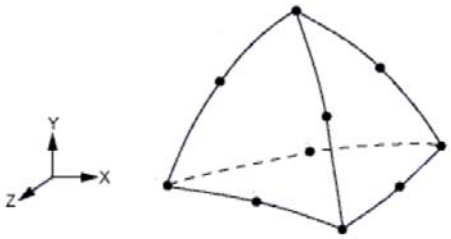

Figure 19. General Geometry and Nodes of Solid 187 Element

The steel material was assumed to have the stress-strain relationship presented in Figure 20. This stress-strain diagram was used in the definition of “Multilinear Kinematic Hardening” material model in order to simulate the behavior under cyclic loading given in Figure 21. This hardening model considers the Bauschinger effect so that the yield surface remains constant in size and translates in the direction of yielding. In Figure 20, the initial slope is equal to the first yielding stress divided by the corresponding strain and is defined as the modulus of elasticity of steel. The Poisson’s ratio was assumed to be 0.3, as usual.

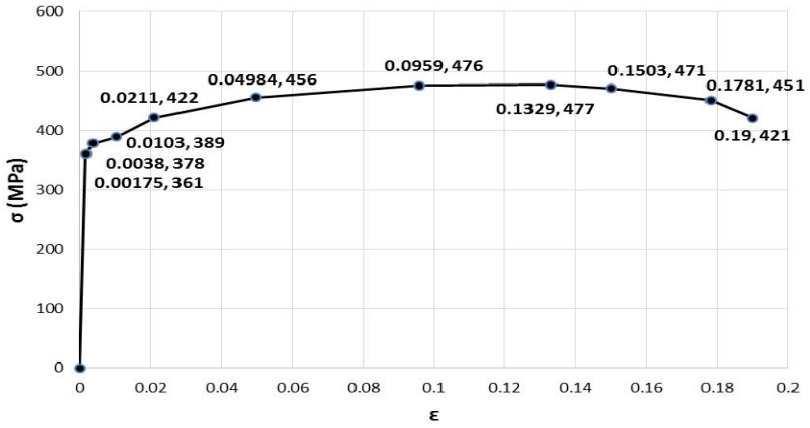

Figure 20. Stress-strain Model of the Steel Material

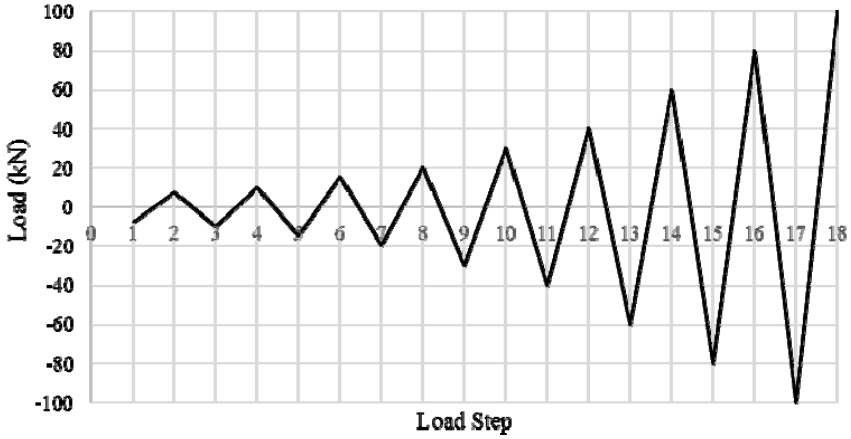

Figure 21. Applied Cyclic Loading Scheme

During the FE analysis, material and geometry nonlinearities were both considered. Iterative analysis was carried out using Newton Raphson method. The cyclic load history was applied with sufficiently small increments to obtain a convergent nonlinear solution. A cyclic loading text input file was prepared to be read from the File pull-down menu while Solution menu tree was kept active. The file has twice as many lines as the number of loadings. One line contains a displacement command with the loaded node number, loading direction and the amount of load and the following line contains the solve command; such as:

D,63303,UX,-7.5
SOLVE
D,63303,UX,7.5
SOLVE
…

In order to draw the force-displacement history plot within ANSYS Time History post-processor, a macro file was generated. After defining the array of the fixed node numbers for each load step increment, the reaction forces at fixed nodes in the loading direction were summed up and combined with the calculated displacement at the location and direction of loading to obtain the load-displacement plot.

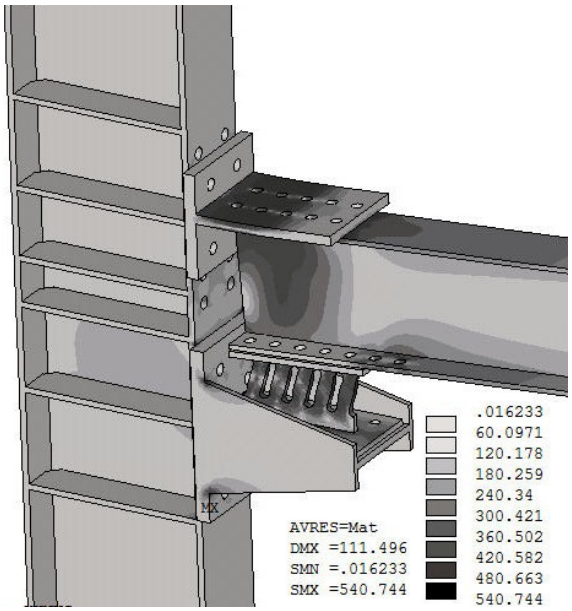

Specimen 12D

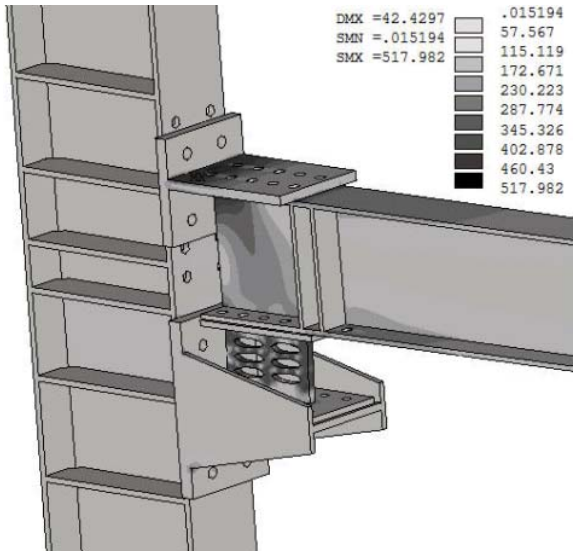

Specimen 15Y

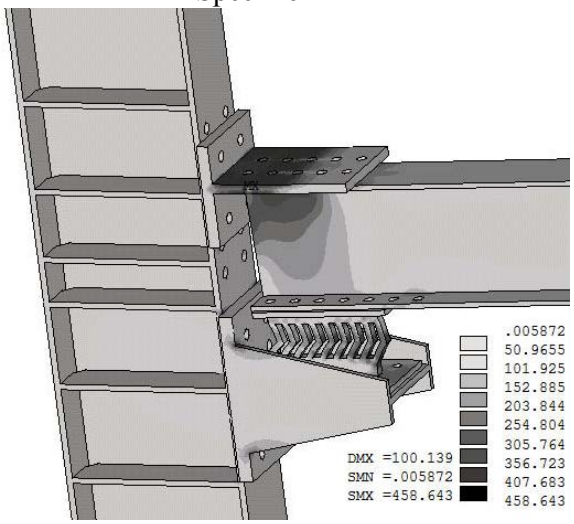

Specimen 22E

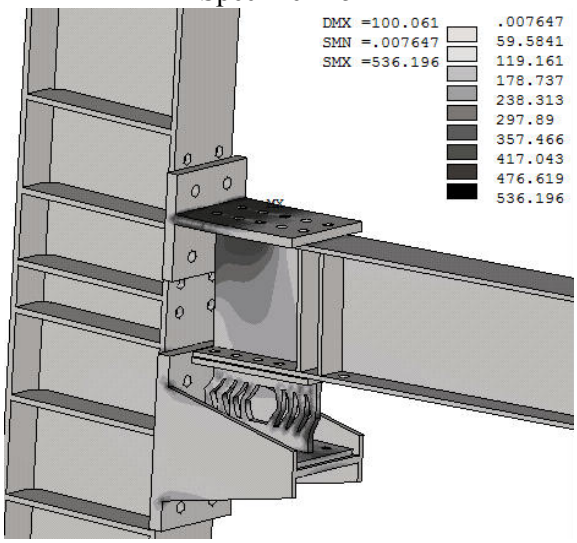

Specimen 15E

Figure 22. Von Misses Stress Contours of Specimens

Von misses stress contours of the specimens are given in Figure 22 and comparison of load-displacement graphs of the specimens are given in Figures 23-27.

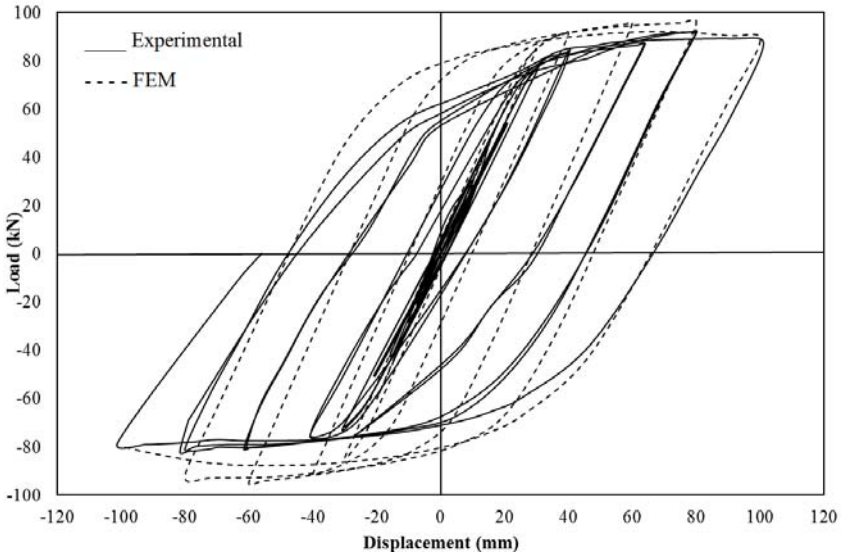

Figure 23. Load-displacement Curve Comparison of Reference Specimen

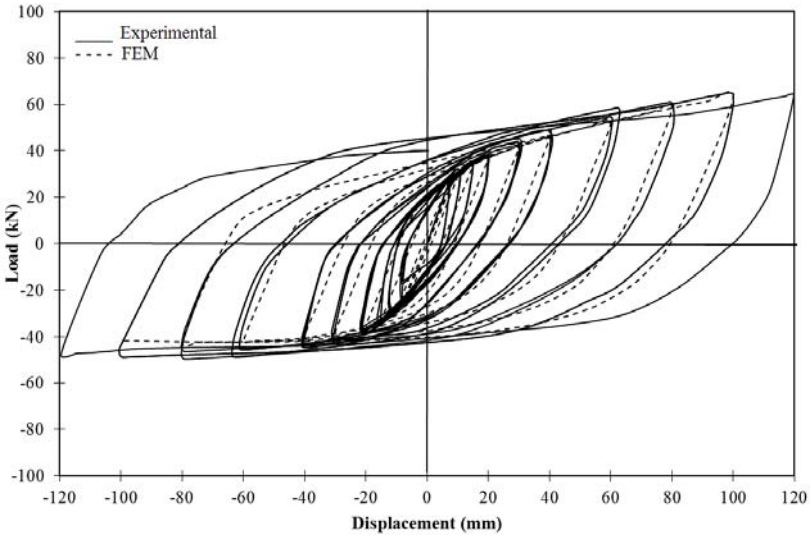

Figure 24. Load-displacement Curve Comparison of Specimen 22E

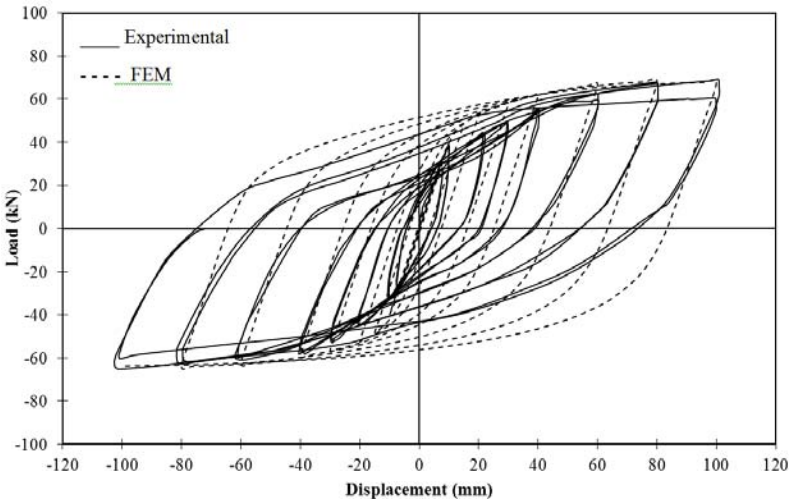

Figure 25. Load-displacement Curve Comparison of Specimen 15 E

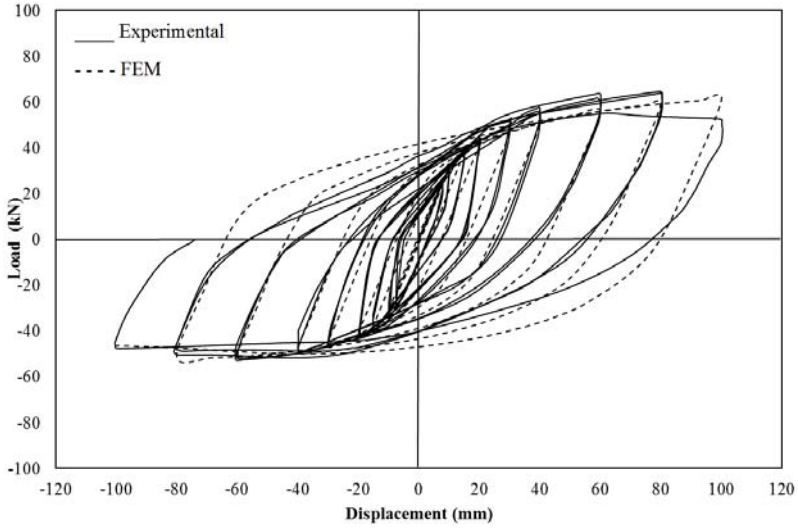

Figure 26. Load-displacement Curve Comparison of Specimen 12D

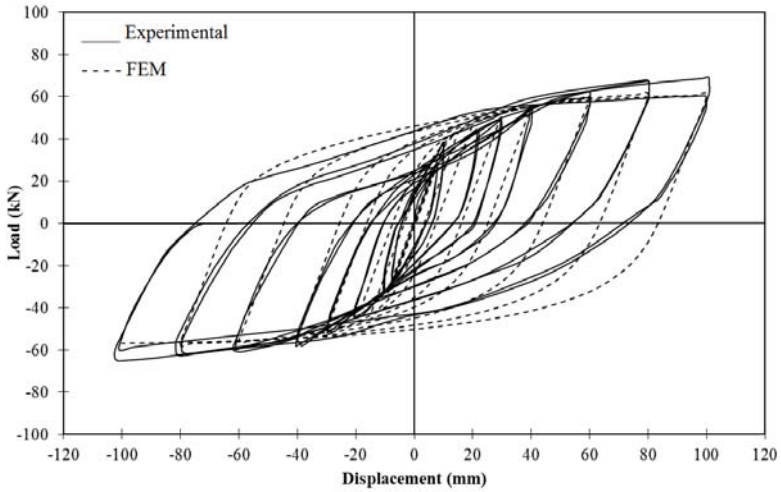

Figure 27. Load-displacement Curve Comparison of Specimen 15 Y

8. RESULTS

The use of slit dampers at beam-column joints of steel frames was investigated analytically by ANSYS Finite Element Software package. It was observed that the experimental and analytical cyclic loading vs. displacement curves were quite close to each other for each test specimen. For the reference specimen, the load values obtained from FEM analysis were found to be higher than the experimental ones. This might be attributed to the reduction in the strength because of the possible micro cracks occurred during the welding of the end plate and the beam. FEM analysis of the specimen 22E resulted in slightly lower load values in the compressive load cycles compared to its experimental counterparts. The approximate values of the peak loads and load cycles indicate that specimens were modeled successfully.

The purpose of this study was damping the energy by the yielding of dampers in order to prevent any possible beam damage at the joint of a steel beam-column under cyclic loads. The applied load that caused yielding of the IPE 270 beam was calculated approximately as 64 kN. In the experimental study, specimen 12D carried a load as much as the calculated theoretical load. In

addition, since the damper yielded by damping the energy before any yielding occurred on the beam of the specimen 12D, no permanent damage was observed either on the beam or the column. The maximum load that can be carried by the specimen N12 from FEM analysis is 5% lower than the experimentally determined load. Damper thickness of the specimen 15D was increased from 12 mm to 15 mm unlike in the specimen 12D. At the same time, in order to prevent a possible damage to the beam, it is reinforced with two stiffeners at the damper ends. The purpose was to increase the load carrying capacity of the joint by preventing a permanent damage to the beam even above the theoretical yield load. The experimental studies showed that a load 15% more than the beam's yield load was carried by the specimen 15D without any damage. It was observed that the highest load value obtained from FEM analysis was 4% less than the experimental one. Specimen 15Y carried 2% more load, as well, than the beam's yield load. In the specimen, the damage was concentrated on the dampers and the beam reinforced by stiffeners had no damage. Exhibiting quite a ductile behavior, specimen 22E carried a load up to the beam's yield limit. FEM model of this specimen displayed the reduction in the load-carrying capacity in the unloading region. Reinforced with stiffeners and attached an L-shaped slit damper skewed in both directions, specimen 15E carried 10% more load than the beam's yield limit and the FEM model was able to approximately simulate this behavior. In the meantime, although the ultimate load carried by the reference specimen was larger than the load carried by all damper added specimens, it was observed that energy consumption rate was not that high. As a matter of fact, specimen 22E consumed 8% more energy. The maximum load carried by the end plated reference specimen was 30%, 19%, 23%, and 26% higher than that of the specimens 12D, 15D, 15E and 15Y, respectively. However, the energy consumed by reference specimen was 9%, 4%, 10% and 13% higher than that of the specimens 12D, 15D, 15E and 15Y, respectively. The reason for this was that the damper yielded before the beam in the damper attached specimens and it absorbed the energy in a ductile manner during collapse.

Table 3. Comparison of Experimental and FEM Results

Specimens	Maximum experimental load carried at the beam end (kN)	Maximum load obtained from FEM (kN)	Experimental to FEM ratio
Reference	91	96	0,95
15D	73	70	1,04
12D	64	61	1,05
15E	70	68	1,03
15Y	68	61	1,11
22E	64	63	1,02

9. CONCLUSIONS

In this paper, experimental and analytical studies were conducted on the behavior of steel slit dampers which can be replaced in an easy, fast and economical way in order to allow putting a steel framed structure back into service immediately after a major earthquake by preventing the damage to the structural system. Therefore slit dampers were considered for this study and the damper geometries were decided based on some preliminary tests. For this purpose, in addition to one conventional end plated joint (reference system), five damper-attached joints: one with 12 mm and the other with 15 mm thick slit dampers, one with 15 mm thick round hole damper, one with 22 mm thick L shaped (single skewed) and the other with 15 mm thick L shaped (double-skewed) damper; were constructed with full scale and experimentally tested in order to evaluate their performance. The 3D Finite Element Model of the tested specimens was created and the nonlinear analyses were performed using ANSYS software package.

The conclusions drawn from the experimental and analytical research are noted below:

1. The proposed damper systems exhibited a stable hysteretic behavior under large story drift. First cycle stiffness rates of two damper attached systems are larger than that of the end plate connected joint and thus, the proposed systems are quite rigid.
2. Proposed damper systems are designed considering the theoretical yield strength of the beam thus enabling the concentration of plastic deformations when the beam and column are within the elastic range at the joints and preventing the damage to the beam and column.
3. FEM analyses which are based on the realistic and nonlinear modeling of the materials used in the experiments produced very similar results to the experimental ones. The cyclic behavior of the test specimens was modeled reasonably and with sufficient approximation.
4. Despite the stable behavior and high plastic deformation capacity of conventional end plate connected joints, the local buckling of the beam after a possible earthquake indicates that the repair and strengthening of the beam is ineffective and unreasonable.
5. It is possible to carry loads and moments up to a certain level of the beam capacity by attaching dampers to a beam-column joint of a steel frame without having any damage on the beam or column. When the loads and moments reach critical levels, the dampers exhibit their expected behavior by first yielding and then reaching their limit states with no damage to the beam and column.
6. The damper produced with L shaped slits consumes a high amount of energy, however, it has a low load carrying capacity in one direction of a cyclic load.
7. It is observed that the geometry of the dampers changed not only the load bearing capacity but also the behavior such as ductility and stiffness.
8. In order to fully grasp the behavior of the proposed damper systems, further research can be performed by first developing different joint and damper types and their FEM models, and then testing them experimentally.

ACKNOWLEDGMENTS

This paper was supported by Scientific Research Projects Office of Selcuk University with Project No. 10101008 and The Scientific and Technological Research Council of Turkey (TUBITAK) with Project No. 110M022.

REFERENCES

[1] Oh, S.-H., Kim, Y.-J. and Ryu, H.-S., “Seismic Performance of Steel Structures with Slit Dampers”, Engineering Structures, 2009, Vol. 31, No. 9, pp. 1997-2008.

[2] Bergman, D.M. and Goel, S.C., “Evaluation of Cyclic Testing of Steel-plate Devices for Added Damping and Stiffness”, 1987, Department of Civil Engineering, University of Michigan.

[3] Tsai, K.-C., et al., “Design of Steel Triangular Plate Energy Absorbers for Seismic-resistant Construction”, Earthquake Spectra, 1993, Vol. 9, No. 3, pp. 505-528.

[4] Kobori, T., et al., “Development and Application of Hysteresis Steel Dampers”, Proceedings of the 10th World Conference on Earthquake Engineering. 1992.

[5] Sabelli, R., Mahin, S. and Chang, C., “Seismic Demands on Steel Braced Frame Buildings with Buckling-restrained Braces”, Engineering Structures, 2003, Vol. 25, No. 5, pp. 655-666.

[6] Clark, P., et al. “Design Procedures for Buildings Incorporating Hysteretic Damping Devices”, Proceedings 68th annual convention. 1999.

[7] Lee, M.H., et al., "Ultimate Energy Absorption Capacity of Steel Plate Slit Dampers Subjected to Shear Force", International Journal of Steel Structures, 2002, Vol. 2, No. 2, pp. 71-79.
[8] Chan, R.W. and Albermani, F., "Experimental Study of Steel Slit Damper for Passive Energy Dissipation", Engineering Structures, 2008, Vol. 30, No. 4, pp. 1058-1066.
[9] Köken, A. and Köroğlu, M.A., "An Experimental Study on Energy Absorption Capacity of steel dampers subjected to shear force" Int. J. Arts Sci., 2011, Vol. 4, No. 2, pp. 25-32.
[10] Köken, A., and Köroğlu, M. A., "Waste Rubber Damper using on Steel Beam to Column Connection," Int. J. Arts Sci., 2012, Vol. 5, No. 4, pp. 217-222.
[11] Koken, A. and Köroğlu, M.A., "Steel Plate Slit Damper using on Steel Frames" e-J. New World Sci. Acad., 2011, Vol. 6, No. 4.
[12] Köken, A. and Köroğlu, M.A., "Experimental Study on Beam-to-Column Connections of Steel Frame Structures with Steel Slit Dampers," Journal of Performance of Constructed Facilities", 2013, Vol. 29, No. 2, pp. 04014066.
[13] Köroğlu, M., "Seismic Damper using on Beam to Column Connections of Steel Frames", Doctor of Thesis, Selcuk University, Institute of Graduate and Applied Sciences, Konya, Turkey, 2012.
[14] Saffari, H., Hedayat, A. and Nejad, M.P., "Post-Northridge Connections with Slit Dampers to Enhance Strength and Ductility", Journal of Constructional Steel Research, 2013, Vol. 80, pp. 138-152.
[15] Pachoumis, D., et al., "Cyclic Performance of Steel Moment-resisting Connections with Reduced Beam Sections-experimental Analysis and Finite Element Model Simulation", Engineering Structures, 2010, Vol. 32, No. 9, pp. 2683-2692.
[16] Committee, S.J.V.G.D., et al., "Recommended Seismic Evaluation and Upgrade Criteria for Existing Welded Steel Moment-frame Buildings", 2000: FEMA.

COMPOSITE EFFECT OF STUB SQUARE STEEL TUBED COLUMNS UNDER AXIAL COMPRESSION

X. H. Zhou[1], D. Gan [1,2]*, J. P. Liu[1] and Y. F. Chen[3]

[1] *Key Laboratory of New Technology for Construction of Cities in Mountain Area (Chongqing University), Ministry of Education, Chongqing 400045, China*
[2] *School of Civil Engineering, Chang'an University, Xi'an 710061, China*
[3] *Department of Civil Engineering, The Pennsylvania State University, Middletown, PA 17057, USA*
**(Corresponding author: E-mail: gandan@cqu.edu.cn)*

Received: 28 January 2016; Revised: 16 December 2016; Accepted: 27 December 2017

ABSTRACT: The in-filled concrete of square tube confined concrete columns (tubed columns for short) is non-uniformly confined and the effectiveness of its confinement is reduced, leading to a complex composite effect. This paper discusses key parameters, including friction, width-to-thickness ratio and chamfered corner radius of steel tubes, which would affect the confinement of square tubes on in-filled concrete. Eighteen specimens with large width-to-thickness ratio and six RC counterparts were tested under axial compression. Four main system parameters were considered in the tests: 1) width-to-thickness ratio (60-160); 2) types of steel tubes (galvanized and ordinary); 3) interface between tube and concrete (reduced friction and not); and 4) with and without reinforcement cage. It was found that the square tubed RC and plain RC columns were characterized by the shear failure mode, but the ductility performance of the tubed columns was much better than the RC specimens. The axial load-carrying capacities of the specimens with smaller friction were slightly lower than those with larger friction. A finite element analysis (FEA) model was developed to analyze the influence of friction and corner radius on of square tubed columns. An effective section confining model considering effective utilization index of square steel tubes was developed to predict the axial load resistances. The results are satisfactory when comparing the predictions to the experimental and nonlinear finite element analysis results.

Keywords: Square steel tubed column, concrete-filled tube column, composite effect, friction coefficient, effective utilization index, axial load-carrying capacities

DOI: 10.18057/IJASC.2018.4.2.8

1. INTRODUCTION

Steel and composite structures composed of steel, concrete and composite members are widely used to-date due to their structural efficiency and economy, especially in mid- and high-rise buildings[1-2]. The square tube confined concrete column (tubed column for short) is a special concrete-filled tube (CFT) column, in which the outer thin-walled square tube does not pass through the beam-column joint to avoid direct axial loading. The longitudinal stress of steel tubes mainly comes from the bond and friction between concrete and steel tube. In order to sustain tensile force and flexural moments, reinforcement cage or steel sections embedded in concrete are also needed in tubed columns in practice (Liu *et al*. [3]). Such structures are referred as "*square tubed reinforced concrete* (STRC) *column*s" (Figure 1a) or "*square tubed steel reinforced concrete* (STSRC) *column*s" (Figure 1b). The use of external tube to confine concrete has become popular in retrofitting concrete structures. In recent years, the research group in Chongqing University makes great efforts to apply tubed columns and their structural systems to newly built buildings and bridges. A connection system, connecting circular tubed reinforced concrete columns to RC beams, was proposed by the authors. The joint system showed superior structural behavior when subjected to axial compression and cyclic testing. (Gan *et al*. [4]).

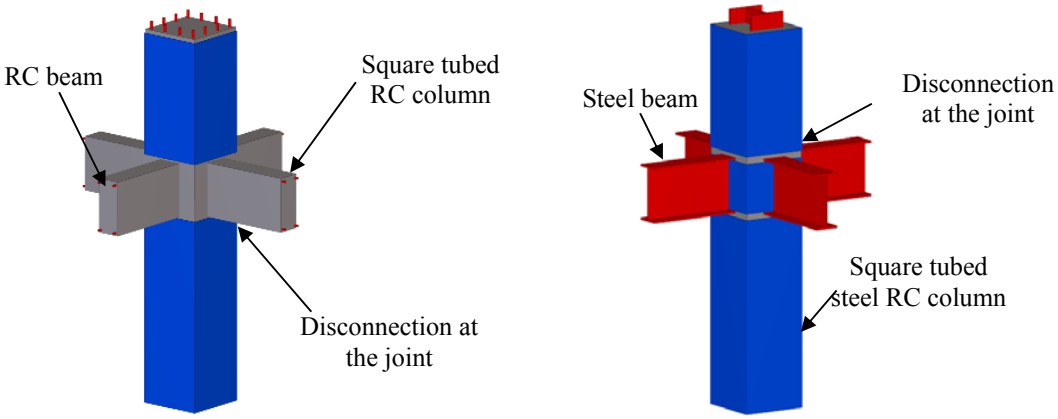

(a) Square tubed RC column (b) Square tubed steel RC column

Figure 1. Square Tubed Columns

Steel tube confines concrete and hence increases the strength and ductility of concrete columns. Many researches have been devoted to the behavior of circular CFT columns, circular tubed columns, and circular tubed columns using oil or other materials to reduce friction coefficient under axial compression (Sakino *et al*. [5], Orito *et al*. [6], Fam *et al*. [7], Han *et al*. [8], and Liu *et al*. [9]). The ductility performance of the circular composite columns tested above was fairly good. Test results also have shown that the axial load capacities of circular tubed columns with reduced friction were slightly higher than those of the conventional tubed columns and that the axial load capacities of both types of tubed columns were higher than those of CFT columns. However, circular tubed columns with reduced friction had the lowest stiffness.

Sakino *et al*. [10-11] investigated the behavior of square tubed plain concrete columns with reduced friction under axial compression. Their tests results showed that the square tube could provide enough confinement effect when the width to thickness ratio of the tube was smaller than 60. Han *et al*. [7] investigated the behavior of square CFT columns, square tubed plain concrete columns and tubed columns using oil to reduce friction coefficient under axial compression. It was found that local buckling of CFT columns occurred earlier and more obviously than that of the tubed columns and that the axial load capacities of square CFT columns were slightly lower than those of square tubed columns. The test results of Zhang *et al*. [12] showed that the axial compressive strength of square tubed columns was greater than that of square CFT columns when the width to thickness ratio (D/t) of tube was 70 and that the trend reversed when width-to-thickness ratio $D/t <$ 47. Yamamoto *et al*. [13] demonstrated that the failure mode was not correlated with the cross section dimension, while the confinement effect was related to the cross section dimension and concrete strength. Kwon *et al.* [14-15] presented an analytical prediction and experimental research for the long term behavior of both circular and square tubed columns and CFT columns. Yu *et al*. [16] proposed a regression formula to predict the axial resistances of square tubed columns based on the experimental and finite element analysis results. Liu *et al*. [3] and Qi *et al*. [17] investigated the axial load behavior of STRC and STSRC stub columns in which the width to thickness varied within the range of 50 and 100, respectively.

The in-filled concrete of square tubed columns is non-uniformly confined and the effectiveness of its confinement is greatly reduced. The system parameters affecting the confinement effect are rather complicated. From the above literature review [7, 10-17], the available research results were focused on tubed plain concrete columns with small dimensions and width-to-thickness ratios (D/t < 100). Experimental and theoretical study on large width-to-thickness ratios (D/t > 100) tubed reinforce concrete columns are still short. Additionally, significant discrepancies exist between the experimental and theoretical results reported by the researchers. To further clarify the main system

parameters affecting the axial compressive strength and to develop a unified method to accurately predict the axial load resistances of square stub columns, experimental and theoretical investigations are presented in this paper to demonstrate the composite effect of stub square tubed RC columns under axial compression.

2. EXPERIMENTAL PROGRAM

2.1 Description of Specimens and Test Set-up

To investigate the effect of bond and friction on composite response, fourteen stub STRC columns with galvanized and ordinary steel, four stub steel tubed plain concrete columns with and without oil (Mobil DTE 25) which was used to reduce the bond and friction of the interface between ordinary steel tube and concrete, and six reference RC stub columns were tested. The tube was made by welding two cold-formed C-shape steel sections. The surface roughness of galvanized tube is smaller than that of ordinary steel tube. Therefore, the friction coefficient and bond strength between the galvanized tube and concrete are smaller.

Figure 2 depicts the general layout of test specimens. A length to width ratio of 3 was selected for the columns in order to ensure the stub column behavior. Two 10mm thick steel endplates were welded at both ends of the column to ensure uniform loading. Two 10mm stripes were cut off from the steel tube at 30 mm away from the both ends of the specimens to avoid carrying loads directly. The details of the specimens and their labeling system of the specimen are shown in Table 1. In the nomenclature of specimen, STRC represents square tubed reinforced concrete specimens; GS represents galvanized steel tube; OS represents ordinary steel tube; STC represents square tubed concrete specimens. As an example, S(GS)-200-1.5-55: S(GS) represents square members with galvanized steel tube; 200 represents outer width D of steel tube; 1.5 represents the nominal thickness of steel tube (t); and 55 represents nominal cubic strength of the concrete. In the STC Group, S-180-3-80 and SU-180-3-80 represent tubed plain concrete columns with and without oil which was used to reduce the bond and friction, respectively.

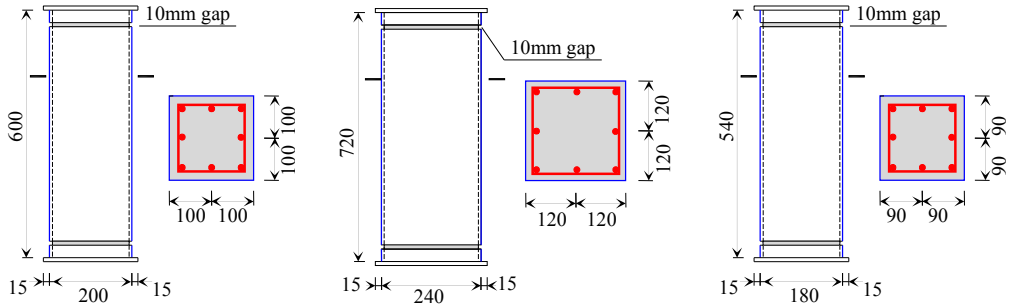

(a) STRC-200 (b) STRC-240 (c) STC-180

Figure 2. The Test Specimens

Table 1. Parameters and Material Strengths of the Test Specimens

Group	Specimen	Steel tube					Concrete	Longitudinal reinforcement			Stirrup (for erection only)		
		t (mm)	D/t	α (%)	f_y (MPa)	f_u (MPa)	f_{co} (MPa)	d (mm)	quantities	f_a (MPa)	d (mm)	spacing	f_b (MPa)
STRC(GS)	S(GS)-200-1.5-55	1.49	134	3.0	314.0	414.9	45.0	19.12	8φ20	480.6	8.02	@200	316.9
	S(GS)-240-1.5-55	1.49	161	2.5					8φ20			@240	
STRC(OS)	S(OS)-200-1.5-55	1.50	133	3.0	364.3	449.0	48.1	19.40	8φ20	477.1	7.82	@200	397.4
	S(OS)-240-1.5-55	1.50	160	2.5					8φ20			@240	
STC	S-180-3-80	3.00	60	6.7	254.0	383.4	59.4	-	-	-	-	-	-
	SU-180-3-80	3.00	60	6.7	254.0	383.4		-	-	-	-	-	-

The parameters depicted in the table include the width to thickness ratios of steel tubes (D/t), the steel ratio α (area of steel tube to the gross cross sectional area of specimen) of steel tubes, the yield strength f_y of steel tubes, the ultimate strength f_u of steel tubes, the concrete compressive strength f_{co} which is determined by prisms with dimensions of 150 mm×150 mm×300 mm, the yield strength f_a of longitudinal reinforcement and the yield strength f_b of stirrups. The cubic (150mm×150mm×150mm) strengths of specimens in Groups STRC(GS), STRC(OS) and STC are 56.2 MPa, 60.1 MPa and 69.9 MPa, respectively. In the following text, for example, S(OS)-200-1 and S(GS)-200-1 are short for S(OS)-200-1.5-55-1 and S(GS)-200-1.5-55-1 respectively. It should be noted that the last numbers "1, 2 or 3" represents the different specimen with the same dimensions and properties.

The RC counterparts were fabricated by removing the steel tube of Specimens S(OS)-200-1.5-55 to ensure the same cured condition with STRC(OS) columns. By doing this, the confining effect of large D/t ratio steel tube could be accurately evaluated. It should be noted that the stirrups of both the STRC and reference RC columns were used to erect the longitudinal reinforcement.

All columns were tested using a 5000 kN hydraulic compression machine (Figure 3). The loading rate was at 1-2 kN/s in the elastic range. The compressive load was applied slowly and continuously near and after the peak load in order to investigate the softening behavior of the columns.

Four linear variable displacement transducers (LVDTs) were used between the end-plates to monitor the axial deformation. The vertical and transverse strain gauges were arranged on two opposite sides. All the specimens were tested in three batches, and three different arrangements of strain gages were adopted. Firstly, for the STC columns, the vertical and transverse strain gauges were only arranged at the mid-point of mid-height of tubes. Secondly, for STRC(OS) columns, strain gages at the mid-point and corners of mid-height of tubes were added. Furthermore, for STRC(GS) columns, transverse strain gauges were added at the top-end of their steel tubes. The strain gauges at the end of tubes were expected to be in tension because they were close to free ends and did not expect to carry any axial load.

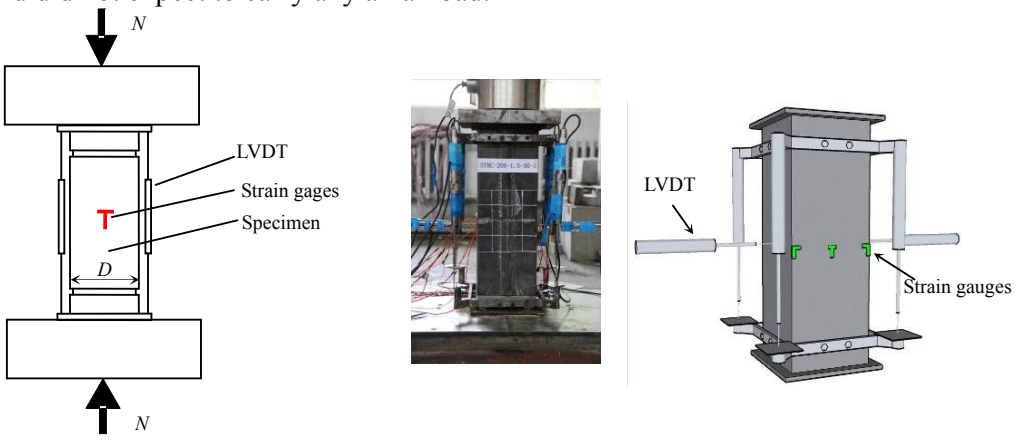

Figure 3. Test Set-up and Instrumentation Layout

2.2 Failure Patterns and Load-deformation Responses

Figure 4 depicts failure patterns of the specimens in Groups STRC(GS), STRC(OS) and STC, and also the contrastive RC specimens. The measured axial load versus axial displacement curves of all the tested columns are shown in Figure 5. As for the RC specimen, the concrete cover was spalled off at the peak load and the axial load decreased quickly. The ductility of RC columns was poor (Figures 4a-b and 5a).

The STRC and STC specimens showed similar shear failure patterns in concrete. The shear angles varied from 45° to 65° (Figures 4c-g). The core concrete crushed severely due to the buckling of longitudinal rebars. It should be noted that due to the "end effect", a local failure pattern of the core concrete occurred among one of the specimens in Groups S(GS)-200 and S(OS)-240 (Figure 4e). The strength of the two specimens was about 20% lower compared with other specimens.

Strength and ductility for the contrastive RC columns were improved by steel tubes with large width to thickness ratio (D/t = 133, 160). The displacement of the STRC specimens increased quickly when loads reached axial load-carrying capacities of the core RC columns (Figures 5a and 5c). STRC(OS) columns had slightly higher axial load-carrying capacities than those of STRC(GS) columns (Figures 5b and 5d), and STC columns without reducing friction had slightly higher axial load-carrying capacities than those of STC columns with reduced friction (Figure 5e). It could be concluded that the thin-walled square steel tube could avoid a brittle failure occurring in RC or plain concrete columns with high-strength concrete. Steel tubes with large width to thickness ratio (D/t =60, 133, 160) could provide moderate confinement effect to RC stub columns.

(a) RC-200 (b) RC-240 (c) S(OS)-200 (d) S(GS)-240

(e) Local failure of S(OS)-240-2 (f) S-180-3-80 (g) SU-180-3-80

Figure 4. Failure Patterns of Columns

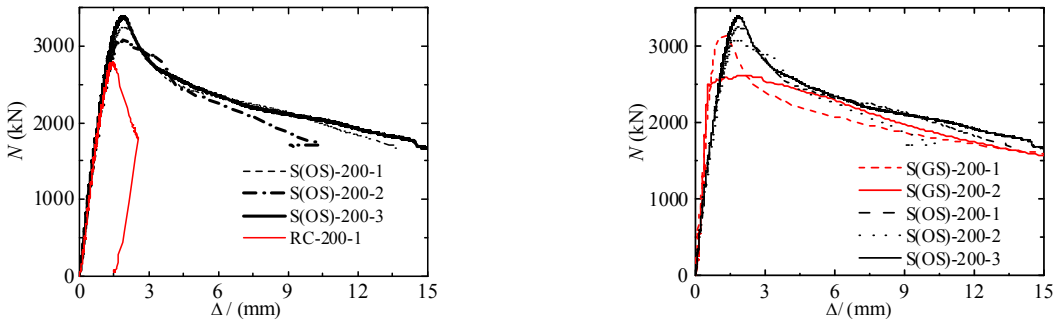

(a) S(OS)-200 and RC-200 (b) S-200

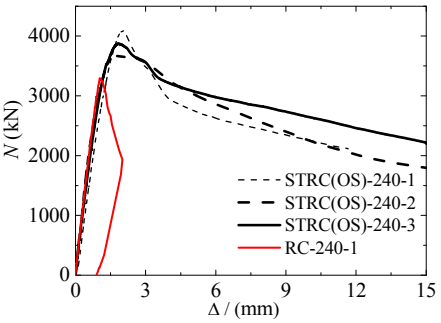

(c) S(OS)-240 and S\RC-240

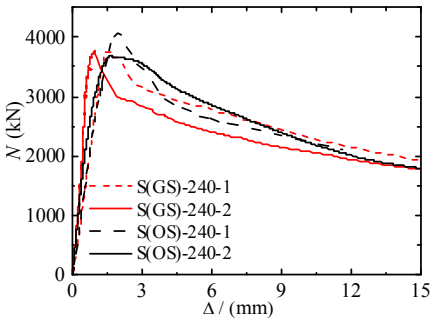

(d) S-240

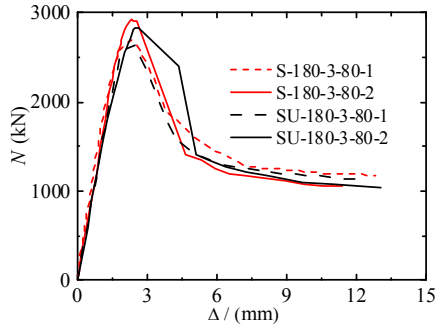

(e) STC

Figure 5. Load-displacement Curves for all the Columns

2.3 Load-strain/Stress Analysis

Strain gauges were placed on the two opposite faces of the steel tube to obtain the strain values during the tests (Figure 6). Average values were chosen. The elastic-plastic analysis method (Zhang *et al*. [18]) was adopted to analyze the stress state in steel tubes based on the measured strains.

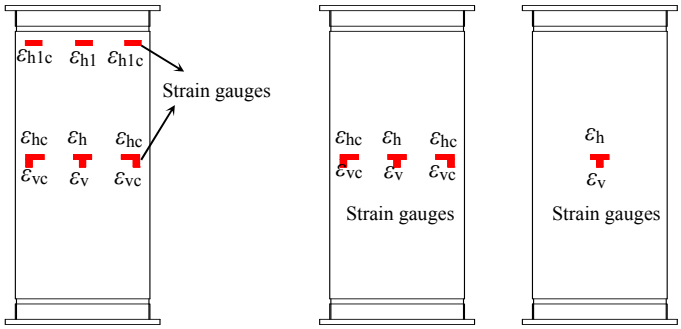

Figure 6. Strain Gauges Arrangement on Steel Tubes

Figure 7 depicts axial load versus strain/stress curves for tubes of representative columns, in which σ_v and σ_h are respectively longitudinal and transverse stresses at the mid-height of columns and σ_z is the equivalent stress. The tension stress σ_{h1} is the transverse stress at the top-end of the tube. The components of strain and stress at corners are represented with subscript "c".

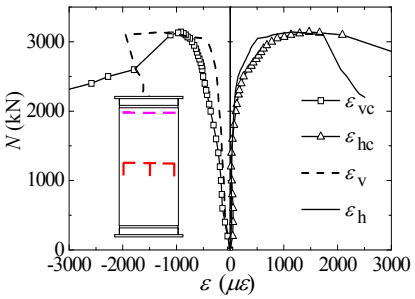

(a1) load-strain curves for mid-height points of S(GS)-200-1

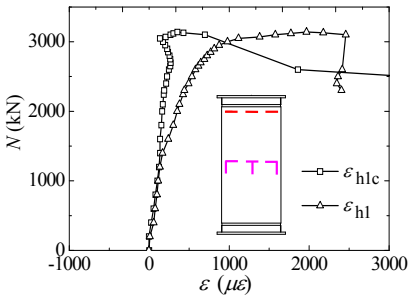

(b1) load-strain curves for top-end points of S(GS)-200-1

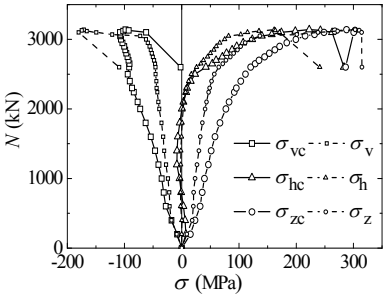

(a2) load-stress curves for mid-height points of S(GS)-200-1

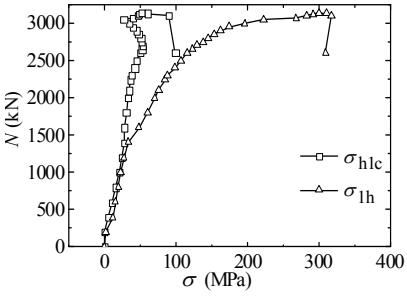

(b2) load-stress curves for top-end points of S(GS)-200-1

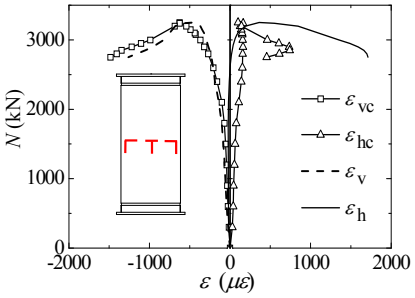

(c1) load-strain curves for mid-height points of S(OS)-200-1

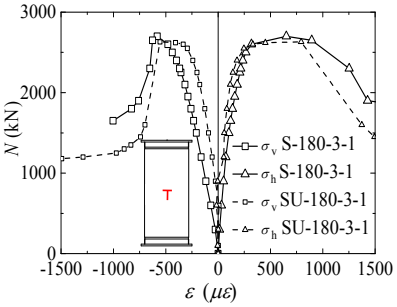

(d1) load-strain curves for mid-height points of STC-180

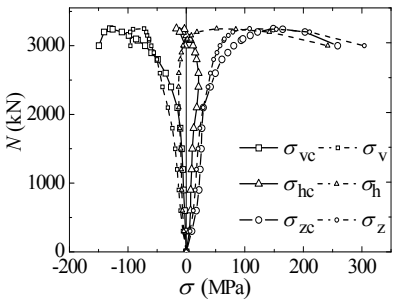

(c2) load-stress curves for mid-height points of S(OS)-200-1

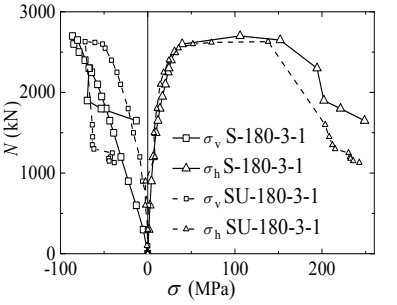

(d2) load-stress curves for mid-height points of STC-180

Figure 7. Load-strain and Load-stress Curves of Steel Tubes

As shown in Figures 7a, 7c and 7d, both transverse and longitudinal strains/stresses at mid-height of the tube follow a development trend. Taking S(GS)-200-1in Figure 7a as an example, at the elastic stage, the vertical and transverse stresses and strains increase linearly due to the bonding action between concrete and steel tube. The vertical strain and stress increase faster than the transverse ones. When axial loads get close to the resistance of the core RC column, the vertical

and transverse stresses increase quickly and show a non-linearity feature. At the peak load, the average equivalent stress of the tube does not reach the yield strength, while at least one corner of the tube yields. After the peak load, the vertical and transverse strains keep increasing and the transverse strain and stresses increase faster than the vertical ones. During the testing, the stress components at the corners are higher than those at the middle position for the same load level for STRC columns

Figure 7b shows the transverse strain and stress at the top end of tube for STRC(GS) columns. The transverse stress and strain increase with the increase of axial load at the elastic stage and the increase is more obvious at the elastic-plastic stage.

During the testing, the longitudinal stresses of Specimens S-180-3-80 are greater than those of Specimens SU-180-3-80 with reducing friction at the same load level (Figure 7d).

2.4 Experiment Results and Analysis

Table 2 lists the peak load and stress components of tubes. N_u denotes the peak load. Specimens S(GS)-200-2 and S(OS)-240-2 are not included when computing the average peak load because of local failure. σ_v, σ_h, and σ_z are the average stresses of the two opposite plates at the same location.

Table 2. Comparison of Experiment Results at Peak Loads

Specimens	N_u(kN)	Average value	σ_{vc}(MPa)	σ_{hc}(MPa)	σ_{zc}(MPa)	σ_v(MPa)	σ_h(MPa)	σ_z(MPa)
S(GS)-200-1	3143.2	3143.2	-98.3	222.9	287.8	-171.0	161.4	302.8
S(GS)-200-2	2623.4		-166.1	-78.0	206.8	31.9	273.3	264.6
S(OS)-200-1	3250.2		-130.2	-16.9	148.7	-72.5	51.6	108.0
S(OS)-200-2	3086.0		-97.6	-67.6	258.8	-146.7	113.7	230.7
S(OS)-200-3	3381.0	3264.0	-193.9	-65.7	186.2	-88.0	70.1	138.7
S(OS)-200-4	3241.3		-179.1	58.5	232.0	-41.5	72.2	100.6
S(OS)-200-5	3361.5		-108.9	125.1	204.3	-103.0	104.4	180.0
RC-200-1	2717.2		-	-	-	-	-	-
RC-200-2	2774.0		-	-	-	-	-	-
RC-200-3	3015.0		-	-	-	-	-	-
S(GS)-240-1	3758.7	3758.9	-35.5	220.0	219.7	-12.9	268.1	274.7
S(GS)-240-2	3759.0		-2.7	299.4	299.4	-41.4	241.4	265.4
S(OS)-240-1	4090.5		-124.0	54.5	184.6	-123.4	26.4	140.3
S(OS)-240-2	3686.5		-183.4	80.2	242.6	-132.6	66.5	177.8
S(OS)-240-3	3872.6	3928.9	-176.1	3.6	190.3	-91.4	68.1	139.1
S(OS)-240-4	3775.8		-155.6	127.7	251.4	-62.1	233.7	271.3
S(OS)-240-5	3976.5		-181.9	101.9	251.9	-94.3	79.9	152.3
RC-240-1	3268.9		-	-	-	-	-	-
RC-240-2	3166.4		-	-	-	-	-	-
RC-240-3	3351.2		-	-	-	-	-	-
S-180-3-80-1	2700.0	2810	-	-	-	-86.3	106.0	166.8
S-180-3-80-2	2920.0		-	-	-	-78.1	120.6	173.4
SU-180-3-80-1	2630.0	2730	-	-	-	-71.8	138.2	184.8
SU-180-3-80-2	2830.0		-	-	-	-62.3	142.8	182.1

The average peak load for STC columns without reducing friction is a slightly higher than STC columns with reducing friction. The average peak loads for STRC(OS) columns are slightly higher than those of the STRC(GS). It could be conclude larger friction coefficients correspond to greater axial load-carrying capacities for square tubed columns. However, the peak loads for circular tubed RC (CTRC) columns with galvanized tube are higher than those of the CTRC columns with ordinary tube although the strengths of concrete and tube are lower than those reported in (Liu *et al.* [9]). Thus, the effect of friction on the composite response of STRC columns is different from that of CTRC columns.

Because the value of friction coefficient of ordinary tubes is higher than that of galvanized tubes, stress concentration at the tube corners does not fully propagate to middle part. Thus, the equivalent stress of the ordinary tube at corner was larger than that at the middle point, and the equivalent stresses between the middle point and corner of the galvanized tube was close to each other. The longitudinal stresses at the middle point for STC columns without reduced friction is higher than STC columns with reduced friction, but this trend is not visible for transverse stresses. Thus, the stress state at the peak load is influenced by the interface between steel tube and concrete. Larger friction coefficient corresponds to larger longitudinal stresses.

The effect of friction coefficient on stress state and axial load-carrying capacity is further discussed in the following finite element analysis section. At the peak load, at least one corner of the tube yields for almost all specimens, while the average equivalent stress does not reach the yield point due to the uncertainties such as imperfections and loading eccentricity involved in the experiments.

3. FINITE ELEMENT ANALYSIS (FEA)

The Damaged Plasticity Model (DPM) for concrete available in ABAQUS (Dassault Systems [19]) was used to analyze the tubed columns subjected to axial compression. A nonlinear finite element (FE) model considering nonlinear material behavior was developed. The FE model was then used to investigate the influence of important system parameters on the ultimate strength of the columns. The steel tube was modelled using 4-node shell elements with reduced integration (S4R). A perfect elastic-plastic model consisting of two distinct loading stages was used to describe the mechanical behavior of the steel. The concrete core was simulated by using 8-node brick elements (C3D8R), with three translation degrees of freedom at each node.

3.1 Material Properties

The strength increase and ductility improvement arise from the confinement effect on the concrete. The increased strength can be achieved by defining a yielding surface. The increased peak strain and the even descending branch of stress-strain curve reflect the ductility improvement. A modified concrete stress-strain curve for tubed columns is proposed based on Li *et al*. [20] (Figure 8).

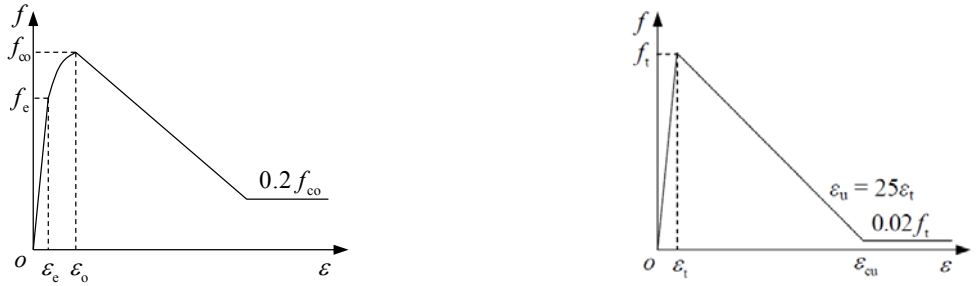

(a) compression (b) tension

Figure 8. Stress-strain Curves for Concrete

The compression stress-strain curve for concrete is

$$f=\begin{cases} E_{\mathrm{c}}\varepsilon+\dfrac{(f_{\mathrm{co}}-E_{\mathrm{c}}\varepsilon_{\mathrm{co}})}{\varepsilon_{\mathrm{co}}^{2}}\varepsilon^{2} & 0\le\varepsilon\le\varepsilon_{\mathrm{e}} \\ f_{\mathrm{co}}-\dfrac{(f_{\mathrm{co}}-f_{\mathrm{e}})}{(\varepsilon_{\mathrm{o}}-\varepsilon_{\mathrm{e}})^{2}}\times(\varepsilon-\varepsilon_{\mathrm{o}})^{2} & \varepsilon_{\mathrm{e}}\le\varepsilon\le\varepsilon_{\mathrm{o}} \\ f_{\mathrm{co}}-\beta\dfrac{f_{\mathrm{co}}}{\varepsilon_{\mathrm{o}}}\times(\varepsilon-\varepsilon_{\mathrm{o}})\ge 0.2f_{\mathrm{co}} & \varepsilon>\varepsilon_{\mathrm{o}} \end{cases} \tag{1}$$

where

f_{co} = the compressive strength of concrete,

E_{c} = the initial Young's modulus of concrete, $E_{\mathrm{c}}=4730\sqrt{f_{\mathrm{co}}}$,

$\varepsilon_{\mathrm{co}}$ = the strain at maximum strength of unconfined concrete f_{co}, $\varepsilon_{\mathrm{co}}=(700+172\sqrt{f_{\mathrm{cu}}})\times10^{-6}$ as given by Guo *et al*. [21], (f_{cu} being the compressive strength for 150×150×150mm cubic specimen),

ε_{o} = the peak strain of concrete for the FE model, $\varepsilon_{\mathrm{o}}=\varepsilon_{\mathrm{cc}}-[(\dfrac{f_{\mathrm{cc}}}{f_{\mathrm{co}}}-1)]\varepsilon_{\mathrm{co}}$,

$\varepsilon_{\mathrm{cc}}$ = the strain at maximum confined strength of concrete f_{cc}, $\varepsilon_{\mathrm{cc}}=[1+5(\dfrac{f_{\mathrm{cc}}}{f_{\mathrm{co}}}-1)]\varepsilon_{\mathrm{co}}$ as given by Mander *et al*. [22],

ε_{e} = the maximum strain for first part of the stress-strain relationships taken as $0.75\varepsilon_{\mathrm{o}}$ here,

f_{e} = compressive stress of concrete at the strain ε_{e}, calculated using Eq. 1, and

β = factor to control the slope of the descending branch, $\beta=0.0243(\dfrac{f_l}{f_{\mathrm{co}}})^{-0.686}\le0.5$.

The compressive strength of confined concrete can be calculated by Eq. 2 (Li *et al*. [20], Mander *et al*. [22])

$$f_{\mathrm{cc}}=\begin{cases} f_{\mathrm{co}}\left(-1.254+2.254\sqrt{1+7.94\dfrac{f_l}{f_{\mathrm{co}}}}-2\dfrac{f_l}{f_{\mathrm{co}}}\right) & f_{\mathrm{co}}<50\mathrm{MPa} \\ f_{\mathrm{co}}\left(-0.413+1.413\sqrt{1+11.4\dfrac{f_l}{f_{\mathrm{co}}}}-2\dfrac{f_l}{f_{\mathrm{co}}}\right) & 80\mathrm{MPa}\ge f_{\mathrm{co}}\ge50\mathrm{MPa} \end{cases} \tag{2}$$

where f_l is the confining stress of the square tube.

A modified model based on reference [22] was suggested for square tubed columns. As a result, f_l is calculated using Eq. 3

$$f_l=k_{\mathrm{e}}f_{\mathrm{r}} \tag{3}$$

where k_{e} is the confinement effectiveness coefficient for square tubed columns defined by the following equation when the area of longitudinal rebars is ignored

$$k_{\mathrm{e}}=\frac{A_{\mathrm{e}}}{A}=\left(1-\sum_{i=1}^{n}\frac{(D_{\mathrm{i}})^{2}}{6D_{\mathrm{i}}^{2}}\right)=1/3 \tag{4}$$

f_{r} is the lateral pressure from the tube assumed to be uniformly distributed over the surface of the concrete core, which is equal to the lateral pressure provided by the circumcircle of the square tube (Figure 9), i.e.

$$f_{\mathrm{r}}=2\frac{tf_{\mathrm{y}}}{\sqrt{2}D-2t} \tag{5}$$

(a) Effectively confined cross section

(b) Lateral pressure f_r provided by the circumcircle of a square section

Figure 9. Effective Confinement Model for Square Tubed Columns

For concrete in tension, a simplified stress-strain relationship was used in the analysis, in which f_t and ε_t are the tensile strength and the strain at the tensile strength of concrete respectively, and ε_{cu} is the ultimate strain of concrete in tension taken as $25\varepsilon_t$ here. The empirical expressions for defining f_t and ε_t are [21]

$$f_t = 0.26 f_{cu}^{2/3} \tag{6}$$

$$\varepsilon_t = 65 \times 10^{-6} f_t^{0.54} \tag{7}$$

In the DPM for concrete, the dilation angle Ψ = 38º was suggested. K_c was defined as $K_c = (\sqrt{J_2})_{TM} / (\sqrt{J_2})_{CM}$, where $0.5 < K_c \leq 1$ and TM and CM designate respectively the "tensile meridian" and the "compressive meridian" on the yield surface. K_c = 0.67 was suggested for square tube confined concrete [19].

3.2 Effect of Friction

Friction is an important factor which influences the composite response of tubed columns as the bond is likely broken during a test. A surface-based interaction with a contact pressure model in the normal direction and a Coulomb friction model in the tangential direction to the surface between steel tube and core concrete (Han *et al*. [23]) was used in the finite element analysis (FEA). The interface elements consist of two matching contact faces of steel tube and concrete elements. The friction coefficient μ between steel and concrete suggested by Rabbat *et al*. [24], Baltay *et al*. [25] and Aly *et al*. [26] is within the range of 0.2~0.65. Therefore, μ = 0.2 was used for galvanized tubes and μ = 0.6 was employed for ordinary tubes. Figure 10 depicts the FEA results for specimens S(OS)-200 and S(GS)-200. The analysis results agree well with the experimental ones. The finite element method and the suggested values for the parameters could also accurately predict the behavior of circular tubed columns (Liu *et al.* [9]).

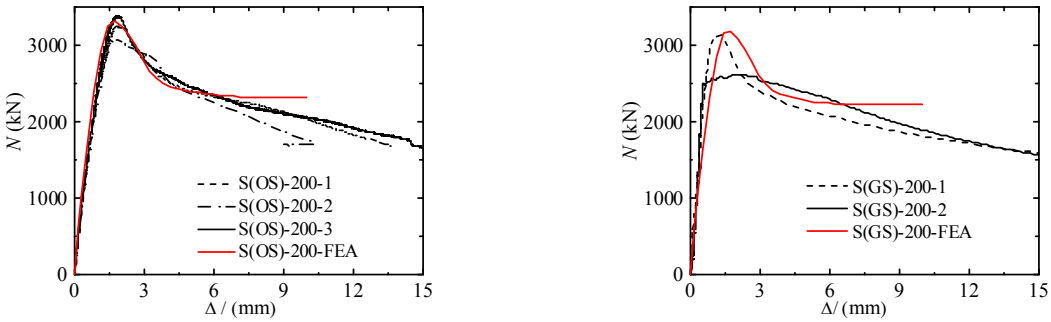

(a) STRC(OS)-200 (b) STRC(GS)-200

Figure 10. Comparison of Load (N)-axial Displacement (Δ) Curves between Test and FEA Results

To investigate the mechanisms of square tubed columns (STC) subjected to axial load, square tubed columns (STCs) were designed first to study the effect of friction coefficient in ABAQUS. All parameters maintained at constant values except the friction coefficient μ changed from 0 to 1.0. The parameters and analysis results are summarized in Table 3. Figure 11 shows the FE model and von Mises stress components for specimen with μ = 0.6, in which the corners of tube yield at the peak load. The FEA results agree well with the experimental ones. The analysis results also show that the specimen with larger friction coefficient yields higher axial load strength. Thus, it is deduced that the square tube is more beneficial to direct bearing of axial loads than concrete confining if it does not buckle. The effectiveness of confinement for square tube is significantly reduced implying that the square tube cannot be fully utilized. This explains that the axial strength of square tubed columns is greater than that of square CFT columns when the width to thickness ratio (D/t) of tube is around 70 and the trend reverses when D/t < 47 as reported by Zhang *et al*. [12]. In order to provide sufficient confinement to concrete core and longitudinal reinforcement, D/t ratio should be limited or a stiffening arrangement should be made for square thin-walled tubes. The strength is little affected when the friction coefficient exceeds 0.6.

Table 3. Effect of the Friction Coefficient on Resistances of STC Specimens

D(mm)	t(mm)	f_y(MPa)	f_{co}(MPa)	μ	Peak load(kN)	Comparisons
200	1.5	310	38.0	0	1613.7	100.0%
				0.2	1649.9	102.2%
				0.4	1673.7	103.7%
				0.6	1687.5	104.6%
				0.8	1693.0	104.9%
				1.0	1693.9	105.0%

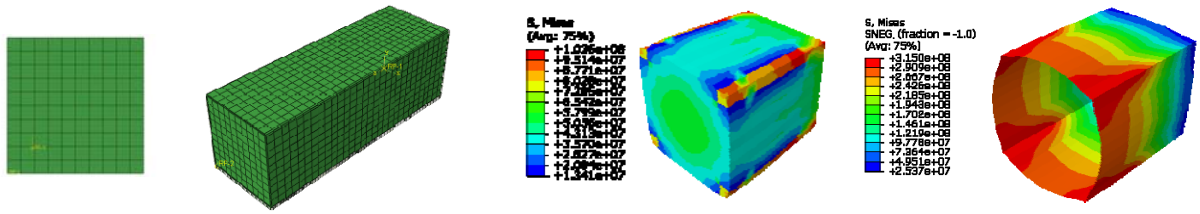

(a) Model for STC-200 (b) Equivalent stress for concrete (Half model) (c) von Mises stress for tube of STC-200

Figure 11. FE Modal and Analysis Results of STC-200

3.3 Effect of the Chamfered Corner Radius

The out-of-plane flexural stiffness of thin-walled tubes is small. Therefore, the tubes provide little confinement pressure by flexure. The confinement effect of square tubes is mainly provided by the arch action at the corners. As such, stress concentration occurs at the corners. The larger the corner radius is, the greater the confinement effect. The square tube changes into a circular one when the corner radius equals to half width dimension. A group of square tubed columns were designed to study the effect of corner radii in ABAQUS. Table 4 lists the dimension, material property, and analysis results, in which S-200 points to a sharp corner and S-200-5mm represents a specimen with 5mm corner radius. It was found the axial load-carrying capacity of specimen S-200-5mm was 11.6% larger compared to specimen S-200. The axial load-carrying capacities of STRC(OS)-200 specimen with 2 mm and 5 mm are 5.8% and 6.8% larger compared to the specimen with sharp corner radius, respectively. The increasing percentages are smaller because of a higher axial load-carrying capacity due to longitudinal rebars. Figure 12 depicts the load-displacement curves. The whole cross section of tube yields for Specimen S-200-5mm, while only the corners of tube yield for specimen S-200 (Figure 13). Chamfered corners can effectively improve the confinement effect of square tubes.

Table 4. Axial Compression Capacities of Specimens with Sharp and Chamfered Corners

Specimens	Width D (mm)	t (mm)	f_y (MPa)	f_{co} (MPa)	μ	Peak load (kN)	Increasing percentage
S-200	200	1.5	315.0	47.4	0.6	1991.7	0
S-200-5mm						2230.0	11.6%
STRC(OS)-200-sharp						3321.8	0
STRC(OS)-200-2mm	200	1.5	364.3	48.1	0.6	3513.7	5.8%
STRC(OS)-200-5mm						3546.8	6.8%

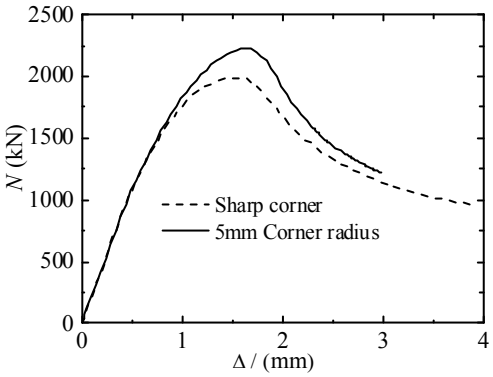

Figure 12. Load-displacement Curves for the Specimens with Sharp Corners and 5mm Corner Radius

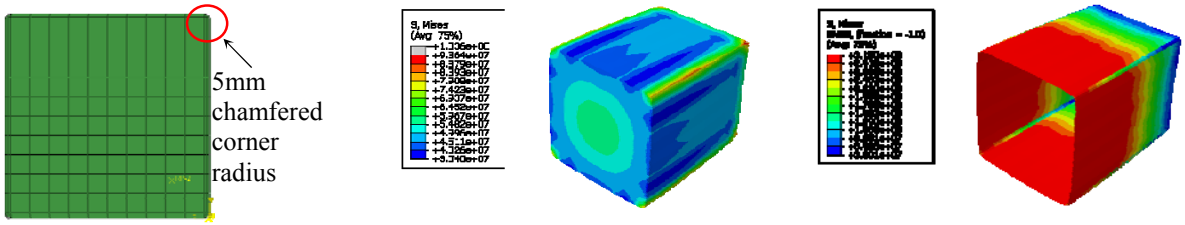

Model for S-200-5mm | Equivalent stress for concrete | von Mises stress for the tube

(a) S-200-5mm

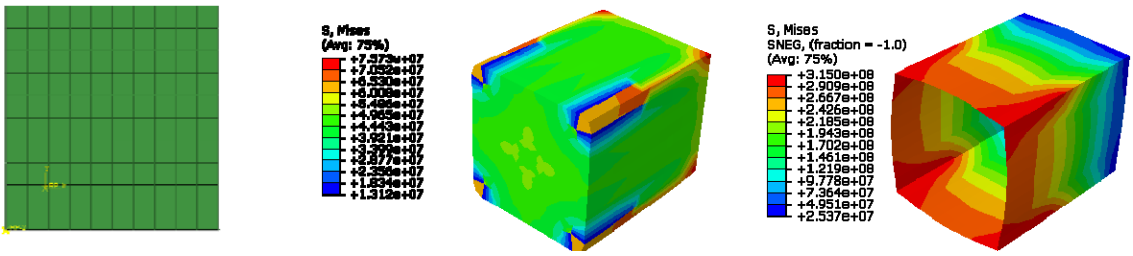

Model for S-200 Equivalent stress for concrete von Mises stress for the tube

(b) S-200

Figure 13. FEA Model and Stress Analysis Results for S-200-5mm and S-200 at Peak Load

The selection of 5 mm represents a typical corner radius of cold-formed square tube being welded at the middle of the plate, as also referenced in (Liu *et al*. [3], Qi *et al*. [17]). In the tests done by Sakino *et al*. [10-11] and Yamamoto *et al*. [13], the square tubes were welded at the sharp corners. In this study, the corner radius of specimens was about 2mm based on the measurement of the tube. The peak loads predicted by the FEA for specimen STRC(OS)-200 are 3321.8 kN (sharp corners), 3513.7 kN (2mm corner radius) and 3546.8 kN (5mm corner radius). The FEA results offer the explanation why there is discrepancy between experimental and theoretical results reported in references. Cold-formed steel tubes are recommended in practice because of better structural behavior due to chamfered corners when square cross sectional columns are used.

4. AXIAL LOAD-CARRYING CAPACITIES OF STUB SQAURE TUBED COLUMNS

Based on the experimental and numerical researches, the difference of axial load-carrying capacities between specimens with different tube or different friction is within 5%, as shown in Table 2 and Table 3. Simply considering the tube as an element to confine the concrete will result in a conservative axial compressive strength.

The axial load-carrying capacity can be determined by

$$N_{\mathrm{u}} = f_{\mathrm{cc}} A_{\mathrm{c}} + f_{\mathrm{a}} A_{\mathrm{a}} \tag{8}$$

where A_{c} and A_{a} are the cross-sectional area of concrete and longitudinal reinforcement (structural steel), respectively; f_{a} is the yield strength of longitudinal reinforcement or structural steel; f_{cc} is the compressive strength of confined concrete.

A modified model based on the effective confinement area method for square stirrups confined concrete (Mander *et al*. [22]) which has been widely accepted was suggested to compute f_{cc} of square tubed columns. In practice, the average stress at the corners does not yield at the peak load due to initial imperfection of the columns and experimental uncertainties, while at least one corner yields for almost all specimens as shown in the previous tests. Thus, an effective utilization index k_{t} was adopted to account for the non-uniform stress distribution on the tube. k_{t} is defined as the ratio of the average stress of the corners to the yield strength of tube. k_{t} can be taken as 0.8 based on the experimental results. The effective lateral confining pressure $f_{\mathrm{r}}^{'}$ can be calculated by

$$f_{\mathrm{r}}^{'} = k_{\mathrm{t}} f_{l} = k_{\mathrm{e}} k_{\mathrm{t}} f_{\mathrm{r}} \tag{9}$$

k_e is given by Eq. 4. The confined compressive strength f_{cc} can be computed by substituting f_r' into Eq. 2.

A total of 124 experimental axial strength values for tubed columns were collected from (Liu *et al*. [3], Han *et al*. [8], Sakino *et al*. [10-11], Zhang *et al*. [12], Yamamoto *et al*. [13], and Qi *et al*. [17]). The considered test parameters for the experimental results include width to tube thickness ratio *D*/*t* (20-162), concrete strength (28.5-132 MPa), and longitudinal reinforce ratio (0-6.5%). The results predicted by Eq. 8 agree well with the experimental results (Figure 14). The average ratio of predicted axial strength to experimental axial strength is 0.92. The root-mean-square deviation is 0.14 and the correlation coefficient is 0.94.

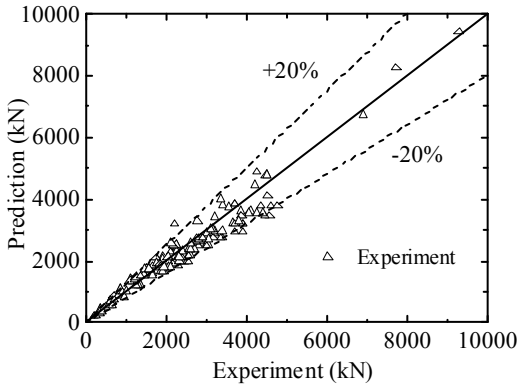

Figure 14. Comparisons between Eq. 8 and the test results

5. SUMMARY AND CONCLUSIONS

This paper describes and discusses the structural behavior of square tubed columns under axial compression experimentally, analytically, and numerically. Based on this study, the following conclusions are offered.

(1) The types of the interface between the tube and concrete cannot influence on the failure modes of the square tubed columns. Shear failure of core concrete occurred in square tubed columns with width-to-thickness ratios of 60-160. Strength and ductility of the contrasting RC columns can be improved by using the tube with large width-to-thickness ratios of 133-160.
(2) For both galvanized and ordinary tubes, the average stress at the corner of the tubes did not yield at the peak load, while at least one corner yielded for almost all the specimens. Larger friction coefficient corresponds to larger longitudinal stresses and slightly larger axial compressive strength.
(3) The predicted results from the nonlinear finite element analysis are in good agreement with the test results. The greater the corner radius is, the larger the axial load capacity. Axial load-carrying capacities between different friction coefficients varied within 5%. There is no need to eliminate the bond and friction effect in practice. Cold-formed steel tubes are recommended in practice because of better structural behavior due to chamfered corners.
(4) A simplified effective confinement model, simply and conservatively considering tubes as elements to confine in-filled concrete together with the effective utilization of square tubes, was proposed to predict axial load-carrying capacities. The predicted results are in good agreement with experimental results.

ACKNOWLEDGEMENT

The authors greatly appreciate the financial supports provided by the National Natural Science Foundation of China (No. 51308051 & 51438001), Chongqing Research Program of Basic Research and Frontier Technology (No. cstc2016jcyjA0284) and the China Scholarship Council. The opinions expressed in this paper are solely of the authors, however.

REFFERENCES

[1] Kang, W.H., Uy, B., Tao, Z. and Hicks, S., "Design Strength of Concrete-filled Steel Columns", Advanced Steel Construction, 2015, Vol. 11, No. 2, pp. 165-184.

[2] Liu, S.W., Liu, Y.P. and Chan, S.L., "Advanced Analysis of Hybrid Steel and Concrete Frames: Part 1: Cross-section Analysis Technique and Second-order Analysis", Jounral of Constructional Steel Research, 2012, Vol. 70, pp. 326-336.

[3] Liu, J.P. and Zhou, X.H., "Behavior and Strength of Tubed RC Stub Columns under Axial Compression", Journal of Constructional Steel Research, 2010, Vol. 66, No. 1, pp. 28-36.

[4] Gan, D., Zhou, X.H., Yan, B., Han, F.L. and Liu, J.P., "Experimental Studies on Structural Behavior of Circular Tubed Reinforced Concrete Joints with Ring Ribs", Journa of Building Structures, 2018, Vol. 39, No. 4, pp. 91-101. (In Chinese)

[5] Sakino, K., Tomii, M. and Watanabe, K., "Sustaining Load Capacity of Plain Concrete Stub Columns Confined by Circular Steel Tube", Proceeding of the International Speciality Conference on Concrete Filled Steel Tubular Structures, Harbin, China, 1985, pp.112-118.

[6] Orito, Y., Sato, T., Tanaka, N. and Watanabe, Y., "Study on the Unbonded Steel Tube Composite System", Proceedings, Composite Construction in Steel and Concrete, Engineering Foundation, 1987, pp. 786-804.

[7] Fam, A., Qie, F.S. and Rizkalla, S., "Concrete-Filled Steel Tubes Subjected to Axial Compression and Lateral Cyclic Loads", Journal of Structural Engineering, 2004, Vol. 125, No. 5, pp.631-640.

[8] Han, L.H., Yao, G.H., Chen, Z.P. and Yu, Q., "Experimental Behaviour of Steel Tube Confined Concrete (STCC) Columns", Steel and Composite Structures, 2005, Vol. 5, No. 6, pp. 459-484.

[9] Liu, J.P., Zhou, X.H. and Gan, D., "Effect of Friction on Axially Loaded Stub Circular Tubed Columns", Advances in Structural Engineering, 2016, Vol. 19, No. 3, pp. 546-59.

[10] Sakino, K. and Sun, Y.P., "Stress-strain Curve of Concrete Confined by Rectilinear Hoop", Journal of Structural and Constructional Engineering, 1994, No. 461, pp. 95-104.

[11] Sakino, K. and Sun, Y.P., "Steel Jacketing for Improvement of Column Strength and Ductility", 12th World Conference on Earthquake Engineering, Auckland, New Zealand, 2000, pp. 2525-40.

[12] Zhang, S.M. and Liu, J.P., "Seismic Behavior and Strength of Square Tube Confined Reinforced-concrete", Journal of Constructional Steel Research, 2007, Vol. 63, No. 9, pp. 1194-1207.

[13] Yamamoto, T., Kawaguchi, J. and Morino, S., "Experimental Study of Scale Effects on the Compressive Behavior of Short Concrete-Filled Steel Tube Columns", Composite Construction in Steel and Concrete IV Proceedings of the Fourth International Conference on Composite Construction in Steel and Concrete, ASCE Conf. Proc., 2000, pp. 879- 890.

[14] Kwon, S.H., Kim, Y.Y. and Kim, J.K., "Long-term Behavior under Axial Service Loads of Circular Columns made from Concrete Filled Steel Tubes", Magazine of Concrete Research, 2005, Vol. 57, No. 2, pp. 87-99.

[15] Kwon, S.H., Kim, T.H. and Kim, Y.Y., "Long-term Behavior of Square Concrete Filled Tubular Columns under Axial Service Loads", Magazine of Concrete Research, 2007, Vol. 59, No. 1, pp. 53-69.
[16] Yu, Q., Tao, Z. and Liu, W., "Analysis and Calculations of Steel Tube Confined Concrete (STCC) Stub Columns", Journal of Constructional Steel Research, 2010, Vol. 66, No. 1, pp. 53-64.
[17] Qi, H.T., Guo, L.H., Liu, J.P. and Gan, D., "Axial Load Behavior and Strength of Tubed Steel Reinforced-concrete (SRC) Stub Columns", Thin-Walled Structures, 2011, Vol. 49, No. 9, pp. 1141-1150.
[18] Zhang, S.M., Guo, L.H. and Ye, Z.L., "Behavior of Steel Tube and Confined Concrete High Strength Concrete for Concrete-filled RHS Tubes", Advances in Structural Engineering, 2008, Vol. 8, No. 5, pp. 101-116.
[19] ABAQUS Version 6.8-1, "User Documentation", Dassault Systems, 2008.
[20] Li, B., Park, R. and Tanaka, H., "Stress-strain Behavior of High-strength Concrete Confined by Ultra-high and", ACI Structural Journal, 2001, Vol. 98, No. 3, pp. 395-406.
[21] Guo, Z.H. and Shi, X.D., "Reinforced Concrete Theory and Analyses. Beijing, China: Tsinghua University Press", 2003. [in Chinese].
[22] Mander, J.B., Priestley, M.J.N. and Park, R., "Theoretical Stress-strain Model for Confined Concrete", Journal of Structural Engineering, 1988, Vol. 114, No. 8, pp. 1804-1826.
[23] Han, L.H., Yao, G.H. and Tao, Z., "Performance of Concrete-filled Thin-walled Steel Tubes under Pure Torsion", Thin-Walled Structures, 2007, Vol. 45, No. 1, pp. 24-36.
[24] Rabbat, B.G. and Russell, H.G., "Friction Coefficient of Steel on Concrete or Grout", Journal of Structural Engineering, 1985, Vol. 111, No. 3, pp. 505-515.
[25] Baltay, P. and Gjelsvik, A., "Coefficient of Friction for Steel on Concrete at High Normal Stress", Journal of Materials in Civil Engineering, 1990, Vol. 2, No. 1, pp. 46-49.
[26] Aly, T., Eichalakani, M. and Thayalan, P., "Incremental Collapse Threshold for Pushout Resistance of Circular Concrete Filled Steel Tubular Columns", Journal of Constructional Steel Research, 2010, Vol. 66, No. 1, pp. 11-18.

STRUCTURAL PERFORMANCE AND DESIGN METHOD OF NEW MORTISE–TENON FULL STEEL-TUBE SCAFFOLD

Liu Hongbo[1,2], Zhou Yuan[2], Chen Zhiua[1,2*] and Liu Qun[3]

[1] *State Key Laboratory of Hydraulic Engineering Simulation and Safety, Tianjin University, Tianjin 300072, China*
[2]*School of Civil Engineering, Tianjin University, Tianjin 300072, China*
[3]*China Academy of Building Research, Beijing 100013, China*
**(Corresponding author: E-mail: zhchen@tju.edu.cn)*

Received: 12 August 2016; Revised: 26 March 2017; Accepted: 25 June 2017

ABSTRACT: A mortise–tenon steel-tube scaffold, a new steel-tube scaffold, was presented based on ancient mortise–tenon joint in wood structure. Because of better joint mechanics and higher bearing capacity than coupler-type steel-tube scaffold, this new scaffold possesses good market potential. Based on an analysis of the bearing mechanism, a finite element numerical analysis model for the mortise–tenon steel-tube scaffold was established in this study, which was validated as reasonable and accurate by experiment data. Influencing laws of storey height, vertical member interval, X-bracing layout, overall structure height, height of bottom horizontal tube, and height of upper cantilever bar on the mortise–tenon steel-tube scaffold were determined through parameter analysis. A simplified calculation formula of ultimate bearing capacity was established, which verified by FEM results and test data. Research results provide important references for future in-depth studies and engineering applications of the mortise–tenon steel-tube scaffold.

Keywords: Mortise–tenon joint, steel-tube scaffold, numerical simulation, parameter analysis, simplified calculation formula

DOI: 10.18057/IJASC.2018.4.2.9

1. INTRODUCTION

Scaffolds have been widely used in engineering construction as temporary supporting structures. Existing common scaffolds mainly include door-type steel-tube scaffold (Figure 1a), inserting-type steel-tube scaffold (Figure 1b), cuplock steel tubular scaffold (Figure 1c) and coupler-type steel-tube scaffold (Figure 1d). Because the scaffolds are usually used as a temporary supporting structure, its structural behavior and design method have not attracted adequate attention. In recent years, scaffold collapse accidents have occurred frequently because of poor site management and unreasonable design, thereby causing huge economic losses and casualties. Therefore, research on structural behavior and design method of scaffolds has attracted increasing attention in recent years.

Although the scaffold is a temporary structure, its mechanical properties are more complicated than those of a permanent steel structure because of complicated structural defects and damage distribution caused by repeated use. Chan et al. [1], Peng et al. [2–6], Yu et al. [7], and Weesner and Jones [8] conducted numerous experimental and theoretical studies on the stability capacity and design method of door-type scaffolds. Micha and Blazik-Borowa [9] determined the capacity of the key joint in inserting-type scaffolds using numerical analysis. Peng et al. [10] investigated the load capacities and failure modes of inserting-type scaffolds by experimental tests. Zhang et al. [11–13] conducted research on cuplock-type scaffolds using the probability-based design method. Beale et al. [14–16], Ao et al. [17], Yue et al. [18] and Liu et al. [19–20] conducted systematic studies on stability capacity and design method of multi-span coupler-type steel-tube scaffold using experimental research and numerical analysis.

(a)Door-type Scaffolds

(b)Inserting-type scaffold

(c)Cuplok-type Scaffold

(d)Steel Tube-Coupler Scaffold

Figure 1. Four Types of Scaffolds

Engineering accident analysis shows that unstable connection performance of joints is the main cause of scaffold collapse [21]. To search for a safe and stable scaffold system, Tianjin University and Tianjin Xunan Jiahui Building Materials Technological Co. Ltd. developed the mortise–tenon steel-tube scaffold based on mortise–tenon joint in ancient wood structure. In this study, a numerical analysis model was proposed to analyze the structural behavior of effects of the mortise–tenon steel-tube scaffold, which was verified by experimental data. And a simplified calculation formula is also proposed to predict the ultimate bearing capacity of the mortise–tenon steel-tube scaffold.

2. STRUCTURAL DETAIL OF MORTISE–TENON STEEL-TUBE SCAFFOLD

The mortise–tenon steel-tube scaffold is composed of horizontal members, vertical members, adjustable support brackets, and ground members as shown in Figure 2. The adjustable support brackets are placed on top of the vertical members for transmitting construction loads. The ground members are set at the bottom of the vertical members to increase stability of the structure.

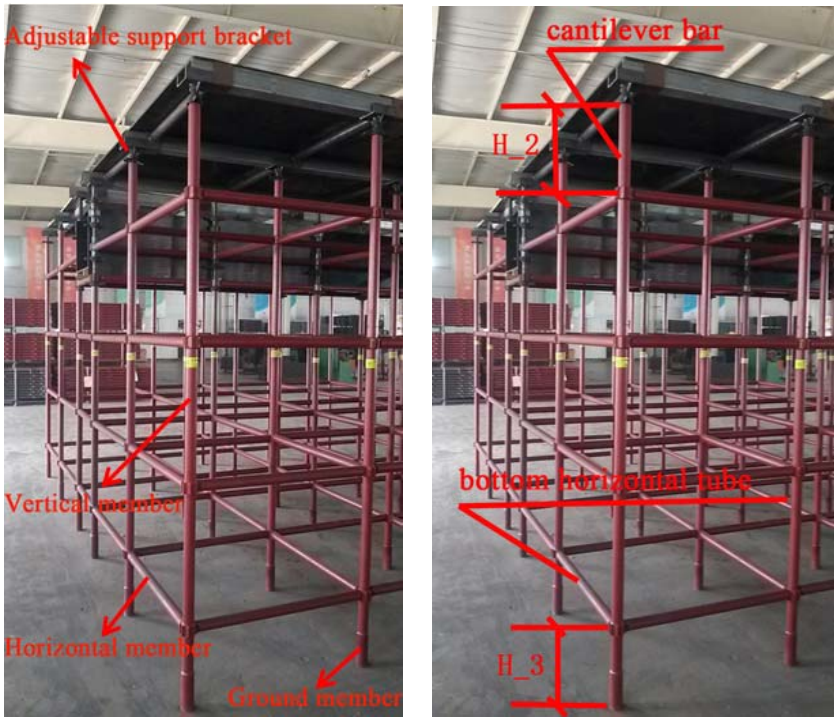

Figure 2. Structure of Mortise–tenon Steel-tube Scaffold

Compared with existing common scaffolds, the mortise–tenon joint is the main innovative point for the mortise–tenon steel-tube scaffold. The design of the mortise–tenon joint is inspired by the mortise–tenon joint in ancient wood structure. In fact, the mortise–tenon joint is a wedged concave-convex connection mode. The wedged convex is the tenon and the wedged concave is the mortise as shown in Figure 3 and Figure 4. The horizontal members are P48.3 mm × 3.5 mm standard steel tube with the tenon at two ends (Figure 3). The vertical members are P48.3 mm × 3.5 mm standard steel tube with the mortise rings (Figure 4). The tenon on the horizontal member is inserted into the mortise ring of the vertical member, which achieves the connection of horizontal and vertical members (Figure 5). Since the mortise–tenon joint has good shear capacity and rotational rigidity, the bearing capacity of the mortise–tenon steel-tube scaffold was higher than that of other scaffolds.

The sleeve coupler is used to connect the vertical steel tubes as shown in Figure 6. The swivel coupler is used to connect the vertical steel tubes and X-bracing steel tubes as shown in Figure 7.

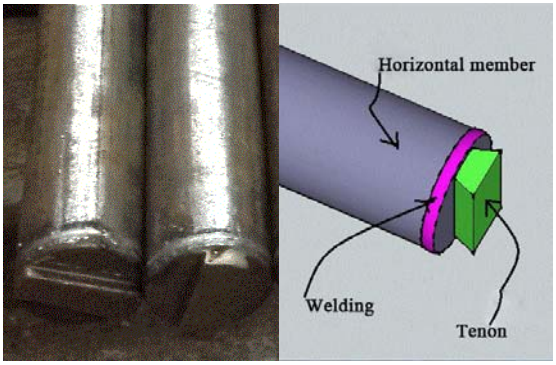

(a) Physical object (b) Model

Figure 3. Horizontal Member

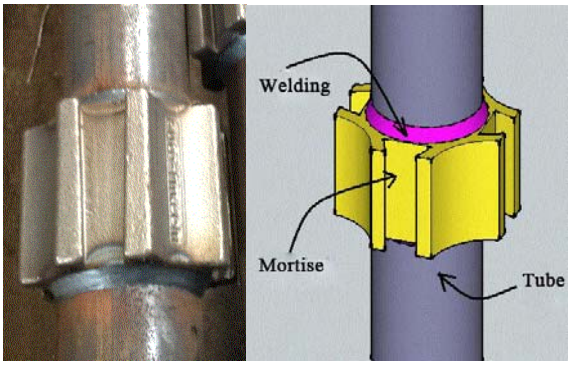

(a) Physical object (b) Model

Figure 4. Vertical Member

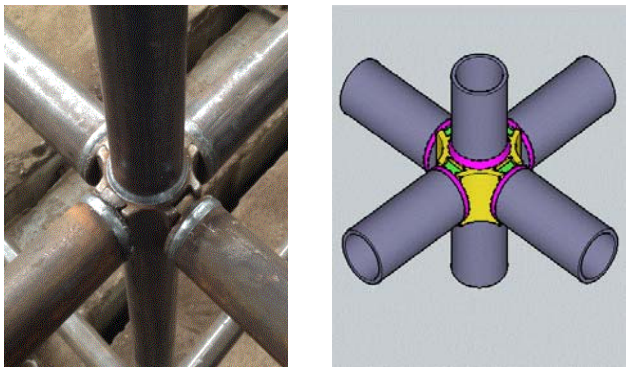

(a) Physical object (b) Model

Figure 5. Mortise–tenon Joint

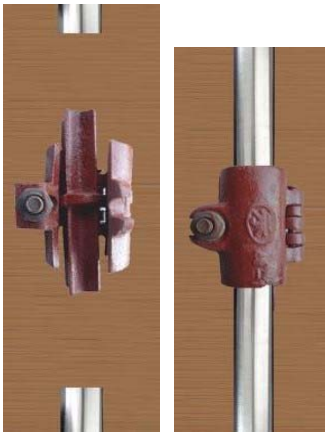

Figure 6. Sleeve Coupler

Figure 7. Swivel Coupler

3. NUMERICAL ANALYSIS MODEL

3.1 Finite element Model

The mortise–tenon joint is a typical semi-rigid node. Thus, the mortise–tenon steel-tube scaffold is a semi-rigid framework structure. In this study, a semi-rigid finite element model for the mortise–tenon steel-tube scaffold was established by ANSYS to accurately analyze its structural behavior.

In the mortise–tenon steel-tube scaffold, the vertical members are continuous at the mortise–tenon joint. The horizontal members are broken at the joint and form the framework structure with the vertical members through the mortise–tenon joint. In this paper, the horizontal and vertical members were simulated by BEAM188 element and the connection of the horizontal and vertical members was simulated by COMBIN14 element, thereby achieving the semi-rigid simulation of the mortise–tenon joint. The datailed modeling steps are as following:

Step 1: The horizontal and vertical member models are established by BEAM188 element according to spatial geometrical position of the structure. The vertical members have the same node at the mortise–tenon joint and the horizontal members have different nodes at the joint (Figure 8). To consider local instability of members, a member between every two joints is divided into 10 segments. In other words, each member are simulated by 10 BEAM188 elements. This model involves the local instability simulation of members and increases numerical analysis accuracy.

Step 2: Translational degrees of three nodes at the vertical–horizontal member joint (UX, UY, and UZ) are coupled by the finite element node coupling technology.

Step 3: COMBIN14 element is established by the horizontal member nodes and the vertical member nodes at the corresponding position. This element is used to simulate semi-rigid features of the mortise–tenon joint. Rigidity value of the COMBIN14 element was determined by tests as shown in Section 3.2.

Step 4: Natural pressure contact occurs between the vertical member and the ground. No relative slippage between members and the ground is found in engineering applications and prototype test. Therefore, a hinge joint can be set at the bottom of the vertical members of the mortise–tenon steel-tube scaffold. In other words, translational degrees of freedom of the bottom nodes of vertical members are constrained. Concentrated force is applied at the top nodes of the vertical element of scaffold structures.

Step 5: The first buckling mode identified from the eigenvalue buckling analysis was generally considered as the most critical one, and applied as initial geometric imperfection in the nonlinear analysis. According to literature, the maximum imperfection allowed in practice is 0.05 m for scaffolds with height less than 10 m. Therefore, an initial geometric imperfection was applied to the model with amplitude of 0.05m and a shape of the first buckling mode.

Step 6: Using Newton–Raphson solving method, the second-order analysis considering the geometric nonlinear effect and material nonlinear effect are accomplished to determine the nonlinear buckling strength and failure mode of the scaffold.

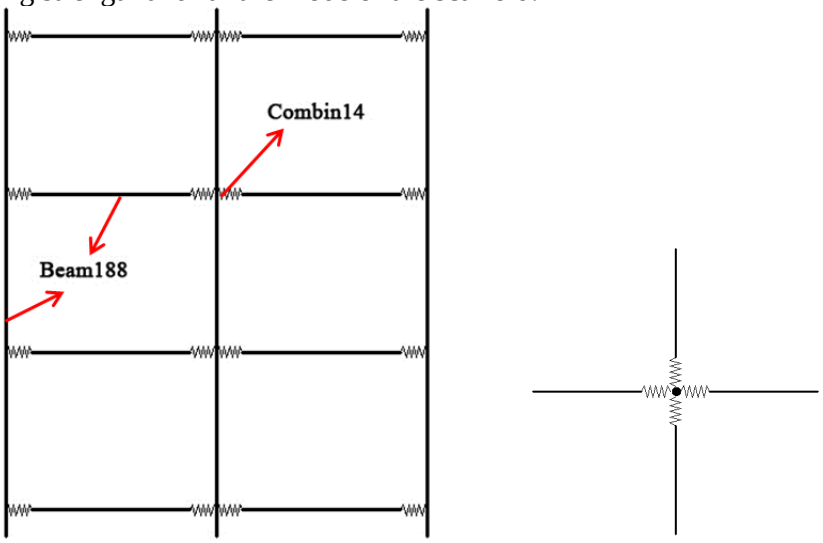

(a) Three-dimensional sketch (b) Plan sketch

Figure 8. FE Model of Connection between Vertical and Horizontal Members

3.2 Values of Key Parameters in FE Model

In the finite element model, the stress-strain relation of steel tubes was simulated by the ideal elastic–plastic model. When analyzing the structural performance of the prototype tested specimens, the basic mechanical properties of the steel tubes (Material model 1 in Table 1) were collected through static tension test. For structural parameter analysis of the mortise–tenon steel-tube scaffold, the basic mechanical properties of the steel tubes (Material model 2 in Table 1) were determined according to national code.

Table 1. Basic Mechanical Properties of Steel Tubes

Parameters	Elasticity modulus (Mpa)	Yield strength (Mpa)	Poisson's ratio
Material model 1	2.25×10^5	360	0.3
Material model 2	2.06×10^5	205	0.3

Rotational stiffness and shear strength of the mortise–tenon joint was determined by tests [21]. The rotational stiffness of three mortise–tenon joint specimens was tested by the loading program in Figure 9. Three Moment-Rotation curves were obtained, as shown in Figure 10. According to the curves in Figure 10, the initial rotational stiffness of three mortise–tenon joints specimens were calculated through linear fitting, and their values were 13.38, 16.07, and $19.80\,kN\cdot m/rad$ respectively. For vertical members of the mortise–tenon steel-tube scaffold, the horizontal members on two sides are connected by two mortise–tenon joints (Figure 5). For the coupler-type steel-tube scaffold, the horizontal members on two sides of the vertical members are connected by a right-angle coupler (Figure 11). Therefore, the rotational constraint stiffness of vertical members in the mortise–tenon steel-tube scaffold has much higher than that in the coupler-type steel-tube scaffold.

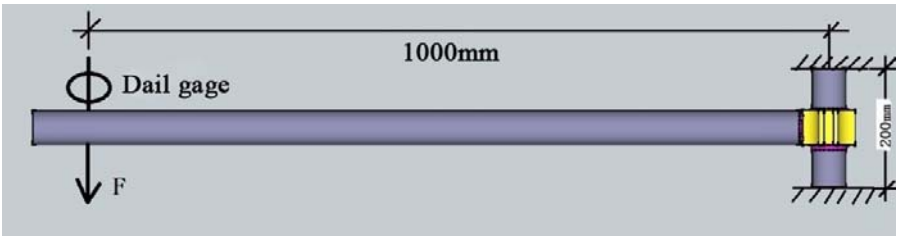

Figure 9. Loading Program of Rotational Stiffness Test of Mortise–tenon Joint

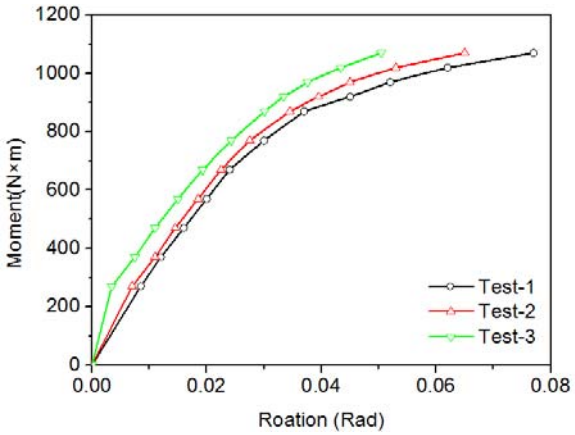

Figure 10. Moment-rotation Curves of Mortise–tenon Nodes

Figure 11. Connection of Horizontal and Vertical Members in Coupler-type Scaffold Structure

Shear strength of the mortise–tenon joint was determined by the loading program shown in Figure 12 [21]. The shear strength of three mortise–tenon joint specimens was tested, and their shear strengths were 94.7, 92.2, and 93.5 kN respectively, which were much higher than the vertical shear strength of the right-angle coupler.

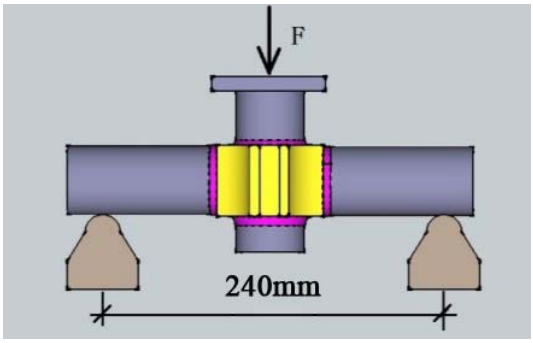

Figure 12. Shear Strength Test of Mortise–tenon Joint

3.3 Experimental Verification

A total of 11 mortise–tenon scaffold prototype tests were carried out from 2013 to 2014 at the Structural Engineering Laboratory of Tianjin University, and these test data were used to verify the accuracy of the numerical analysis model. Structural layout and basic geometric parameters of the 11 test models are shown in Figures. 13~14 and Table 2. Four 10 m high loading frames were fabricated for the tests. Two 50-ton hydraulic jacks were fastened to the top of each loading frame, and applied vertical loads to the two top steel distribution beams. The loads were then transferred to a group of bottom steel distribution beams in the perpendicular direction, and finally to the scaffold system, as shown in Figure 15. In this way, vertical uniform loads were applied to the top of the scaffold system through two steel tubes right below the bottom distribution beams and the U-heads. Based on the finite element analysis model presented in Sections 3.1 and 3.2, the ultimate bearing capacities and failure modes of these 11 test models were analyzed and compared with those from the test results. The results are presented in Table 3 and Figures. 15~17. As shown in Table 3, the maximum error between the numerical analysis and test results of the ultimate bearing capacity is 30.87% and the average error are 11.02%. The buckling form of the mortise–tenon scaffold with X-bracing is mainly the local lateral buckling of the vertical members at the upper two-storey vertical members as shown in Figure 15. The buckling form of the mortise–tenon scaffold without

X-bracing is mainly the overall lateral buckling of the structure as shown in Figure 16. Though comparison the bearing capacities, failure modes and load-displacement curves as shown in Figures. 15~17, it is clear that numerical analysis results are in accordance with test results. In other words, the proposed numerical analysis model can reasonably predict the ultimate bearing capacity and failure mode of the mortise–tenon steel-tube scaffold.

The prototype test model of the mortise–tenon steel-tube scaffold (ST5) has consistent structural parameters of the prototype test model of the coupler-type mortise–tenon steel-tube scaffold (ST6) [19]. Their ultimate bearing capacities are 69.4 kN and 20.68 kN, respectively. Under the same structural parameters, the ultimate bearing capacity of the mortise–tenon steel-tube scaffold is approximately 235.59% higher than that of the coupler-type steel-tube scaffold.

Table 2. Prototype Test Model of Mortise–tenon Scaffold

No.	S_1(m)	S_2(m)	H_1(m)	n	m	X-bracing
ST1	0.9	0.9	0.6	5	12	N
ST2	0.9	0.9	0.6	5	12	Y
ST3	0.6	0.6	1.2	6	6	N
ST4	0.6	0.6	1.2	6	6	Y
ST5	0.6	0.6	0.6	6	12	N
ST6	0.9	0.9	1.2	4	6	N
ST7	0.9	0.9	1.2	4	6	Y
ST8	0.9	0.9	1.8	4	4	N
ST9	0.9	0.9	1.8	4	4	Y
ST10	1.2	1.2	1.2	3	6	N
ST11	1.2	1.2	1.2	3	6	Y

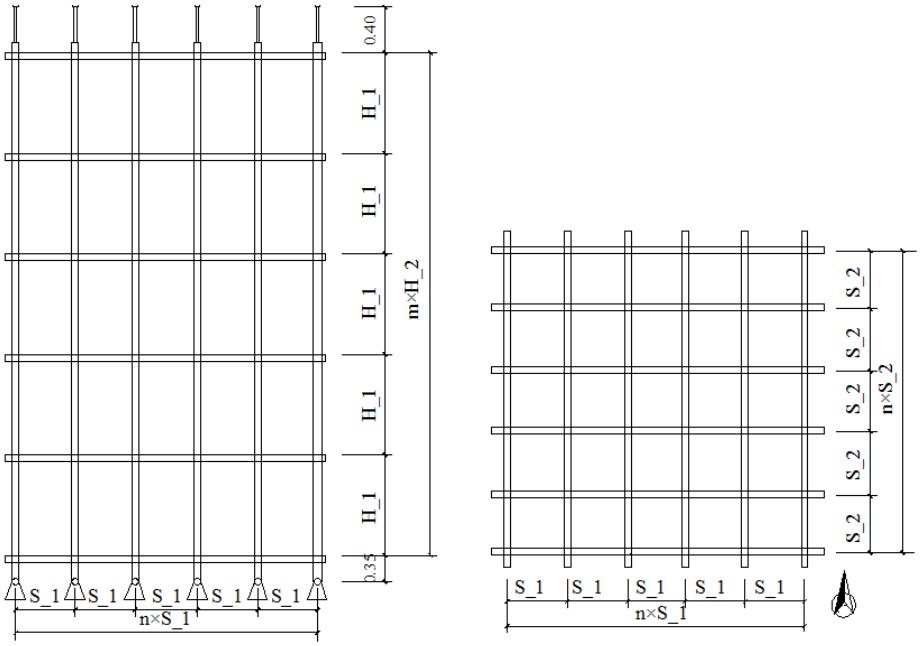

(a) Vertical view (b) Plan view

Figure 13. Schematic View of Prototype Test Model of Mortise–tenon Scaffold without X-bracing

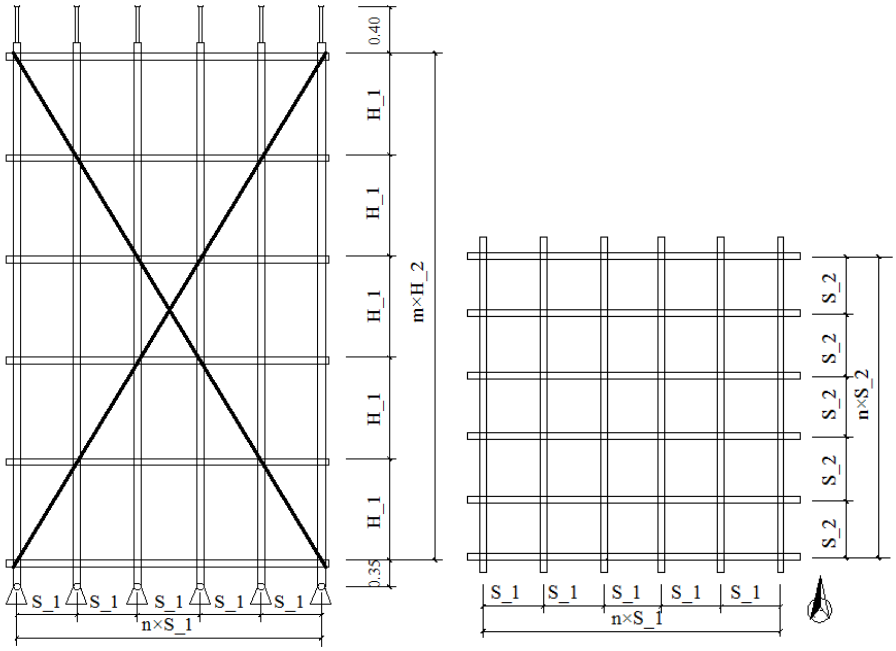

(a) Vertical view (b) Plan view

Figure 14. Schematic View of Prototype Test Model of Mortise–tenon Scaffold with X-bracing

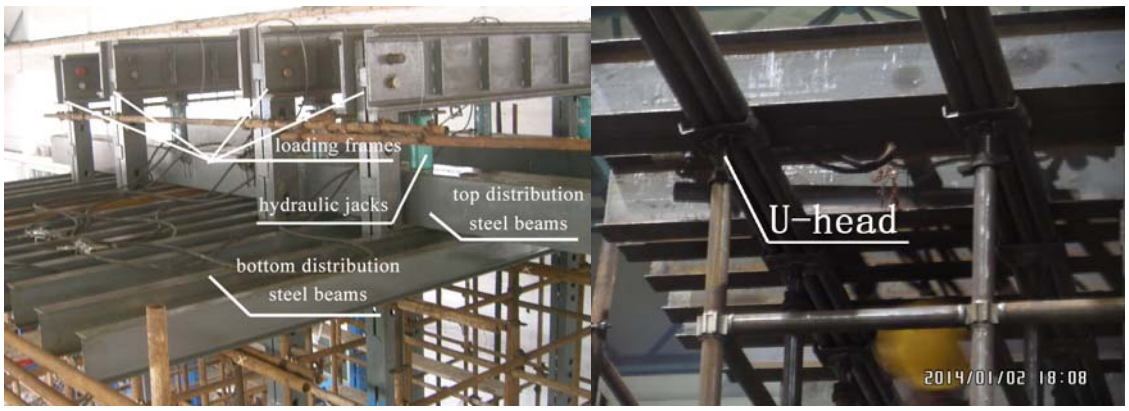

Figure 15. Loading Mechanism and Test Set-up

Table 3. Comparison between Test Results and FE Result of Ultimate Bearing Capacity

No.	Test result(kN)	FE result (kN)	Error	No.	Test result(kN)	FE result(kN)	Error
ST1	45.8	59.9	30.87	ST7	56.0	58.0	3.51
ST2	73.8	71.0	–3.86	ST8	24.0	24.3	1.17
ST3	44.5	36.5	–17.94	ST9	46.4	46.2	–0.36
ST4	68.1	64.3	–5.62	ST10	37.5	32.7	–12.70
ST5	69.4	61.3	–11.64	ST11	46.9	57.5	22.59
ST6	38.0	33.8	–11.00				

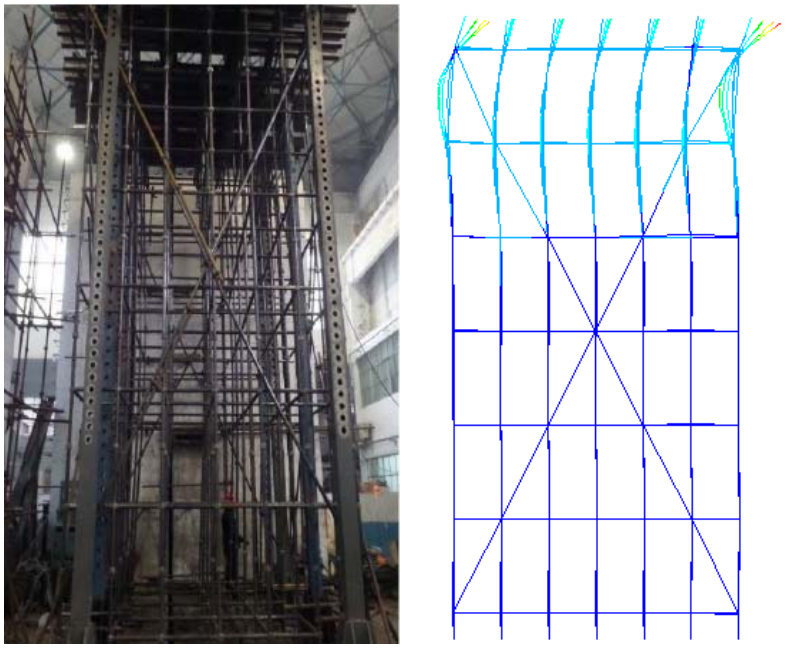

(a) Test (b) Finite element

Figure 15. Failure Mode Comparison of Test Model 4

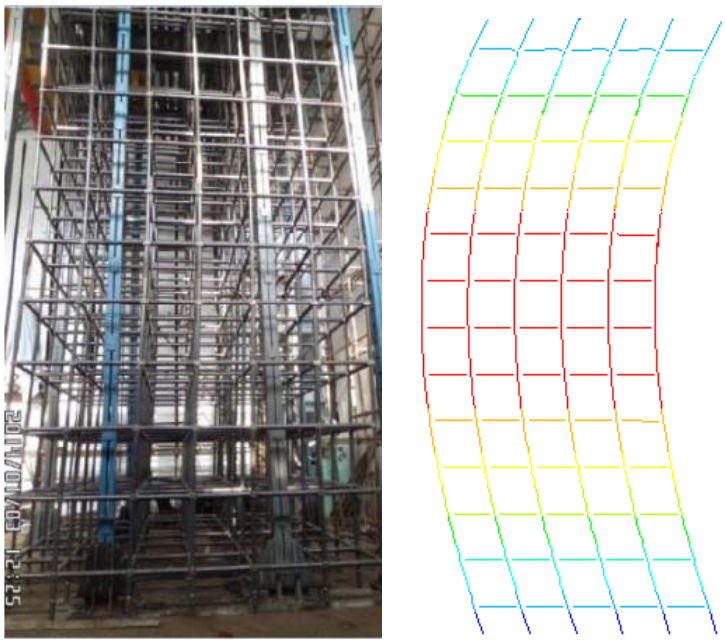

(a) Test (b) Finite element

Figure 16. Failure Mode Comparison of Test Model 5

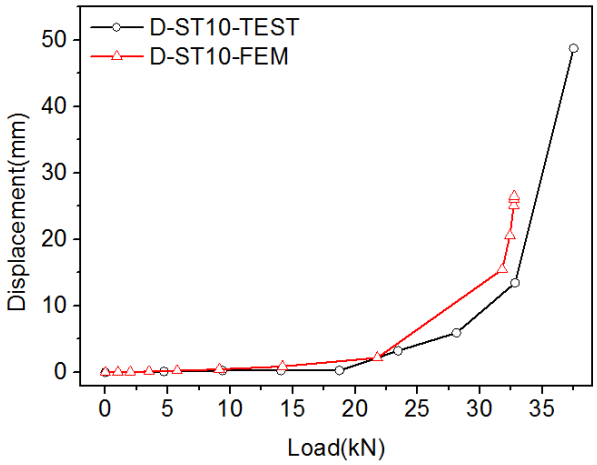

Figure 17. Load-Displacement Curves Comparison of Test Model 10

4. ANALYSIS OF STRUCTURAL PERFORMANCE

In this section, the effect of structural parameters on structural behavior of the mortise–tenon steel-tube scaffold is discussed using the numerical analysis method. In the numerical simulation of the mortise–tenon steel-tube scaffold test model in Section 3, the basic mechanical parameters of the steel-tube materials were determined through static tension tests so that the numerical simulation would approximate the actual performance of the test model. However, the purpose of numerical analysis of the mortise–tenon steel-tube scaffold in this section was to provide references for engineering applications. Therefore, the mechanical properties of the steel-tube materials in this section were determined according to the national code (Material model 2 in Table 1).

In the engineering application of the mortise–tenon steel-tube scaffold, the steel tube and mortise–tenon joint are constants for the easy materials reuse. The steel tube generally uses P48 mm × 3.5 mm and the mortise–tenon joint matches that of the steel tube. Therefore, the main influencing factors of the structural performance of the mortise–tenon steel-tube scaffold are the geometric parameters, including storey height, vertical member interval, height of bottom horizontal tube (H_3 shown in Figure, 2), height of cantilever bar (H_2 shown in Figure, 2), overall structure height and X-bracing layout. In this study, the effects of these factors were studied through a series parameter analysis.

To analyze the effects of storey height and vertical member interval on the structural performance, the overall structure height, height of the bottom horizontal tube, and height of the cantilever bar were fixed at approximately 8m, 0.35m, and 0.4 m respectively, and No X-bracing was used. A total of 25 structural models with different storey height and vertical member intervals were established. Their ultimate bearing capacities were obtained as shown in Figures. 18 and 19. It is clear that the vertical member interval had a minor effect on the ultimate bearing capacity, but the storey height influenced significantly. The ultimate bearing capacity decreased by approximately 13%–23% when the storey height increased by 0.3 m. The smaller the structure height is, the greater is the bearing capacity reduction.

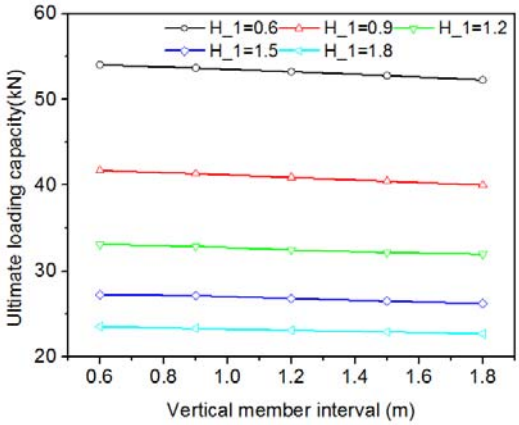

Figure 18. Parameter Analysis of Vertical Interval

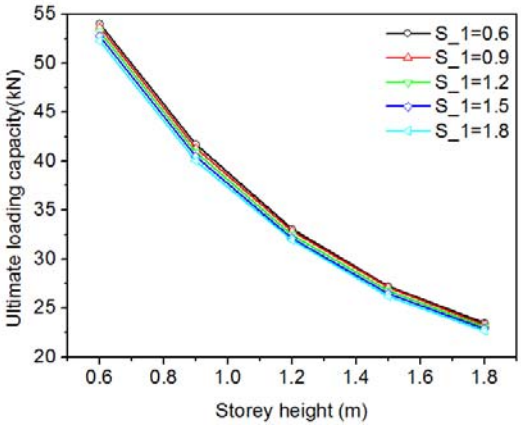

Figure 19. Parameter Analysis of Member Storey Height

To analyze the effects of the height of the bottom horizontal tube and the height of the cantilever bar on the structural performance of the mortise–tenon steel-tube scaffold, the overall structure height, storey height, and vertical member interval were fixed at approximately 8m, 0.9m–1.8m, and 0.9m respectively. No X-bracing was used. A series of analysis models were established with different height of the bottom horizontal tube and height of the cantilever bar. In the parameter analysis of height of the bottom horizontal tube, the height of the cantilever bar was fixed at 0.4 m. In the parameter analysis of the cantilever bar height, the height of the bottom horizontal tube was fixed at 0.35 m. Results are presented in Figures. 20 and 21. It is clear that when the storey height was higher than 0.9 m, the height of the bottom horizontal tube and the cantilever bar basically had little effect on the ultimate bearing capacity. When the storey height was less than 0.9 m, the height of the bottom horizontal tube was less than 0.3 m, and the height of the cantilever bar was less than 0.4 m. The ultimate bearing capacity of the structure remained basically the same despite the height variation of the bottom horizontal tube and the cantilever bar. When the storey height is more than 0.9 m, the height of the bottom horizontal tube increases to 0.4 m and 0.5 m, and the ultimate bearing capacity decreases by 9% and 19% up to the maximum; when the cantilever height increases to 0.5 m, the ultimate bearing capacity decreases by 7% up to the maximum.

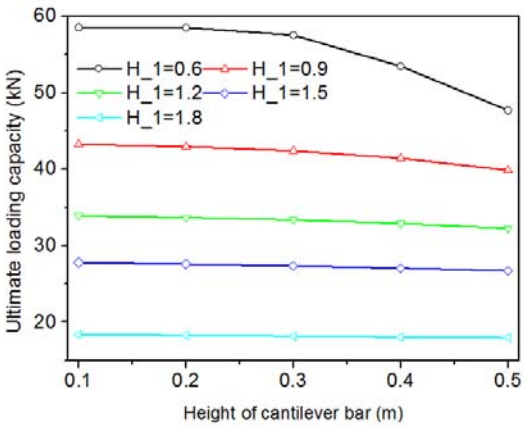

Figure 20. Parameter Analysis of Height of Cantilever Bar

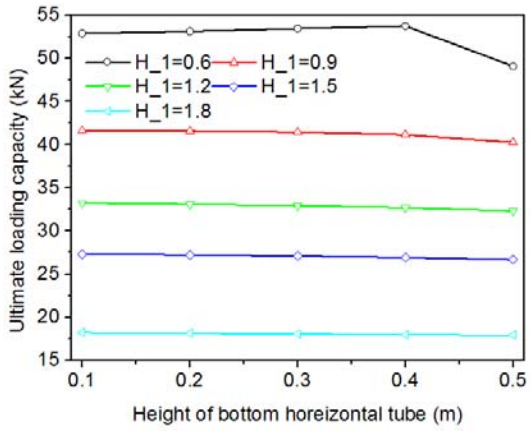

Figure 21. Parameter Analysis of Height of Bottom Horizontal Tube

In order to analyze the effect of X-bracing on the ultimate loading capacity, the X-bracings were set in all models established for the storey height and vertical-member interval parameter analysis. The analysis results were shown in Figure 22, and it is clear that the X-bracing layout have strengthened the ultimate bearing capacity significantly. The strengthen effect is closely related to the storey height but less correlated to the vertical member interval. The average strengthen coefficients of the ultimate bearing capacity were 1.0, 1.24, 1.45, 1.49, and 1.30 when the storey heights were 0.6, 0.9, 1.2, 1.5, and 1.8 m.

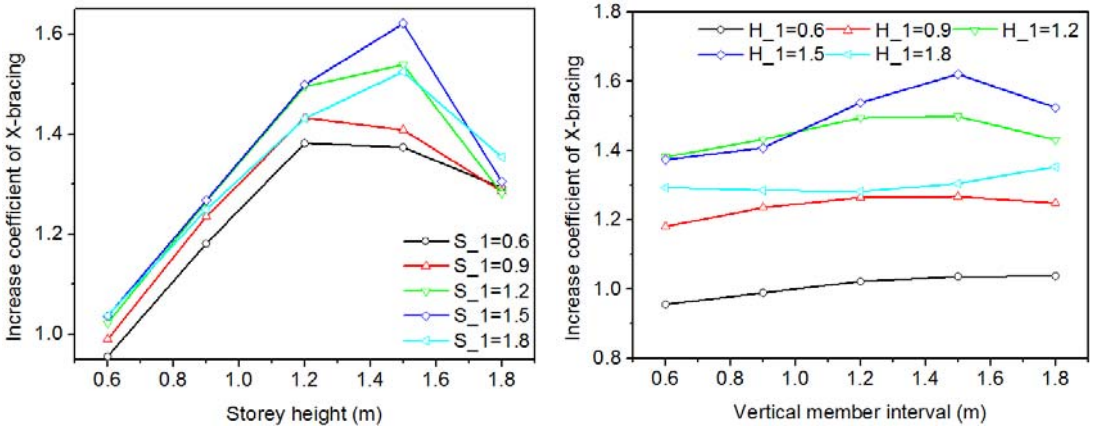

(a) Variation of storey height (b) Variation of vertical member interval

Figure 22. Effect of X-bracing Layout on Ultimate Bearing Capacity

The effect of the overall structure height on the ultimate bearing capacity was also studied through a series of models without X-bracing. In these models, the overall structure height was different, but the vertical member interval (0.9 m), storey height (0.9, 1.2, or 1.5 m), height of bottom horizontal tube (0.35 m), and height of cantilever bar (0.4 m) were fixed. The analysis results are shown in Figure 23. The overall structure height affected the ultimate bearing capacity significantly. Such an effect decreased with the increase of the overall structure height. Furthermore, the negative correlation between the overall structure height and the ultimate bearing capacity was further intensified as the storey height increased. When the overall structure heights were 8, 12, 16, and 20 m, the ultimate bearing capacity decreased by approximately 19%, 27%, 30%, and 29% compared with the capacity when the overall structure height was 4 m.

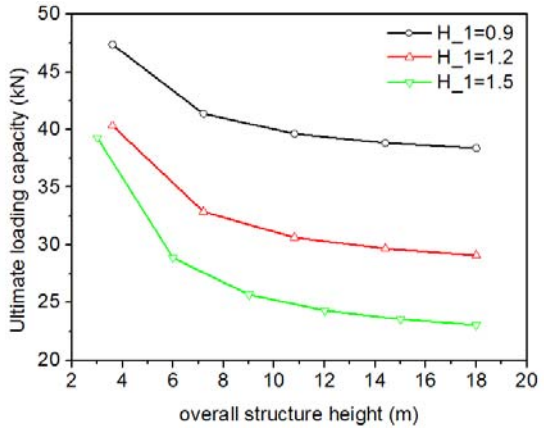

Figure 23. Overall Structure Height Effect on the Bearing Capacity

5. DESIGN METHOD

Based on parameter analyses in Section 4, the main influencing factors om the ultimate bearing capacity of the mortise–tenon steel-tube scaffold are storey height, height of bottom horizontal tube, height of cantilever bar, X-bracing layout, and overall structure height. Among them, storey height is the most important influencing factor. In this section, coefficients β_1, β_2, β_3, and β_4 were introduced to consider the effects of the X-bracing layout, height of bottom horizontal tube, height of cantilever bar, and overall structure height on the ultimate bearing capacity respectuvely. The ultimate bearing capacity of the mortise–tenon steel-tube scaffold was calculated from

$$P_{cr} = \frac{\beta_1 \beta_2 \beta_3 \beta_4 N_f}{\gamma_s}, \tag{1}$$

where N_f is the standard value of the ultimate bearing capacity of the mortise–tenon steel-tube scaffold without X-bracing. This value is only related to storey height and can be determined according to Table 4; β_1 is the influence coefficient of X-bracing, which is only related to storey height and can be determined according to Table 5; β_2 is the influence coefficient of the height of the bottom horizontal tube, which is only related to the height of the bottom horizontal tube and can be determined according to Table 6; β_3 is the influence coefficient of the height of the cantilever bar, which is only related to the height of the cantilever bar and can be determined according to Table 7; β_4 is the influence coefficient of overall structure height, which is related to the overall structure height and storey height and can be determined according to Table 7; γ_s is the safety factor and is determined as 1.5 according to engineering experiences [22].

To verify the calculation accuracy of the proposed prediction formula (1), 11 structural models of the mortise–tenon steel-tube scaffold were designed randomly. The ultimate bearing capacities were determined by both FE numerical analysis method presented in Section 4 and the proposed prediction formula (1). Comparison results are listed in Table 8. The maximum error between the calculated results and the FE numerical simulation results was 6.08%, which could meet engineering application requirements.

Table 4. Basic Bearing Ability of Mortise–tenon Steel-tube Scaffold

Storey height (m)	0.6	0.9	1.2	1.5	1.8
Bearing capacity of single member (kN)	52.30	40.02	31.94	26.20	22.66

Table 5. Increase Coefficient of X-bracing

Storey height (m)	0.6	0.9	1.2	1.5	1.8
Increase coefficient of bearing capacity	1.01	1.24	1.45	1.49	1.30

Table 6. Adjustment Coefficients of Height of Bottom Horizontal Tube and Height of Cantilever Bar

Height (m)	0.1	0.2	0.3	0.4	0.5
Adjustment coefficients of height of cantilever bar	1.00	1.00	1.00	0.91	0.81
Adjustment coefficients of height of bottom horizontal tube	1.00	1.00	1.00	1.00	0.93

Table 7. Adjustment Coefficients of Overall Structure Height

Storey height (m)	Overall structure height (m)				
	4	8	12	16	20
0.6	1.07	1.00	0.96	0.93	1.07
0.9	1.15	1.00	0.96	0.94	0.93
1.2	1.22	1.00	0.93	0.90	0.88
1.5	1.35	1.00	0.94	0.85	0.84
1.8	1.50	1.00	0.72	0.64	0.60

Table 8. Comparison between Simplified Calculation Results and Numerical Simulation Results

H	H_1	S_1	H_2	H_3	X-bracing	$P_{cr\text{-}FEM}$	$P_{cr\text{-}S}$	Error
16.0	0.9	0.9	0.3	0.4	N	38.84	37.79	–2.70
7.95	0.9	0.9	0.3	0.4	N	41.34	40.02	–3.19
7.95	0.9	0.9	0.3	0.5	N	39.87	40.02	0.38
7.95	0.9	0.9	0.5	0.4	N	40.29	40.02	–0.67
7.95	1.2	0.9	0.3	0.4	N	32.86	31.94	–2.80
7.95	1.8	0.9	0.3	0.4	N	23.29	22.66	–2.71
7.95	0.9	0.9	0.3	0.4	Y	51.07	49.62	–2.84
7.95	0.9	0.9	0.3	0.5	Y	46.78	49.62	6.07
7.95	0.9	0.9	0.5	0.4	Y	51.89	49.62	–4.37
7.95	1.2	0.9	0.3	0.4	Y	47.80	46.31	–3.12
7.95	1.8	0.9	0.3	0.4	Y	29.93	29.46	–1.57

6. CONCLUSIONS

The structural performance of the mortise–tenon steel-tube scaffold, a new scaffold system, was studied through finite element numerical simulation. A simplified calculation formula of the ultimate bearing capacity is also presented in this paper. Based on this study, the following conclusions are obtained:

1) A numerical analysis model for the mortise–tenon steel-tube scaffold is presented based on the finite element method and semi-rigid frame theory, which was verified by 11 prototype test data.
2) Under the same structural parameters, the ultimate bearing capacity of the mortise–tenon steel-tube scaffold without X-bracing is approximately 235.59% higher than that of the coupler-type scaffold. Therefore, the mortise–tenon steel-tube scaffold has significantly better structural performance than the coupler-type scaffold.
3) The X-bracing layout, storey height, and overall structure height influence the ultimate bearing capacity of the mortise–tenon steel-tube scaffold significantly, but the vertical member interval, height of bottom horizontal tube, and height of cantilever bar influence the ultimate bearing capacity slightly.

4) When the storey heights are 0.6, 0.9, 1.2, 1.5, and 1.8 m, the ultimate bearing capacities of the scaffold with X-bracing increase by 1.0, 1.24, 1.45, 1.49, and 1.30 times more than those of the scaffold without X-bracing.
5) When the overall structure height is 8, 12, 16, and 20 m, the ultimate bearing capacities are approximately 19%, 27%, 30%, and 29% lower than the capacities when the overall structure height is 4 m.
6) A calculation formula was presented to calculate the bearing capacity of the mortise–tenon steel-tube scaffold, and the maximum error between calculated results of the simplified calculation formula and the finite element numerical simulation results was 6.08%.

ACKNOWLEDGMENT

This study was supported by the Tianjin Urban and Rural Construction Commission (Grant No. 2015-4).

REFERENCES

[1] Chan, S.L., Zhou, Z.H., Chen, W.F., Peng, J.L. and Pan, A.D., “Stability Analysis of Semi-rigid Steel Scaffolding”, Eng Struct 1995, Vol. 17, pp. 568-74. http://www.sciencedirect.com/science/article/pii/014102969500011U

[2] Peng, J.L., Pan, A.D., Rosowsky, D.V., Chen, W.F., Yen, T. and Chan, S.L., “High Clearance Scaffold Systems during Construction－1: Structural Modeling and Modes of Failure”, Eng Struct 1996, Vol. 18, pp. 247-257. http://www.sciencedirect.com/science/article/pii/0141029695001441

[3] Peng, J.L., Pan, A.D., Rosowsky, D.V., Chen, W.F., Yen, T. and Chan, S.L., “High Clearance Scaffold Systems during Construction－2: Structural Analysis and Development of Design Guidelines”, Eng Struct 1996, Vol. 18, pp. 258-267. http://www.sciencedirect.com/science/article/pii/014102969500145X

[4] Peng, J.L., Pan, A.D., Chen, W.F., Yen, T. and Chan, S.L., “Structural Modeling and Analysis of Modular Falsework Systems”, ASCE J Struct Engng 1997, Vol. 123, pp. 1245–51. http://ascelibrary.org/doi/abs/10.1061/(ASCE)0733-9445(1997)123:9(1245)

[5] Peng, J.L., Pan, A.D. and Chan S.L., “Simplified Models for Analysis and Design of Modular Falsework”, J Construct Steel Res, 1998, Vol. 48, pp. 189-209. http://www.sciencedirect.com/science/article/pii/S0143974X98001989

[6] Peng, J.L., Pan, A.D. and Chen, W.F., “Approximate Analysis Method for Modular Tubular Falsework”, ASCE J Struct Engng, 2001, Vol. 127, pp. 256–63. http://ascelibrary.org/doi/abs/10.1061/(ASCE)0733-9445(2001)127:3(256)

[7] Yu, W.K., Chung, K.F. and Chan, S.L., “Structural Instability of Multi-storey Door-type Modular Steel Scaffolds”, Eng Struct, 2004, Vol. 26, pp. 867-61. http://www.sciencedirect.com/science/article/pii/S0141029604000549

[8] Weesner, L.B. and Jones H.L., “Experimental and Analytical Capacity of Frame Scaffolding”, Eng Struct, 2001, Vol. 23, pp. 592-99. http://www.sciencedirect.com/science/article/pii/S0141029600000870

[9] Pienko, M. and Blazik-Borowa, E., “Numerical Analysis of Load-bearing Capacity of Modular Scaffolding Nodes”, Eng Struct, 2013, Vol. 48, pp. 1-9. http://www.sciencedirect.com/science/article/pii/S0141029612004701

[10] Peng, J.L., Wu, C.W., Chan, S.L. and Huang, C.H., "Experimental and Numerical Studies of Practical System Scaffolds", J Construct Steel Res, 2013, Vol. 91, pp. 64-75. http://www.sciencedirect.com/science/article/pii/S0143974X13002216

[11] Zhang, H., Rasmussen, K.J.R. and Ellingwood, Bruce R., "Reliability Assessment of Steel Scaffold Shoring Structures for Concrete Formwork", Eng Struct, 2012, Vol. 36, pp. 81-89. http://www.sciencedirect.com/science/article/pii/S0141029611004731

[12] Zhang, H. and Rasmussen, K.J.R., "System-based Design for Steel Scaffold Structures using Advanced Analysis", J Construct Steel Res, 2013, Vol. 89, pp. 1-8. http://www.sciencedirect.com/science/article/pii/S0143974X13001557

[13] Zhang, H., Chandrangsu, T. and Rasmussen, K.J.R., "Probabilistic Study of the Strength of Steel Scaffold Systems", Struct Saf, 2010, Vol. 32, pp. 393–401. http://www.sciencedirect.com/science/article/pii/S0167473010000196

[14] Godley, M.H.R and Beale, R.G., "Sway Stiffness of Scaffold Structures", The Structural Engineer, 1997, Vol. 75, No. 1, pp. 4-12.

[15] Beale, R.G. and Godley, M.H.R., "Numerical Modeling of Tube and Fitting Access Scaffold Systems", Advanced Steel Construction, 2006, Vol. 2, pp. 199-223. http://ascjournal.com/

[16] Beale, R.G., "Scaffold Research: A Review", J Construct Steel Res, 2014, Vol. 98, pp. 188-200. http://www.sciencedirect.com/science/article/pii/S0143974X14000388

[17] Ao, H.F. and Li, G.Q., "Investigation of Overall Load-bearing Stability Capacity of Tube-and-coupler Scaffolds", Chinese Quarterly of Mechanics, 2004, Vol. 25, pp. 213-218. (In Chinese)

[18] Yue, F., Yuan, Y., Li, G.Q., Ye, K.M., Chen, Z.M. and Wang, Z.P., "Wind Load on Integral-lift Scaffolds for Tall Building", ASCE, J Struct Engng, 2005, Vol. 131, pp. 816-24. http://ascelibrary.org/doi/abs/10.1061/(ASCE)0733-9445(2005)131:5(816)

[19] Liu, H.B., Zhao, Q.H., Wang, X.D., Zhou, T., Wang, D., Liu, J. and Chen, Z.H., "Experimental and Analytical Studies on the Stability of Structural Steel Tube and Coupler Scaffolds without X-bracing", Eng Struct, 2010, Vol. 32, pp. 1003-1015. http://www.sciencedirect.com/science/article/pii/S0141029609004210

[20] Liu, H.B., Chen, Z.H., Wang, X.D. and Zhou, T., "Theoretical Analysis and Experimental Research on Stability Behavior of Structural Steel Tube and Coupler Falsework with X-bracing", Advanced Steel Construction, 2010, Vol. 6, No. 4, pp. 946-962. http://ascjournal.com/

[21] He, X.Y., "Study of the Ultimate Bearing Capacity of Full-hall Formwork Support System of Mortise and Tenon Joints", Tianjin: Tianjin University, 2014. (In Chinese)

[22] Christopher Souder. Temporary Structure Design. Wiley, 2014.

NUMERICAL ANALYSIS OF PLAIN AND STEEL FIBER REINFORCED CONCRETE FILLED STEEL TUBULAR SLENDER COLUMN

Kingsley U. Ukanwa[1,*], Charles G. Clifton[1], James B.P. Lim[1], Stephen Hicks[2] and Umesh K. Sharma[3]

[1] *Department of Civil Engineering, The University of Auckland, Auckland, New Zealand*
[2] *New Zealand Heavy Engineering Research Association, HERA House, Auckland, New Zealand*
[3] *Department of Civil Engineering, India Institute of Technology, Roorkee, India*
**(Corresponding author: E-mail: kuka298@aucklanduni.ac.nz)*

Received: 8 August 2016; Revised: 20 April 2017; Accepted: 14 May 2017

ABSTRACT: Concrete filled steel tube columns (CFST) have many potentials which include; high seismic resistance, high load bearing capacity, and fire resistance without external protection. Some major projects worldwide has adopted the use of this type of column member extensively, for columns in both the gravity systems and the seismic resisting systems. Experimental tests performed on concrete filled steel tube columns at ambient temperature indicates that, the use of steel fibre reinforced concrete infill affects the crack width propagation of the concrete. This paper presents an advanced 3D numerical model which predicts the behaviour of a CFST column filled with steel fibre reinforced concrete, taking into account the increased tensile strength of the concrete which affects the column ductility. For columns subjected to compression loading only, it is recommended to use a high strength concrete, and also increase the thickness of the steel tube rather than using a steel tube with a higher yield strength. For slender square columns loaded under large eccentricity, it is recommended to use an e/D (eccentricity/depth) ratio value less than 0.5 for design purposes, to avoid the premature fracture of the loaded end of the column having smaller steel tube thickness.

Keywords: Concrete filled tubular columns, steel fibre reinforced concrete, finite element analysis, composite column, square hollow steel section

DOI: 10.18057/IJASC.2018.4.2.10

1. INTRODUCTION

Concrete filled steel tube (CFST) columns are an increasingly popular form of construction. The advantages of CFST include a high compression strength, good ductility, reduction in size of the column, ease of construction and potential fire resistance ratings (Zhao et al. [1]). The 1995 Kobe earthquake in Japan influenced the emphasis on CFST construction whereby, emphasis was placed on ductility, energy absorption and performance in seismic zones (Kitada [2]).

Steel tube local buckling is one of the critical issues to consider when designing a steel tube column. Researchers have indicated that addition of a concrete infill to the steel tube will reduce the effects of local buckling (Brauns [3], Ellobody, Young and Lam [4]). Steel fiber reinforced concrete infill is a popular type of concrete infill due to the advantages of increasing the tensile strength of the concrete and controlling the crack width of the concrete core (Ellobody [5], Zhao et al. [6]). Comprehensive experimental and numerical experiments conducted by (Zeghiche and Chaoui [7]) together with (Johansson and Gylltoft [8]), showed that it is possible to achieve ductility in the column by also using concrete strength higher than 50MPa.

Ellobody [5], showed that addition of fiber to plain concrete increases its flexural and tensile strength, which results in superior post-elastic material properties. The various parameters that affect the behaviour of steel fiber reinforced concretes which includes its matrix strength, fiber type, fiber Young's modulus, fiber dosage and fiber tensile strength. Figure 1 shows a comparison between the stress - strain curve of plain and steel fiber reinforced concrete.

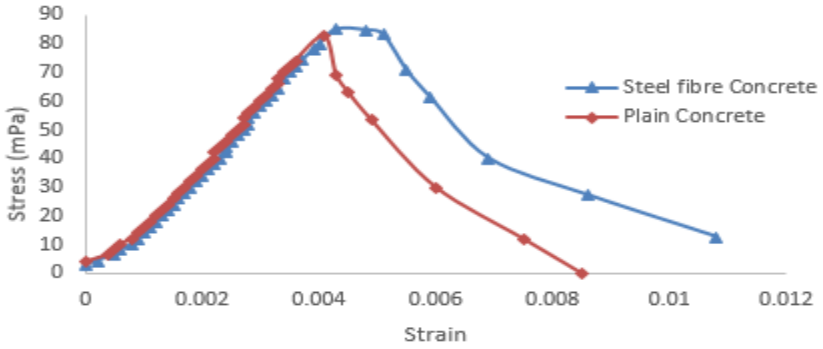

Figure 1. Comparison of Stress–strain Curves of Plain and SFR Concrete

Eltobgy [9], observed that the use of steel fibre reinforced concrete improved the structural stability of a CFST columns and the slenderness ratio is also an important factor that govern its behaviour.

Gopal and Manoharan [10], carried out tests on 12 slender circular steel tubular columns filled with both plain and steel fiber reinforced concrete. The specimens were tested under eccentric axial loading to investigate the effects of fiber reinforced concrete on the ultimate strength and behaviour of the composite columns. It was reported that the use of fiber reinforced concrete as infill for tubular steel gives the column additional strength and ductility.

Tokgoz and Dundar [11], conducted experimental tests on 16 concrete filled steel tubular columns, each tubular column was filled with either plain or steel fibre reinforced concrete. The columns were loaded axially with different levels of eccentricity having an e/D ratio between 0.5-0.67 where e is the eccentricity and D is the depth or height of the column. It was reported that the inclusion of steel fiber to the concrete improved the ductility and deformation of the column. The steel fibres, however, had little effect on the ultimate strength capacity of the column.

The main objective of the study reported herein is to investigate numerically the behaviour of axially loaded steel fiber reinforced CFST column. The numerical model is validated by comparison with experimental data reported in the literature, and also the Eurocode 4 part 1-1 [12] design model. Sixteen composite columns were simulated from experimental tests carried out by Tokgoz and Dundar [11] from the literature and the main variables for the columns were the cross-section, slenderness, concrete compressive strength and the load eccentricity. The ultimate strength and load-deflection profile of the columns were analysed and compared to the experimental results. A parametric study was also carried out to investigate the influence of the steel yield strength, steel tube thickness and concrete compressive strength to the ultimate strength and ductility of the column.

2. FINITE ELEMENT MODELLING

2.1 General

To analyse the behaviour of plain and steel fiber reinforced CFST column, A three dimensional non-linear finite element CFST column was modelled using ABAQUS [13].

A total of 38 CFST columns were modelled; 16 of these columns were from the literature which was used to validate the numerical simulation. The remaining 22 were used for the parametric studies. All the columns were of length of 1250 mm which had similar length with the experimental study. The material properties and geometry of the columns are summarized in Table 1(a) and (b). The slenderness (λ), concrete cylindrical compressive strength (f_c), steel yield strength and ultimate tensile strength (f_y &f_u) and steel ratio (δ) are also shown.

Table 1a. ABAQUS CFST Column Model for Validating Experimental Study

S/N	B x D x t mm	B/t	e/D	L/D	ex mm	ey mm	λ	δ	f_c MPa	f_y MPa	f_u MPa
1	60 x 60 x 5	12.00	0.50	20.83	30	30	0.76	0.71	51.48	290	360
2	60 x 60 x 5	12.00	0.50	20.83	30	30	0.77	0.70	54.13	290	360
3	60 x 60 x 5	12.00	0.67	20.83	40	40	0.77	0.69	56.24	290	360
4	60 x 60 x 5	12.00	0.67	20.83	40	40	0.77	0.69	58.67	290	360
5	70 x 70 x 5	14.00	0.50	17.86	35	35	0.66	0.67	51.48	290	360
6	70 x 70 x 5	14.00	0.50	17.86	35	35	0.66	0.66	54.13	290	360
7	70 x 70 x 5	14.00	0.64	17.86	45	45	0.67	0.65	56.24	290	360
8	70 x 70 x 5	14.00	0.64	17.86	45	45	0.67	0.64	58.67	290	360
9	80 x 80 x 4	20.00	0.50	15.63	40	40	0.59	0.57	51.48	290	360
10	80 x 80 x 4	20.00	0.50	15.63	40	40	0.60	0.56	54.13	290	360
11	80 x 80 x 4	20.00	0.63	15.63	50	50	0.60	0.55	56.24	290	360
12	80 x 80 x 4	20.00	0.63	15.63	50	50	0.61	0.54	58.67	290	360
13	100 x 100 x 4	25.00	0.50	12.50	50	50	0.48	0.51	51.48	290	360
14	100 x 100 x 4	25.00	0.50	12.50	50	50	0.49	0.49	54.13	290	360
15	100 x 100 x 4	25.00	0.60	12.50	60	60	0.49	0.48	56.24	290	360
16	100 x 100 x 4	25.00	0.60	12.50	60	60	0.50	0.47	58.67	290	360

Table 1b. ABAQUS CFST Column Model for Parametric Study

S/N	B x D x t mm	B/t	e/D	L/D	ex mm	ey mm	λ	δ	f_c MPa	f_y MPa	f_u MPa
1	100 x 100 x 4	25.00	0.00	12.50	0	0	0.48	0.51	50.10	290	360
2	100 x 100 x 4	25.00	0.00	12.50	0	0	0.49	0.50	52.17	290	360
3	100 x 100 x 4	25.00	0.25	12.50	25	25	0.48	0.51	50.10	290	360
4	100 x 100 x 4	25.00	0.25	12.50	25	25	0.49	0.50	52.17	290	360
5	100 x 100 x 4	25.00	0.00	12.50	0	0	0.51	0.56	50.10	350	430
6	100 x 100 x 4	25.00	0.00	12.50	0	0	0.51	0.55	52.17	350	430
7	100 x 100 x 4	25.00	0.25	12.50	25	25	0.51	0.56	50.10	350	430
8	100 x 100 x 4	25.00	0.25	12.50	25	25	0.51	0.55	52.17	350	430
9	100 x 100 x 4	25.00	0.50	12.50	50	50	0.51	0.55	51.48	350	430
10	100 x 100 x 4	25.00	0.50	12.50	50	50	0.51	0.54	54.13	350	430
11	100 x 100 x 6	16.67	0.00	12.50	0	0	0.46	0.63	50.10	290	360
12	100 x 100 x 6	16.67	0.00	12.50	0	0	0.47	0.62	52.17	290	360
13	100 x 100 x 6	16.67	0.25	12.50	25	25	0.46	0.63	50.10	290	360
14	100 x 100 x 6	16.67	0.25	12.50	25	25	0.47	0.62	52.17	290	360
15	100 x 100 x 6	16.67	0.50	12.50	50	50	0.47	0.62	51.48	290	360
16	100 x 100 x 6	16.67	0.50	12.50	50	50	0.47	0.61	54.13	290	360
17	100 x 100 x 6	16.67	0.00	12.50	0	0	0.49	0.67	50.10	350	430
18	100 x 100 x 6	16.67	0.00	12.50	0	0	0.50	0.66	52.17	350	430
19	100 x 100 x 6	16.67	0.25	12.50	25	25	0.49	0.67	50.10	350	430

20	100 x 100 x 6	16.67	0.25	12.50	25	25	0.50	0.66	52.17	350	430
21	100 x 100 x 6	16.67	0.50	12.50	50	50	0.49	0.66	51.48	350	430
22	100 x 100 x 6	16.67	0.50	12.50	50	50	0.50	0.65	54.13	350	430

The steel contribution ratio δ and slenderness λ were calculated based on Eurocode 4 Part 1.1 [12] as follows.

$$\delta = \frac{A_a \times f_y}{N_{pl}} \tag{1}$$

Where A_a is the area of steel and N_{pl} is the squash load of the column.

$$\lambda = \sqrt{\frac{N_{pl}}{N_{cr}}} = \sqrt{\frac{A_c f_c + A_a f_y}{\frac{\pi^2 EI}{L^2}}} \tag{2}$$

Where A_c is the area of concrete and EI = $E_s I_s$ + 0.6E_{cm}; I_s and I_c are the second moment of inertia of the steel tube and concrete core respectively, E_s is the modulus of elasticity of steel and E_{cm} is the secant modulus of elasticity of concrete.

The CFST models were classified into six sets, Sb-t-e-f_y-I-P, Sb-t-e-f_y-III-P and Sb-t-e-f_y- V-P were modelled without using steel fibres, while a 0.75% volume of steel fiber was added to model Sb-t-e- f_y -II-SF, Sb-t-e-fy-IV-SF and Sb-t-e- f_y -VI-SF. The following label were used; "Sb-t- e- f_y -f_c-p/sf" where "b" is the columns breadth, "t" is the steel tube thickness "e" is the eccentric distance of the applied axial load, "f_y" is the steel yield strength, "f_c" is the concrete cylindrical strength, "p/sf" indicates whether it is a plain or steel fibre reinforced concrete infill.

2.2 Finite Element Mesh and Geometry

The main parameters of the model are the column breadth (B), the depth (D), the steel tube thickness (t) and the loading eccentricity (e). The plain and steel fiber CFST columns were modelled using shell and solid elements. The steel tube consisted of four-nodded quadrilateral shell element (S4R), while eight-nodded solid elements (C3D8R) with reduced integration were used for the concrete core. The loading end plate was modelled as rigid (R3D4) to enable an even stress distribution of the eccentric axial load to the column.

2.3 Boundary Condition and Column Loading

The column was modelled with a pin-pin end condition. A reference point was created on the loading plate to indicate the position of the ex and ey eccentric distance of the applied load.

2.4 Material Modelling of Steel Tube

The stress–strain curves for the steel tubes were taken from values used in the experimental tests conducted by Tokgoz and Dundar [11]. A modulus of elasticity of 200GPa and Poisson's ratio of 0.3 was employed. The yield stress and ultimate tensile strength values are also shown in Table 1(a) and (b) above.

2.5 Modelling of Confined Concrete

The concrete core was modelled using the concrete damaged plasticity (CDP) model available

in the standard and explicit material library (ABAQUS [13]). The concrete damaged plasticity model uses stress-strain relationships to correlate parameters for relative concrete damage for both tension and compression under uni-axial loading as shown in Figures 2(a) and 2(b).

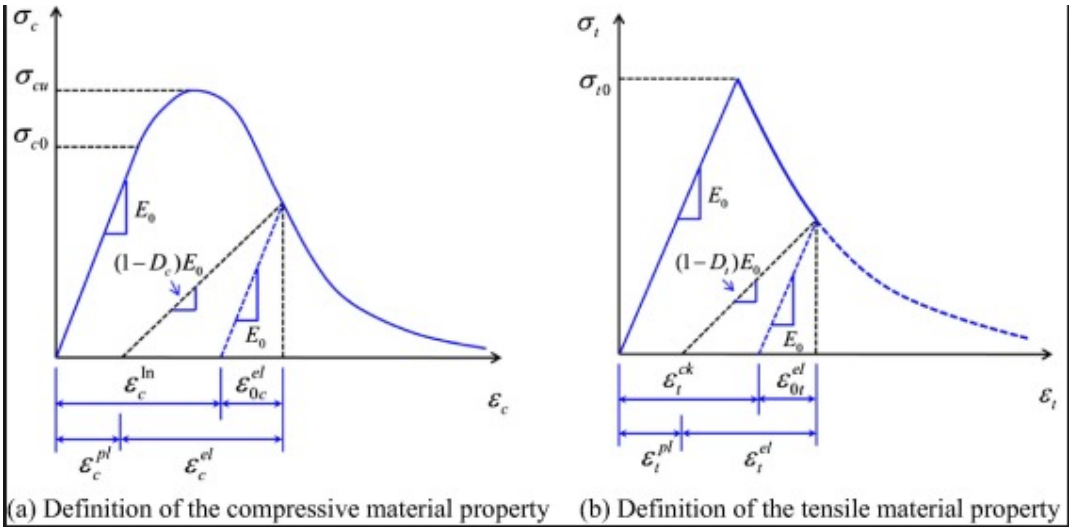

Figure 2. Concrete Damaged Plasticity Model

$$D = \frac{E}{E_0} \tag{3}$$

Where, D is the damage parameter of concrete in compression and tension, E_0 is the initial (undamaged) elastic stiffness of the material, E is the damaged elastic stiffness of the confined concrete and d_t and d_c are the damage indices of concrete in tension and compression. Eq. 3 was used in calculating the damage parameters under uni-axial tension and compression.

The approach used to model the effects of confinement of plain and steel fiber reinforced concrete was similar to the approach used by (Dai and Lam [14]). Figure 3 shows the equivalent uniaxial representation for the stress-strain curve of confined and unconfined concrete. f_c is the unconfined concrete cylindrical compressive strength which is equal to $0.8f_{cu}$; where f_{cu} is the cube compressive strength of the unconfined concrete. The unconfined strain (ε_c) value is taken as 0.003 for plain concrete as recommended by the ACI Specification (ACI [15]). f_{cc} and ε_{cc} are the confined concrete compressive strength and confined strain, respectively. As described by Mander et al. [16].

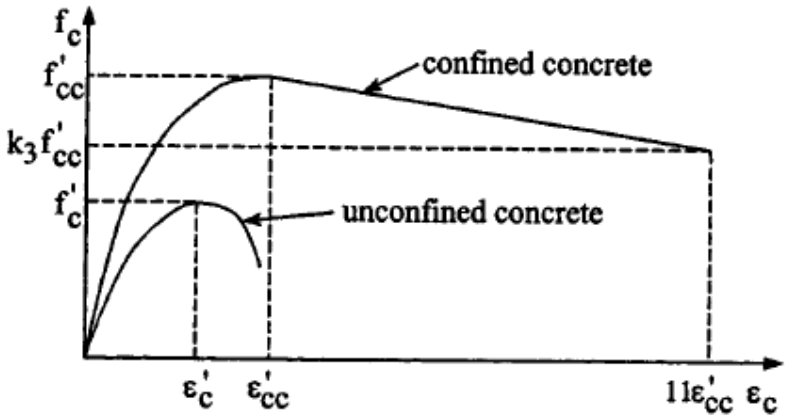

Figure 3. Confined Concrete Stress-strain Curve

$$f_{cc} = f_c + k_1 f_l \tag{4}$$

$$\varepsilon_{cc} = \varepsilon_c \left(1 + k_2 \frac{f_l}{f_c} \right) \tag{5}$$

Where f_l = lateral confining pressure from the steel tube section.

$$f_l = \frac{2\sigma\theta t}{D} \tag{6}$$

Where $\sigma\theta = 0.1\, f_y$ proposed by Mander et.al. [1 6] .

The factors k_1 and k_2 in Eqs. 4 and 5 are taken as 4.1 and 20.5 respectively, as given by Richart, Brandzaeg and Brown [17].

The equivalent stress–strain curves of unconfined and confined concrete are expressed in three parts. The first part defines the initial limit stress, which is taken as 0.5 f_{cc} as given by Hu et al. [18]. The Young's modulus of confined concrete is calculated using the empirical formula provided in the ACI code [15], given in Eq. 7.

$$E_{cc} = 4700\sqrt{f_{cc}}\, Mpa \tag{7}$$

Where f_{cc} is the strength of confined concrete. The Poisson's ratio of confined concrete is taken as 0.2 as given in EN 1992-1-1 [19]. The second part defines the nonlinear portion of the stress-strain curve starting from the proportional limit stress 0.5 f_{cc} to the confined strength of the concrete f_{cc} . This part of the curve was proposed by Saenz [20] and can be determined from Eq. 8.

$$f = \frac{E_c \varepsilon_c}{1 + (R + R_E - 2)\left(\frac{\varepsilon}{\varepsilon_{cc}}\right) - (2R - 1)\left(\frac{\varepsilon}{\varepsilon_{cc}}\right)^2 + R\left(\frac{\varepsilon}{\varepsilon_{cc}}\right)^2} \tag{8}$$

$$R_E = \frac{E_{cc}\varepsilon_{cc}}{f_{cc}} \tag{9}$$

$$R = \frac{R_E (R_\sigma - 1)}{(R_\sigma - 1)^2} - \frac{1}{R_\varepsilon} \tag{10}$$

Where the constants Rσ and Rε are equal to 4 as recommended by Hu and Schnobrich [21].

The third part defines the descending value of the confined concrete stress–strain curve; this part starts from the maximum confined concrete strength f_{cc} to a lower value $rk_{3c}\, f_{cc}$ with a corresponding strain value of $11\varepsilon_{cc}$ as proposed by Hu et al. [18].

2.6 Material Modelling of Steel Fiber

The steel fiber dosage used in the model was a 0.75% volume (58.88 kg/m^3) as described in the experimental tests. Table 2 shows the material geometry of the steel fiber is given in Musmar [22], Eq. 11 to determine the value of the tensile strength of the concrete.

Table 2. Steel Fibre Geometry

S.F Type	Density kg/m^3	%volume	Dosage (kg/m^3)	Length mm	Diameter mm
Hooked End	7850	0.75%	58.88	35	0.55

$$f_{sp} = \left(0.6 + 0.4\left(v_f \times \frac{L_f}{d}\right)\right) \times \sqrt{f_c'} \qquad (11)$$

Where f_{sp} is the concrete tensile strength in MPa, vf is the fiber volume, Lf = length of fiber, d = diameter of fiber and f_c is the compressive strength of concrete.

2.7 Concrete – Steel Tube Interface

Contact between the steel and concrete were modelled as a general contact. Friction between the two faces is maintained throughout when in contact. After conducting a parametric study for the coefficient of friction, 0.2 was chosen as it gave the best match for friction between the steel tube and concrete surfaces.

3. RESULTS AND DISCUSSION

The ultimate axial load and moment values for each column were reported in Table 3. Figure 4 shows the graphical plot of force vs B/t ratio, while Figure 5 shows graphical plot of moment vs B/t ratio for plain and steel fibre reinforced concrete infill for the CFST columns. It can be seen that the use of steel fibre reinforced concrete infill had little effect on the ultimate strength of the column. The steel tube thickness and load eccentricity are important factor which governed the ductility and ultimate strength of the columns.

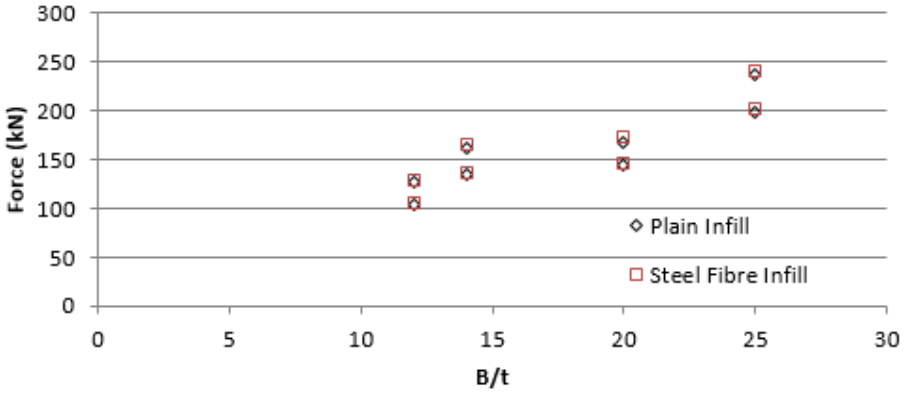

Figure 4. Force vs B/t Ratio

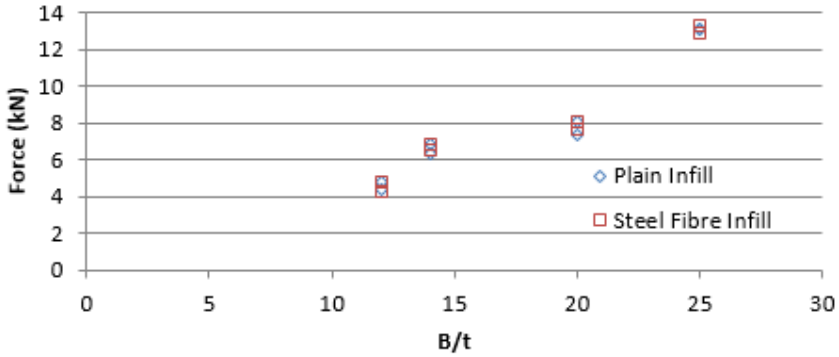

Figure 5. Moment vs B/t Ratio

Table 3. Finite Element Analysis Result

Model No.	Pp (kN)	PSF (kN)	MP (kN.m)	MSF (kN.m)
S60-5-30-290	126.6	128.1	4.36	4.3
S60-5-40-290	104.7	105.8	4.78	4.83
S70-5-35-290	161.3	164.8	6.31	6.57
S70-5-45-290	134.4	137.2	6.86	6.89
S80-4-40-290	167.8	173.8	7.39	7.72
S80-4-50-290	144.6	146.3	8.04	8.04
S100-4-50-290	237.5	239.9	13.06	12.88
S100-4-60-290	198.2	201.6	13.15	13.27

4. PARAMETRIC STUDY

Prior to a sensitivity analysis, The FEA results were validated with the laboratory experiments which is discussed extensively in the next section. The parameters investigated includes; the steel tube thickness, concrete compressive strength, e/D ratio and steel tube yield strength. Table 4 shows the result obtained from the parametric study.

Table 4. CFST Parametric Study

Model No.	PP (kN)	PSF (kN)	fy (MPa)	B/t
S100-4-0-290	826.9	867.3	290	25
S100-6-0-290	1006	1038.17	290	16.67
S100-4-0-350	927.3	963.6	350	25
S100-6-0-350	1147	1182	350	16.67
S100-4-25-290	364.6	401.3	290	25
S100-6-25-290	468	517.13	290	16.67
S100-4-25-350	408	449.1	350	25
S100-6-25-350	524.7	577.5	350	16.67
S100-4-50-290	237.5	239.9	290	25
S100-6-50-290	311.2	317	290	16.67
S100-4-50-350	269.8	276.7	350	25
S100-6-50-350	354.9	353.8	350	16.67

4.1 Steel Tube Thickness

For an increase in steel tube thickness from 4mm to 6mm there was a 21% increase in ultimate strength for columns loaded under compression only. For columns loaded with combined compression and bending, the increase recorded was about 32%. Figure 6 shows the steel tube thickness has a significant effect on the ductility of the columns. For columns having a depth over thickness (D/t) ratio greater than 18 and eccentricity over depth (e/D) ratio greater than 0.5, there was an uneven stress distribution during the early stages of load application which resulted in a premature plastic deformation at the top of the steel tube perpendicular to the eccentric load direction.

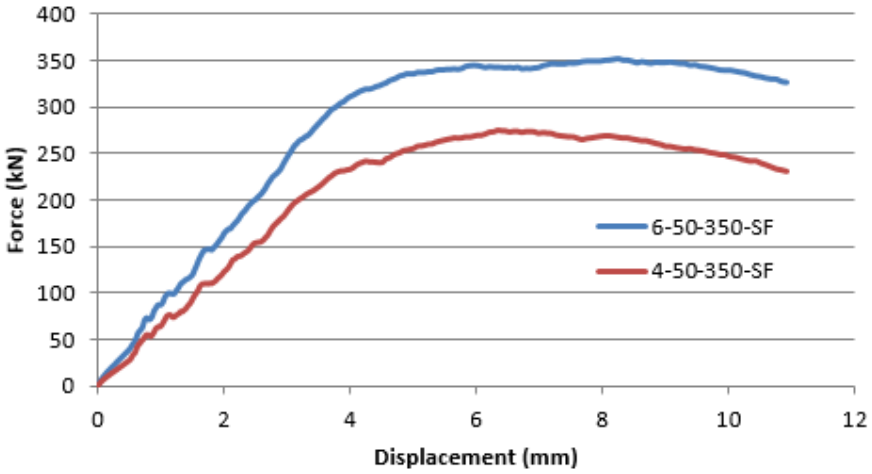

Figure 6. Steel Tube Thickness Effectiveness

4.2 Concrete Compressive Strength

The concrete compressive strength had little effect on the ultimate strength value recorded for each column due to the slenderness of the column. Figures 7 (a) and 7(b) shows columns filled with steel fibre reinforced concrete (SFRC) and plain concrete. The SFRC columns maintained its ultimate strength value for a longer time period and therefore, gave the column a better ductility. For columns filled with plain concrete, there was a sudden drop in the strength of the columns. Figures 8(a) and 8(b) shows columns subjected to combine bending and compression, it was observed that columns filled with steel fibre reinforced concrete maintained 85% of its axial strength while the displacement increased.

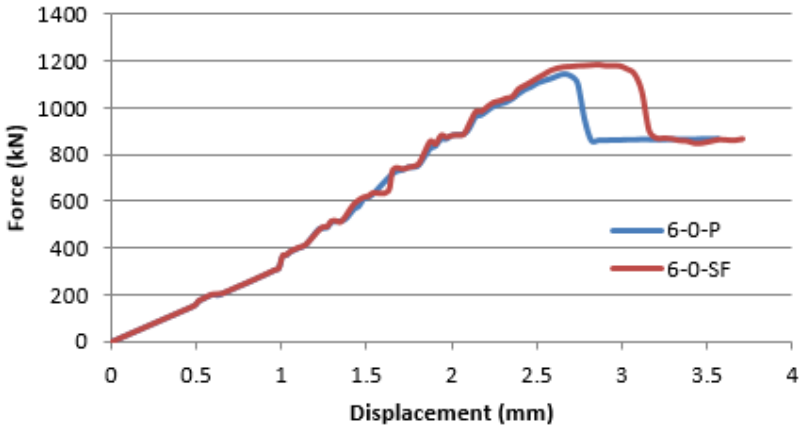

(a) 6 mm steel tube thickness

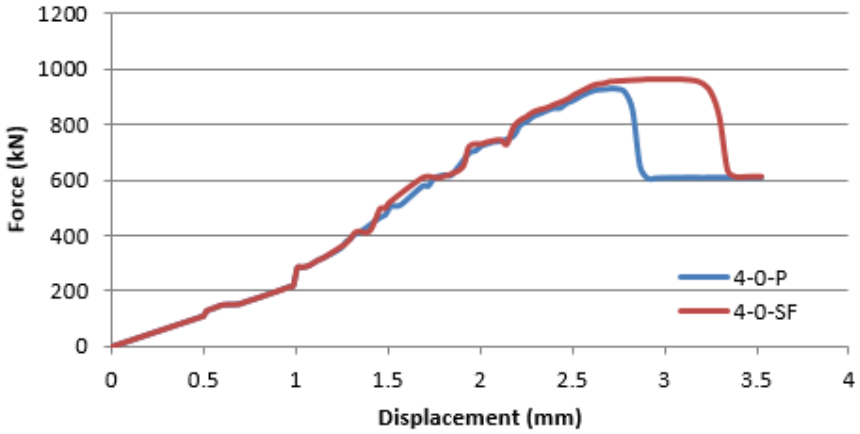

(b) 4 mm steel tube thickness

Figure 7. Effectiveness of Concrete Compressive Strength under Compression Only

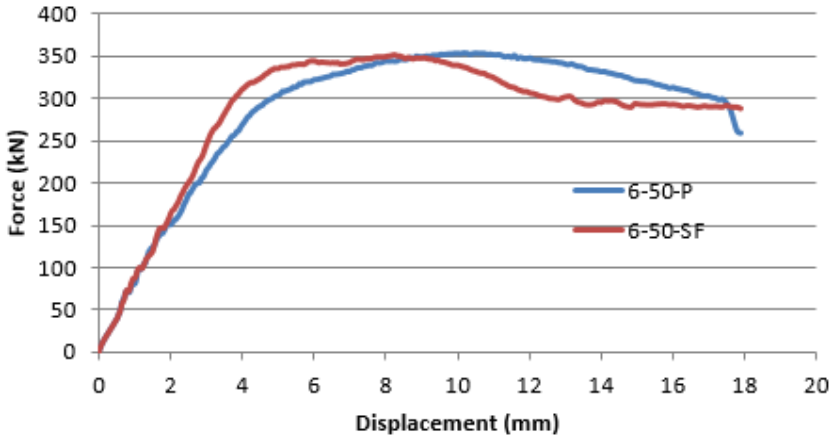

(a) 6 mm steel tube thickness

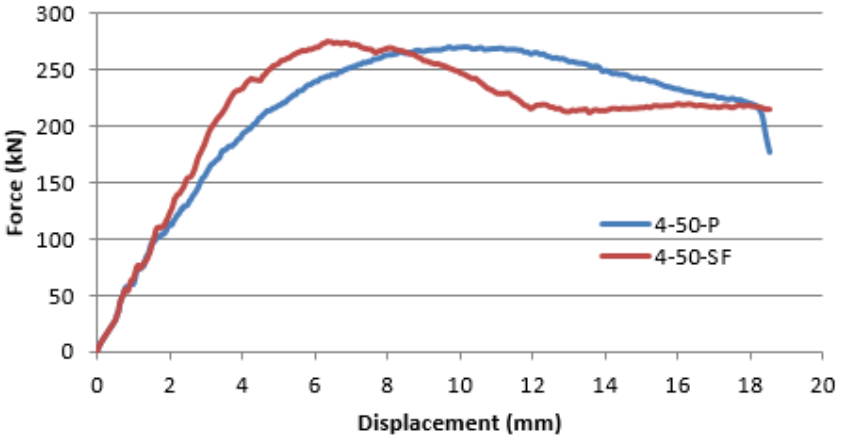

(b) 4 mm steel tube thickness

Figure 8. Effectiveness of Concrete Compressive Strength under Combine Bending and Compression

4.3 Load Eccentricity

The e/D ratio of the column was a contributing factor to the ultimate strength and moment values recorded. Figure 9 (a) shows for a 10mm increase in eccentric load distance of the columns, there was an average of 20% decrease in the ultimate strength value recorded for all CFST columns, however, the moment values recorded were not significantly affected. Figure 9 (b) shows there was an average of 6% increase in moment value recorded, with a 10mm increase in the eccentric load distance of the applied axial load.

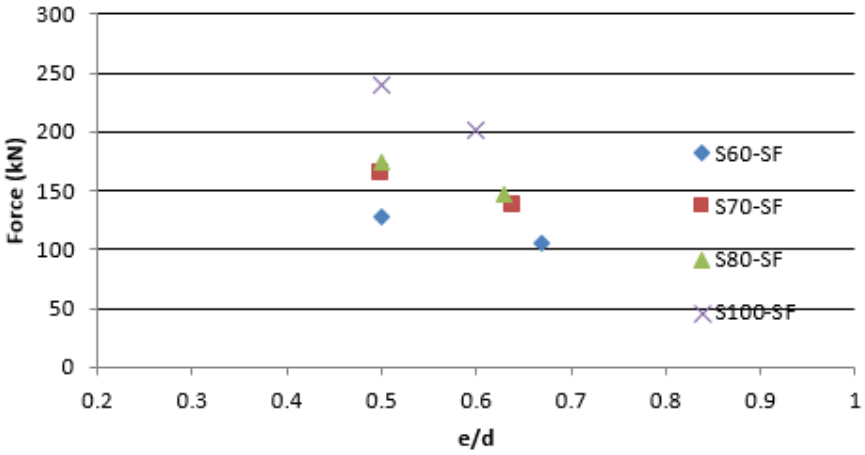

(a) Force Vs e/D ratio

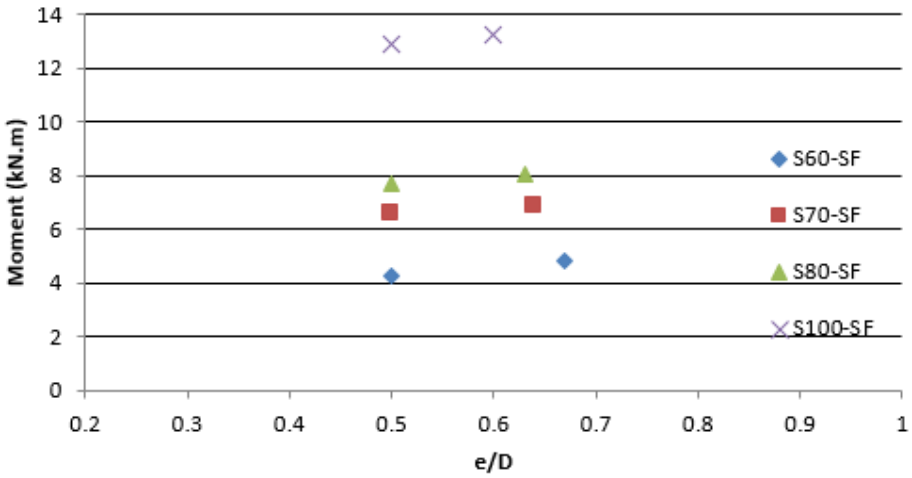

b) Moment Vs e/D ratio

Figure 9. Effectiveness of e/D Ratio of the Column

4.4 Steel Tube Yield Strength

The steel tube yield strength contributed significantly to the ultimate axial strength, but did not affect the ductility of the column. For a 20% increase in the steel tube yield strength there was a corresponding 14% increase in the axial strength of the column. Figure 10 shows the load deflection curve comparison of columns having similar geometries, but different steel tube yield strength.

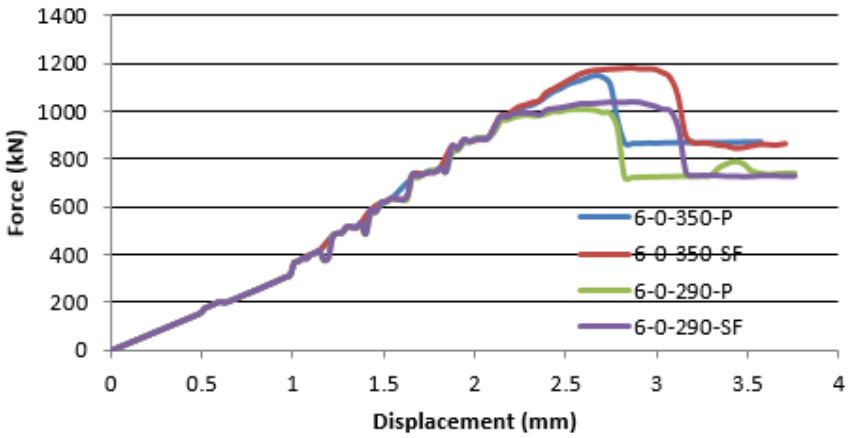

Figure 10. Steel Tube Yield Strength Effectiveness

4.5 Concrete Infill Type

The addition of steel fibre to the concrete increases the tensile strength of the concrete and also controls the crack width propagation of the column. For columns filled with steel fibre reinforced concrete, the tensile damage of the concrete was relatively low compared to columns filled with plain concrete and this affected the crack propagation and ductility of the column. Figures 11(a) and (b) shows the concrete tensile damage for S60-5-30-290-I-P and S60-5-30-290-II-SF respectively, when a load of 100kN was applied to the column.

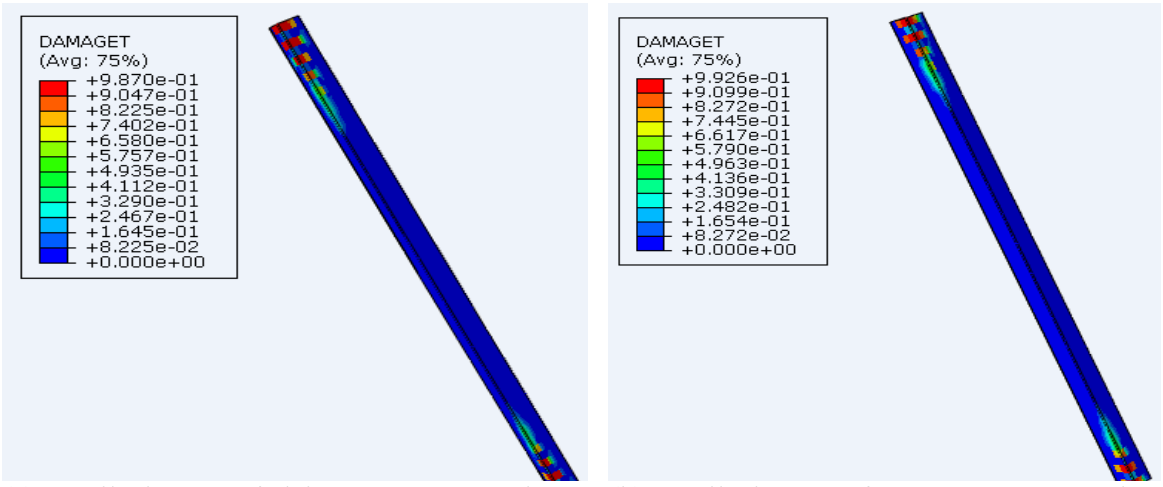

(a) Tensile damage of plain Concrete at 100kN (b) Tensile damage of SFR concrete at 100kN

Figure 11. Effectiveness of Concrete Infill

5. COMPARISON OF FINITE ELEMENT ANALYSIS WITH LABORATORY EXPERIMENT AND EUROCODE 4 DESIGN GUIDE

There was good correlation between recorded values obtained from the numerical analysis when compared to the experimental and Eurocode 4 values. The axial compressive strength known as the squash load of a tubular column is calculated by adding the strength of its members as given in Eurocode 4 Part 1-1. A further calculation needs to be carried out when the column is loaded under combined compression and bending. The ultimate axial strength obtained from the finite element

(PFEA) analysis, laboratory experiments (PEXP) and Eurocode 4 calculations (PEC4) are reported in Table 5. The squash load for a fully encased concrete filled steel tube column according to Eurocode 4 is calculated using Eq. 12. Figures 12(a) and (b) shows the plot of force vs moment, while Figures 13 (a) to (d) shows the load deflection curve comparison for the laboratory experiments and FEA.

$$P_{EC4} = A_a f_y + A_c f_c \quad (12)$$

Where f_y is the yield strength of the structural steel, f_c is the cylindrical compressive strength of concrete. A_a and A_c are the area of steel and concrete respectively.

The moment (M) of the column at mid-height was calculated using the equation $M = P \times (e + d_m)$ where P is the ultimate load, e is the eccentric distance and d_m is the deflection of the column at mid-height.

Table 5. Finite Element Analysis, Laboratory Experiments and Eurocode 4 Comparison

Model No.	P_{FEA} kN	P_{EXP} kN	P_{EC4} kN	M_{FEA} kN.m	M_{EXP} kN.m	M_{EC4} kN.m	$\frac{P_{EXP}}{P_{FEA}}$	$\frac{P_{EC4}}{P_{FEA}}$	$\frac{M_{EXP}}{M_{FEA}}$	$\frac{M_{Ec4}}{M_{FEA}}$
S60-5-30-290-I-P	126.6	128	127.6	4.36	4.48	3.83	1.01	1.01	1.03	0.88
S60-5-30-290-II-SF	128.1	124	129.7	4.3	4.5	3.89	0.97	1.01	1.05	0.91
S60-5-40-290-III-P	104.7	97	110.3	4.78	4.6	4.42	0.93	1.05	0.96	0.92
S60-5-40-290-IV-SF	105.8	104	112	4.83	4.63	4.48	0.98	1.06	0.96	0.93
S70-5-35-290-I-P	161.3	168	162.6	6.31	6.41	5.69	1.04	1.01	1.02	0.90
S70-5-35-290-II-SF	164.8	174	165.7	6.57	6.46	5.80	1.06	1.01	0.98	0.88
S70-5-45-290-III-P	134.4	142	144.8	6.86	6.61	6.52	1.06	1.08	0.96	0.95
S70-5-45-290-IV-SF	137.2	148	147.1	6.89	6.65	6.62	1.08	1.07	0.97	0.96
S80-4-40-290-I-P	167.8	173	184.5	7.39	7.65	7.38	1.03	1.10	1.04	1.00
S80-4-40-290-II-SF	173.8	175	189	7.72	7.9	7.56	1.01	1.09	1.02	0.98
S80-4-50-290-III-P	144.6	147	158.8	8.04	7.87	7.94	1.02	1.10	0.98	0.99
S80-4-50-290-IV-SF	146.3	156	160.5	8.04	7.92	8.02	1.07	1.10	0.99	1.00
S100-4-50-290-I-P	237.5	245	255.2	13.06	12.99	12.76	1.03	1.07	0.99	0.98
S100-4-50-290-II-SF	239.9	248	258.9	12.88	13.13	12.95	1.03	1.08	1.02	1.01
S100-4-60-290-III-P	198.2	218	225.6	13.15	13.33	13.53	1.10	1.14	1.01	1.03
S100-4-60-290-IV-SF	201.6	222	227.2	13.27	13.44	13.63	1.10	1.13	1.01	1.03
Mean							**1.03**	**1.07**	**1.00**	**0.96**
Standard Deviation							**0.05**	**0.04**	**0.03**	**0.05**

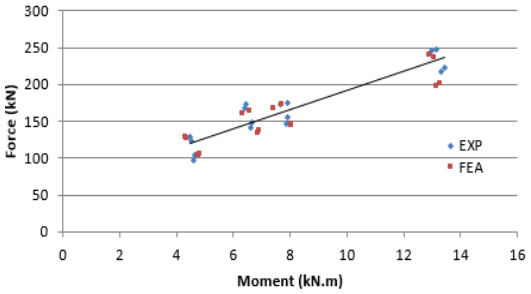

(a) Comparison of FEA with experiment

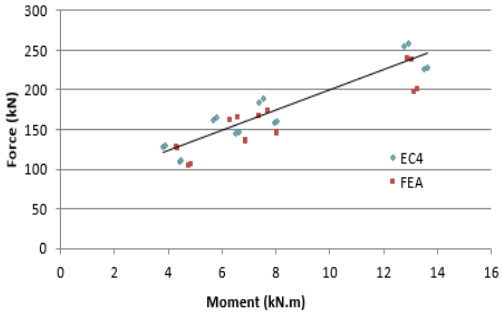

(b) Comparison of FEA with Eurocode 4

Figure 12. Force vs Moment Plot Comparison

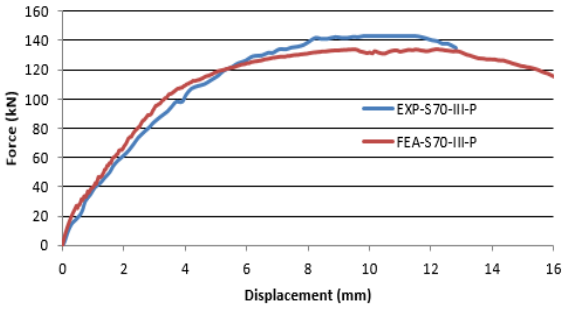

(a) Force vs Displacement

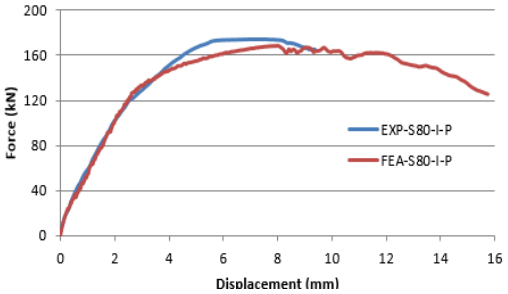

(b) Force vs Displacement

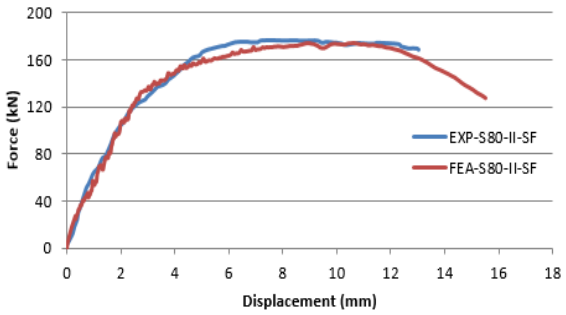

(c) Force vs Displacement

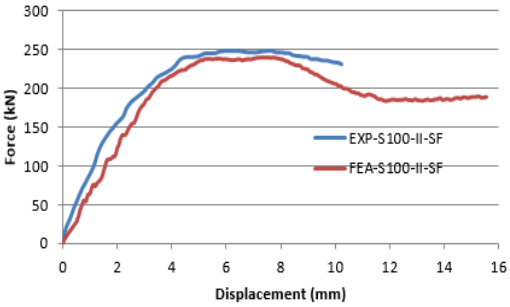

(d) Force vs Displacement

Figure 13. Force vs Displacement Curve FEA and Laboratory Experiment Comparison

6. CONCLUSIONS

The computational finite element modelling of concrete filled steel tubular column with plain and steel fiber reinforced concrete infill is presented in this study. There was a good agreement between ultimate strength and moment values of the columns when compared to values obtained from experimental data and Eurocode 4 Part 1-1.

Addition of steel fiber to the concrete had little effect on the ultimate strength of the column. However, this affected the ductility and crack width propagation of the column and also increased the concrete tensile strength. This indicates that for CFST columns filled with steel fiber reinforced concrete, the column will have a higher ductility when compared to using a plain concrete infill. The steel tube yield strength had an effect on the ultimate axial strength of the column; however, it did not contribute to the ductility of the column. It is recommended to increase the steel tube thickness rather than using a steel tube section with a higher yield strength for design purposes. Using an e/D ratio less than 0.5 for the construction of slender columns is recommended so as to utilize the full section of the column when loaded axially.

ACKNOWLEDGEMENTS

The authors wish to express gratitude to the Heavy Engineering Educational & Research Foundation (HEERF) for their scholarship support. The authors also acknowledge the contribution of NeSI high-performance computing facilities to the results of this research. NZ's national facilities are provided by the NZ eScience Infrastructure and funded jointly by NeSI's collaborator institutions and through the Ministry of Business, Innovation & Employment's Research Infrastructure programme.

REFERENCES

[1] Han, L, Zhao, X. and Lu, H., "Concrete-filled Tubular Members and Connections", CRC Press. 2014.

[2] Kitada, T., "Ultimate Strength and Ductility of State-of-the-art Concrete-filled Steel Bridge Piers in Japan", Eng. Struct., 1998, Vol. 20, No. 4-6, pp. 347-54.

[3] Brauns, J., "Analysis of Stress State in Concrete-filled Steel Column", Journal of Constructional Steel Research ", 1999, Vol. 49, No. 2, pp.189-96.

[4] Ellobody, E., Young, B. and Lam, D., "Behaviour of Normal and High Strength Concrete-filled Compact Steel Tube Circular Stub Columns", Journal of Constructional Steel Research, 2006, Vol. 62, No. 7, pp. 706-15.

[5] Ellobody, E., "Numerical Modelling of Fibre Reinforced Concrete-filled Stainless Steel Tubular Columns", Thin-Walled Structures, 2013, Vol. 63, pp. 1-12.

[6] Zhao, Lok, Li, and Lim, "Behavior of Steel Fiber Reinforced Concrete under Dynamic Load, Proc., 4th Asia-Pacific Conf. on Shock and Impact Loads on Structures: CI-Premier, Singapore, 2001.

[7] Zeghiche, J. and Chaoui, K., "An Experimental Behaviour of Concrete-filled Steel Tubular Columns", Journal of Constructional Steel Research, 2005, Vol. 61, No. 1, pp. 53-66.

[8] Johansson, M. and Gylltoft, K., "Structural Bhavior of Slender Circular Steel-concrete Composite Columns under Various Means of Load Application", Steel and Composite Structures 2001, Vol. 1, No. 4, pp. 393-410.

[9] Eltobgy, H.H., "Structural Design of Steel Fibre Reinforced Concrete in-filled Steel Circular Columns", Steel and Composite Structures, 2013, Vol. 14, No. 3, pp. 267-82.

[10] Gopal, S.R. and Manoharan, P.D., "Experimental Behaviour of Eccentrically Loaded Slender Circular Hollow Steel Columns in-filled with Fibre Reinforced Concrete", Journal of Constructional Steel Research, 2006, Vol. 62, No. 5, pp. 513-20.

[11] Tokgoz, S. and Dundar, C., "Experimental Study on Steel Tubular Columns in-filled with Plain and Steel Fiber Reinforced Concrete", Thin-Walled Structures, 2010, Vol. 48, No. 6, pp.414-22.

[12] CEN. EN 1994-1-1, Eurocode 4: Design of Composite Steel and Concrete Structures–Part 1-1: General Rules and Rules for Buildings, Comité Européen de Normalisation 2005.
[13] Simulia, D. ABAQUS 6.13 User's Manual. Dassault Systems, Providence, RI 2013.
[14] Dai, X. and Lam, D., "Numerical Modelling of the Axial Compressive Behaviour of Short Concrete-filled Elliptical Steel Columns", Journal of Constructional Steel Research, 2010, Vol. 66, No. 7, pp. 931-42.
[15] ACI B. 318-Building Code Requirements for Reinforced Concrete and Commentary, American Concrete Institute International 1999.
[16] Mander, J.B., Priestley, M.J. and Park, R., "Theoretical Stress-strain Model for Confined Concrete", J. Struct. Eng., 1988, Vol. 114, No. 8, pp. 1804-26.
[17] Richart, F.E., Brandtzaeg, A. and Brown, R.L., "A Study of the Failure of Concrete under Combined Compressive Stresses, 1928.
[18] Hu, H., Huang, C., Wu, M., Wu, Y., "Nonlinear Analysis of Axially Loaded Concrete-filled Tube Columns with Confinement Effect", J. Struct. Eng., 2003, Vol. 129, No. 10, pp. 1322-9.
[19] CEN E. Eurocode 2: Design of Concrete Structures, European Committee for Standardization, 1992.
[20] Saenz, LP., "Equation for the Stress-strain Curve of Concrete", ACIJour. 1964, Vol. 61, No. 9, pp. 1229-35.
[21] Hu, H. and Schnobrich, W.C., "Constitutive Modeling of Concrete by Using Nonassociated Plasticity", J. Mater. Civ. Eng., 1989, Vol. 1, No. 4, pp. 199-216.
[22] Musmar, M., "Tensile Strength of Steel Fiber Reinforced Concrete", Contemporary Engineering Sciences, 2013, Vol. 6, No. 5, pp. 225-37.

SECOND ANNOUNCEMENT AND CALL FOR PAPERS

NINTH INTERNATIONAL CONFERENCE ON ADVANCES IN STEEL STRUCTURES (ICASS 2018)

5-7 December 2018 - Hong Kong, China

Jointly organised by

The Hong Kong Institute of Steel Construction
&
Department of Civil and Environmental Engineering
The Hong Kong Polytechnic University

This will be the ninth in the international conference series on Advances in Steel Structures, with the first, second, third and sixth of the conferences series held in Hong Kong, fourth in Shanghai, fifth in Singapore, seventh in Nanjing and eighth in Portugal. As with the eight previous successful conferences, this conference is intended to provide a forum for researchers and professionals to discuss and disseminate recent advances in analysis, behaviour, design and construction of steel, aluminium and composite steel-concrete structures.

Those wishing to participate in the conference are invited to submit short 200-400 word abstracts for papers related to the general topics of the conference, which are: Aluminium and Glass Structures, Analysis Method, Cold-Formed Steel, Composite Construction, Connections, Design, Experiment, Expert Systems, Fatigue and Fracture, Frames, Offshore Platforms, Performance-based Structural Design, Prefabricated Construction, Scaffolding, Seismic-resistant Structures, Stability Design, Steel, Steel Structures, Structural Health Monitoring, Structural Optimisation, Structural Stability and Sustainability. Selected papers will also be published in the International Journal of Advances in Steel Construction which carries a mission of technology transfer and is widely circulated among the engineering and building professionals.

Please use the template to prepare an abstract and send it to ICASS2018@outlook.com. Abstracts and papers will be peer-reviewed by the Scientific Committee.

香港鋼結構學會 Hong Kong Institute of Steel Construction
THE HONG KONG POLYTECHNIC UNIVERSITY 香港理工大學
DEPARTMENT OF CIVIL AND ENVIRONMENTAL ENGINEERING 土木及環境工程學系 CEE

INTERNATIONAL SCIENTIFIC COMMITTEE

F.G. Albermani (Australia)
R. Beale (UK)
F.S.K. Bijlaard (Netherlands)
R. Bjorhovde (USA)
M.A. Bradford (Australia)
D. Camotim (Portugal)
J.M. Castro (Portugal)
T.H.T. Chan (Australia)
W.F. Chen (USA)
Y.Y. Chen (China)
S.P. Chiew (Singapore)
Y.S. Choo (Singapore)
G.G. Deierlein (USA)
S.L. Dong (China)
D. Dubina (Romania)
L. Gardner (UK)
H.B. Ge (Japan)
Y. Goto (Japan)
Y.L. Guo (China)
L.H. Han (China)
G.J. Hancock (Australia)
T. Helwig (USA)
S. Herion (Germany)
B.A. Izzuddin (UK)
J.P. Jaspart (Belgium)
S.A. Jayachandran (India)
T.L. Karavasilis (UK)
S.E. Kim (Korea)
S. Kitipornchai (Australia)
K. Kwok (Australia)
D. Lam (UK)
S.S. Law (China)
W. Li (China)
G.Q. Li (China)
J.Y.R. Liew (Singapore)
D. Lignos (Switzerland)
L.R.O. de Lima (Brazil)
T.H. Lip (Australia)
E.M. Lui (USA)
Y.L. Mo (USA)
D.A. Nethercot (UK)
J.G. Nie (China)
J.A. Packer (Canada)
J.L. Peng (Taiwan)
X.D. Qian (Singapore)
K. Rasmussen (Australia)
J. Ricles (USA)
J.M. Rotter (UK)
R. Sause (USA)
P. Schaumann (Germany)
N.E. Shanmugam (Singapore)
Y.J. Shi (China)
G. Shi (China)
G.P. Shu (China)
X.P. Shu (China)
L.S.da Silva (Portugal)
N. Silvestre (Portugal)
G.S. Tong (China)
N.S. Trahair (Australia)
K.C. Tsai (Taiwan)
C.M. Uang (USA)
B. Uy (Australia)
M. Veljkovic (Netherlands)
P.C.G. da S. Vellasco (Brazil)
A. Wadee (UK)
F. Wald (Czech)
A. Walicka (Poland)
E. Walicki (Poland)
L.J. Wang (China)
W. Wang (China)
Y.C. Wang (UK)
C.M. Wang (Australia)
D. White (USA)
E. Yamaguchi (Japan)
Y.B. Yang (China)
Q.R. Yue (China)
R. Zandonini (Italy)
X.L. Zhao (Australia)
X.H. Zhou (China)
R.D. Ziemian (USA)

IMPORTANT DATES

First call for paper:	1 January 2018
Abstract submission deadline:	1 March 2018
Notification of abstract acceptance:	1 April 2018
Full paper submission:	1 June 2018
Notification of full paper acceptance:	1 August 2018
Early bird registration:	on or before 1 September 2018
Announcement of programme:	1 October 2018

REGISTRATION FEE

The conference registration fee is US$750 (Early bird registration before 1st September 2018)/US$850, which covers conference proceedings, conference banquet, lunches and refreshments.

OFFICIAL LANGUAGE

English will be the official language of the Conference for both oral and written presentations.

PROCEEDINGS

The proceedings of the conference will be published by the Hong Kong Institute of Steel Construction.

ORGANISING COMMITTEE

Siu-Lai Chan (Chair) Tak-Ming Chan (Co-Chair) Songye Zhu (Co-Chair)
Yaopeng Liu Siwei Liu

LOCAL SCIENTIFIC COMMITTEE

Francis.T.K. Au	Goman.W.M. Ho	Y.Q. Ni	A.S. Usmani
C.M. Chan	Eddie S.S. Lam	S.J. Pan	Y. Xia
W.T. Chan	Paul H.F. Lam	Derek K.L. So	Jackie Yau
Edward S.C. Chan	C.K. Lau	Andrew K.W. So	Ben Young
W.K. Chow	Andy Lee	Ray K.L. Su	W.K. Dominic Yu
Reuben Chu	Y.S. Liu	J.G. Teng	S.W. Yuen
J.G. Dai	S.H. Lo	Ben Tse	Z.H. Zhou

SUPPORTING INSTITUTIONS

ASCE HONG KONG SECTION
HKIE THE HONG KONG INSTITUTION OF ENGINEERS 香港工程師學會 — Civil, Fire and Structural Divisions
RCATISE Research Centre for Advanced Technology in Structural Engineering, The Hong Kong Polytechnic University

SUPPORTING JOURNAL

ADVANCED STEEL CONSTRUCTION an international journal

ORGANIZING PARTNER

NIDA®

For further information, please contact:
Carol Deng - Conference Secretary
E-mail: icass2018@outlook.com
Address: International Journal of Advanced Steel Construction, CEE, The Hong Kong Polytechnic University, Hong Kong, China.

CONFERENCE WEBSITE:
http://www.icass2018.com

ORDER FORM

ISSN 1816-112X

Advanced Steel Construction, an international journal

Indexed by the Science Citation Index Expanded, Materials Science Citation Index and ISI Alerting Services

From: _____

To: ***Secretariat, Advanced Steel Construction, an international journal***
Fax: (852) 2334-6389

I/ We would like to enter a subscription to the ***International Journal of Advanced Steel Construction (IJASC)*** *published by The Hong Kong Institute of Steel Construction.*

Please complete the form and send to:

International Journal of Advanced Steel Construction
c/o Department of Civil and Environmental Engineering
The Hong Kong Polytechnic University
Hunghom, Kowloon, Hong Kong

Fax: (852) 2334-6389 Email: ceslchan@polyu.edu.hk

Published by : The Hong Kong Institute of Steel Construction
Website: http://www.hkisc.org/

Please tick the appropriate box

- ❑ Please enter my hard-copy subscription **(4 issues per year)**.
- ❑ Please send me a complimentary copy of the *Advanced Steel Construction, an International Journal (IJASC).*

Please tick the appropriate box(es)

	Print	**On-line is free**
Personal	❑ US$ 125	
Institutional	❑ US$ 280	

Total Amount **US$** _____

Methods of payment *(please tick the appropriate box(es))*

- ❑ Please invoice me
- ❑ Cheque enclosed for US$ _____ payable to Hong Kong Institute of Steel Construction Limited (No personal cheque accepted)

Ship to

Name (Prof./ Dr./ Mr./ Ms.) _____
Address _____
_____
_____
City/ State/ Postal Code _____
Country _____
Email _____ Fax _____